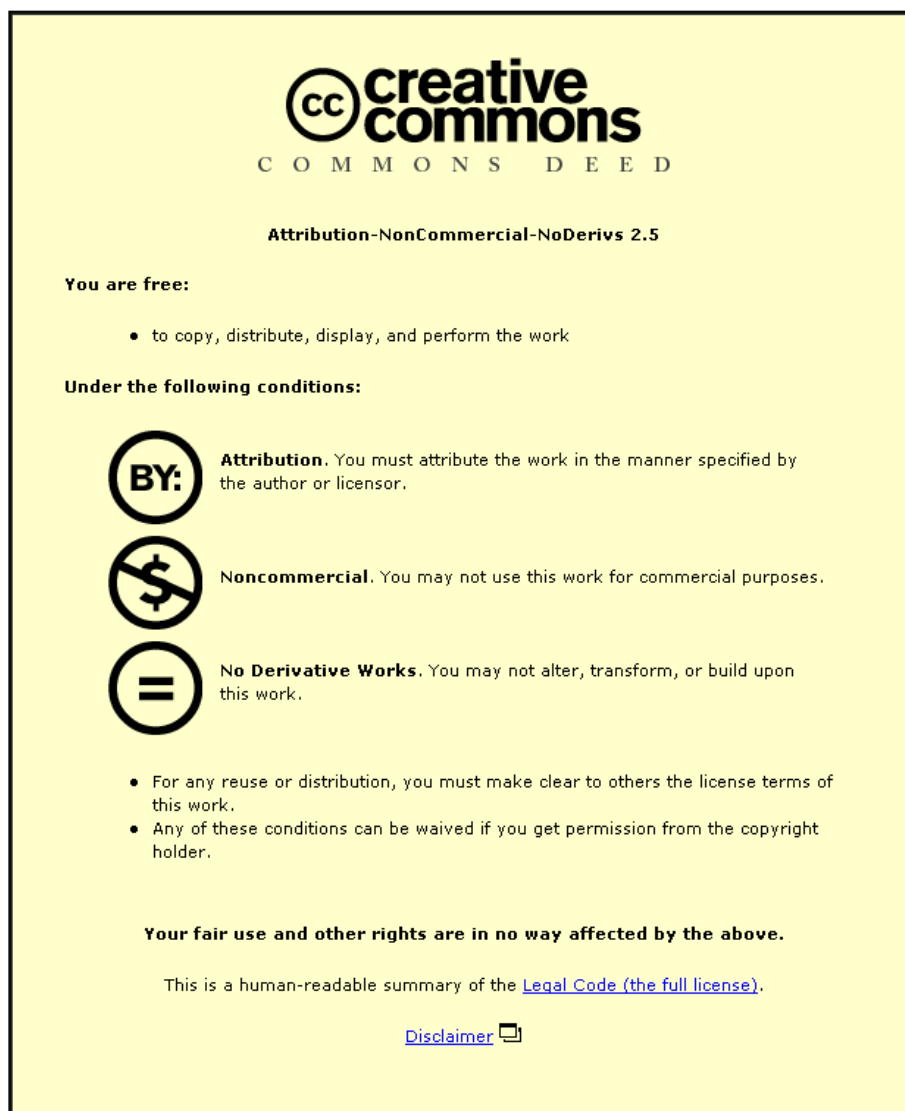


This item was submitted to Loughborough University as a PhD thesis by the author and is made available in the Institutional Repository (<https://dspace.lboro.ac.uk/>) under the following Creative Commons Licence conditions.



For the full text of this licence, please go to:
<http://creativecommons.org/licenses/by-nc-nd/2.5/>

Modelling thin film growth over realistic time scales

by

Sabrina Blackwell

A Doctoral Thesis

Submitted in partial fulfilment of the requirements for the award of
Doctor of Philosophy of Loughborough University

September 2012

Abstract

Energy security and supply is a key problem for the UK in the coming years. Photovoltaics have an important role to play in this. In order for demand to be met, continued research into new materials and methods of production is necessary. By modelling deposition techniques using classical molecular dynamics (MD), an atomistic scale understanding can be obtained. Combining this with long time scale dynamics (LTSD) techniques allows us to also model diffusion and surface growth over realistic time scales. The LTSD technique applied throughout this project is an on-the-fly Kinetic Monte Carlo (otf-KMC) method, which determines diffusion pathways and barriers, in parallel, with no prior knowledge of the involved transitions. These simulation techniques allow parameters such as deposition energy, substrate bias and plasma pressure to be easily changed to gain understanding of their effects. During this project, growth via industrial scale deposition techniques has been simulated, including evaporation (thermal and electron beam), ion-beam assisted evaporation and reactive magnetron sputtering.

Metal thin films, of interest due to their uses in reflectors in concentrator photovoltaics, electrical conductors in the monolithic interconnect processes and back contacts, were investigated using otf-KMC. Ag and Al film growth was simulated for around 0.3 seconds of real time. It was found that Ag has the ability to grow smooth surfaces, using several mechanisms including multiple-atom concerted motion, exchange mechanisms, and damage and repair mechanisms. Ag (111) and (100) surfaces grew dense, complete and crystalline films when sputtering was simulated, however, evaporation deposition produced incomplete layers. The inclusion of Ar in the ion-beam assisted evaporation of Ag (111) aided growth by transferring extra energy to the surface allowing increased diffusion and atomic mixing. Al (111) and (100), however, show different patterns. Growth by evaporation deposition and magnetron sputtering actually produced very similar results. The inclusion of the ion-beam assist on the (111) surface actually damaged the film, producing sub-surface Ar clusters where Al atoms were displaced, creating voids throughout the film. Otf-KMC methods enabled the investigation of specific mechanisms allowing film growth and a very important transition enabling the smooth and complete Al film growth was found to be the Ehrlich-Schwoebel (ES) barrier. The ES barrier involves an atom dropping off a step edge of an island and this barrier was found to be much smaller for the Al surfaces, therefore allowing the more complete growth from both evaporation and sputtering.

Metal oxides are also of great interest in the photovoltaic industry. The rutile TiO_2 (110) surface was investigated using single point depositions, high temperature MD and otf-KMC. Otf-KMC enabled the simulation for up to 9 seconds of real time, totally inaccessible using traditional simulation methods. Results concluded that the evaporation deposition process produced a void filled, incomplete structure, even with the use of a low energy ion-beam assist, this material is of interest for dye-sensitised solar cells where a dye is injected into the voids. Sputtering, however, produced dense and crystalline film, which is much more applicable to anti-reflective coatings where a crystalline structure is required. Mechanisms which

enabled crystalline rutile to form were also investigated, highlighting Ti interstitial annealing in the presence of an O rich surface as an important rutile growth mechanism.

ZnO, an inorganic compound with many uses including transparent conductive oxides, is investigated in the most stable wurtzite phase. The O-terminated $(000\bar{1})$ polar surface was used as the substrate for otf-KMC growth simulations, where around 1 second of real time was simulated. Evaporation deposition of a stoichiometric distribution of deposition species was found to produce the best quality film, however, a phase boundary was observed where an area of zinc blende forms within the wurtzite. Sputtering resulted in a denser, more complete and crystalline structure due to the higher deposition energy of arriving species, similar to the TiO_2 results. Post-annealing at 770K did not allow complete recrystallisation, resulting in films with stacking faults where monolayers formed in the zinc blende phase. Annealing at 920K, however, in some cases enabled the complete recrystallisation of films back into the wurtzite structure. Although, the higher annealing temperature did not always enable recrystallisation and in some cases both wurtzite and zinc blende phases existed in the same layer, resulting in a phase boundary. An important mechanism for the nucleation of ZnO growth was found to be the formation and vibration of Zn_xO_y strings on the surface, which after hundreds of milliseconds formed the desired hexagonal structure.

Combining MD and otf-KMC enabled the simulation of systems over very large time scales which were previously totally inaccessible. Key mechanisms occurring during the growth of metals and metal oxides were investigated, providing a much more precise understanding of how growth occurs. It is clear from the work that the deposition technique used plays a significant role on the resulting film quality and surface morphology and we are now able to provide an insight into the optimum conditions under which complete, crystalline layers can form.

Acknowledgements

I am very thankful to all my supervisors, Dr. Steven Kenny, Prof. Roger Smith and Prof. Mike Walls, for giving me the opportunity to undertake this PhD and for providing excellent guidance throughout the entire project.

I owe huge thanks to Louis Vernon for developing the on-the-fly Kinetic Monte Carlo software, used throughout this work. Marc Robinson also deserves thanks for the development of the visualisation software which was key in the analysis and understanding of growth mechanisms. I am also grateful to my other colleagues in the group, Chris Scott and Zainab Al-Tooq especially, for many helpful discussions in the office. I must also thank Dr. Carlos F. Sanz-Navarro for his part in the development of the LBOMD molecular dynamics package which is used throughout this work.

I must also thank Loughborough University for the funding which allowed me to carry out this work and for providing the facilities to undertake the research.

I am very grateful to my loving parents and sister for their continued encouragement and support throughout the PhD, which at times kept me going.

Contents

1	Introduction	1
1.1	Research Aims	1
1.2	Simulation Techniques	2
1.3	Experimental Techniques	4
1.4	Materials of Interest	10
1.5	Thesis Layout	11
2	Methods I: Molecular Dynamics	13
2.1	Introduction	14
2.2	Evolving the System	15
2.3	Interatomic Potentials	16
2.3.1	Lennard-Jones Potential	17
2.3.2	Embedded Atom Method	18
2.3.3	Ziegler-Biersack-Littmark (ZBL) Potential	20
2.3.4	Coulomb Potential	21
2.3.5	Fixed Charge Potential	22
2.3.6	Variable Charge Potential	23
2.3.7	Albe ZnO Potential	24
2.3.8	Reactive Force Field Potential	25
2.4	Interatomic Potential Optimisation	26
2.5	Energy Minimisation Techniques	27
2.6	Boundary Conditions	27
2.6.1	Fixed/Free Boundary Conditions	28
2.6.2	Periodic Boundary Conditions	28
2.6.3	Thermal Layers	28
2.7	Visualisation	30
3	Methods II: Long Time Scale Dynamics	31
3.1	Introduction	31
3.2	Double-ended Search Methods	34
3.2.1	The Nudged Elastic Band method	34
3.2.2	The Simple-String method	36
3.2.3	Chosen Method	37
3.3	Single-ended Search Methods	37
3.3.1	Search Initialisation	38
3.3.2	The Dimer method	39

3.3.3	The Activation Relaxation technique	41
3.3.4	The Relaxation and Translation method	42
3.3.5	Chosen Method	43
3.4	Example of Transition Found	43
3.5	Kinetic Monte Carlo	44
3.6	On-the-fly KMC	46
3.6.1	Transition searches	47
3.6.2	Filtering of Irrelevant Transitions	48
3.7	Parallelisation	49
4	Simulation of Silver and Aluminium Thin Film Growth	51
4.1	Introduction	51
4.2	Previous Work	53
4.2.1	Experimental	53
4.2.2	Simulation	54
4.3	Growth Simulations	56
4.4	Deposition on the Ag (111) Surface	58
4.4.1	Evaporation Deposition	59
4.4.2	Stacking Faults and Twinning	60
4.4.3	Deposition by Ion-Beam Assisted Evaporation	61
4.4.4	Sputter Deposition	63
4.4.5	Mid Deposition Energy: 10 eV	65
4.5	Deposition on the Ag (100) Surface	66
4.5.1	Evaporation Deposition	67
4.5.2	Sputter Deposition	67
4.5.3	Mid Deposition Energy: 10 eV	70
4.6	Deposition on the Al (111) Surface	70
4.6.1	Evaporation Deposition	71
4.6.2	Deposition by Ion-Beam Assisted Evaporation	72
4.6.3	Sputter Deposition	73
4.6.4	Mid Deposition Energy: 10 eV	76
4.7	Deposition on the Al (100) Surface	77
4.7.1	Evaporation Deposition	78
4.7.2	Sputter Deposition	79
4.7.3	Mid Deposition Energy: 10 eV	80
4.8	Discussion	81
5	Simulation of Titanium Dioxide Thin Film Growth	84
5.1	Introduction	84
5.2	Previous Work	86
5.2.1	Experimental	86
5.2.2	Simulation	88
5.2.3	Modelling the TiO ₂ Interactions	90
5.3	Single Point Depositions on the Rutile (110) Surface	91
5.3.1	Typical Defects	92
5.4	High Temperature MD: An Initial Insight into Rutile Growth	106

5.4.1	20 eV and 40 eV Depositions at 1000 K	106
5.4.2	Higher Energies	109
5.4.3	Drawbacks of High Temperature Growth	110
5.5	Otf-KMC: Depositions on the Rutile (110) Surface	112
5.5.1	Modelling Specific PVD Methods: Evaporation Deposition	113
5.5.2	Modelling Specific PVD Methods: Ion-Beam Assisted Evaporation	115
5.5.3	Modelling Specific PVD Methods: Sputter Deposition	117
5.5.4	Other Deposition Energies	120
5.5.5	Growth Mechanisms	123
5.6	Discussion	126
6	Simulation of Zinc Oxide Thin Film Growth	130
6.1	Introduction	130
6.2	Previous Work	132
6.2.1	Experimental	132
6.2.2	Simulation	134
6.3	Initial Testing of Interatomic Potentials	135
6.3.1	O-terminated Surface	136
6.3.2	Zn-terminated Surface	136
6.3.3	Interatomic Potential and Polar Surface for Growth	139
6.4	Growth Simulations	141
6.4.1	Post-Annealing	142
6.5	Deposition on the ZnO (000 $\bar{1}$) Surface	142
6.5.1	Evaporation Deposition	143
6.5.2	Sputter Deposition	148
6.5.3	Growth Mechanisms	153
6.5.4	Stacking Faults	155
6.6	Discussion	157
7	Conclusions	161
7.1	Future Work	165
	References	167

List of Figures

1.1	An illustration of where modelling techniques lie in comparison to one another. Long time scale dynamics techniques allow the largest time scale for simulations, allowing simulation over realistic times.	2
1.2	Thornton's structure zone model [12], showing the relationship between the surface morphology, deposition temperature and the pressure. Image taken from [12].	5
1.3	A chart showing all available techniques for deposition of thin films. The two main strands separate into either liquid deposition or vapour deposition. Physical vapour deposition (PVD) is highlighted due to its focus during this research.	5
1.4	The evaporation deposition technique, using an electron beam to heat the source material up and enable flow of atoms and clusters to the substrate. A large distance between the crucible and substrate aids film uniformity.	7
1.5	The addition of an ion source to the evaporation technique allows a high energy ion-beam (Ar) to target the surface. The ion-beam bombards the substrate during deposition, densifying the film.	8
1.6	The magnetron sputtering deposition scheme, where either a DC, pulsed DC, AC or RF power supply may be used, depending upon the target material and whether reactive sputtering is being used.	9
1.7	The simplified structure of a dye sensitised solar cell where AZO may act as the TCO, porous TiO ₂ allows dye molecules to form bonds and a back contact is made from metal, such as Ag or Al.	11
2.1	Diagram illustrating how an MD simulation works. The simulation starts with initial positions described for atoms, forces are then calculated along with accelerations of particles. All atoms are moved to their new positions using the integration equation and time is incremented one time step. The MD scheme is repeated until either a time limit is reached, or the user ends the simulation.	14
2.2	The L-J potential function plotted on a graph, showing where the force is repulsive, equal to zero and attractive.	18

2.3	During a growth simulation of TiO_2 , the bottom layer of the lattice employs fixed boundary conditions, with all other edges being periodic apart from the surface itself which is free. A Berendsen thermostat is attached to the two layers which lie above the fixed layer, which will allow for system heating and cooling.	29
2.4	The user interface of the AVA suite [8], used throughout this project to visualise data and produce POV-ray images and video clips. For each image produced, the time of the simulation, number of atoms and the breakdown of species is shown. Colouring options are available, atoms may be coloured by species, height, displacement, range, etc. The highlighted button allows extra options such as cropping, displacement, viewing a range of atom numbers, etc. All these options make the AVA suite a very useful analysis tool.	30
3.1	Illustration of the NEB method which calculates the MEP with the prior knowledge of both initial and final system configurations. Both the MEP guess and the true MEP found using the NEB method are highlighted here. Image taken from [82].	35
3.2	Illustration of the dimer, where the real force \mathbf{F}_R acting on the dimer is decomposed into parallel and perpendicular components with respect to each end of the dimer.	39
3.3	Definition of the ART, where an initial offset from the origin in a random direction \mathbf{N} gives the point \mathbf{R} . The force acting on \mathbf{R} is decomposed into parallel and perpendicular components, \mathbf{F}_P and \mathbf{F}_T . A modified force \mathbf{G} acts to move \mathbf{R} towards the saddle point.	41
3.4	Illustration of the RAT method where a random displacement vector describes a new point \mathbf{R} , which is then relaxed in the direction of the perpendicular force component.	42
3.5	An O ad-atom diffuses along the trench of the rutile surface with an energy barrier height of 0.68 eV. The images show the initial, saddle and final system configurations.	44
3.6	The NEB calculations for the diffusion of an O ad-atom along the rutile surface trench.	44
3.7	Illustration of the otf-KMC method, used to simulate growth by calculating configuration specific transitions at each step.	46
3.8	A ZnO ($000\bar{1}$) surface on which an O_2 dimer rotates typically every 2.08×10^{-9} seconds. No net diffusion is added to the simulation by the rotation of the dimer, therefore it is acceptable to filter out this transition.	48
3.9	The Al (100) surface on which an Al trimer re-orders with low energy barriers (<0.2 eV). Four different orderings are shown with arrows highlighting the movement of atoms. By the final image, the initial ordering has been revisited. These transitions require filtering out to avoid unnecessary calculations.	49

3.10	The parallelisation model, where one processor simulates a deposition and n-1 processors run transition searches, saddle relaxing and barrier calculations, until the required number of searches has been exceeded.	50
4.1	The fcc structure of Ag and Al, showing both the (111) and (100) surfaces.	52
4.2	The fcc and hcp stacking sequences, of which the first is the more stable for Ag and Al. However, if growth occurs in the hcp sites stacking faults and twin boundaries form. Three layers are shown to illustrate the stacking sequences.	53
4.3	Example of the initialisation of a deposition cluster before the MD phase begins. The species to be deposited is initialised 10 Å above the surface.	57
4.4	An Ag trimer on the (111) surface, acting as a nucleation site for the growth.	58
4.5	A four atom cluster on the Ag (111) surface during early stages of evaporation growth, switching between ABC and ABAB stacking sequences. 0.4 eV is required for this transition, with only half of that energy required to switch back to the preferred ABC sequence. Once a fifth atom attaches to the cluster, it becomes pinned to the layer it is in. Atoms are coloured by height, with the cluster being in red.	60
4.6	Ag (111) growth via evaporation deposition after 0.29 s of real time. 675 atoms have been added to the system, equivalent to three complete monolayers, corresponding to a growth rate of ten monolayers per second which is used for all simulations. Six partially formed layers have grown, although all are in the ABAB stacking sequence rather than the preferred ABC. Atoms are coloured by height in Å, according to the colour bar, with the original surface at 7 Å.	60
4.7	Ag (111) growth via evaporation deposition with ion-beam assist, where Ar ions bombard the surface at 100 eV, after 0.38 s of real time. Ar ions strike the surface with equal probability as an Ag atom. The extra energy, which is transferred to the system from Ar bombardment, promotes atomic mixing and increased surface diffusion, leading to more complete layers. From the addition of 675 atoms, five partially formed monolayers have grown all in the correct ABC stacking sequences.	62
4.8	Atoms from the original Ag (111) substrate, showing atom positions after the simulation of evaporation deposition with the ion-beam assist. A high portion of original substrate atoms travel up to and above the original surface during the simulation due to displacement and mixing from high energy ion bombardment.	62
4.9	Ag (111) growth from sputtering, after 0.27 s of real time. 675 atoms added to the system result in four newly formed layers, the first one of which is complete.	64

- 4.10 Ag (111) growth by magnetron sputtering, simulating 0.34 s of real time, including the effect of the Ar present in the plasma where there was equal likelihood that an Ag atom or an Ar atom would strike the surface. 675 atoms added results in four newly formed layers, similar to the simulation without Ar. 64
- 4.11 Two atom concerted motion requiring 0.44 eV to occur. Layers are able to self-complete by the filling in of vacancies with this mechanism. 65
- 4.12 The important ES transition requires 0.42 eV to occur on the Ag (111) surface. This ES transition allows completion of layers, however, as it is a higher energy barrier than that of the diffusion of a single ad-atom, it is not observed very frequently. Atoms are coloured according to height, where blue is the bottom, then green, then yellow and red. 65
- 4.13 Ag (111) growth where atoms arrived at the substrate with 10 eV. Four partially formed layers have grown, most of which are in the preferred ABC stacking sequence, however, the third new layer has switched to hcp stacking. 66
- 4.14 Ag (100) growth via evaporation deposition after 0.23 s of real time, with the addition of 600 atoms (equivalent to three complete monolayers). Six incomplete monolayers are produced as evaporation does not transfer enough energy for surface diffusion and thus layer completion to occur. The original substrate was at 10 Å. 67
- 4.15 Ag (100) growth by magnetron sputtering, simulating 0.23 s of real time. The addition of 600 atoms produced three almost complete monolayers, along with a fourth incomplete monolayer just beginning. 68
- 4.16 The respective energy barrier heights for all those transitions observed during the Ag (100) growth simulations. For both evaporation and sputter growth a sharp peak is observed at around 0.33 eV, which was found to be small cluster formations and rearrangements on the surface. Transitions requiring between 0.3 eV and 0.4 eV were shown to be larger cluster formation, rearrangement and addition to islands. Barriers around 0.41 - 0.42 eV represent bonding and de-bonding from the step edge of single atoms. Single ad-atom hops required 0.65 eV to take place; with such a large energy barrier this single ad-atom hop was rarely utilised (in less than 0.05 % of transitions). 69
- 4.17 The ES barrier was found to be identical as on the (111) surface. 0.42 eV is required for an Ag atom to drop off the edge of a step. This transition rarely occurred, however, due to other transitions requiring less energy. 69

- 4.18 Ag (100) growth where atoms arrived at the substrate with 10 eV. The film is more complete than that grown by evaporation as the deposition energy is one order of magnitude higher, therefore transferring more energy to the surface atoms and allowing increased diffusion. However, it is clear that the higher energy sputter depositions do produce even more complete, dense, crystalline films due to the increased deposition energy. 70
- 4.19 A five atom cluster on the Al (111) surface which switches from ABC to ABAB stacking sequences with a relatively low barrier of 0.3 eV. During later steps of the simulation, the cluster switches back to ABC stacking with a lower barrier and growth continues in the correct stacking formation, perhaps by chance. Atoms are coloured by height of monolayer with red being the cluster on top. 71
- 4.20 Al (111) growth via evaporation deposition after 0.29 s of real time. 672 atoms have been added to the system, equivalent to three complete monolayers. Two complete layers are formed, along with a third almost complete and a fourth just beginning. The original substrate was at 12 Å. 72
- 4.21 The film completes via this ES barrier, which allows layer-by-layer growth where atoms drop off step edges with a very low barrier (0.07 eV). The Al (111) grown via evaporation is clear evidence that this ES barrier plays an important role in the type of growth observed and hence the quality of the resulting film. 73
- 4.22 Al (111) growth via evaporation deposition with ion-assist, where Ar ions bombard the surface with 100 eV of kinetic energy. Here 0.31 s of real time is simulated. From the addition of three monolayers of atoms, no complete monolayers have been formed. In fact, the original substrate itself is damaged from the high energy Ar impacts which penetrate three layers deep in some cases. Sub-surface Ar clusters have displaced Al atoms, creating large Al voids in the substrate. Four new monolayers, all incomplete, are formed. 74
- 4.23 Layers of Al (111) after evaporation growth with ion-beam assist. Layers are ordered left to right, beginning with the deepest layer and ending with the very top new layer. The newly grown layers are incomplete and Ar has created voids in the Al structure by sitting in subsurface Ar clusters. Al atoms are slightly larger diameter, with the Ar represented by smaller spheres. 74
- 4.24 Al (111) thin film growth by magnetron sputter deposition after 0.3 s of real time. Three monolayers of Al are deposited onto the surface and four new monolayers are created, two of which are complete and the fourth has only 5 atoms. Due to the higher energy impacts than evaporation deposition, increased atomic mixing is observed. 75

4.25	Al (111) thin film growth via magnetron sputter deposition after 0.35 s of real time, including the effect of the Ar present in the plasma. After the deposition of three monolayers onto the surface, four new monolayers are created, two of which are complete and the third is only missing 4 atoms which are sit on top creating a fourth monolayer. Atoms are coloured by height in Å.	76
4.26	An island formed on the Al (111) surface has a vacancy within it. Here, two Al atoms slide across in a concerted motion, filling the vacancy. The energy barrier for this transition is 0.25 eV, which is highly accessible within the time frame between successive impacts. Atoms are coloured by height.	76
4.27	Al (111) growth where atoms arrived at the substrate with 10 eV. The low ES barrier allows complete layers to form easily and deposition energy becomes much less important. Simulations of evaporation deposition, sputter deposition and the 10 eV deposition produce very similar results.	77
4.28	A two atom concerted replacement mechanism is shown on the Al (100) surface. Initial, saddle and final configurations are shown. This mechanism allows single Al atoms to diffuse across the surface, requiring 0.27 eV. Atoms are coloured by height, dark blue being the surface.	78
4.29	Al (100) growth from evaporation deposition simulated over 0.15 s of real time. 384 atoms are added to the system, equating to three complete monolayers. Four new monolayers are formed, two of which are complete. The original substrate was at 14.5 Å.	78
4.30	The ES barrier on Al (100) is calculated to be 0.24 eV. Relative to monomer diffusion (0.27 eV), the ES barrier will occur more often between deposition events, thus enabling layer-by-layer growth.	79
4.31	Al (100) growth produced from magnetron sputtering over 0.18 s of real time. From three monolayers added, two complete monolayer are formed, with the third missing only two atoms, which we would expect would fill in and complete if the simulation was to continue.	79
4.32	Al (100) growth where atoms arrived at the substrate with 10 eV. The film is more complete than that grown by evaporation as the deposition energy is one order of magnitude higher, therefore transferring more energy to the surface.	80
5.1	The TiO ₂ rutile unit cell, where larger red spheres represent O and smaller silver spheres represent Ti (this scheme will be used throughout this chapter). The directions are indicated. [5].	85
5.2	The structure of the rutile (110) surface. O ad-rows run in the [110] direction, with trenches running parallel between individual ad-rows. The Ti atoms sitting in the trenches are the 5-fold coordinated Ti and those sitting directly below the O ad-row are the 6-fold coordinated Ti.	86

5.3	The species that are deposited normally to the (110) surface in order to provide initial statistical data on the behaviour of different deposition species.	91
5.4	The deposition area, the unit cell, is highlighted on the rutile TiO ₂ (110) surface. Deposition of all species onto a point in this irreducible area provides statistically meaningful results.	91
5.5	The initialisation of a deposition species above the surface before a single point deposition onto the rutile surface.	92
5.6	A Ti interstitial, commonly formed in the first layer of the rutile TiO ₂ lattice, views from the side of the lattice and above are shown.	93
5.7	An O interstitial formed in the first layer of the rutile TiO ₂ lattice.	93
5.8	The number of interstitials created in the Ti depositions at different energies. 90% of 20 eV depositions produce either 1 or 2 interstitials, similar to 40 eV depositions, although at 100 eV we begin to see around 20% of the cases producing 3 interstitials. 100 eV depositions peak at 2 interstitials, but produce up to 7.	94
5.9	The number of interstitials created in the O depositions. At 20 eV and 40 eV, we observe predominantly no interstitials or in around 20% of cases only 1 interstitial. At 100 eV, often 2 or 3 interstitials are created, however, up to 7 are seen. O ₂ depositions produce very similar data so we are omitting the graph.	95
5.10	The number of interstitials created in the TiO depositions for all three energies. 20 eV depositions more often form either 1 or 2 interstitials and 100 eV depositions are more likely to produce 2 or 3 interstitials. This is due to higher energy depositions disturbing the lattice more, knocking atoms into interstitial locations.	95
5.11	The number of interstitials created during TiO ₂ depositions. At 20 eV we see predominantly either 0 or 1 interstitial, although up to 3 interstitials are observed. However, at 100 eV, we see a peak at 2 interstitials created, with a maximum of 6.	96
5.12	The depth of interstitials during Ti depositions. 20 eV and 40 eV are similar, with most interstitials ending up in the 1st layer of the lattice, whilst 100 eV produces interstitials in the top 7 layers of the lattice due to the higher energy deposition allowing atoms to penetrate the lattice with more energy.	97
5.13	The depth of interstitials during O depositions. 20 eV and 40 eV are similar, most interstitials end up in the 1st layer of the lattice. 100 eV, however, allows interstitials to penetrate as deep as the 6th layer but in almost 50% of cases interstitials only reach the 1st layer.	98
5.14	The depth of interstitials during TiO depositions. 20 eV and 40 eV allow interstitials to form in the 1st layer of the lattice, with up to 10% forming in the 2nd layer. 100 eV, however, interstitials equally in the 1st and 2nd layers, and as deep as the 7th layer.	98
5.15	Two examples of Ti vacancy sites.	99

5.16	An O atom has been knocked out of its position in the surface ad-row creating an O vacancy. This often occurs when a cluster knocks the atom out of its lattice site.	99
5.17	The number of vacancies created from O deposition at all energies. More often we see few or no vacancies, but at 100 eV we see up to 16.	99
5.18	The number of vacancies created from Ti deposition. We see a shift for 20 eV depositions, from predominantly 0 vacancies with O depositions, to predominantly 1 vacancy with Ti depositions. At 100 eV, vacancies created peak at 2.	100
5.19	The number of vacancies created during the deposition of TiO ₂ clusters. At 20 eV and 40 eV predominantly 0 or 1 vacancies are formed and at 100 eV, in 80% of cases, 0 to 4 vacancies are formed.	100
5.20	Clusters deposited at 20 eV produce a higher percentage of Ti rather than O vacancies, especially when there is a Ti atom within the cluster.	101
5.21	Clusters deposited at 40 eV. We observe from O deposition slightly more O vacancies produced, but for the other clusters we again see a higher proportion of Ti vacancies.	101
5.22	Deposition at 100 eV, where we observe for all clusters a slightly higher proportion of Ti vacancies produced. An average of around 58% are Ti.	102
5.23	O ad-atoms on the surface of a rutile TiO ₂ lattice.	103
5.24	Two Ti ad-atom locations on the rutile surface.	103
5.25	Ad-atoms created during O ₂ deposition. At 20 eV and 40 eV, it is likely that 2 ad-atoms will be created. At 100 eV, we may see more ad-atoms created due to the higher deposition energy knocking some surface O atoms out of their location and into ad-atom sites.	103
5.26	Ad-atoms created during Ti deposition. As expected, predominantly no ad-atoms are created at 20 eV. However at 40 eV and 100 eV, we see that a vacancy may be created during the deposition. This is due to the higher energy knocking atoms on the surface out of their locations into ad-atom sites.	104
5.27	During Ti deposition we observe very little sputtering from the surface. It is only when reaching 100 eV that a very small amount of sputtering does occur.	105
5.28	During O ₂ deposition we observe a higher proportion of reflections/sputtering than during Ti depositions. Up to 30% of depositions have caused 1 atom to leave the surface either by reflection or sputtering. Very rarely, 2 atoms are ejected or reflected.	105
5.29	The rutile TiO ₂ substrate on which 20 eV and 40 eV depositions occur during high temperature growth. The substrate contains 432 atoms in four layers, where 288 atoms are O and 144 are Ti. The lattice is 12 Å deep.	107

- 5.30 TiO₂ growth at 1000 K, where a random mix of clusters arrive at the substrate with 20 eV. Using a small lattice, we see that after 135 successive depositions (252 atoms added), we have some uniform growth. Two complete layers have been successfully formed and no interstitials or defects are present below the surface. 108
- 5.31 TiO₂ growth at 1000 K where a random mix of clusters arrive at the substrate with 40 eV. After 100 depositions, 177 atoms have been added. As with the 20 eV growth, we see uniform growth, however, more defects exist below the surface. 108
- 5.32 TiO₂ growth at 1000 K, with 100 eV depositions of a stoichiometric distribution of ad-units. The lattice started with 1920 atoms, illustrated here is the growth after 185 successive depositions (345 atoms have been added to the system). We observe a highly defective growth, with many voids due to sputtering of atoms and a high portion of Ti interstitials. 109
- 5.33 The growth resulting from the stoichiometric deposition of TiO₂ onto a rutile TiO₂ surface. 110
- 5.34 The growth resulting from Ti rich distributions of deposition species onto a rutile TiO₂ surface. 111
- 5.35 The growth resulting from O rich distributions of deposition species onto a rutile TiO₂ surface. 111
- 5.36 The resulting growth of rutile TiO₂ after 1 eV depositions, simulating 5.8 seconds of evaporation deposition. The entire lattice is shown, with a breakdown of the newly deposited layers. Atoms are either coloured by height using the key or using the original Ti and O colour scheme. Layers are incomplete as atoms do not have sufficient kinetic energy to mix efficiently during the ballistic phase of the deposition. 114
- 5.37 The growth of TiO₂ with an ion-beam assist, where Ar bombarded the surface with 40 eV. 6.2 seconds of real time are simulated. The Ar impacts supplied extra energy to the surface, promoting mixing and diffusion, thus enabling a slightly more crystalline surface to form. Ar atoms implanted within the lattice are coloured in green, implantation occurs down to the 2nd layer deep of the original substrate. 115
- 5.38 The growth of TiO₂ with an ion-beam assist, where Ar bombarded the surface with 100 eV. 5.2 seconds of real time are simulated. The higher energy of the ion-beam caused increased damage to the film, leading to a loss of crystallinity and the formation of voids. Ar now implants as deep as the 4th layer of the original substrate. 116
- 5.39 The Ti sub-lattice after Ar bombardment. Ti atoms are grey and Ar atoms are green. Ar in the lattice sits in one of two sites, either in an interstitial location between Ti layers or as a substitutional defect. 117

- 5.40 The resulting growth obtained from the simulation of magnetron sputter deposition where the effect of Ar is ignored. 5.3 seconds of real time are simulated. Layers are much more complete and crystalline than those obtained from evaporation deposition simulations. Ti interstitials are still evident throughout the layers, but the 1st and 2nd new layers especially are crystalline, missing only some Ti atoms from crystal sites. 118
- 5.41 The resulting growth from the simulation of magnetron sputter deposition of TiO_2 and Ar simultaneously, where 4.3 seconds of real time are simulated. Layers are much more complete and crystalline than those obtained from the evaporation deposition simulations. It was assumed that an Ar bombardment at 40 eV occurred with equal probability as a Ti_xO_y molecule deposition. There is not a huge difference from the Ar bombardment. Layers are still more complete and crystalline than evaporation and Ti interstitials are still present. Ar penetrates the surface, relaxing in sites as deep as the 2nd layer of the original substrate. 119
- 5.42 The final positions of those atoms from the original substrate (both O and Ti atoms) coloured by height, after the deposition of 4 monolayers. The simulation that included the effect of Ar suffered more disruption and damage to the original substrate. Ar bombardment disrupts the surface more than Ti_xO_y molecule depositions alone, suggesting that Ar should enable or allow more atomic mixing and diffusion to occur. 120
- 5.43 Ar atoms which have remained implanted within the film. 0.06% of Ar remains implanted, in close agreement with the $\sim 1\%$ observed experimentally. Atoms are coloured by height, with the surface height indicated by the line. 121
- 5.44 The resulting growth from 10 eV depositions onto the rutile surface, where 6.2 seconds of real time are simulated. Growth is more complete and crystalline than the evaporation growth but not as good quality as the sputter growth. 121
- 5.45 The resulting growth from 30 eV depositions, where 6.4 seconds of real time are simulated. The film appears very similar to that produced by 10 eV depositions, with increased atomic mixing occurring during the ballistic phase. Some new layers are complete and crystalline, similar to 40 eV depositions simulating sputtering. 122
- 5.46 Higher energy depositions, where atoms arrive at the surface with 100 eV, simulating 8.7 seconds of real time. Growth results in a somewhat dense film. However, there is a huge presence of Ti interstitials throughout the film, as deep as the 4th layer of the original substrate. 123
- 5.47 The depth of formed Ti interstitials against the deposition energy. The higher the energy of deposition, the deeper within the original substrate are Ti interstitials formed. 124

- 5.48 A Ti interstitial in the 1st layer is drawn out by the presence of an O rich surface (not shown here), requiring 0.61 eV to take place. The atoms are coloured by height and only Ti is shown. 124
- 5.49 An O ad-atom diffuses along the trench, requiring between 0.65 eV and 0.75 eV. This diffusion enables the movement of surface O towards a Ti interstitial rich area, thus lowering the Ti interstitial escape barrier and encouraging the rutile growth mechanism to take place. 125
- 5.50 An O ad-atom sitting in the trench above the 5-fold coordinated Ti row diffuses across to fill an O ad-row vacancy, requiring 0.81 eV for the transition. 125
- 5.51 A multi-atom, concerted motion, allowing the diffusion of a TiO_3 unit across the surface. 3 atoms move in this transition, requiring 0.83 eV. Initial and final configurations are shown along with the intermediate saddle point to illustrate the transition pathway. . . . 126
- 6.1 View from above, where three monolayers of ZnO have been sliced out in order to illustrate the stacking sequences. The image on the left shows the wurtzite structure with AaBbAa... stacking, and on the right is the zinc blende AaBbCc.. structure. In the wurtzite structure the fcc hollows are clearly seen throughout the film, whereas the zinc blende structure involves filling these fcc hollows. Smaller spheres represent Zn, whilst larger red spheres represent O. 131
- 6.2 With its hexagonal structure, wurtzite requires arriving atoms to follow the hexagonal nature in order to continue the crystalline growth. The unit cell is shown, with the high-symmetry adsorption sites for arriving species. 132
- 6.3 ZnO journal publications from 1990 to 2011. Information was sourced from the Web of Knowledge. 133
- 6.4 The deposition took place on the unit cell, an area of irreducible symmetry, which is highlighted here on the O-terminated $(000\bar{1})$ surface. Deposition of all species onto a point in this irreducible area provides statistically correct results by modelling depositions onto 1000 random points within this area. 135
- 6.5 A comparison of the Albe and ReaxFF potentials used to model depositions onto the O-terminated surface. Statistics are shown for the depth of penetration of the deposited species or reflection rate. The key is shown. 137
- 6.6 A comparison of the Albe and ReaxFF potentials used to model depositions onto the O-terminated surface. Statistics are shown for the number of atoms either sputtered or reflected off the substrate during depositions. The key is shown. 138

- 6.7 A comparison of the Albe and ReaxFF potentials used to model depositions onto the Zn-terminated surface. Statistics are shown for the number of atoms either sputtered or reflected off the substrate during a deposition. The key is shown. 140
- 6.8 The evaporation deposition grown ZnO film, where a stoichiometric distribution of species was deposited. Larger spheres represent O and smaller spheres represent Zn. Atoms are coloured by height as shown on the colour bar. Layers have been broken down for clarity purposes, with the original surface at top left, followed by first new layer and so on, ending with the last new layer. The second new layer shows a stacking fault where atoms are not in correct sites. . . 144
- 6.9 The post-annealed evaporation grown film where a stoichiometric distribution of species was deposited. The system was heated to 770 K for 10 ns to simulate the post-annealing treatment. Results indicate that the temperature is not high enough for complete recrystallisation to take place. The first new layer is complete, the post-annealing process has removed a point defect which was previously present. The second new layer, however, has failed to recrystallise into the correct sites and a stacking fault previously apparent has formed a phase boundary due to the annealing process allowing the layer to become O deficient (this is discussed later). 144
- 6.10 The post-annealed evaporation grown film where a stoichiometric distribution of species was deposited. The system was heated this time to 920 K to simulate a more aggressive post-annealing treatment. In this case perfect, crystalline ZnO has formed. The first, second and third new layers are all in the wurtzite phase with no stacking faults or phase boundaries present. 145
- 6.11 ZnO film growth obtained from the evaporation of an O deficient distribution of deposition species. The film is incomplete with voids where many O vacancies are present. Five new layers are partially formed, demonstrating a low density throughout the new layers. The deposited layers have switched to the zinc blende structure, indicating that the O deficiency throughout the film promotes stacking faults. 146
- 6.12 The post-annealed O deficient film, where the system was heated to 920 K during post-annealing. The energy transferred through the lattice from the annealing treatment has enabled atoms to move to lattice sites and to densify. However, all of the new layers still exhibit the zinc blende structure, sitting in the AaBbCc... sequence. 146
- 6.13 ZnO film growth obtained from the evaporation of an O rich distribution of deposition species. Although layers still exhibit point defects and vacancies, most of the new atoms sit in correct wurtzite sites. 147

- 6.14 The resulting film from the sputter deposition of an O rich distribution of species, after the deposition of the equivalent to three new layers. Due to new layers not being totally complete we have four new layers. However, with only 21 atoms in the fourth layer, we would expect these to complete the layer below if growth continued and reached a steady state. The first new layer is stoichiometric and complete, whilst the second and third new layers are very slightly O deficient and not all atoms are sitting in correct lattice sites. . . . 148
- 6.15 The post-annealed, sputter deposited film, where an O rich distribution of deposition species was used. The post-annealing treatment involved heating the system to 920 K for 10 ns. The first two new layers are now perfectly crystalline and in the wurtzite phase. The third new layer is O deficient and a stacking fault with a phase boundary has formed between the wurtzite and zinc blende phases. 149
- 6.16 The resulting film from the sputter deposition of an O deficient distribution of deposition species. The first new layer sits in the correct wurtzite phase suggesting that the 40 eV deposition energy can be sufficient to produce some crystallinity, however, the second new layer has an area of O deficiency where some atoms are sitting in the zinc blende phase. 150
- 6.17 Post-annealing the film grown by O deficient evaporation at 920 K allows atoms to diffuse to neighbouring lattice sites. In this case, however, due to an inherent O deficiency in the second new layer before annealing, a phase boundary forms around an area of zinc blende. 150
- 6.18 A sputter deposited film where the distribution of deposition species was a stoichiometric mix where most species arrived at the surface as ZnO units (sputtering A distribution described in table 6.1). O deficiency is evident throughout the deposited film (10% O deficient), although the original surface and the first new layer are almost perfect with only one point defect from a missing O atom. The second new layer does have higher O deficiency, with stacking faults and O vacancies. 151
- 6.19 A sputter deposited film where the distribution of deposition species was a stoichiometric mix where most species arrived at the surface as single Zn or O species (sputtering B distribution described in table 6.1), resulting in high O deficiency (18% O deficient). The original substrate exhibits an O vacancy and the first new layer exhibits a large O deficiency along with a highly mismatched phase structure. The O deficiency and high defect density has allowed a phase boundary (highlighted) to form between the wurtzite and zinc blende phases. The second new layer is also O deficient and highly mismatched with stacking faults and point defects throughout. . . 152

- 6.20 The post-annealed, sputter deposited film, where the stoichiometric sputtering B distribution of deposition species was used. The post-annealing treatment, heating the system to 920 K for 10 ns, has not been capable here of recrystallising the atoms. Instead, stacking faults already present have become fixed in, with phase boundaries forming around areas of zinc blende. 152
- 6.21 A Zn atom on the surface is often bound by a O or O₂ dimer to form a ZnO₍₂₎ cluster, both of which are illustrated here. The energy required for a ZnO ad-unit to diffuse on the surface is between 0.15 eV and 0.35 eV, whereas a ZnO₂ unit requires much less (usually <0.1 eV). Smaller, grey spheres represent Zn, whilst larger, red spheres represent O. 154
- 6.22 During a simulation, interstitials form below the surface due to bombardment and disruption of the surface. The energy required for this Zn interstitial, marked in yellow, to diffuse to its correct lattice site, is 0.09 eV. This small barrier indicates that this is a key mechanism by which Zn atoms reach their correct sites and thus crystalline ZnO is formed. 154
- 6.23 Two ZnO units marked by the arrows move as indicated towards a Zn₂O₂ string to form a longer string. The Zn atom lies under the O atom in the unit and is not visible in (a). This transition involves a concerted motion of 5 atoms, requiring 0.44 eV to occur. Smaller spheres represent Zn, larger spheres represent O and the atoms are coloured by height, where the atoms higher up are lighter in colour. 155
- 6.24 Zn_xO_y strings on the ZnO surface act as a nucleation site for growth. These strings move with small energy barriers (0.2-0.3 eV), as shown in the first two configurations. The third configuration shows strings forming together with new atoms joining on to make larger structures, overcoming a barrier of 0.42 eV. Finally, after hundreds of milliseconds, a hexagonal structure forms, as required for the crystalline ZnO growth. 155
- 6.25 Growth switching between the preferred, more stable wurtzite structure and the zinc blende structure often occurs during a simulation. The energy difference for the O atom, marked in yellow, to switch to the zinc blende phase is <0.05 eV. This small difference in energy enables atoms and layers to switch to the zinc blende phase. 156

6.26 Sputtered growth using the O deficient distribution of deposition species. Annealing at 920 K attempts to recrystallise the film, however, due to an already inherent defect in the layer and an O deficit, annealing actually forms a phase boundary in the layer. On the right is an image taken from above a stacking fault. The highlighted area shows a zinc blende phase within a wurtzite structure, forming a phase boundary. On the left is a simple, atomistic diagram of the stacking fault where the light, transparent green circles represent an O vacancy. Arrows show clearly where atoms would need to diffuse for reordering to the wurtzite phase. 157

List of Tables

4.1	Transition barriers for single ad-atom and small cluster diffusion on the Ag (111) surface.	59
4.2	Transition barriers for ad-cluster diffusion on the Ag (100) surface.	68
4.3	Transition barriers for single ad-atom and small cluster diffusion on the Al (111) surface.	71
4.4	Transition barriers observed on the Al (100) surface.	77
5.1	The distribution of various deposition species arriving at the rutile surface (shown as a %).	107
5.2	The variation in O and Ti atoms in specific layers of the lattice deposition by evaporation. The 4th layer of the original substrate and up to the 3rd newly deposited layer are shown. The original substrate has a slight Ti excess, in the form of interstitials, whilst in new layers a deficit is observed for both O and Ti.	114
5.3	The variation in O and Ti atoms in specific layers of the lattice after sputter growth, showing O and Ti excess and deficits. The 4th layer deep into the original substrate, up to the 3rd newly deposited layer, are shown. Further new layers are not included due to not yet having reached steady states.	118
6.1	The distribution of various deposition species arriving at the surface at normal incidence (shown as a %).	143

Chapter 1

Introduction

1.1 Research Aims

Understanding thin film growth is important to many high technology industries such as photovoltaics, semiconductor optics, windows and more. Throughout this thesis, photovoltaic technology is the main focus due to the important role it will play in the coming years to assist in meeting the energy demands across the world. Thin film growth is achieved using a deposition technique to deposit a chosen material onto a substrate. Switching between deposition techniques leads to a notable difference in the resulting film morphology, quality and properties. The aim of this thesis is to simulate the growth of thin films by well known deposition techniques and to understand where the differences in resulting film structures come from. This is of great interest since it provides a more precise understanding of exactly how and why the use of different deposition techniques results in varying film quality.

A comprehensive comparison of metal and oxide thin film growth using industrially scalable physical vapour deposition (PVD) methods has been achieved. Evaporation (thermal and electron beam) and reactive magnetron sputtering are important PVD methods used within industry where it is known that these processes produce different film morphologies. The difficulty, however, has been identifying the causes and mechanisms behind these differences in the film structures and compositions. For example, it is known that during TiO_2 sputter deposition many Ti interstitials are formed and their exposure to an oxygen rich surface results in their annealing, allowing stoichiometric, complete, crystalline films to form [1]. However, the problem is that the mechanism required for this to occur is not understood sufficiently

for experimental parameters to be manipulated in an intelligent way.

Therefore, the goal of the work is to gain a more precise understanding of the mechanisms which allow metal and oxide films to grow either complete and crystalline or incomplete and porous thin films. All the materials simulated during this project have uses in the Photovoltaic industry in both their crystalline and porous forms, so the ability to understand which deposition parameters can create a specific growth morphology is very useful. Growth simulations are carried out using new long time scale dynamics techniques where traditional molecular dynamics (MD) is used to simulate a deposition by running molecular dynamics (MD) for some time and then on-the-fly kinetic Monte Carlo (otf-KMC) is used to search for transitions between each step.

1.2 Simulation Techniques

Computer simulation allows a deeper insight into growth mechanisms and methods. Linking simulation knowledge with experimental knowledge will enable the mechanisms of thin film growth to be understood in much more depth. Traditional simulation methods allow only the simulation of small systems over very small time scales but our long time scale dynamics techniques overcome this time scale problem, as illustrated in figure 1.1.

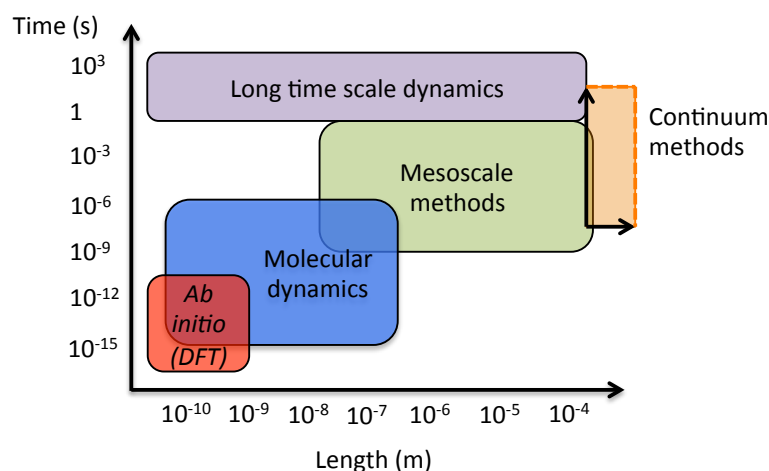


Figure 1.1: An illustration of where modelling techniques lie in comparison to one another. Long time scale dynamics techniques allow the largest time scale for simulations, allowing simulation over realistic times.

Ab initio techniques are some of the most accurate methods for simulation [2] as fewer assumptions are made. All interactions are calculated from first principle quantum mechanics. Density functional theory (DFT) [3] is a popular *ab initio* method due to its high accuracy, however, only short system sizes over small time scales can be simulated due to the large computational overhead of DFT. Although DFT cannot realistically model systems over large time scales, it is very useful for the parameterising of potentials.

Molecular dynamics refers to methods where empirical potentials are used to model the interaction between atoms; larger systems can be simulated for longer time scales, up to $\sim 10^{-6}$ seconds or $\sim 1 \mu\text{ s}$. This type of technique includes many-body potentials and pair potentials, the latter of which enables simulation over longer time scales due to the decrease in cost of the potential at the expense of accuracy. Approaching larger time scales and system sizes, mesoscale and continuum methods come into use. These are useful in the investigation of entire system properties such as strain but not applicable to our research. Long time scale dynamics techniques, however, allow simulation of atomic systems over realistic time scales. Long time scale dynamics techniques are used throughout this project in order to enable realistic and applicable simulation; chapter 3 describes the techniques in detail.

Long time scales dynamics requires the implementation of numerous techniques in order to simulate thin film growth via various deposition techniques. To simulate a deposition event, traditional MD was used. The Loughborough MD package (LBOMD) [4] was used throughout this project to perform the MD work (later described in chapter 2). When simulating a system using MD, it is necessary to describe the interatomic interactions. Specific potentials were chosen based on the material being simulated and all of the potentials used are later described in chapter 2. The otf-KMC (on-the-fly Kinetic Monte Carlo) method, discussed in chapter 3, allows the employment of transition searches at each step of the simulation. The main parts of this method include the relaxation and translation method (RAT) [5], which searches for saddle points and the nudged elastic band method (NEB) [6, 7], which calculates the energy barriers. Required during the MD and otf-KMC phases, is an energy minimisation technique, which allows all atoms in a configuration to relax into minimum energy sites. A conjugate gradient minimiser is used for this. The strength of these methods is the ability to run in parallel, over multiple cores, thus allowing simulations to be performed in a realistic time scale. For this project, the otf-KMC frame work already existed and only modification

and editing were required to enable the methods to be applicable to all of the systems investigated. When visualising data, an atomic visualisation and analysis (AVA) suite was used [8], enabling real time visualisation and the Persistence of Vision Raytracer (POV-ray) [9] rendered images which are used throughout this thesis.

1.3 Experimental Techniques

Surface morphology, quality of growth and defect density are all very important in thin film growth; optical and electrical properties of a film are greatly affected by changes in these. Experimentally, thin film growth can be achieved via many different deposition techniques. The deposition technique used influences the growth of a film. Depositing the same material using two different techniques may result in completely different film growth. In experiment the reasons for these differences are not always fully understood.

Previously, groups have investigated the structural evolution of thin films. Barna studied the stages of film evolution and various structural preconditions [10, 11]. Thornton's structure zone model [12] shows the relationship between the substrate temperature, kinetic energy of ions and the deposition rate, which are all parameters that change according to the deposition technique. Figure 1.2 illustrates the relationship between the surface morphology, the deposition temperature and the pressure.

Deposition techniques produce unique types of growth. Thornton's model shows that if the Ar pressure and temperature are high, as seen in some techniques, then the growth will be represented by zone 3 (with a crystalline structure). Whereas, if the temperature is low, the structure is more likely to be porous. Our simulations aim to allow the prediction of which deposition technique will produce the best quality, most crystalline films.

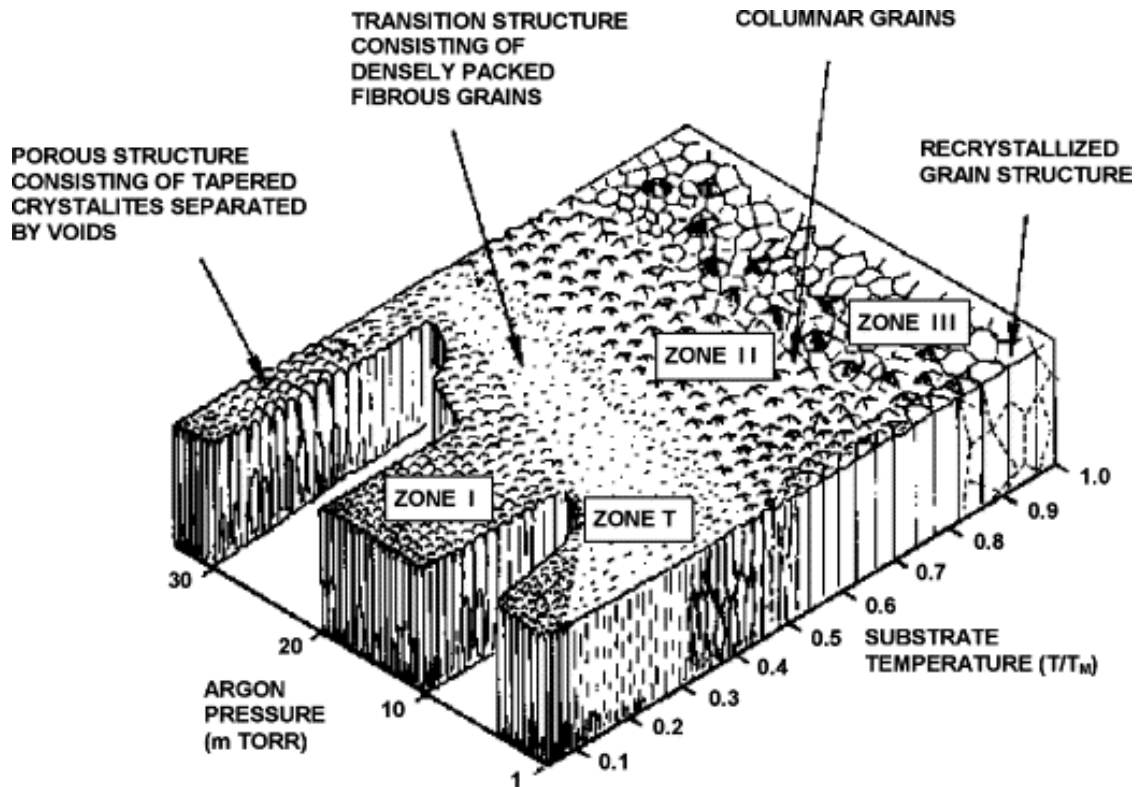


Figure 1.2: Thornton's structure zone model [12], showing the relationship between the surface morphology, deposition temperature and the pressure. Image taken from [12].

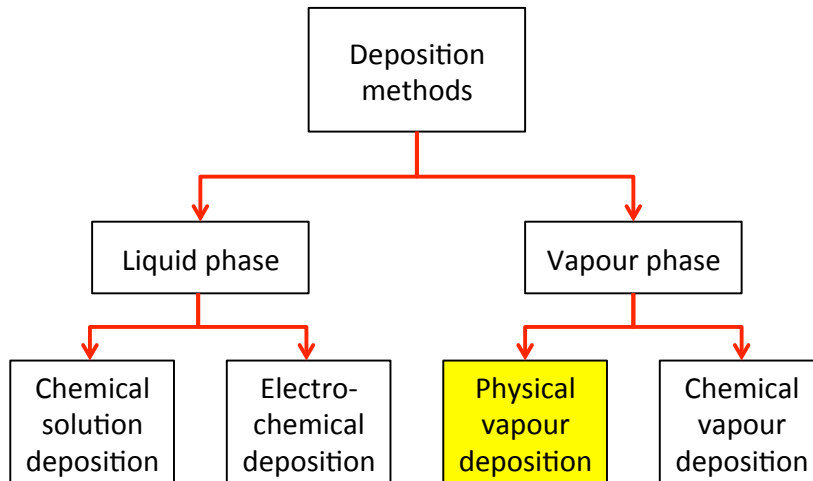


Figure 1.3: A chart showing all available techniques for deposition of thin films. The two main strands separate into either liquid deposition or vapour deposition. Physical vapour deposition (PVD) is highlighted due to its focus during this research.

Many different deposition techniques exist, including liquid and vapour methods.

Material is deposited, in some fashion, onto a given substrate until the required amount of material has been added. The deposition flux and rate depends upon which technique is used. Figure 1.3 illustrates the different deposition methods that exist.

Deposition methods fit into two main categories, liquid phase deposition or vapour phase deposition. Within the liquid phase, either chemical solution or electrochemical deposition (CSD or ECD) methods are available. The first of these methods describes spin-on, dip and aerosol deposition, where the material to be deposited is applied in a liquid or solution form onto the substrate. The substrate acts as a physical support to the material and there is no reaction. Temperature is then introduced to the substrate in order to dry and densify the film. The latter method, electrochemical deposition, involves deposition of a film of solid metal by dipping an electrically conducting surface into a solution of ions.

The vapour phase can also be split into two categories, chemical or physical vapour deposition (CVD or PVD). CVD techniques are based on chemical processes occurring on the surface. Vapour diffuses towards the surface and is adsorbed, a surface chemical reaction is catalysed by the surface and then desorption of the reaction by-products takes place.

PVD methods rely on mechanical, electromechanical or thermodynamic methods for the deposition of a solid thin film and are usually directional allowing for better control, taking place within a vacuum chamber. Examples include evaporation (thermal and electron beam), magnetron sputtering, pulsed laser deposition and cathodic arc deposition. During this project, we model the growth of thin films via PVD due to its large scale industrial use and the differences in thin films produced by various PVD methods. We focus here on evaporation (thermal and electron beam) and magnetron sputtering.

Evaporation deposition can be carried out either thermally or by using an electron beam, providing extremely flexible deposition techniques, able to coat almost any material. All evaporation deposition processes take place within a vacuum chamber, with a crucible holding the material placed opposite a substrate. During thermal evaporation the crucible is heated using methods such as resistance heating or RF coil until such a time that the material begins to evaporate, following an evaporation flow towards the substrate. Atoms do not have much kinetic en-

ergy due to the slow process of evaporating, therefore it is realistic to assume that atoms travelling towards the substrate do so with a kinetic energy of typically <1 eV. Electron beam evaporation submits the material inside the crucible to a direct electron-beam from an electron source nearby. A magnetic field is used to steer the electron beam onto the crucible, allowing atoms to slowly leave the crucible and move towards the substrate. Atoms travel with similar kinetic energy to thermal evaporation (<1 eV). During this work, this low arrival energy will provide a basis for simulating this technique. Figure 1.4 illustrates the evaporation technique, showing the electron beam option.

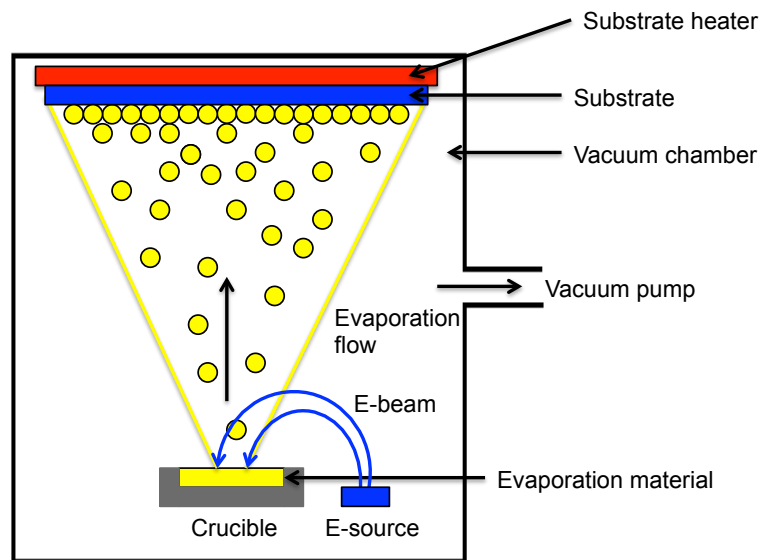


Figure 1.4: The evaporation deposition technique, using an electron beam to heat the source material up and enable flow of atoms and clusters to the substrate. A large distance between the crucible and substrate aids film uniformity.

Films grown by evaporation tend to be porous and incomplete, which is useful for some applications such as in dye sensitised solar cells, however, often a crystalline film is desired. A high energy ion source (usually Ar) may be used to densify the film. An ion source is attached to an evaporation set up in order to allow an ion beam to bombard the surface during growth. This ion-beam, where Ar ions can have up to 100 eV of kinetic energy, introduces extra energy into the growing film to enhance atomic mixing and densification. Figure 1.5 illustrates the addition of the ion source, showing the coinciding ion-beam and evaporation flow.

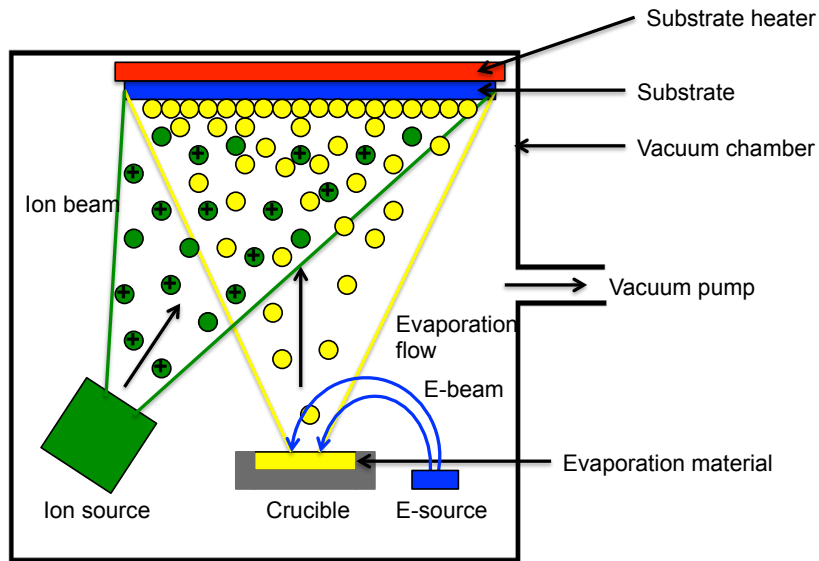


Figure 1.5: The addition of an ion source to the evaporation technique allows a high energy ion-beam (Ar) to target the surface. The ion-beam bombards the substrate during deposition, densifying the film.

Magnetron sputtering differs from the evaporation technique. Atoms are sputtered from a ‘target’ by Ar ions and then flow through a plasma towards the substrate. Behind the target, within the magnetron, is a permanent magnet configuration, illustrated in figure 1.6. Before the coating process takes place, typically a pressure of 10^{-6} torr must be achieved. Only then can a controlled flow of Ar or any other inert gas be introduced. If reactive sputtering is taking place then oxygen or some other reactive gas is also introduced to the chamber. The magnets create a magnetic field around the target. A high voltage (typically -300V or more) is then applied to the target, thus ionising the Ar gas forming a plasma along the magnetic field. Ar atoms within the plasma become ionised and positively charged, therefore creating free electrons. Ar ions then continuously bombard the negatively charged target at high energy, causing sputtering of the material providing that the energy transferred normal to the surface by the ion is greater than about 3 times the surface binding energy. Once sputtered, atoms are accelerated towards the substrate due to the bias voltage which is applied. This technique involves the arrival of target atoms at the substrate with much greater kinetic energy than that seen in evaporation, typically around 40 eV. During this project, this arrival energy will provide a basis for simulating this technique.

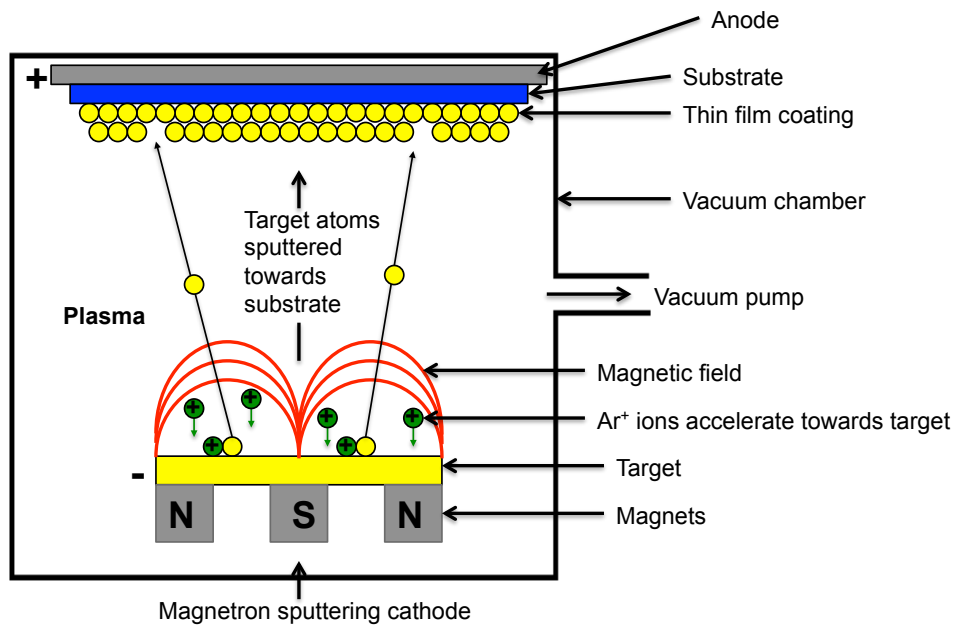


Figure 1.6: The magnetron sputtering deposition scheme, where either a DC, pulsed DC, AC or RF power supply may be used, depending upon the target material and whether reactive sputtering is being used.

During reactive sputter deposition, Ar is present both in the magnetron plasma and in the reactive plasma. Back reflection of Ar neutral atoms from the target onto the substrate occurs during the deposition [13], densifying the film. Therefore, within the chamber there is a similar probability that an Ar ion/atom or target species will strike the substrate. The energy of an Ar ion striking the substrate would be similar to the energy of the bias voltage (40 eV). This flux of Ar towards the substrate may help densify the film, although it may also cause sputtering from the surface. This will be investigated throughout this work. It is worth noting, however, that in some cases, back reflection of Ar does not occur in cases where the mass of Ar exceeds the mass of the target element. In these cases, an ion assist may be applied by unbalancing of the magnetron, allowing flux to leak away towards to substrate, drawing plasma towards the film.

Deposition techniques have many parameters which experimentalists can alter to achieve a different film property. The main parameters, applicable to most deposition techniques include the following:

- Type of power supply.
- Gas mixture within the vacuum along with the pressure and flow rate.

- Deposition rate.
- Deposition temperature.
- Deposition time which controls the film thickness.
- Dynamic or static substrate.
- Stoichiometry of source material.

The benefit of simulation methods is the ability to investigate some of these parameters without the need for carrying out any experiments.

During this work, the experimental deposition techniques described above are simulated using long time scale techniques, enabling a more precise understanding of the exact role of deposition technique on the deposited films morphology and properties.

1.4 Materials of Interest

Photovoltaics, a key industry in the future of energy supply, requires the deposition of layers into a multilayer stack. As stated, the chosen deposition technique plays a significant role on the quality of the deposited film. Many materials are involved in the production of thin films, some of which are investigated during this project. Previously, the photovoltaic market has been dominated by first generation crystalline silicon solar cells. Thin film photovoltaics are a second generation of solar cell where production costs are lower due to the significantly lower material consumption. Preparation involves the deposition techniques described above, with the option to deposit roll-to-roll due to the flexibility of thin films. Thin film photovoltaics include technologies such as optical coatings, dye sensitised solar cells and ceramic coatings. Figure 1.7 illustrates the structure of a dye sensitised solar cell. Al doped ZnO (AZO) can be used for the transparent conducting oxide (TCO), TiO₂ is used in its porous form to allow dye molecules to bind to it and finally, the back contact is made from metal.

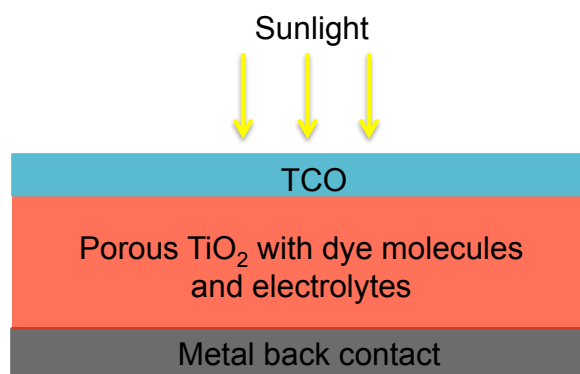


Figure 1.7: The simplified structure of a dye sensitised solar cell where AZO may act as the TCO, porous TiO₂ allows dye molecules to form bonds and a back contact is made from metal, such as Ag or Al.

Here, the materials used for all three parts of this cell are investigated, although all the materials do have other applications which will also be discussed. Ag and Al are two popular metals used in concentrator photovoltaics, electrical conductors in the monolithic interconnect processes for thin film photovoltaics (a-Si, CdTe and CIGS) and also back contacts as shown here. For all of these applications, similar deposition techniques are employed. TiO₂, in its dense and crystalline form, may be used as an anti-reflective coating or in its porous form within a dye sensitised solar cell as shown here. Simulation of TiO₂ deposition enables us to understand, experimentally, how to achieve a specific quality of film. AZO has photovoltaic uses particularly in transparent electrodes due its wide band gap of 3.37 eV. The most common use of ZnO is the doped Al TCO application. AZO typically has around 0.5% of Al, thus for the purpose of simulations only intrinsic ZnO is investigated. ZnO is also used as an intrinsic n-type semiconductor.

1.5 Thesis Layout

Chapter 2 introduces MD, with descriptions of all the interatomic potentials used throughout the work. We then discuss energy minimisation techniques, which are used frequently in simulations. Boundary conditions, which are applied to all growth simulations, are explained. Chapter 3 goes on to introduce the long time scale dynamics techniques, which enable the longer time scales to be simulated. Single and double-ended search methods, which allow for the searching of saddle points and exact calculation of barriers, are introduced along with an example of their implementation. The otf-KMC technique is thoroughly explained, including

some examples of transitions which are deemed irrelevant to thin film growth so can be filtered by the methods. The way in which the MD and otf-KMC methods combine and work in parallel using a server and many client processors is also illustrated. Chapters 4, 5 and 6 present the findings of this thesis. Metal, TiO_2 and ZnO thin films have been investigated using simulation techniques including high temperature MD, MD and otf-KMC. Specific PVD techniques, including evaporation, ion-beam assisted evaporation and magnetron sputtering, have been modelled in order to simulate thin film growth. Finally, chapter 7 draws some conclusions and suggests some avenues for future work.

Chapter 2

Methods I: Molecular Dynamics

This chapter introduces molecular dynamics (MD), explaining how computing techniques can be used to simulate the movement and interaction of atoms over time using Newton's second law of motion. An MD simulation required a description of the terms by which the atoms interact during the simulation. During this project interatomic potentials are used to describe this interaction. The specific interatomic potential chosen is dependant upon the system which is being modelled. Many interatomic potentials are applied throughout this research to describe all the specific material interactions and are described below. During an MD simulation, it is at times necessary to minimise a lattice configuration such that all atoms move to minimum energy sites, the methods available for this minimisation are described in this chapter. When performing a simulation there are certain system constraints which can be used to create a more realistic simulation; boundary conditions can be either fixed, free or periodically described in order to mimic the behaviour of a larger bulk. If periodic boundary conditions are employed then the Ewald method is used to evaluate the electrostatic energy and forces. Thermal layers may also be attached to a system in order to allow initial heating (thermalising) of a lattice and also to extract excess heat from systems after successive atomic impacts, such as those required for the simulation of thin film growth. Also introduced here are the the data visualisation methods employed throughout this work in order to allow instant visualisation of data and the production of POV-ray rendered images which can be linked together to form video clips.

2.1 Introduction

Molecular dynamics (MD) is an atomistic computer simulation technique, which uses classic mechanics in order to follow the evolution of a system over time. The forces on the atoms are calculated using a material specific interatomic potential (later described in the section ‘Interatomic Potentials’). Newtons second law is then used to determine the acceleration of the atoms using the known forces and positions;

$$\mathbf{F}_i = m_i \ddot{\mathbf{r}}_i, \quad (2.1)$$

where \mathbf{F}_i is the force exerted on the particle i , m_i is it’s mass and $\ddot{\mathbf{r}}_i$ is it’s acceleration. Integration of Newton’s second law then yields a trajectory describing the positions, velocities and accelerations of the particles as they vary with time. The method is deterministic; once the positions and velocities of each atom are known, the state of the system can be predicted at any time in the past or the future. Figure 2.1 shows the procedure of a classical MD simulation.

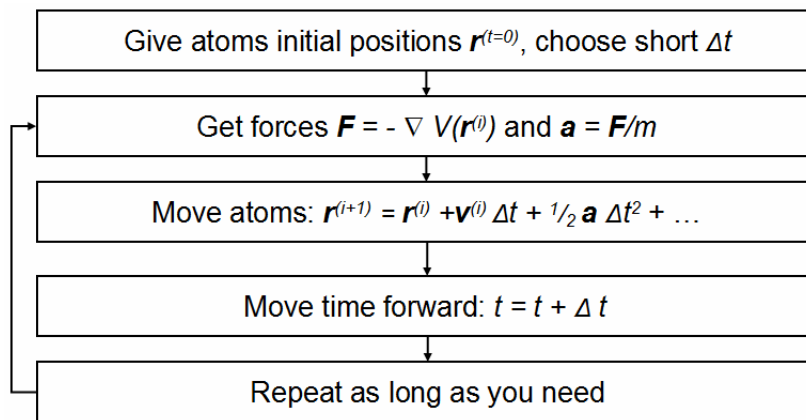


Figure 2.1: Diagram illustrating how an MD simulation works. The simulation starts with initial positions described for atoms, forces are then calculated along with accelerations of particles. All atoms are moved to their new positions using the integration equation and time is incremented one time step. The MD scheme is repeated until either a time limit is reached, or the user ends the simulation.

Simulation techniques have evolved in recent years, allowing us to perform simulations allowing investigation of atomistic behaviour that is very difficult to reproduce or understand experimentally. MD was originally conceived in the mid 20th century within theoretical physics, where atoms were considered as rigid spheres and

simple interaction potentials were used [14]. MD methods quickly gained interest from materials scientists, biochemists and biophysicists. The application of MD in physics has become very useful in examining the dynamics of atomic level phenomena, such as film growth, simulated in this project. One of the first MD simulations able to model atomic interaction realistically was Rahman's 1964 study of modelling liquid Ar [15] using a Lennard-Jones interatomic potential [16]. Moore's law states that over the history of computing hardware, the number of transistors on integrated circuits doubles approximately every two years [17]. MD simulations jumped on the back of the Moore's law explosion and followed the expansion of computing power with an expansion of simulation power and ability. Simulations jumped from hundreds of atoms to millions of atoms. The time scale problem, however, still exists, with MD only allowing simulation of atomistic systems over typically picosecond time scales.

LBOMD (Loughborough molecular dynamics) is a package developed at Loughborough University [4] and is used throughout this project to perform all MD simulations. LBOMD is an MPI-based Fortran90 code created for simulating nano-indentation and collision cascades within solids. The code is written in such a way that the user can monitor parameters including current simulation time, total system energy, thermostat type, system temperature, the time of the next output file event, how frequently data is written out and the temperature of the thermostat. Therefore, the code is very useful for the analysis of output, such as the temperature as a function of time or how well energy is conserved.

2.2 Evolving the System

Common to all MD simulations is the method of evolving the system in time. The velocity Verlet [18] algorithm is used in this work, advancing the trajectory of atoms using a fixed finite time step, Δt . This algorithm is derived from a Taylor series expansion, where the position and velocity of each atom at each time step are determined by;

$$\mathbf{r}_i(t + \Delta t) = \mathbf{r}_i(t) + \mathbf{v}_i(t)\Delta t + \frac{\mathbf{F}_i(t)}{2m_i} \Delta t^2, \quad (2.2)$$

$$\mathbf{v}_i(t + \Delta t) = \mathbf{v}_i(t) + \frac{\mathbf{F}_i(t + \Delta t) + \mathbf{F}_i(t)}{2m_i} \Delta t, \quad (2.3)$$

where \mathbf{r}_i is the position, \mathbf{v}_i is the velocity, m_i is the mass of atom i and t is the current time. The accuracy of the position and velocity in this method can be shown to be of the order of Δt^2 with global error in position. If our systems do not include thermalisation, they are Hamiltonian and energy is conserved. This energy conservation is dependant on the magnitude of movement of atoms between each force evaluation, therefore the time step must vary as a function of the maximum velocity. LBOMD makes the time step dependant on the maximum kinetic energy within the system and the distance of closest approach, with a typical time step of 10^{-15} seconds.

When simulating single cascades in a metallic system, millions of atoms can be simulated for nanoseconds, as only very short range forces are considered. Conversely, more complicated systems such as oxides considered in this work, have a short range interaction which acts over 5-10 Å plus a long range interaction, which need to be considered. Therefore, system sizes of complicated systems must be limited in order to simulate any realistic time scale. During this work, where multiple impacts are considered, system sizes between 900 and 2000 atoms are simulated for up to 10 ps to simulate a deposition.

2.3 Interatomic Potentials

Central to an MD simulation is the definition of an interatomic potential function or a description of the terms by which the particles in the simulation will interact. Until this potential is known, time cannot be evolved using the velocity Verlet method described previously. The most accurate force calculations are *ab initio* [2], however, these calculations are far too computationally expensive to be used for the simulations throughout this research. *Ab initio* modelling can, however, be useful for parametrisation of empirical potential functions, providing more accurate potentials for use in MD simulations. The traditional method for deriving a function to describe the interatomic behaviour was based on choosing a fixed analytical functional form and using experimental data to parameterise the function.

The earliest and simplest form of potential is the pair potential. Based on the separation (r_{ij}) of a pair of atoms i and j , the energy E_i of atom i is given by the

sum over all pairs of i and j ;

$$E = \frac{1}{2} \sum_{i \neq j} V(r_{ij}) \quad (2.4)$$

Pair potentials of this form are widely used due to their simplicity. However, pair potentials fail to model some metals with great accuracy as they can incorrectly estimate the structural relaxation around defects, hence overestimating the vacancy formation energy. Therefore, pair potentials are now generally used only for the modelling of rare gases. For ionic materials, the pair potential can be further broken down into long range and short range elements. The long range element is the Coulombic interaction, accounting for the bulk of cohesive energy in the system and the short range element is mainly repulsive. This long range Coulombic interaction is time consuming to calculate as it requires all atoms in the system to be considered, so algorithms including Distributed Parallel Multipole Tree Algorithm (DPMTA) [19] and the Ewald method [20] exist to speed up the calculations.

2.3.1 Lennard-Jones Potential

A pair potential commonly used is the Lennard-Jones potential [16]. Successfully applied to model the interaction of Ar and other gases [15], the L-J potential is one of the earliest interatomic potentials. The model, proposed by John Lennard-Jones in 1924 [16], consists of two parts; a steep repulsive term and then a smoother, attractive term. The L-J potential is important as it often forms the basis of other, more complicated potentials. One of the earliest recorded uses of the L-J potential in a simulation was in 1957 when Wood and Parker applied the potential to a study of the behaviour of liquid Ar [21].

The form of the L-J potential function is given by;

$$V_{r_{ij}} = 4\epsilon \left[\left(\frac{\sigma}{r_{ij}} \right)^{12} - \left(\frac{\sigma}{r_{ij}} \right)^6 \right] \quad (2.5)$$

where ϵ is the depth of the potential well (i.e. the energy), r is the distance between two particles i and j and σ is the finite distance at which the inter-particle potential is zero, which is related to the interatomic separation at the potential

minima ($r_m = 2^{1/6}\sigma$). Figure 2.2 illustrates the L-J potential function, showing where the repulsive and attractive terms are important.

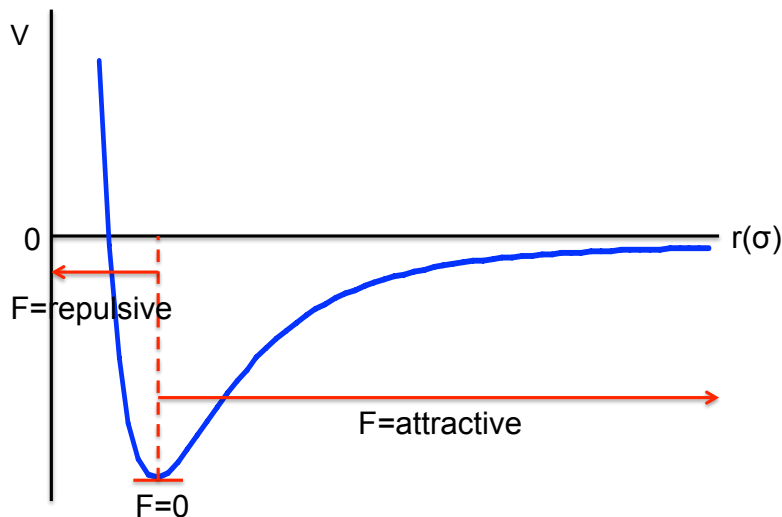


Figure 2.2: The L-J potential function plotted on a graph, showing where the force is repulsive, equal to zero and attractive.

The first term is the repulsive term describing Pauli repulsion at short ranges, where no two identical fermions (electrons) can simultaneously occupy the same quantum state. The second term describes the van der Waals attraction at long ranges. The attractive term has physical justification due to its functional form, however, the repulsive term has no theoretical justification and is used for convenience because it can approximate the Pauli repulsion and because it is more computationally efficient to calculate r^{12} as the square root of r^6 . The L-J potential described here is the 12-6 potential. R. A. Buckingham later proposed a simplification of the L-J potential, the Buckingham (6-exp) potential [22], where the repulsive term is replaced with a more flexible parameter exponential from the Born-Mayer potential.

2.3.2 Embedded Atom Method

Daw and Baskes [23–25] took the pair potential and expanded it into the embedded atom method (EAM), where unlike the pair potential, the energy of an atom is dependant on the local binding environment. The method adds an embedding term to the pair potential, so that it takes into account the lattice structure around the currently evaluated atom by considering the electron density ρ at that point and

factors in the corresponding energy required to embed the atom. This provides a better description of metals than pair potentials. The total energy of atom i , E_i , involves an embedding term representing the electron density of each atomic site and a pairwise sum of interactions between atoms;

$$E_i = F_\alpha \left(\sum_{i \neq j} \rho_\beta(r_{ij}) \right) + \frac{1}{2} \sum_{i \neq j} U_{\alpha\beta}(r_{ij}) \quad (2.6)$$

where

$$\rho_i = \sum_j \phi_j(r_i). \quad (2.7)$$

Here, r_{ij} is the interatomic separation between two atoms i and j , $U_{\alpha\beta}$ is a short-range pair interaction between this pair of atoms, ρ_β is the contribution to the electron charge density from atom j of type β at the location of atom i and F_α is an embedding function that represents the energy required to place atom i of type α into the electron cloud. Baskes later published the modified EAM (MEAM) [26], an extension of the EAM to include angular forces. To evaluate a given atoms embedding function, the electron density at the position of atom i is calculated from atomic densities, described by a density function $\phi_j(r)$.

The EAM is a popular method used for semi-empirical calculations in close packed metals as it combines simplicity with many-atom effects [27]. Purely metallic systems investigated in this research required force calculations which were performed using the EAM potential. When simulating silver systems, an EAM potential developed by Ackland was used [28, 29]. The functional form of the Ackland EAM potential is given by;

$$V = \sum_{j>i} V_2(r_{ij}) + \sum_i F_i \left(\sum_{j>i} \phi_{ij}(r_{ij}) \right) \quad (2.8)$$

where V_2 is the pairwise interaction, ϕ_{ij} is the contribution of the atom j to the density of the electron field around the atom i and F_i is the embedding energy term. These functions take on the following forms;

$$V_2(r) = \sum_k a_k (r_k - r)^3 H(r_k - r), \quad (2.9)$$

$$F(\rho) = -\sqrt{\rho} + c_2 \rho^2 + c_4 \rho^4, \quad (2.10)$$

$$\phi(r) = \sum_k A_k (R_k - r)^3 H(R_k - r). \quad (2.11)$$

where H is the Heaviside step function and A_k , a_k , R_k and r_k are parameters that depend on the atomic species of i and j . The parameters for the Ag potential can be found in the following papers [28,29].

For the aluminium system, Voter and Chen's EAM potential [30] was used to perform the calculations. A universal function, scaling the cohesive energy of most metals, is taken here to fit the embedding function. In their model, the pair interaction was taken to be a Morse potential;

$$\rho(r) = D_M \{1 - \exp[-\alpha_M(r - R_M)]\}^2 - D_M \quad (2.12)$$

where parameters D_M , R_M and α_M define depth, distance to the minimum and a measure of curvature near the minimum. The density function is taken as;

$$\rho(r) = r^6 [e^{\beta r} + 2^9 e^{-2\beta r}] \quad (2.13)$$

where β is adjustable and 2^9 is a relative normalisation factor. To ensure continuity between the potential and first derivatives, a cut-off function is used during the fitting procedure. The parameters for the Al potential can be found in the following paper [30].

2.3.3 Ziegler-Biersack-Littmark (ZBL) Potential

The ZBL potential form [31] is a repulsive pair potential, which has become an industry standard for close range interactions. The ZBL provides the ability to model the repulsive interaction between nuclei at very small distances, preventing the penetration of shells of atoms. Ziegler, Biersack and Littmark took scattering angles of pairs of atoms and were able to fit the ZBL potential to 522 pairs of atoms. The ZBL works by the assumption that the Coulombic forces are shielded by the electron cloud over a certain distance, while modelling the close range repulsion between atomic nuclei. The equation below illustrates the ZBL;

$$\phi(r) = \frac{1}{4\pi\epsilon_0} \frac{Z_1 Z_2}{r} \zeta \left(\frac{r}{a} \right) \quad (2.14)$$

where Z_1 and Z_2 represent the charges on the atoms and ϵ_0 represents the permittivity of vacuum. ζ is the shielding term; as $r \rightarrow 0$, $\zeta \rightarrow 1$, and a represents the screening range (Bohr radius).

The majority of potential functions fail to correctly and accurately describe the short range interactions and thus incorporate the ZBL, which describes the screened Coulombic nature of short range repulsion. The ZBL is then matched up to the main potential by comparing to an interpolated spline function. We have a purely ZBL potential $\phi(r_{ij})$ (cutoff $< x_1$) and a Coulombic potential $U(r_{ij})$ (region $> x_2$), where r is the interatomic separation. The spline function $s(r_{ij})$ acts between these two points, x_1 and x_2 , to join the functions with smooth continuous derivatives. Giving the overall expression for the potential function U_T as;

$$U_T(r_{ij}) = \begin{cases} \phi(r_{ij}) & \text{if } r_{ij} \leq x_1, \\ s(r_{ij}) & \text{if } x_1 < r_{ij} < x_2, \\ U(r_{ij}) & \text{if } r_{ij} \geq x_2 \end{cases} \quad (2.15)$$

The parameters for fitting the spline to the ZBL are derived as required. During this research, a noble gas is included in some simulations. Calculations of the ZBL interaction between noble gases and other metallic or oxide materials were performed using a purely repulsive ZBL potential as described above.

2.3.4 Coulomb Potential

When modelling ionic materials, the electrostatic forces between charged particles must be considered. The Coulomb potential describes the interaction between two charged particles and is directly proportional to the size of the charges, whilst inversely proportional to their separation (r_{ij});

$$V_{LR}(r_{ij}) = \frac{1}{4\pi\epsilon_0} \frac{q_i q_j}{r_{ij}} \quad (2.16)$$

where q_i and q_j are the respective charges on atoms i and j and ϵ_0 is the permit-

tivity of free space. When q_i and q_j have the same sign, V_{LR} will be positive (i.e. the atoms repel). Conversely, when q_i and q_j have opposite signs, V_{LR} will be negative (i.e. the atoms attract). The Coulombic interaction is a long range function, where to evaluate the potential energy function, all particles in the system must be considered. This would be very computationally expensive due to the high number of computations which would be required. Fortunately, numerous algorithms exist which can be used to speed up these long ranged calculations. Used for non-periodic systems, the distributed Parallel Multipole Tree Algorithm (DPMTA) [19], which is based on the Fast Multipole Algorithm [32], treats a group of particles located a large distance away from a single particle as a single entity. This greatly reduces the number of calculations required, reducing the entire simulation region into well separated areas using the Barnes and Hut ‘tree code’ algorithm [33]. These regions are then allowed to interact. When dealing with periodic systems, however, the Ewald method [20] is used. The method involves the decomposition of the electrostatic potential into short and long range components. The short range part sums quickly in real space, while the long range part sums quickly in Fourier space.

2.3.5 Fixed Charge Potential

Fixed charge potentials are known to provide excellent values for most bulk attributes of TiO_2 . The most commonly used fixed charged potential was implemented in 1991 by Matsui and Akaogi [34], parameterised to reproduce all of the TiO_2 polymorphs and thus widely used [35–37]. The potential is given by;

$$U_{ij} = \frac{q_i q_j}{r_{ij}} - \frac{C_i C_j}{r_{ij}^6} + f(B_i + B_j) e^{-\frac{A_i + A_j - r_{ij}}{B_i + B_j}} \quad (2.17)$$

where the first term represents the electrostatic, Coulombic part (described above), the second term represents the dispersion (van de Waals force) and the last term represents the repulsion interaction. The van de Waals and repulsion terms together constitute a Buckingham potential.

The fixed charge nature of this potential means that it deals poorly with locally non-stoichiometric configurations. The variable charge potential described next has been proven to deal with these configurations in a much better way [5].

2.3.6 Variable Charge Potential

The most commonly used fixed charge potential described above has been compared to a well known variable charge potential (Hallil *et al.* [38]), where results suggested that the variable charge potential models interfaces and surfaces and locally non-stoichiometric configurations much more accurately [5]. As our research involves the modelling of surfaces and non-stoichiometric configurations, a variable charge potential is described here. A method for predicting charge variation of atoms was published by Rappé and Goddard in 1991, the QEq scheme [39]. This charge equilibrating scheme allowed charges to change depending on the neighbouring configuration, something never considered in fixed charge potentials. The charge dependant energy of the ions is given by;

$$E_i = E_i(0) + \chi_i^0 q_i + \frac{1}{2} J_i^0 q_i^2 \quad (2.18)$$

where χ_i^0 corresponds to the electronegativity (the desire of the ion to gain some charge) and J_i^0 corresponds to the hardness, acting as a penalty for atoms which gain too much charge. The total energy, E_i , is iteratively minimised due to charge using the conjugate gradient method, where a constrained minimisation is performed such that the sum of charges is zero.

Hallil *et al.* developed the SMB-QEq potential for TiO₂, a second-moment-Buckingham potential using the QEq scheme in 2006 [38]. They recognised that the Morse repulsive potential was unsatisfactory for describing the energy associated with oxygen defects, thus introduced an N-body potential [40] that was previously used in describing metallic alloys.

Vernon published a modified form of the SMB-QEq potential, the MQEq potential [1, 5]. A new Ti-O interaction was introduced, based on the second moment tight binding approach, attempting to compensate for the covalent energy of the bond;

$$E_i = \sum_j A_{IJ} e^{-P_{IJ}(r_{ij}/r_0^{IJ}-1)} - \left(\sum_j \sigma_{IJ}^2 e^{-2q_{IJ}(r_{ij}/r_0^{IJ}-1)} \right)^{1/2} \quad (2.19)$$

where the first pairwise sum is a Born-Mayer potential [41] and the second is an N-body sum providing the energy contribution from the covalent bond.

The O-O interaction required modification as DFT calculations showed that that O₂ dimers on the surface are mobile and play an important role in reducing energy barriers for Ti interstitials [42]. The modification was made such that the bulk parameters remained unchanged, with an attractive interaction between atoms within an O₂ molecule at the surface. A many-body switching function was added, switching between a L-J potential [16] between two O atoms in the presence of no other neighbouring atoms and a Buckingham potential [22] when the O atoms are within a bulk, which enables the potential to correctly model the formation and deposition of the O₂ dimer molecules on the surface. A screening function calculates the screening factor, which is then combined with a switching factor. From these, the potential V_{ij} can be calculated;

$$V_{ij} = \textit{Switching} \times (\textit{LJ}(r_{ij}) - \textit{Buck}(r_{ij})) + \textit{Buck}(r_{ij}) \quad (2.20)$$

where clearly with no neighbours, the *Switching* function evaluates to zero thus leaving just a L-J interaction. However, with a large number of neighbours lying within a cut-off range, the screening will be close to 1 thus leaving a purely Buckingham interaction.

In the original potential, the Ti-Ti interaction was undefined, so a short range repulsive ZBL [31] interaction was added with a cut-off occurring between 1.5 and 2.5 Å. O hardness was reparameterised from 12.63 to 18.3 as excessive charge transfer was seen when compared to equivalent processes using DFT, resulting in an artificially high Ti interstitial escape barrier [43].

This modified SMB-QEq potential is used later on in this thesis, in the chapter ‘Simulation of Titanium Dioxide Thin Film Growth’, for describing the interactions in a TiO₂ system.

2.3.7 Albe ZnO Potential

Albe *et al.* in 2006 employed an analytic bond-order potential (ABOP) scheme [44, 45], which had already been used successfully for modelling purely metallic, covalent, molecular and mixed ionic-covalent systems [44–48]. Therefore, it offered the ability to describe all interactions within the ZnO system. Although in many situations neglecting the charges is deemed acceptable, the ABOP is limited

if internal/external electric fields become dominant, as would occur at a material interface or at the surface. The restriction to first nearest neighbours implies a zero energy difference between two common ZnO phase structures (wurtzite and zinc blende).

Albe *et al.* employed PONTIFIX in order to fit parameter sets to the ABOP scheme [49]. The ABOP scheme gives the total energy as a sum over individual bond energies;

$$E = \sum_{i>j} f_{ij}^c(r_{ij}) \left[V_{ij}^R(r_{ij}) - \underbrace{\frac{b_{ij} + b_{ji}}{2}}_{b_{ij}} V_{ij}^A(r_{ij}) \right] \quad (2.21)$$

where a Morse like pair potential is adopted for the pair-like attractive ($V^A(r)$) and repulsive ($V^R(r)$) terms. Later on in this thesis, in the chapter ‘Simulation of Zinc Oxide Thin Film Growth’, initial tests of this potential are documented.

2.3.8 Reactive Force Field Potential

Conventional potentials such as L-J [16] potentials do not model the bond orders. Reactive force field (ReaxFF) is a bond order potential which allows for a more general description of chemistry, where all energy terms are dependant upon the bond order. In 1985, Abell produced a general expression for binding energy as a sum of near neighbour pair interactions, moderated by the local atomic environment [50]. In the 1990’s, Tersoff and Brenner apply this to silicon systems [51, 52]. Stuart *et al.* in 2000 developed a reactive potential for hydrocarbons [53]. Van Duin *et al.*, not long after, published their reactive potential for hydrocarbons, calling it “ReaxFF” [54], for use in MD simulations. During the following years the ReaxFF potential was extended to various materials [54–56].

The total energy of the system is expressed as the sum of all the terms which describe the individual chemical bonds in the material;

$$\begin{aligned}
E_{system} = & \underbrace{E_{bond} + E_{vdWaals} + E_{Coulomb}}_{\text{2-body}} + \underbrace{E_{valency\ angle}}_{\text{3-body}} + \underbrace{E_{torsion}}_{\text{4-body}} \\
& + \underbrace{E_{over} + E_{under}}_{\text{multi-body}}
\end{aligned} \tag{2.22}$$

where each expression is in terms of bond order with all interactions being calculated between all the atoms in the system. The E_{bond} expression comes from the bond energy between atoms i and j , which depends not only on the bond distance but more importantly on the bond order. $E_{vdWaals}$ accounts for short distance repulsion and long distance attraction. $E_{Coulomb}$, similar to the van der Waals interaction, is taken into account for all atom pairs. The shielded Coulomb potential is used to adjust for orbital overlapping between atoms close to one another. $E_{valency\ angle}$ has three main functions, firstly to ensure that the energy contribution from the valence angle term goes to zero as the bond orders in the valence angle goes to zero. In order to reproduce the stability of systems with two double bonds sharing an atom in a valency angle, an energy penalty is also introduced. As $E_{valency\ angle}$ is a 3-body term, a 3-body conjugation term is included. $E_{torsion}$ ensures that torsion rotation barriers are accounted for, while also including the contribution of conjugation effects to the molecular energy. Finally, the E_{over} and E_{under} terms either impose an energy penalty on systems with an over-coordinated atom or take into account the energy contribution for the resonance of the electron between attached under-coordinated atomic centres.

As with the previously described ZnO Albe potential [48], initial tests of the ReaxFF potential are also documented later on in this thesis.

2.4 Interatomic Potential Optimisation

Given a pair of atoms i and j , for most interatomic potentials, there will be a separation R_{ij}^{max} where the energy between the two atoms can be considered small enough to be ignored. With this method, it becomes necessary only to evaluate the potential energy of a system when $R_{ij} < R_{ij}^{max}$. The value of R_{ij}^{min} is of great importance, if it is very large then there will be a large discontinuity in the function leading to a lack of energy conservation. It is, therefore, necessary to consider a

cut-off function enabling smooth convergence to zero, as discussed previously with the ZBL function. In order to reduce computing time, a cut-off (R_{ij}^{max}) is applied such that the potential is only calculated for atoms within the cut-off distance.

2.5 Energy Minimisation Techniques

During a simulation, it often is necessary to minimise a configuration of atoms such that all atoms relax into their minimum energy sites. This is necessary between successive atomic impacts to ensure the lattice is in its minimum energy state. Minimisation is also required during the saddle point search methods, discussed in the next chapter.

Various energy minimisation techniques exist; steepest descent, conjugate gradient and quasi-newton. The first technique finds a local minimum by taking steps proportional to the negative of the gradient of the function at a point. However, convergence is slow near the minimum as the gradient is approaching zero. The second technique adjusts the configuration of the system based on the energy gradient generated by previous and current coordinates, allowing travel to the minimum.

During this project, the energy minimisation technique employed is the conjugate gradient scheme, due to its efficiency in convergence to a minimum. It was previously found that the Polak-Ribière method [57] performed better in practice than the Fletcher-Reeves method [58], with quicker convergence to the minimum when used alongside the ‘regula falsi’ line minimiser [5]. During this work this Polak-Ribière conjugate gradient method was applied.

2.6 Boundary Conditions

A limitation of MD is the size of the system that can be modelled, which depends on the particular problem under investigation. It is, however, possible for many applications to keep the system size small whilst retaining some of the properties of a larger system. Such models require the implementation of boundary conditions which are either fixed, free or periodic.

2.6.1 Fixed/Free Boundary Conditions

When using fixed boundary conditions the outer layer(s) of atoms are fixed, allowing reproduction of lattice strain. The fixing of outer layers applies an artificial pressure on atoms inside the bulk. When simulating low energy single impacts onto a surface, fixed boundaries are appropriate as atomic disruption is minimal. However, when simulating surface growth with multiple impacts at higher energies, the boundaries become important for accurate representation of a bulk. When performing single impacts, all edges were fixed, excluding the surface which remained free. A fixed boundary must be employed on the bottom layer of a lattice during a deposition simulation, otherwise atoms would move by conservation of momentum.

2.6.2 Periodic Boundary Conditions

Alternatively, periodic boundaries may be employed. Surface growth requires periodic boundaries to ensure accurate atomic diffusion at or near the boundaries. Period boundary conditions (PBC's) allow much more flexibility during a simulation, working by tessellating the lattice in all periodic directions in such a way that an atom crossing a periodic edge will wrap around the lattice, re-entering from the opposite side in order to mimic a bulk. An atom close to a periodic edge will view all of the opposite edges' atoms as neighbours, interacting with them as normal. Due to the nature of the research carried out in this project, our substrates are rectangular in shape and periodic boundary conditions in the x and z dimensions (parallel to the surface) are employed during growth simulations to allow this mimicking of a larger bulk.

2.6.3 Thermal Layers

When impacts occur on a large system containing billions of atoms, energy would eventually dissipate away from the area of impact. However, when using a small sized lattice to model this with either fixed or periodic boundaries, energy is conserved within the system. Successive impacts, required when simulating surface growth, would result in the system heating up rapidly. One function of a thermal layer is to extract this excess heat from the system after each impact. Also important is the initial heating of a lattice. In practice, surface growth is carried out at a desired temperature. Another function of the thermal layer is to increase

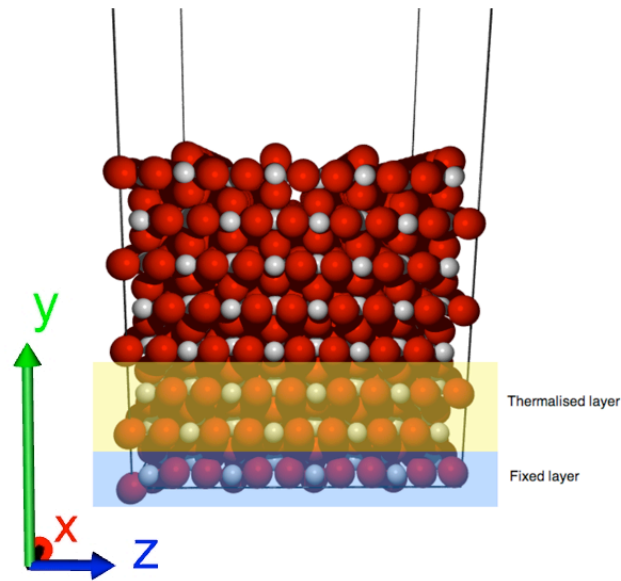


Figure 2.3: During a growth simulation of TiO₂, the bottom layer of the lattice employs fixed boundary conditions, with all other edges being periodic apart from the surface itself which is free. A Berendsen thermostat is attached to the two layers which lie above the fixed layer, which will allow for system heating and cooling.

the system temperature as desired before an impact is simulated, ensuring that conditions are as close to reality as possible. Thermal layers are incorporated into systems in order to act as a heat bath to extract excess energy transferred by an impact and to ensure the system is at the correct temperature before a deposition.

Numerous thermostats exist and two popular methods include the Berendsen thermostat [59] and the Nosé-Hoover thermostat [60–62]. The Berendsen thermostat controls the temperature by scaling the velocity of each particle at each time step. The thermal layer controls the temperature by either reducing energy or giving extra energy to atoms near a boundary, which then collide with free atoms in the system. This method allows gradual reduction of the whole system temperature. The Nosé-Hoover thermostat controls the temperature instead by modifying the equation of motion, adding a friction coefficient, which is used for constraining the temperature. As with the Berendsen thermostat, temperature can be increased or decreased using this method. During the research carried out in the project we choose to use the Berendsen thermostat due to the speed at which it can bring a system of atoms to the desired temperature as it is faster than the Nosé-Hoover. Figure 2.3 illustrates how the thermal and fixed layers fit into a lattice.

2.7 Visualisation

During MD simulations, real time results can be stored with relevant atomic positions and energy data. Data visualisation is a huge advantage and very useful tool in data analysis and understanding mechanisms and patterns. Throughout this research, data was visualised using the atomic visualisation and analysis (AVA) suite, developed in 2010 [8]. Figure 2.4 illustrates the user interface of the software. This suite was written in a mix of C and python code, with the ability to render lattices using POV-ray. Almost all of the lattice images included in this work were produced using the suite. The ability to produce real-time images of simulations was very useful for both analysis and initial testing of simulations to ensure that the methods were working correctly. The AVA suite is able to produce successive images of thousands of steps of otf-KMC, enabling us to create video clips of thin film growth by linking together all these images.

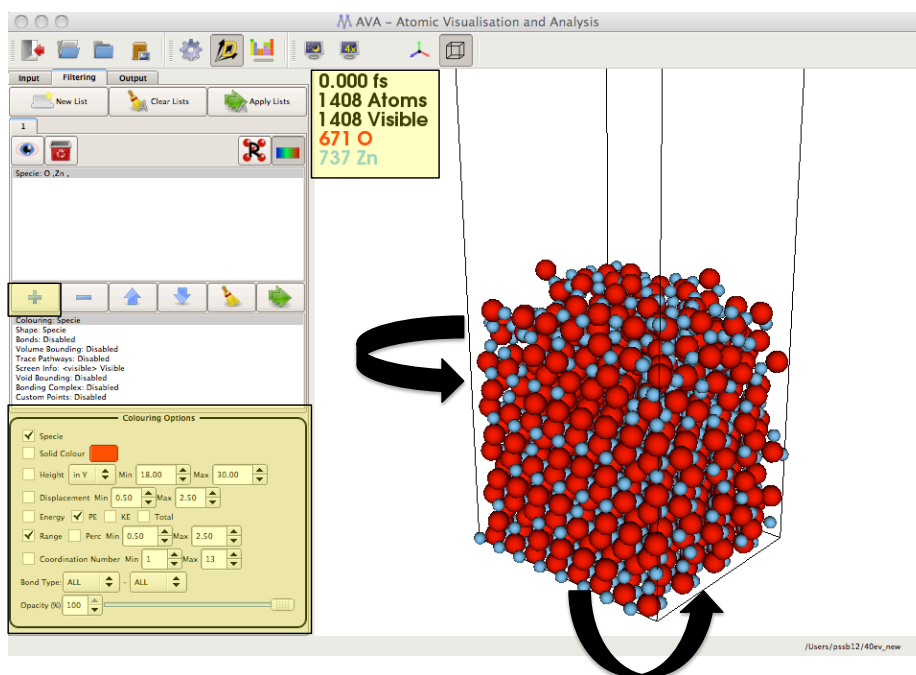


Figure 2.4: The user interface of the AVA suite [8], used throughout this project to visualise data and produce POV-ray images and video clips. For each image produced, the time of the simulation, number of atoms and the breakdown of species is shown. Colouring options are available, atoms may be coloured by species, height, displacement, range, etc. The highlighted button allows extra options such as cropping, displacement, viewing a range of atom numbers, etc. All these options make the AVA suite a very useful analysis tool.

Chapter 3

Methods II: Long Time Scale Dynamics

3.1 Introduction

Computer simulation is a powerful tool, but due to computational limitations it is still important to choose the most appropriate modelling technique for the system. Figure 1.1, previously introduced, shows where different modelling techniques fit onto a scale of time against size of system. Despite advances in computational power, using MD alone to model large atomic systems over time scales greater than nano seconds is computationally unfeasible. Any atomistic process with a high transition barrier is unlikely to have enough localised energy to take place within the standard MD time frames but will still need to be accounted for when extrapolating the atomistic behaviour over longer time scales. A simple way to increase the time scale of MD simulations is artificially to increase the deposition rate, however, this may lead to biased growth dynamics where diffusion events do not have time to occur during subsequent depositions. Another option to allow these less frequent diffusion events to occur is to raise the temperature such that diffusion events are scaled in proportion with the deposition rate, however, this also results in biasing of the dynamics due to non-linearity of the attempt frequency for transitions.

Long time scale dynamics (LTSD) allows the modelling of large systems over longer time scales, therefore becoming a very useful technique for surface growth. As illustrated in figure 1.1, LTSD fills a gap for simulation time scales that no other technique can realistically reach. The combination of MD and LTSD methods allows

simulation over a longer period of time without biasing of dynamics from increasing the temperature. LTSD techniques use the harmonic transitions state theory (hTST). Here, we introduce and utilise a relatively novel LTSD method, on-the-fly kinetic Monte Carlo (otf-KMC) [63]. Within otf-KMC, exploration of the potential energy surface (PES) is necessary in the search for transition pathways and saddle points. Saddle point search algorithms can be divided into two categories, double-ended search methods and single-ended search methods. The first category involves chain-of-states methods, which require the knowledge of both initial and final states of the system, the nudged elastic band (NEB) method [6, 7, 64] and the simple-string method [65, 66] are examples. The latter category involves minimum mode following methods, which only require knowledge of the initial system state in order to calculate a saddle point, such as the dimer method [67], the activation and relaxation technique (ART) [68, 69] and the relaxation and translation (RAT) method [5].

LTSD techniques, specifically KMC driven, have previously been used for various applications, including surface growth, grain boundary investigation, multi-atom surface processes and decomposition dynamics. Henkelman and Jónsson apply KMC methods to the Al (100) surface, where growth is simulated for some milliseconds. The surface was found to grow smoothly even at low temperatures due to low diffusion barriers [63]. They went on to investigate multi-atom transitions on the Al (100) and Cu (100) surfaces. KMC enables the investigation of non-trivial transitions by using random vector methods to find saddle points. Over 80% of transitions on the Al (100) surface were found to involve two or more atoms in multi-atom concerted motions [70]. MD alone would not have allowed the investigation of multi-atom transitions on such a large scale. Mei *et al.* combine the dimer and DFT calculations to study the decomposition of methanol on Cu (110), showing that LTSD techniques can be very useful when investigating complex catalytic reaction mechanisms by modelling the dynamics of surface chemistry from first principles [71, 72]. Pedersen *et al.* use LTSD techniques to investigate the behaviour of grain boundaries in copper. Adaptive KMC was used to study the atomistic structure of the boundaries and the mechanism of annealing at low temperature. The simulations were completed over a 10 day period, which using traditional MD, would have required 15 years [73]. Island nucleation of Ag on the Pu (111) surface has also been investigated using KMC methods [74], illustrating again the broad applications of the LTSD method. Vernon applied otf-KMC methods to TiO₂ systems, simulating the growth for several seconds of real time [5].

Other techniques exist for the acceleration of dynamics, parallel replica dynamics, hyperdynamics and temperature accelerated dynamics (TAD) are some examples. The parallel replica dynamics method proposed by Voter [75] is a simple, accurate way of accelerating dynamics with the only assumption being that infrequent events obey first order kinetics. The method involves replication of an entire system onto M parallel processors. A short de-phasing stage allows the momenta to be periodically randomised to eliminate correlations between replicas. Each processor carries out an independent MD trajectory until a transition is detected in any of the replicas. Thus the method allows exploration of the basin M times faster than on one single processor. When a transition is found, all processors terminate and the clock is advanced by the time of all replicas. Parallel replica dynamics have been successfully used to simulate Ag (111) islands, observing mostly concerted motions [76] and Cu (100) has also been simulated over extended time scales with 90% efficiency of surface vacancy diffusion [75].

Hyperdynamics, a method also introduced by Voter, evolves a system by modifying the potential surface by adding a non-negative bias potential. A classical trajectory is then used to evolve the dynamics [77]. Effectively, this method works by increasing the potential and thus increasing the rate of escape from different states. The bias potential should give a large boost factor, whilst sustaining low computational overhead. Voter investigated the diffusion mechanisms of a 10-atom Ag cluster on Ag (111), concluding that the hyperdynamics method linked with traditional MD is a promising method for extending time scales [78]. Sorensen and Voter also introduced the TAD method, also using hTST, which accelerates the dynamics of a system by raising the temperature. Events that should not have occurred at the lower temperature are filtered out [79]. Due to the use of hTST, TAD is approximate, however, for applications involving solids this approximation is acceptable. Many groups have used TAD and MD combined to effectively simulate thin film growth of metals. Montalenti *et al.* simulate the deposition of 4 monolayers of Ag onto the (100) surface with a boost of several orders of magnitude over traditional MD [80]. Sprague *et al.* also successfully apply TAD methods to the growth of Cu on the Ag (001) surface, simulating experimental deposition rates [81].

The otf-KMC method is chosen for this project due to the simplicity to apply the method in parallel. Transition searches can be performed on n processors, with the MD simulating a deposition on a single processor in parallel. For larger systems,

transition searches can also be localised to a subset of the system if appropriate, thus speeding up the method. Otf-KMC also has the ability to investigate non-intuitive concerted, multi-atom transitions which could not be predicted in advance. Many transitions found throughout this research rely on concerted motions for growth mechanisms to occur. Saddle point search algorithms will now be introduced.

3.2 Double-ended Search Methods

Within the otf-KMC method, in cases when both initial and final states of a transition are known, a double-ended search method may be employed to calculate minimum energy pathways and hence the height of the energy barrier. However, it can sometimes be more efficient to use a single-ended search with low accuracy, and then use a double-ended search to finish the calculation. Described here are the NEB and simple-string methods.

3.2.1 The Nudged Elastic Band method

The NEB method is a widely used technique, introduced in 1998 [64] by Jónsson *et al.* and later improved by Henkelman [6,7]. The method returns the height of an energy barrier between initial and final configurations of a transition, along with the minimum energy pathway (MEP). The method is a chain-of-states method, which involves placing a discrete number of images along an initial MEP guess, creating a band of evenly spaced images. Artificial spring forces are introduced to ensure the constant even spacing between images. The MEP always passes through at least one first order saddle point, described as the union of steepest descent paths from the saddle point to the minima. Two of the initial images are fixed (the initial and final states of the system) as shown in figure 3.1, where $n-1$ vectors join each point to its neighbour.

The real force vector, \mathbf{F}_i , acting on image i , can be decomposed into parallel and perpendicular force components with respect to the tangent vector $\hat{\tau}_i$. This tangent vector, $\hat{\tau}_i$, for image i is dependent upon the potential energy (V) relative to its

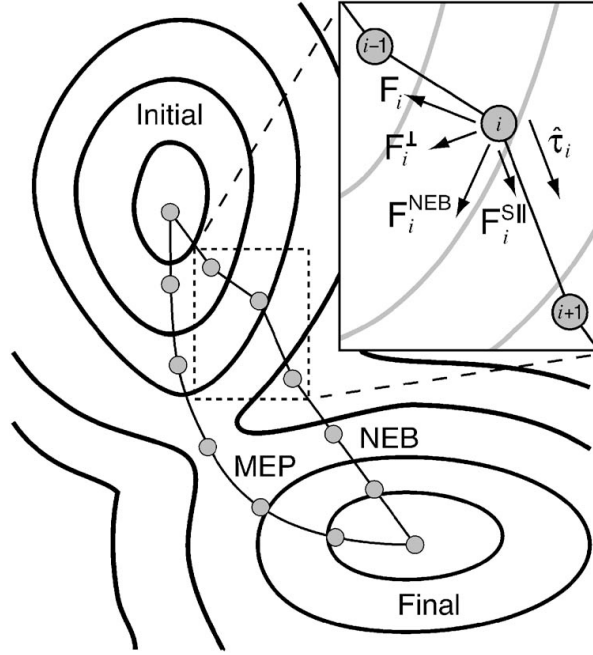


Figure 3.1: Illustration of the NEB method which calculates the MEP with the prior knowledge of both initial and final system configurations. Both the MEP guess and the true MEP found using the NEB method are highlighted here. Image taken from [82].

neighbour;

$$\hat{\tau}_i = \begin{cases} \mathbf{R}_{i+1} - \mathbf{R}_i & \text{if } V_{i-1} \leq V_i \leq V_{i+1}, \\ \mathbf{R}_i - \mathbf{R}_{i-1} & \text{if } V_{i-1} \geq V_i \geq V_{i+1}, \\ (\mathbf{R}_{i+1} - \mathbf{R}_i) \cdot V_{max} + (\mathbf{R}_i - \mathbf{R}_{i-1}) \cdot V_{min} & \text{if } V_i \leq V_{i-1} \leq V_{i+1}, \\ (\mathbf{R}_{i+1} - \mathbf{R}_i) \cdot V_{min} + (\mathbf{R}_i - \mathbf{R}_{i-1}) \cdot V_{max} & \text{if } V_i \leq V_{i+1} \leq V_{i-1}, \end{cases} \quad (3.1)$$

where V_{min} and V_{max} are the minimum and maximum absolute energy differences between V_{i-1} , V and V_{i+1} and \mathbf{R}_i is the position of the i_{th} image [6]. The tangential component is removed from \mathbf{F}_i , leaving the perpendicular component \mathbf{F}_i^\perp . An artificial spring force, $\mathbf{F}_i^{S||}$, is introduced acting parallel to $\hat{\tau}_i$ between the images places along the MEP. $\mathbf{F}_i^{S||}$ is given by;

$$\mathbf{F}_i^{S||} = k(|\mathbf{R}_{i+1} - \mathbf{R}_i| - |\mathbf{R}_i - \mathbf{R}_{i-1}|)\hat{\tau}_i \quad (3.2)$$

where k is the spring constant. The magnitude of $\mathbf{F}_i^{S||}$ scales with the separation of the images along the MEP, the further apart images are, the greater the spring force is.

In order to relax images on the MEP, a modified NEB force acts on each image i . This force, \mathbf{F}_i^{NEB} , is the sum of the perpendicular component of the real force \mathbf{F}_i^\perp and the artificial spring force $\mathbf{F}_i^{S||}$;

$$\mathbf{F}_i^{NEB} = \mathbf{F}_i^\perp + \mathbf{F}_i^{S||} \quad (3.3)$$

The entire system is then considered to be a point in $3N$ i space and is relaxed using a conjugate gradient minimiser [57]. The perpendicular component of force \mathbf{F}_i^\perp allows the NEB to relax laterally downhill towards the MEP, as the spring force $\mathbf{F}_i^{S||}$ retains the equal spacing of images along the MEP. Throughout this project, typically 10 images have been used for the MEP, allowing parallelisation of the method.

Typically, none of the images of the MEP land exactly on a saddle point. The saddle will usually lie between two images resulting in a small inaccuracy in the barrier calculation. The climbing NEB [7] is a modification of NEB allowing more accurate barrier calculation. The force is modified after relaxation of the system such that the highest energy image is allowed to move upwards towards the saddle;

$$\mathbf{F}_{i_{max}} = \mathbf{F}_i - 2\mathbf{F}_{i\tau} \quad (3.4)$$

Ignoring the spring force allows the highest energy image to move towards the saddle and the real force \mathbf{F}_i is reflected parallel to the tangent vector. The climbing NEB allows relaxation onto the MEP, whilst also converging the highest energy image onto the saddle point. This method allows exact calculating of the barrier height for any given transition where both initial and final states are known.

3.2.2 The Simple-String method

The original string method [65] is similar to the NEB. Each image in the string has a tangent vector calculated following the minimum energy pathway (MEP) and the force on the image is decomposed into two components (parallel and perpendicular). The perpendicular force vector is then minimised, relaxing images perpendicular to the string. The string was developed to avoid the artificial penalty from the application of the spring constant in the NEB. The construction of the tangent vector at each image along the string in the NEB involves linear displacement vectors, however, the string method constructs cubic splines at each image using the force

and energy and then the tangent is described as the vector parallel to the cubic spline.

Due to the original method being difficult and complex to implement, in 2007 a simplified string method [66] was proposed. The simplification came from the removal of all features apart from the interpolation of images along the string. The method involves the relaxation of images at each step in the direction of real force where there is no longer any decomposition of components of force. The displacement vector mainly pushes images towards their minima. Implementation of the simple string requires a sequence of vectors constructed such that every image is joined together with images evenly distributed ensuring even spacing along the sequence. Therefore, the component of force that carries the image toward the minima is compensated for by the requirement of equal spacing.

3.2.3 Chosen Method

The NEB is very useful due to the potential to run multiple searches over numerous processors, enabling parallelisation. The NEB may also require less force evaluations than the String Method, as little as half the number. An investigation into the number of force evaluations required to find barriers for simple O ad-atom hop on the rutile TiO_2 surface was carried out by Vernon, concluding that the NEB required 60% of the number of force evaluations required by the simple string method [5]. However, the simple string method has been successfully applied by other groups, therefore the choice of the method is largely dependant upon the implementation. The NEB is used throughout this project to calculate the energy barriers, with typically 10 images used for the MEP, allowing the searches to run in parallel.

3.3 Single-ended Search Methods

When only the initial state of a system is known, a single-ended search method following a minimum mode of curvature may be employed to converge to the saddle point. Using single-ended and double-ended search methods together can be ideal for complex systems where a single-ended search, with a low accuracy, can locate saddle points and then a double-ended search can calculate the MEP related to the

saddle point in order to accurately calculate the transition barrier. Described here are the dimer [67], ART [68,69] and RAT [5] methods.

3.3.1 Search Initialisation

All three methods require the construction of a random displacement vector for off-setting the lattice configuration from the minimum energy. Henkelman and Jónsson initially suggest a method of displacing each free coordinate in relation to a Gaussian distribution of width 0.1 \AA [67]. Previously tested by Vernon, a simple vector of length $3N$ where each element contains a random number from -1 to 1 , which is normalised and multiplied by a step-size, was found to allow convergence to all the expected saddle points available on both silver and titania surfaces. Fixed and randomised step sizes were tested by Vernon, with randomised step sizes between 0.1 and 0.5 \AA providing the quickest convergence [5].

Single-ended search methods require the limitation of the configuration search space, where only the coordinates of interest are included in the search for a saddle point. A simple solution would be to only include those atoms within a cut-off radius of the defect, however, the cut-off radius must be large enough for the configuration space to include all relevant saddle points. It has been suggested that with a system of 300 atoms, using fewer than 20 atoms in the search configuration would miss many important saddle points [63]. Another solution, applied throughout this project, was developed by Gordon [83]. A search array is created, containing all atoms in close enough range to the defect to be of possible interest. During execution of a search method, the force acting on atoms outside of those in the array is monitored. If the force surpasses a given limit then the atoms within the array are frozen whilst all other atoms are able to relax. This method enables a smaller search array, thus smaller configuration space, to be used, therefore providing optimum performance. A problem created by allowing outside atoms to relax is the potential for the drift of atoms when PBC's are in use. Compensation for this involves the calculation of the average displacement vector for all moving atoms and if this surpasses a limit, we subtract this from each atoms unique displacement vector.

3.3.2 The Dimer method

Henkelman and Jónsson in 1999 developed the dimer method [67], which uses an abstract dimer to represent two offset points in $3N$ configuration space. The method involves manipulation of the dimer, as illustrated in figure 3.2.

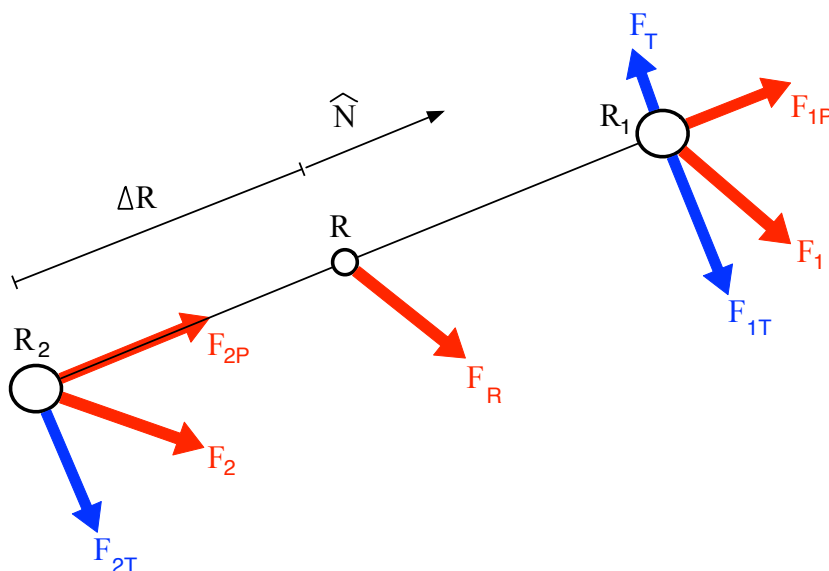


Figure 3.2: Illustration of the dimer, where the real force \mathbf{F}_R acting on the dimer is decomposed into parallel and perpendicular components with respect to each end of the dimer.

The first step of the dimer method is the offsetting of the point \mathbf{R} along a random displacement vector $\hat{\mathbf{N}}$. Two replica images of the system, \mathbf{R}_1 and \mathbf{R}_2 , are separated from their common midpoint \mathbf{R} by a distance $\Delta\mathbf{R}$ such that;

$$\mathbf{R}_1 = \mathbf{R} + \Delta\mathbf{R}\hat{\mathbf{N}} \quad (3.5)$$

and

$$\mathbf{R}_2 = \mathbf{R} - \Delta\mathbf{R}\hat{\mathbf{N}} \quad (3.6)$$

where $\Delta\mathbf{R}$ can be chosen depending on the surface. Henkelman and Jónsson previously suggest value for $\Delta\mathbf{R}$ of $1 \times 10^{-3} \text{ \AA}$, although larger displacements did improve results on some PES. Any saddle point will lie on a line of minimum curvature, hence by generating various random dimers, we can follow the lines of minimum curvature to various saddle points.

The method now contains two main parts, dimer rotation and dimer translation.

The first, dimer rotation, allows the dimer to find the lowest curvature mode through minimisation. The force acting on each point is decomposed into parallel and perpendicular components, giving the global rotational force to be;

$$\mathbf{F}_{\mathbf{T}} = \mathbf{F}_{1\mathbf{T}} - \mathbf{F}_{2\mathbf{T}} \quad (3.7)$$

where $\mathbf{F}_{i\mathbf{T}}$, the perpendicular component is achieved by subtracting the parallel component;

$$\mathbf{F}_{i\mathbf{T}} = \mathbf{F}_i - (\mathbf{F}_i \cdot \hat{\mathbf{N}})\hat{\mathbf{N}}, \quad \text{for } i=1,2 \quad (3.8)$$

The energy of the dimer is minimised with respect to this rotational force, $\mathbf{F}_{\mathbf{T}}$, thus rotating the dimer to a line of lowest curvature of the PES. The minimisation of $\mathbf{F}_{\mathbf{T}}$ involves a conjugate gradient [57] step, which selects the plane of minimisation and then uses a rotational equivalent minimiser to reduce the component of rotational force. Numerous methods for the rotational minimisation were tested by Henkelman and Jónsson, including the modified newton method, harmonic approximation and the ‘regula falsi’ estimation.

The second part involves translation of the dimer. A first order saddle point on a PES is at a maximum along the lowest curvature direction, whilst at a minimum in all other directions. A scheme is used to enable the dimer to aggressively travel out of regions of positive curvature, whilst a second scheme enables the convergence onto the saddle point. To enable these schemes to work the curvature of the PES is needed;

$$C = \frac{(\mathbf{F}_2 - \mathbf{F}_1) \cdot \hat{\mathbf{N}}}{2 \Delta R} \quad (3.9)$$

When near to a minimum, C will be positive due to a greater force acting on \mathbf{R}_2 than on \mathbf{R}_1 . As we get closer to the saddle, C will thus become negative. Hence the dimer is translated using a modified force \mathbf{F}_m ;

$$\mathbf{F}_m = \begin{cases} \mathbf{F}_{\mathbf{P}} & \text{if } C > 0, \\ \mathbf{F} - 2\mathbf{F}_{\mathbf{P}} & \text{if } C \leq 0. \end{cases} \quad (3.10)$$

where the component of the real force parallel to the dimer ($\mathbf{F}_{\mathbf{P}}$) is given by;

$$\mathbf{F}_{\mathbf{P}} = (\mathbf{F} \cdot \hat{\mathbf{N}})\hat{\mathbf{N}} \quad (3.11)$$

Movement of the dimer along this modified force will bring it to a saddle point.

3.3.3 The Activation Relaxation technique

The ART [68, 69] was developed by Barkema and Mousseau and is an alternative to the dimer method. The technique involves two steps, activation of the system to move from a local minimum to a nearby saddle point and then relaxation from the saddle point into a corresponding minimum. We consider a single point in $3N$ space traversing the PES, where at each step a random displacement vector \mathbf{N} is constructed, tethering the displaced point \mathbf{R} to the origin \mathbf{R}_0 . Figure 3.3 illustrates how the forces acting on the point \mathbf{R} are decomposed into parallel and perpendicular components with respect to \mathbf{N} .

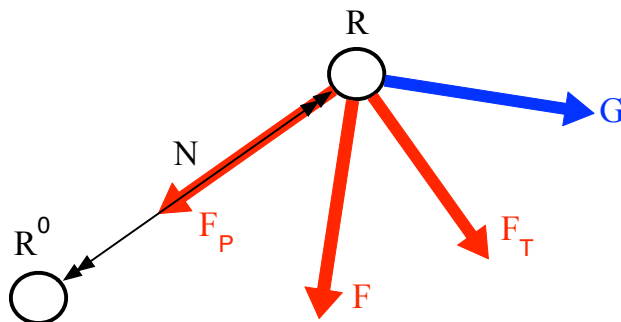


Figure 3.3: Definition of the ART, where an initial offset from the origin in a random direction \mathbf{N} gives the point \mathbf{R} . The force acting on \mathbf{R} is decomposed into parallel and perpendicular components, \mathbf{F}_P and \mathbf{F}_T . A modified force \mathbf{G} acts to move \mathbf{R} towards the saddle point.

Once the point \mathbf{R} has been displaced from the origin, a modified force \mathbf{G} is constructed using both components of \mathbf{F} ;

$$\mathbf{G} = \mathbf{F}_T - \alpha \mathbf{F}_P \quad (3.12)$$

where α is a control parameter that alters the aggressiveness of the search. A large value for α will enable \mathbf{R} to climb away from the minimum quickly, however, this may miss the saddle point, whilst a smaller α will focus on lateral minimisation towards the MEP, thus becoming less efficient. A value for α of $0.15/|\mathbf{R} - \mathbf{R}_0|$ was suggested by Barkema and Mousseau [68, 69]. By moving in the direction of \mathbf{G} , we are minimising laterally, whilst climbing parallel to the displacement vector \mathbf{N} .

3.3.4 The Relaxation and Translation method

The RAT method, developed by Vernon [5], is very similar to the ART method. As with ART, a single point in $3N$ space traversing the PES is considered, at each step a random displacement vector \mathbf{N} tethers the displaced point \mathbf{R} to the origin. The forces acting on the new point \mathbf{R} are decomposed into parallel and perpendicular components, with respect to \mathbf{N} .

The method consists of two main steps. The first part, force minimisation, involves the point \mathbf{R} being allowed to move within the plane bound by the perpendicular and tether vectors. Figure 3.4 illustrates how \mathbf{R} moves, sometimes by large distances, relaxing the perpendicular component of force.

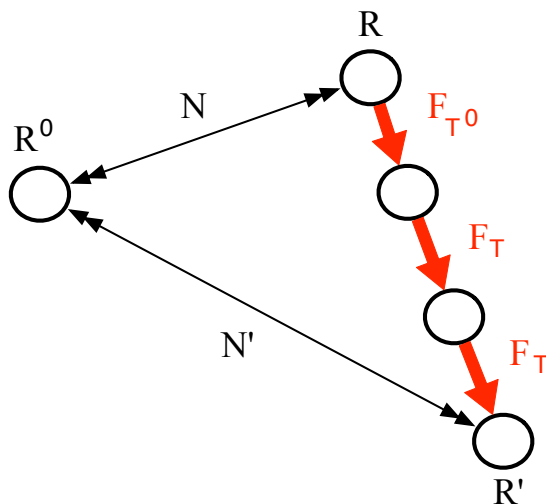


Figure 3.4: Illustration of the RAT method where a random displacement vector describes a new point \mathbf{R} , which is then relaxed in the direction of the perpendicular force component.

The relaxation of a system can sometimes require large movements and thus Vernon developed a simple algorithm to dynamically modify the relaxation step size by monitoring the change in force between steps [5];

$$(\mathbf{F}_{T_i} - \mathbf{F}_{T_{i-1}})/\mathbf{F}_{T_i} < \epsilon, \quad (3.13)$$

where ϵ was typically 0.2. If this equation is satisfied then the step size is scaled by $1+\epsilon$, otherwise we half the step size [5]. This ensures that if during a minimisation step the force changes by less than 20% relevant to the current step, the step is made more aggressive. However, if the force changes by more than 20%, the algo-

rithm ensures that the step size decreases to allow the accurate convergence onto the minima. Vernon suggests that this algorithm requires around 4 force evaluations per minimisation [5].

The second part involves translation of the point \mathbf{R} . A trailing historical point is used to decompose the forces acting on the current search vector. After each relaxation step, the vectors \mathbf{N} and \mathbf{N}' define the initial displacement of the points \mathbf{R} and \mathbf{R}' . With these displacement vectors, the new translation direction vector is,

$$\mathbf{N}_i = \frac{\mathbf{N} + \mathbf{N}'}{|\mathbf{N} + \mathbf{N}'|} \quad (3.14)$$

where \mathbf{N} is a vector of unit length and \mathbf{N}' is not. The saddle point was then found by taking the dot product of the displacement between the current and initial positions, with the force acting on the current position. Once this is positive, the saddle point has been crossed.

3.3.5 Chosen Method

Vernon carried out initial tests of the single-ended search methods, using each method to search for saddle points on a 2D distorted eggbox potential. The tests concluded that the RAT method performed the best, with the least average number of function evaluations and the highest convergence rate [5]. Another benefit of the RAT method was the bias created towards finding the lower energy barriers. For these reasons and the complex surfaces used during this project, the RAT is used to search for saddle points.

3.4 Example of Transition Found

The search methods introduced in this chapter allow transitions to be found during simulations. The RAT method is used to locate unique saddle points on a surface and then the saddle point is minimised into a new minimum. The NEB method is then applied with knowledge of the initial and final system configurations in order to find the barrier height more exactly. One of the surfaces investigated during this thesis is rutile TiO_2 . A typical transition on this surface is the diffusion of an O ad-atom along the trench, illustrated in figure 3.5, where the energy barrier is 0.68

eV. The NEB method provides the energy variation as a function of the separation. Figure 3.6 illustrates the calculations, where the height of the barrier is clear.

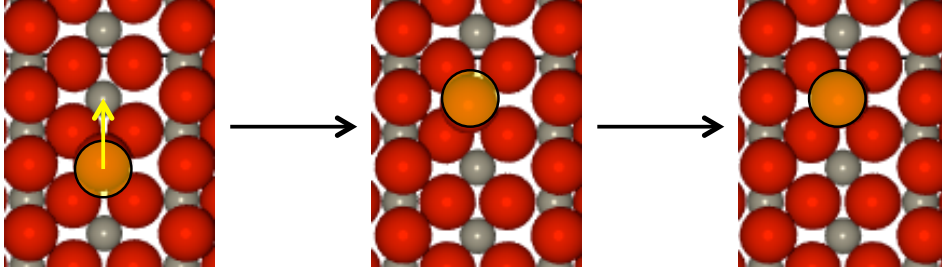


Figure 3.5: An O ad-atom diffuses along the trench of the rutile surface with an energy barrier height of 0.68 eV. The images show the initial, saddle and final system configurations.

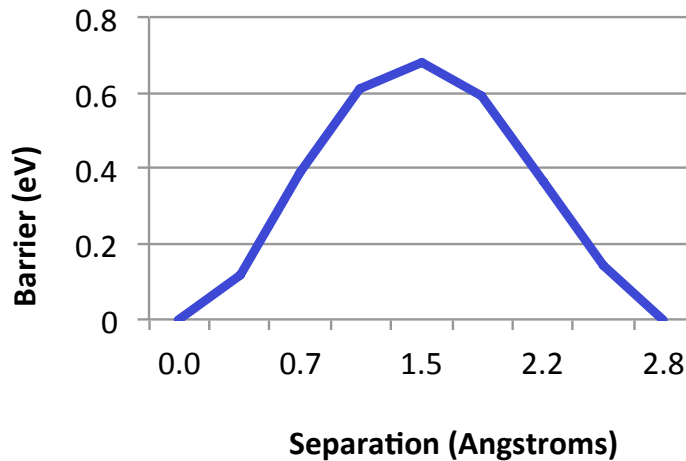


Figure 3.6: The NEB calculations for the diffusion of an O ad-atom along the rutile surface trench.

3.5 Kinetic Monte Carlo

KMC is a LTSD method, which allows time evolution of simulations whilst keeping the dynamics of the system realistic. Traditional applications of KMC assigns atoms to lattice sites and predefines all possible transitions. Diffusion of lattice defects is a probabilistic process which depends on lattice temperature, the barrier height and the attempt frequency. To recreate stochastic behaviour we use the Arrhenius Equation;

$$\text{Escape Frequency} = \nu \exp(-E_b/k_B T) \quad (3.15)$$

where ν is the transition prefactor, E_b is transition barrier, k_B is the Boltzmann constant and T is the temperature (Kelvin). ν can be calculated for each transition using the Vineyard [84] method, but due to time limitations we take the prefactor to be 10^{13} (this has been previously tested by Vernon for surface processes and found to be a good estimation [5]).

Once the RAT and NEB methods have been used to find all possible transitions for a given configuration and the attempt frequencies and energy barriers have been calculated, we can determine the relative probability of each transition being chosen. The steps required to complete a KMC run are set out below:

- 1- Set the time $t = 0$.
- 2- Produce a list of all possible events for the given configuration.
- 3- For each transition barrier on the list, use the Arrhenius equation to calculate transition rates, along with the sum of all rates R .
- 4- A random number (P) is generated between 0 and R .
- 5- Decide which event to carry out by cumulatively going through each event until P is passed.
- 6- Carry out the event and move forward one step.
- 7- Update the time of the system $t = t + \delta t$ where δt is given by:
$$\delta t = -\log u/R$$
 where u is a random number generated between 0 and 1.
- 8- Loop back to step 2.

Performing KMC with a pre-defined transition list is very appealing for simple, symmetric crystal structures, but as systems become more complex this type of KMC becomes very difficult to use. When systems become highly defective we have to compile huge lists of all possible transitions, which is both very time consuming and decreases the accuracy of the model, since some transitions may be missed from the list. One method available to rectify this issue is on-the-fly KMC, where transitions are calculated ‘on-the-fly’ at each step from the current configuration and are not pre-specified.

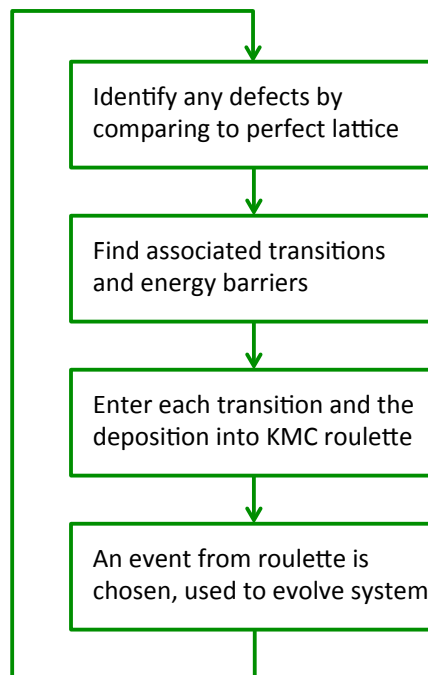


Figure 3.7: Illustration of the otf-KMC method, used to simulate growth by calculating configuration specific transitions at each step.

3.6 On-the-fly KMC

In 2001, Henkelman and Jónsson published the on-the-fly method in order to avoid the time consuming work of cataloging every possible transition for each step [63]. They produced a transition finding algorithm that would find all possible transitions for each step, saving huge amounts of time and effort and allowing for a far more complex surface to be simulated.

The fundamental steps of the on-the-fly KMC method applied to deposition and growth are illustrated in figure 3.7. The system must first have any defects identified by comparison to a perfect, crystalline lattice, which allows for a limitation of configuration search space as previously discussed, providing a search space of only defects and those atoms nearby. Transition search methods, here the RAT and NEB, are used to find all unique transitions and corresponding energy barriers. The unique transitions and the external deposition event are entered into a KMC roulette where one event is chosen and used to evolve the system one step.

3.6.1 Transition searches

The transition search step is a fundamental part of the simulation method as this is where saddle points are located and barriers are calculated. Once we have the configuration search space calculated, we must decide how many transition searches to carry out. Literature suggests that 50 searches are sufficient when investigating Al diffusion [85]. The number of transition searches required for any given configuration changes, however, due to the complexity of the system. Thus a more complex system with more defects would require tens of hundreds of searches to be confident that all diffusion pathways were being explored. Vernon chose to, rather than initialise a given number of searches, apply a time limit to each search [5]. This time limit was typically 20 minutes and this was the time allowed to elapse between unique transitions being found. So if, after 20 minutes, another unique transition had not been found then the search was stopped, completing the step and moving on.

We found, however, that this time limit was a crude way of ending searches. With our complex systems the time limit method meant that important transitions could be missed. Therefore, we introduced a transition search count variable, which allows the searches to end once the chosen search count is reached. 200 searches have been used throughout this project, as this was found to be sufficient for most transitions to be found, even on complicated surfaces.

The RAT method is used to locate saddle points, whilst the NEB is used to accurately calculate the energy barrier of the transition, as described previously. In order to keep computing costs to a minimum, we must apply a stopping criteria to the RAT part to keep the methods as efficient as possible. The criteria ensures that the RAT method will stop if the barrier climbs above 2 eV, the function evaluations exceed 1500 or if the distance moved exceeds 10 Å. Once one of these criteria are fulfilled, that specific RAT search will end and if the number of transition searches performed is less than 200, another transition search will begin. If, however, transition searches exceed 200, the KMC roulette will be entered and an event will be chosen.

3.6.2 Filtering of Irrelevant Transitions

During otf-KMC simulations, some system configurations include irrelevant transitions, which do not add to any net diffusion. These are unhelpful and taking up large amounts of simulation time. An example of an irrelevant transition is O₂ dimer rotation on a zinc oxide surface. Rotation around a central point of the dimer occurs on very small time scales, typically every 2.08×10^{-9} seconds, as shown in figure 3.8. This rotation provides symmetrical states only and no new states are explored through this rotation. It was necessary, therefore, to modify the otf-KMC perl codes so that a filter was added to the transition search step.

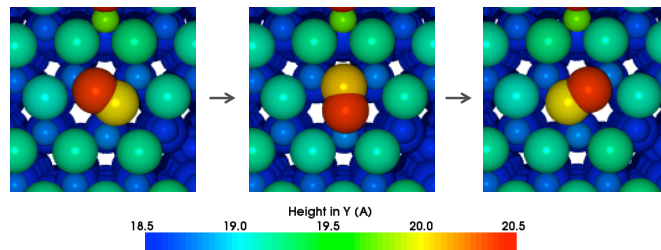


Figure 3.8: A ZnO (000 $\bar{1}$) surface on which an O₂ dimer rotates typically every 2.08×10^{-9} seconds. No net diffusion is added to the simulation by the rotation of the dimer, therefore it is acceptable to filter out this transition.

At times, it was not possible to identify one barrier which was taking up large amounts of computing time, so instead it was necessary to block out low energy barriers altogether as they added no net surface diffusion. An example of this situation is the Al (100) surface, where a trimer on the surface continuously re-orders with energy barriers below 0.2 eV, as shown in figure 3.9. After inspection of other low energy (<0.2 eV) barriers, it was found that the majority of transitions were trimers re-ordering, therefore it was possible to filter out all low energy barriers to save computational time, especially early on in the simulations. This is described later on for each specific surface.

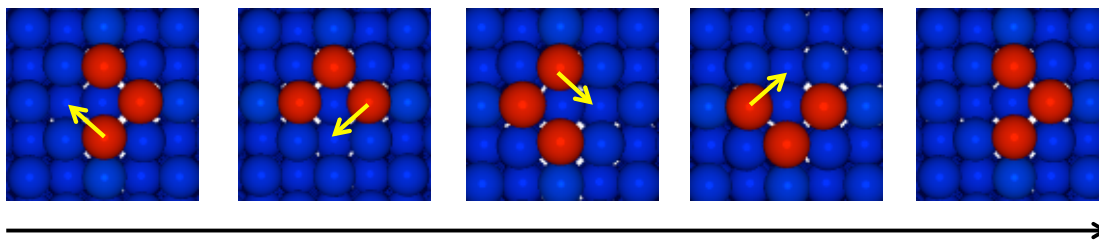


Figure 3.9: The Al (100) surface on which an Al trimer re-orders with low energy barriers (<0.2 eV). Four different orderings are shown with arrows highlighting the movement of atoms. By the final image, the initial ordering has been revisited. These transitions require filtering out to avoid unnecessary calculations.

3.7 Parallelisation

To efficiently perform long time scale dynamics growth simulations, it is necessary to parallelise simulations such that MD and otf-KMC are split over n processors. Figure 3.10 demonstrates the parallelisation model, where MD simulates a deposition event on one single processor, whilst transition searches and barrier calculating are employed on multiple $(n-1)$ processors. Incorporated in the simulation codes is the ability to initialise transition searches on multiple processors. The files required are copied to each processor where transition searches are performed and if successful, minimisation and barrier calculation are also performed. If a transition search is unsuccessful then the relevant processor begins another search, providing that the number of required searches (200) has not yet been reached. During this project, between 8 and 48 processors were used in parallel on Loughborough University's high performance computer (a 1,956 core 64-bit Intel Xeon cluster supplied by Bull). The exact number of processors used was simulation specific and optimised for maximum efficiency in each case.

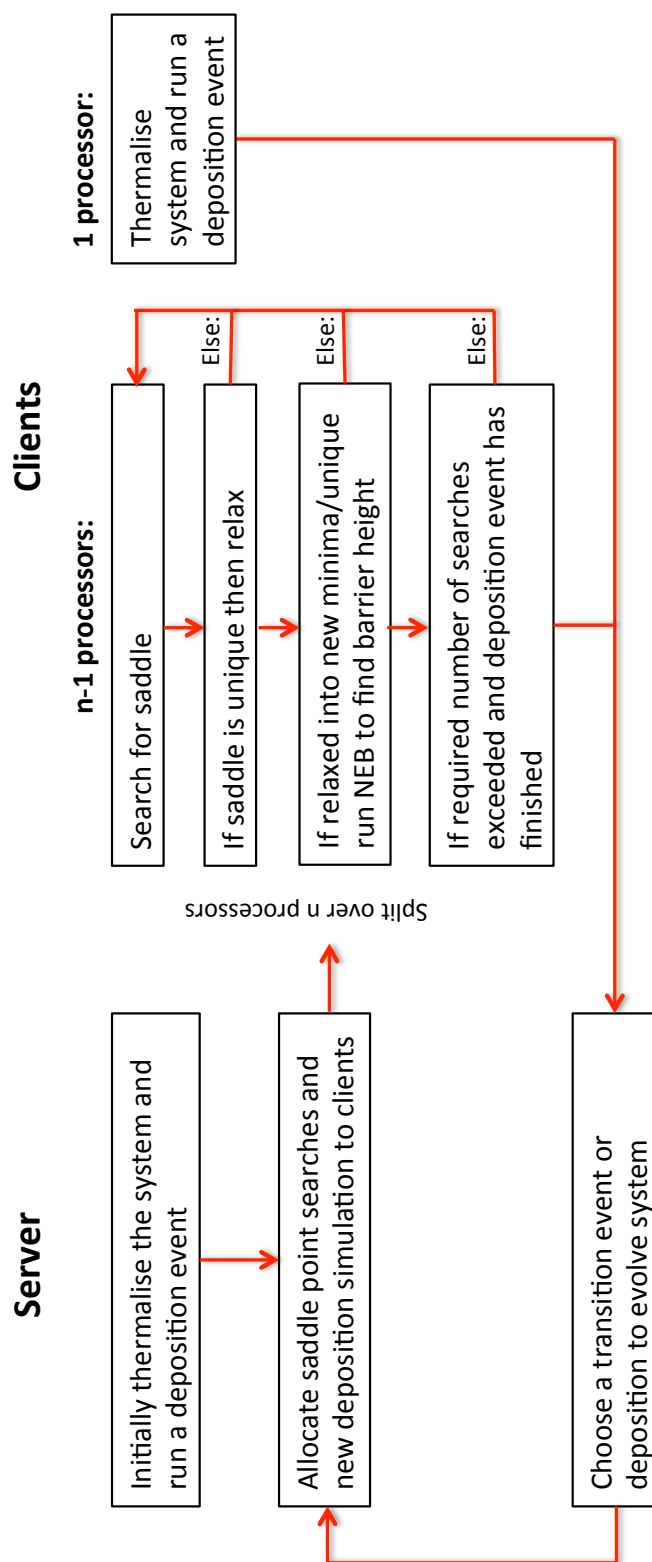


Figure 3.10: The parallelisation model, where one processor simulates a deposition and $n-1$ processors run transition searches, saddle relaxing and barrier calculations, until the required number of searches has been exceeded.

Chapter 4

Simulation of Silver and Aluminium Thin Film Growth

4.1 Introduction

Thin films of metals such as Ag and Al have important industrial applications based on their optical and electrical properties. Ag is the highest electrically conductive element and the highest thermally conductive metal. It also has one of the highest optical reflectivities, outdone slightly by Al particularly in parts of the visible and UV spectrum. Ag lends itself to many uses in electronics, mirrors, optics and medical sectors. Of particular interest in this research is the use of Ag in electrical contacts and electrical conductors in the monolithic interconnect processes for thin film photovoltaics (a-Si, CdTe and CIGS), reflectors in concentrated photovoltaics [86–88] and back contacts in solar cells. Al, the world’s most widely used non-ferrous metal, is used in applications including construction, packaging, bicycle frames, electrical power lines and in Al doped ZnO transparent conducting oxide layers. Here, we are interested in the uses of Al in photovoltaic applications, including substrates and back contacts in thin film solar cells and reflectors in concentrated photovoltaics. Many Ag and Al applications in photovoltaics coincide, allowing us to consider them both within one chapter.

The structures of Ag and Al are very similar as both crystals are arranged in the face-centred cubic (fcc) structure, shown in figure 4.1. On both (111) and (100) surfaces, three adsorption sites exist, the ‘on-top’ site, ‘bridging’ site and ‘hollow’ sites, all of which have different local symmetries and lead to different coordination geometries. During this chapter, both surfaces of Ag and Al will be investigated.

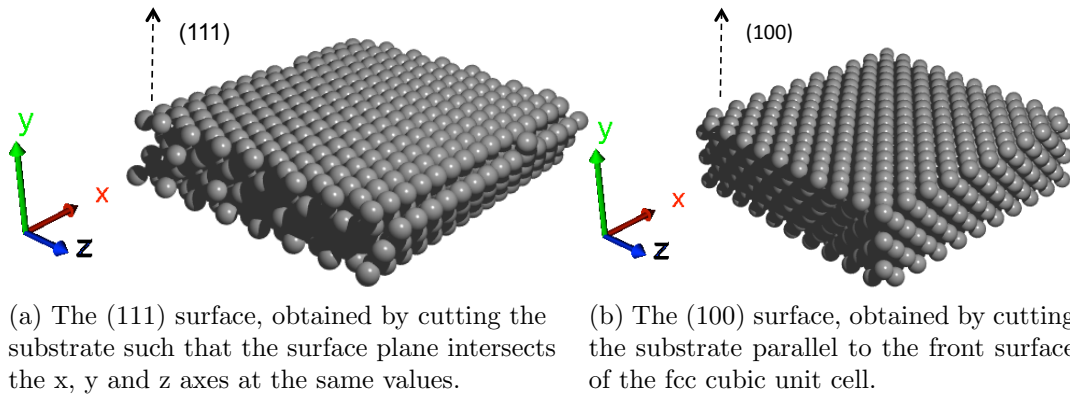
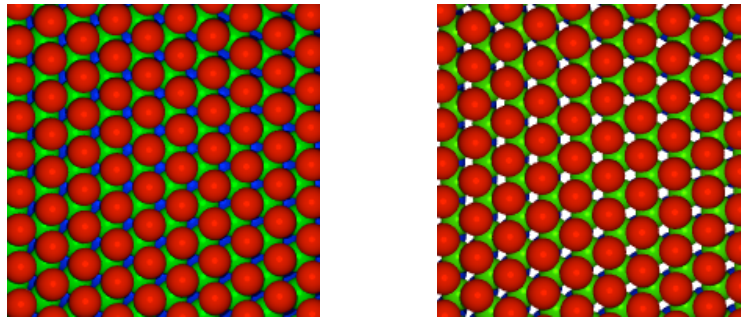


Figure 4.1: The fcc structure of Ag and Al, showing both the (111) and (100) surfaces.

In some cases, notably in stacking faults and twins, the crystals can alter from fcc to the hexagonal close-packed (hcp) structure. The fcc and hcp structures are closely related, both based upon stacking sequences where layers are close-packed. The fcc structure bases itself upon a packing sequence ..ABCABC.. where each letter represents a layer. The hcp structure, however, has a packing sequence of ..ABABA. Figure 4.2 illustrates the fcc and hcp sequences. The fcc structure is the most stable, although it is known that metal thin films can and do contain stacking faults and twins where the hcp structure forms [89]. This is further investigated later in the chapter. Some of the work included in this chapter has been published in peer-reviewed journals and conference proceedings [90–92].



(a) The more stable fcc stacking sequence, where layers are stacked in three different sites: ..ABCABC..
 (b) The hcp sequence, where layers are stacked in only A and B sites: ..ABABAB..

Figure 4.2: The fcc and hcp stacking sequences, of which the first is the more stable for Ag and Al. However, if growth occurs in the hcp sites stacking faults and twin boundaries form. Three layers are shown to illustrate the stacking sequences.

4.2 Previous Work

Metal thin films span many industrial applications from electronics to construction to photovoltaics, therefore much work has been carried out investigating metal films both experimentally and theoretically. By exploring previous work, we can see where gaps exist in the current research.

4.2.1 Experimental

Ag and Al thin films can be deposited using a variety of industrial scale processes, including evaporation (thermal and electron beam) [93], ion-beam assisted evaporation [94] and magnetron sputtering [95], all of which are PVD processes [96]. These deposition techniques were introduced in chapter 1. The evaporation process involves evaporation of either Ag or Al atoms onto the substrate, where arriving atoms have a kinetic energy of typically <1 eV. A high energy ion source (usually Ar) may be used to densify the film, for example a 100 eV ion-beam will introduce extra energy into a film [94] to enhance mixing. In Al films specifically, experimental studies have shown that high energy Ar ion bombardment from the ion-beam can damage substrates by the formation of subsurface Ar agglomeration [97–100].

Magnetron sputtering, either RF, DC or pulsed DC power, deposits a thin film by sputtering of a metallic target. A high voltage is applied to the target to ionise an Ar plasma within the vacuum, thus promoting the bombardment of the target by Ar

ions and causing target material to be sputtered. Target atoms reach the substrate with typically 10's of eV of kinetic energy. Ar in the plasma also bombards the substrate with a similar kinetic energy, either by back reflection from the target or by an additional ion assist [13]. This Ar bombardment has been shown to improve the density of films due to the bombardment transferring momentum to the substrate, thus enhancing surface mobility. Stoichiometry is also affected [94,101,102].

Stacking faults and twin boundaries have been observed experimentally in thin metal films. Howe *et al.* used medium energy ion scattering to show that stacking faults exist in Ag films deposited on Al (111) [89]. Two layers of Ag continued in the fcc stacking sequence, but thereafter, hcp and fcc twin-type stacking faults occurred in the film. Other groups have also investigated stacking fault behaviour in metals. Fourné *et al.* evaporated Al on Ag and Ag on Al subsequently taking STM images. Strain was the main interest of the work, however, they also found that stacking faults form to relieve the strain [103]. Experimental studies on the structural evolution of thin films were carried out by Barna [10]. Al, among other materials, was deposited and studied to gain a greater understanding of the stages of film evolution through processes including nucleation.

4.2.2 Simulation

In order to perform simulations of metal thin film growth, the definition of appropriate interatomic potentials is first required. Chapter 2 introduced the EAM potential form, an expansion of the pair potential where the energy of an atom is dependent on the local binding environment, which was first proposed by Daw and Baskes in 1983 for the application to H in metals [23,24]. Soon after, the potential was parameterised for the application to simple metals [25]. Baskes extended the EAM to include angular forces, MEAM, parameterising this for Si, Ge and cubic materials and impurities [26,104,105]. In 1993, Daw *et al.* published a review of EAM theories, stating that the EAM is a popular and efficient method for semi-empirical calculations in close packed metals [27]. Ackland later formalised the EAM potential for Ag [28,29]. Voter and Chen also formalised the EAM for Ni and Al systems by fitting the EAM to experimental data [30].

Many groups have published work on modelling surface growth, surface diffusion and grain growth in Ag and Al. As early as 1966, Schwoebel and Shipsey first inves-

tigated the diffusion on step-edges, highlighting an important transition whereby an atom drops off a step edge of an island [106, 107]. The corresponding barrier is the Ehrlich-Schwoebel (ES) barrier and has recently been investigated on the Ag (111) surface by Li *et al.*, concluding that it does have a significant role [108]. In 1991, Lui *et al.* applied the EAM potential to fcc metals, including Ag and Al, investigating the self-diffusion of single ad-atoms on the surface. They concluded that the EAM potential provided activation energies that were generally consistent with experimental data [109]. Voter's group have published many studies on thin film metals. In 1997, hyperdynamics was used to examine the diffusion mechanisms of a 10-atom cluster on the Ag (111) surface [78]. Sorensen and Voter then applied TAD to Ag (100), however, found it may not allow the observation of multi-atom concerted transitions [79], which have been found to be very important in metal thin film growth [70]. Henkelman and Jónsson investigated the number of atoms involved in transitions on the Al (100) surface using KMC methods. In 80% of transitions, two or more atoms were involved [?]. Traditional MD has also been used to simulate Ag grain growth, however, the time scales are so short that results cannot be applied to experimental results. Interestingly, however, stacking faults were observed over MD time scales [110]. Looking at more specific simulations of deposition techniques, Georgieva *et al.* in 2011, used TAD to simulate the diffusion processes seen during the magnetron sputter deposition of Mg-Al-O films [111]. Petrov *et al.* investigated the microstructural evolution during thin film Al growth using simulation and experiment together. Al sputter deposition was simulated and compared to TEM images in order to characterise the structural evolution of the film [11].

Stacking faults and twins, observed experimentally, have also been investigated at the atomistic level using simulation methods. Woodruff and Robinson, using DFT, found that for Ag (111) the stacking fault energy for a clean surface layer is very low and hence will occur frequently [112]. Meyer and Lewis's study agrees with this; using a tight-binding potential for the MD simulation, they found that the stacking fault energy for Ag is small and also decreases with an increasing temperature [113]. Looking specifically at the Al system, Xu *et al.* studied twin boundary and stacking fault energies on the (111) surface, comparing the energy for an fcc/hcp interface to a kink in the surface [114].

4.3 Growth Simulations

In this chapter, Ag and Al deposition is simulated using long time scale dynamics techniques. Chapter 2 introduced and described the MD methods which are used to model a deposition, whilst the off-KMC methods described in chapter 3 are used to search for transitions at each step. When modelling a deposition, MD is used to describe the interatomic interactions as time evolves by applying interatomic potentials. For modelling the interactions required in this chapter, the embedded atom method is applied. The EAM, developed by Daw and Baskes [23–25], describes an interaction where the energy of an atom is dependent on the local binding environment. The EAM is a popular choice for the modelling of close packed metals, combining simplicity with many-atom effects [27]. Ackland parameterised an EAM potential for use in describing Ag-Ag interactions [29]. For the Al-Al interactions, Voter and Chen previously derived a useful EAM potential, in which the pair interaction was taken to be a Morse interaction [30]. Ar is included in some simulations, therefore the Ar-Ar, Ag-Ar and Al-Ar interactions also require describing. A Lennard-Jones simple pair potential modelled the interaction between Ar atoms [115], whilst a ZBL purely repulsive potential simulated the Ag-Ar and Al-Ar interactions [31].

Typical system sizes were between 4 and 8 monolayers deep, with between 128 and 225 atoms per monolayer. Periodic boundary conditions have been applied in each case to the x and z dimensions to allow atoms to wrap around and thus mimic a bulk. The bottom layer of the lattice is fixed to ensure stability, with a Berendsen thermostat [59] attached to the two layers above the bottom to control the system temperature. In order to simulate a deposition, the chosen species is initialised some 10 Å above the surface, as demonstrated in figure 4.3. The deposition species is given the desired kinetic energy in the direction of the surface. When evaporation deposition is simulated, atoms are assumed to arrive with ~ 1 eV, whereas during sputtering the energy is much higher at ~ 40 eV. Species are given energy according to a normal distribution function, with a standard deviation of one tenth of the deposition energy. For example, a 1 eV deposition will have a standard deviation of 0.1 eV. The x and z coordinates of the deposition species are completely random, so that the deposition may occur anywhere on the surface, replicating realistic conditions.

Once the chosen deposition species is initialised above the surface with a direction

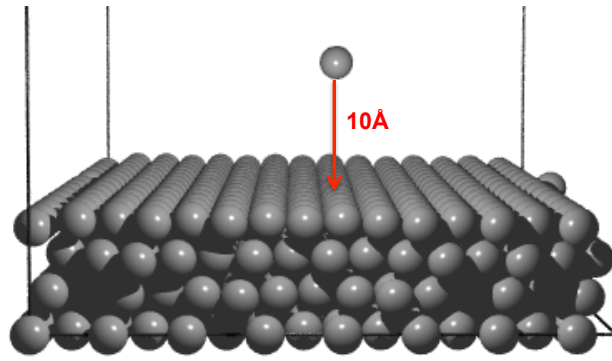


Figure 4.3: Example of the initialisation of a deposition cluster before the MD phase begins. The species to be deposited is initialised 10 Å above the surface.

and the desired kinetic energy, MD evolves the system, allowing the deposition species to impact normally to the surface, simulating a deposition. MD runs for between 4 and 10 ps, depending upon the deposition technique. Evaporation requires only 4 ps for the energy and heat to dissipate, however, the higher energy sputter depositions require up to 10 ps. During MD the interatomic potentials described previously are used to calculate the forces on atoms. The system was then relaxed using the conjugate gradient minimisation technique and transition searches were employed using the RAT and NEB methods. As described in chapter 3, otf-KMC simulates the growth by choosing either a deposition event or a transition at each step. The deposition event requires a “rate”. The deposition rate is an important parameter in experimental film growth and here we recreate the deposition rate by specifying a deposition frequency. During experimental metal thin film growth the deposition rate is typically around 10 monolayers per second. Considering that the monolayer sizes range from 128 to 225 atoms, we assume a deposition frequency of 2000 Hz will provide a similar growth rate. Another important parameter for experimental techniques is the deposition temperature. During simulations, the higher the deposition temperature, the more computing time is required. Therefore, we assume 350 K is a suitable temperature, which is also reasonable from an experimental point of view. The temperature is kept constant with the help of the Berendsen thermostat. These methods continue until three monolayers of atoms are deposited, simulating seconds of real time. Here, the MD and otf-KMC combine working over typically 24 cpu cores.

The (111) and (100) surface of Ag and Al are used as substrates. During initial stages of growth on each of the four substrates, the simulation was taking up a

lot of cpu time due to the high mobility of monomers and dimers on the surface. Once these atoms come together to form clusters they are less mobile. Therefore, a trimer was chosen as a nucleation site for the growth to begin. On all four surfaces a trimer, either Ag or Al respectively, was initially placed on the surface in the correct fcc lattice sites as shown in figure 4.4.

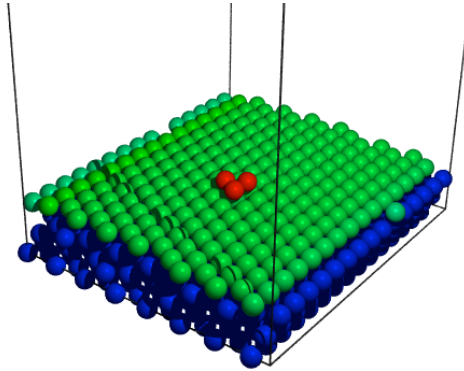


Figure 4.4: An Ag trimer on the (111) surface, acting as a nucleation site for the growth.

As described in chapter 3, during some simulations, there is a need to filter out irrelevant transitions. During early simulations on the Al (100) surface, we observed that trimers were diffusing with very small barriers, consuming large amounts of computing time. Figure 3.9, shown in chapter 3, illustrates the movement of the trimer, where continuous re-ordering occurs with low barriers (< 0.2 eV). These transitions were adding no net surface diffusion to simulations, thus we were able to filter them out. Inspection of other barriers below 0.2 eV indicated that the majority of these barriers belonged to trimer re-ordering, therefore by simply ignoring transitions with barriers < 0.2 eV we were able to retain important transitions, while eradicating the irrelevant ones. The other metal surfaces did not encounter this problem when starting with a trimer on the surface, hence no other minimum barrier heights were set.

4.4 Deposition on the Ag (111) Surface

The first surface investigated in this chapter, Ag (111), acts as the substrate for the simulation of evaporation deposition, ion-assisted evaporation deposition and magnetron sputter deposition. These PVD techniques, introduced in chapter 1, are

of great interest. In order to gain a more rounded understanding of metal thin film deposition, a deposition energy between that used for evaporation and sputtering is also modelled (10 eV). MD and Otf-KMC simulations enable simulation of the growth of three monolayers of Ag. Resulting films and specific growth mechanisms and transitions are investigated.

4.4.1 Evaporation Deposition

On the (111) surface, transition barriers for single ad-atoms and small clusters were initially calculated and are shown in table 4.1. Single ad-atoms and smaller clusters are planar and require as little as 0.12 eV to diffuse, whereas larger clusters required up to 0.45 eV. Bonding to a step edge of a single ad-atom required very little energy, however, 0.74 eV was required for the de-bonding. Figure 4.5 illustrates a four atom cluster diffusing during early stages of growth, where the cluster diffuses between stacking sequences with an energy barrier of 0.4 eV. It is clear, however, that single ad-atom hops and step edge bonding requiring only 0.12 eV, should dominate the simulation.

Monomer hop	Dimer hop	Trimer rotation	Trimer hop
0.12 eV	0.22 eV	0.23 eV	0.28 eV
4-mer hop	5-mer hop	Bond to step edge	De-bond from step edge
0.40 eV/0.26 eV	0.45 eV	0.12 eV	0.74 eV

Table 4.1: Transition barriers for single ad-atom and small cluster diffusion on the Ag (111) surface.

Figure 4.6 illustrates the resulting growth of Ag (111) via evaporation deposition, where Ag atoms arrive at the substrate with kinetic energy of <1 eV. It is clear that layers are incomplete and vacancies are present in the film. 675 atoms (equivalent to three monolayers) have been deposited onto the substrate, but these atoms actually produce six new layers, all of which are incomplete. Due to atoms arriving at the substrate with such low kinetic energy, there is not enough energy for layers to self-complete via surface diffusion. No mixing occurs between the original substrate and the newly grown material.

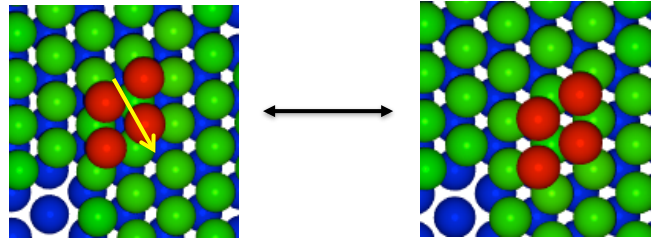


Figure 4.5: A four atom cluster on the Ag (111) surface during early stages of evaporation growth, switching between ABC and ABAB stacking sequences. 0.4 eV is required for this transition, with only half of that energy required to switch back to the preferred ABC sequence. Once a fifth atom attaches to the cluster, it becomes pinned to the layer it is in. Atoms are coloured by height, with the cluster being in red.

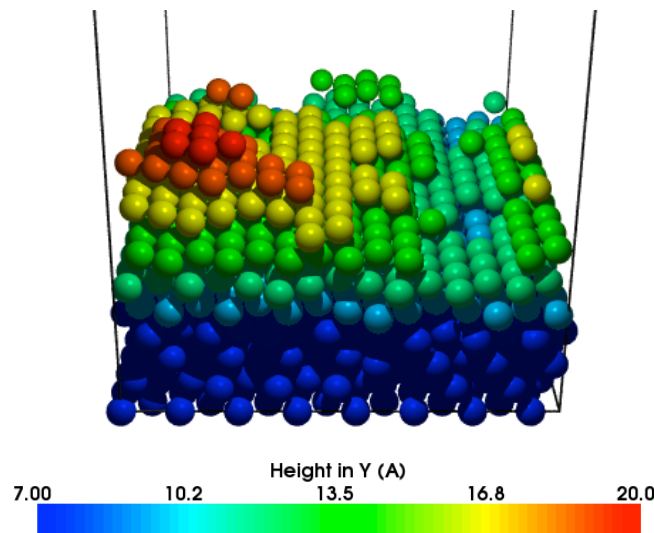


Figure 4.6: Ag (111) growth via evaporation deposition after 0.29 s of real time. 675 atoms have been added to the system, equivalent to three complete monolayers, corresponding to a growth rate of ten monolayers per second which is used for all simulations. Six partially formed layers have grown, although all are in the ABAB stacking sequence rather than the preferred ABC. Atoms are coloured by height in Å, according to the colour bar, with the original surface at 7 Å.

4.4.2 Stacking Faults and Twinning

Previous experiments using low energy ion scattering to examine the first few layers grown by vapour deposition have shown that growth does not always occur in a completely crystalline manner. It was found that Ag structures, once grown, can contain stacking faults and twin boundaries [89]. In this simulation, stacking faults in the film are observed and a mechanism for twinning would be the coexistence of two clusters on the surface both pinned in different positions and growing into

a twin boundary. Ag (111) is in a close packed structure, with an ABC stacking sequence. It was calculated that a trimer on the (111) surface diffuses from the ABC sequence to the ABAB sequence with a relatively low energy barrier of 0.28 eV (which has rate of $4.8 \times 10^8 \text{ s}^{-1}$, compared to deposition rate of $2.0 \times 10^3 \text{ s}^{-1}$). A cluster on the surface may switch between stacking sequences during the early stages of growth, however, when a cluster reaches five atoms, the energy barrier increases to 0.45 eV (see table 4.1). This means that the cluster is less mobile and additional atoms arriving at the surface can aggregate around it. During the early stages of growth by evaporation deposition, atoms sat in the ABAB sequence. The new layers were then pinned to this stacking sequence and all new layers grew in this manner, producing a stacking fault throughout the new film. The substrate, however, stayed in the original fcc stacking sequence.

4.4.3 Deposition by Ion-Beam Assisted Evaporation

In experimental growth of thin films, ion-beam assist is often used to improve the quality of the crystalline growth. Here, we model the ion-beam process by MD. Ar ions/neutrals with 100 eV of kinetic energy are assumed to bombard the surface at normal incidence. The Ar ion flux is assumed to be the same as that of the arriving Ag atoms, so that during the roulette process an Ar atom at 100 eV or an Ag atom at 1 eV is chosen with equal probability. The Ar ions help to densify the material [94, 101, 102] and also promote increased surface atomic diffusion as the bombardments transfer kinetic energy to the system. Figure 4.7 shows the resulting growth when an Ar ion-beam assist is used along side the evaporation method. New layers sit in the correct stacking sequence, contrary to what was seen without the ion-beam assist. Due to the high impact energy of Ar, penetration deep into the lattice was observed, however, by the end of the simulation all Ar had escaped from the substrate due to the low diffusion barriers. Previous otf-KMC simulations from literature have shown that residual Ar in Au films diffuses with very low energy barriers, many below 0.1 eV [90]. Figure 4.8 illustrates the high portion of mixing occurring between atoms in the original substrate and the newly deposited atoms. Contrary to what was seen in the pure evaporation growth, here we see mixing due to the Ar bombardment, whereby original atoms are displaced, transferring kinetic energy to the surface.

By direct comparison of figures 4.6 and 4.7, we observe differences in film growth

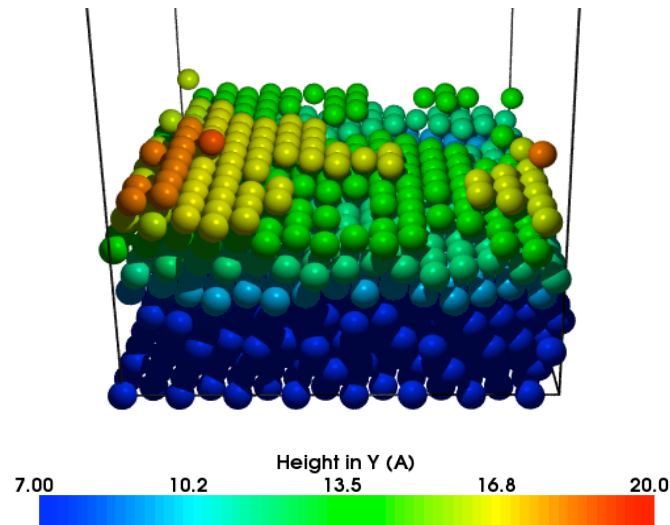


Figure 4.7: Ag (111) growth via evaporation deposition with ion-beam assist, where Ar ions bombard the surface at 100 eV, after 0.38 s of real time. Ar ions strike the surface with equal probability as an Ag atom. The extra energy, which is transferred to the system from Ar bombardment, promotes atomic mixing and increased surface diffusion, leading to more complete layers. From the addition of 675 atoms, five partially formed monolayers have grown all in the correct ABC stacking sequences.

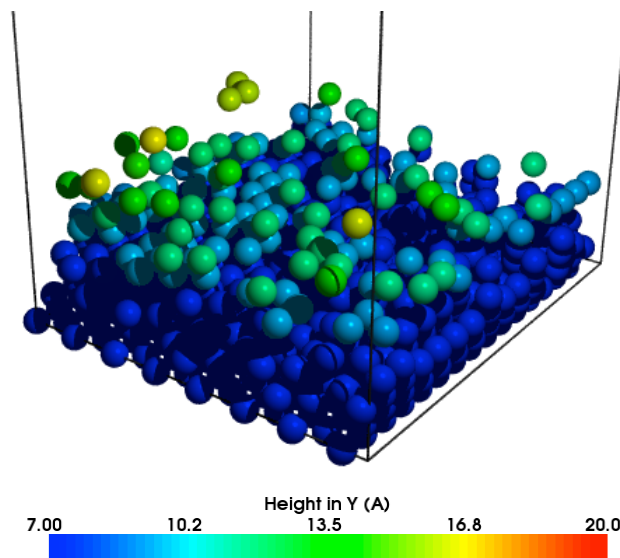


Figure 4.8: Atoms from the original Ag (111) substrate, showing atom positions after the simulation of evaporation deposition with the ion-beam assist. A high portion of original substrate atoms travel up to and above the original surface during the simulation due to displacement and mixing from high energy ion bombardment.

by evaporation and ion-beam assisted evaporation. Firstly, in the case of no ion-assist, six partially formed new layers are grown, whereas with the ion-assist only five partially formed layers are grown. This confirms that the ion-assist does aid the densification of the film through transferring extra kinetic energy to the system. Mixing is observed between the original substrate and the newly deposited atoms only when the ion-beam assist is included, otherwise no mixing at all occurs. Stacking faults are present in the evaporated film, with layers forming in ABAB stacking sequence. Addition of the ion-beam assist provides enough kinetic energy to the film to eradicate stacking faults and the film grows in the preferred ABC manner.

4.4.4 Sputter Deposition

Sputter deposition is modelled by assuming that Ag atoms arrive normally to the surface with an energy of ~ 40 eV. In a magnetron sputtering device Ar is also present in the plasma, either in the form of back reflection from the target or as an ion assist in some situations, as described in chapter 1. This flux of Ar is assumed to arrive with similar energy to the Ag. However, in order to separate out the effects of Ar, two simulations have been performed. Figure 4.9 illustrates Ag growth excluding the effects of the Ar and figure 4.10 includes Ar. Again the Ar and Ag fluxes are assumed to be equal. The two simulations produce almost identical growth, with the first new layer being complete and substantial mixing occurring in the ballistic phase between the original substrate and deposited atoms, allowing subsequent layers to form almost completely. The temperature increases during the ballistic phase, but this is soon damped out by the layers held at constant temperature. No stacking faults are observed due to the higher impact of arriving atoms transferring enough energy to the substrate to promote correct stacking. No Ar is retained within the film due to high Ar diffusion rates and Ar reflection.

Comparing the resulting growth of Ag (111) by evaporation, ion-beam assist and sputtering, it is clear that evaporation deposition produces incomplete, void filled structures where stacking faults can also occur. The addition of the ion-beam introduces energy to the system allowing increased diffusion and slightly better crystallinity in the correct stacking sequence. Sputtering, with and without the inclusion of the Ar in the plasma, produces films that are more dense, almost crystalline [94, 101, 102] and sit in the correct ABC stacking.

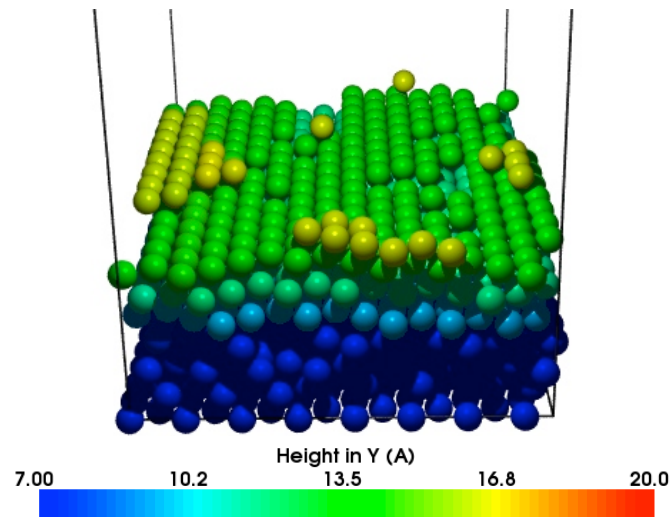


Figure 4.9: Ag (111) growth from sputtering, after 0.27 s of real time. 675 atoms added to the system result in four newly formed layers, the first one of which is complete.

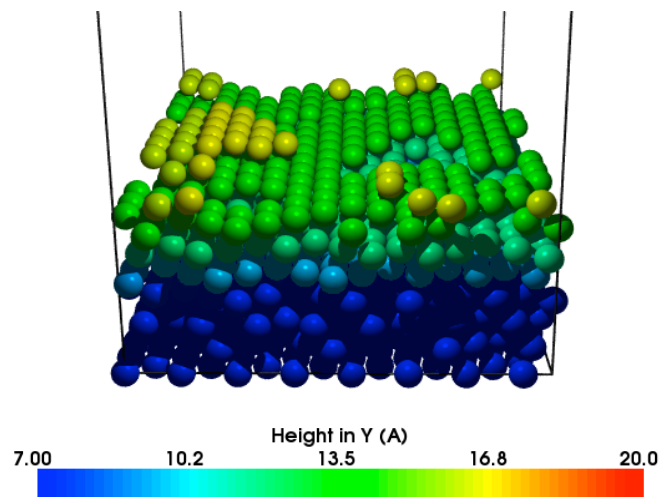


Figure 4.10: Ag (111) growth by magnetron sputtering, simulating 0.34 s of real time, including the effect of the Ar present in the plasma where there was equal likelihood that an Ag atom or an Ar atom would strike the surface. 675 atoms added results in four newly formed layers, similar to the simulation without Ar.

Numerous growth mechanisms are observed during Ag (111) growth. Multiple atom concerted motions, exchange and replacement mechanisms and vacancy filling mechanisms allow the completion of layers. The strength of the otf-KMC method is the ability to study, in detail, these multiple atom transitions [?]. Multiple atom concerted motions are often observed, requiring little energy to occur. Figure 4.11 shows an example of two atoms moving in a concerted motion, sliding across to fill

a vacancy in the film, with a barrier of 0.44 eV.

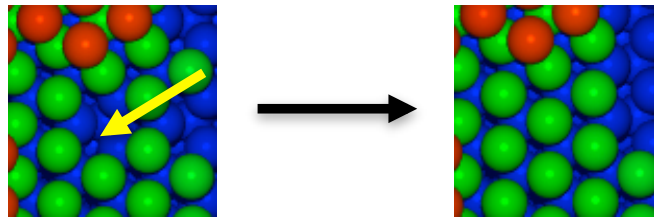


Figure 4.11: Two atom concerted motion requiring 0.44 eV to occur. Layers are able to self-complete by the filling in of vacancies with this mechanism.

Figure 4.12 illustrates layer completion by the Ehrlich-Schwoebel (ES) barrier, a classic mechanism previously reported [106, 107], where an atom drops off a step edge of an island. In the case of Ag (111), the barrier is calculated to be 0.42 eV. Transitions of this kind enable films to grow in a layer-by-layer manner, however, as the ES barrier here (0.42 eV) is higher than a single ad-atom hop (0.12 eV), it will not occur many times in comparison to single ad-atom hops.

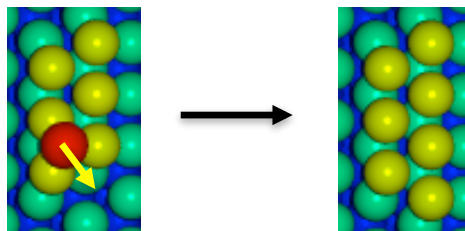


Figure 4.12: The important ES transition requires 0.42 eV to occur on the Ag (111) surface. This ES transition allows completion of layers, however, as it is a higher energy barrier than that of the diffusion of a single ad-atom, it is not observed very frequently. Atoms are coloured according to height, where blue is the bottom, then green, then yellow and red.

4.4.5 Mid Deposition Energy: 10 eV

1 eV and 40 eV deposition energies simulate the evaporation and sputter deposition techniques respectively. A mid energy was also chosen for a separate simulation in order to provide a more rounded understanding of the effect of deposition energy on thin film growth. Figure 4.6 shows similar results to the growth achieved from the simulation of sputter deposition, with slightly less completeness. With a deposition energy an order of magnitude higher than that used in evaporation, 10 eV

provides sufficient energy for most atoms to move to their correct lattice sites and produce more complete layers. However, 10 eV is not a high enough deposition energy to ensure that stacking faults do not occur. The third new layer has switched to the hcp stacking sequence and instead of sitting in the C position, the layer has switched to the B position, allowing the hcp ABAB sequence to occur. As already shown, the higher energy depositions from sputtering provide the required energy for atoms to move to correct lattice sites, thus eliminating any stacking faults.

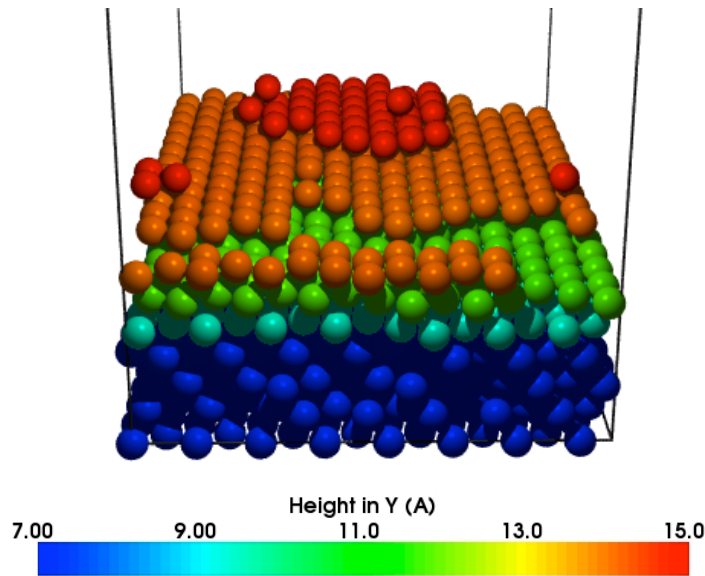


Figure 4.13: Ag (111) growth where atoms arrived at the substrate with 10 eV. Four partially formed layers have grown, most of which are in the preferred ABC stacking sequence, however, the third new layer has switched to hcp stacking.

4.5 Deposition on the Ag (100) Surface

Simulations are now repeated with the (100) surface acting as a substrate. The effect of Ar bombardment during both the evaporation and sputtering processes is not investigated on the (100) surface due to computational limitations, however, we assume that the effects will be similar to those seen on the (111) surface. Again, a mid energy between the 1 eV for evaporation and 40 eV for sputtering is also simulated for a greater understanding (10 eV deposition energy).

4.5.1 Evaporation Deposition

Figure 4.14 shows resulting film growth from low energy evaporation deposition of single Ag atoms onto the Ag (100) substrate. Three complete monolayers were added to the system, but it can be seen that new growth produces six new monolayers, of which none are complete. Vacancies are evident throughout the new film, which would lead to poor optical and electrical properties when used in photovoltaic devices. Evaporation, as suggested earlier, involves atoms arriving at the surface with very little kinetic energy, hence on arrival at the surface very few atoms have the energy to diffuse into preferential locations. It is for this reason and the lack of atomic mixing, that highly incomplete layers are observed.

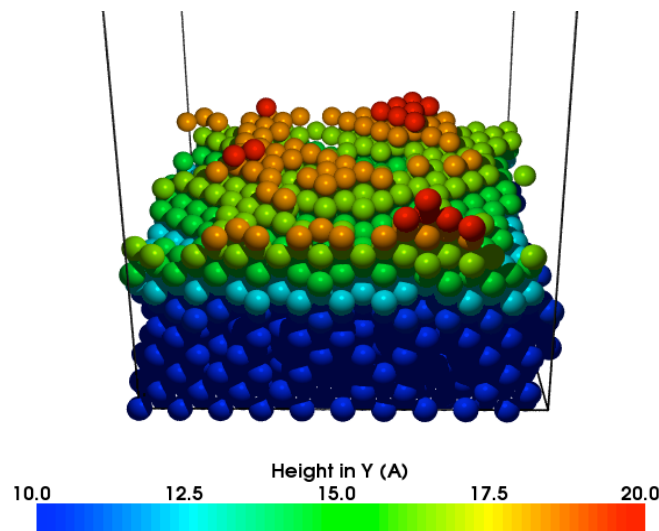


Figure 4.14: Ag (100) growth via evaporation deposition after 0.23 s of real time, with the addition of 600 atoms (equivalent to three complete monolayers). Six incomplete monolayers are produced as evaporation does not transfer enough energy for surface diffusion and thus layer completion to occur. The original substrate was at 10 Å.

4.5.2 Sputter Deposition

Growth shown in figure 4.15 is produced from our model of sputter depositions of Ag, excluding the contribution of Ar from in the plasma. It can be observed that almost complete layers have formed, similar to the Ag (111) simulation.

When depositing on Ag (100), the calculated energy barriers were often greater than those seen with Ag (111), typically ranging from 0.33 eV to 0.65 eV. It was

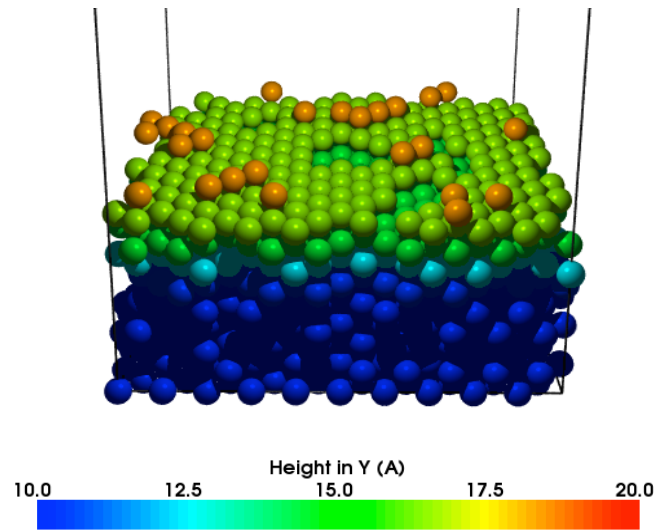


Figure 4.15: Ag (100) growth by magnetron sputtering, simulating 0.23 s of real time. The addition of 600 atoms produced three almost complete monolayers, along with a fourth incomplete monolayer just beginning.

observed that the film grew via clusters, through the formation of islands on the surface with single ad-atoms joining the islands until they met and formed a new monolayer. It was determined that a single Ag ad-atom transition on the surface required 0.65 eV to diffuse, whereas cluster rearrangements and formation required as little as half of this energy, as depicted in the graph shown in figure 4.16 and listed in table 4.2. Ag (100), therefore, grows via small clusters on the surface which join, forming a layer, rather than single atom diffusion as seen with the Ag (111). The energy required for atoms to bond to step edges (0.41 eV) was actually less than required for a single monomer hop (0.65 eV), agreeing with previous statements that cluster rearrangement often occurs.

Monomer hop	Small cluster (2/3 atoms) formation and rearrangement	Large cluster (4+ atoms) formation and rearrangement
0.65 eV	0.33 eV	0.3-0.4 eV
<hr/>		
Bond to step edge	De-bond from step edge	
0.41 eV	0.42 eV	

Table 4.2: Transition barriers for ad-cluster diffusion on the Ag (100) surface.

The ES barrier was 0.42 eV on the (100) surface, identical to the (111) surface. Figure 4.17 illustrates the ES transition, however, due to the high barrier the transition was not frequently observed. With an even higher energy barrier (0.65 eV),

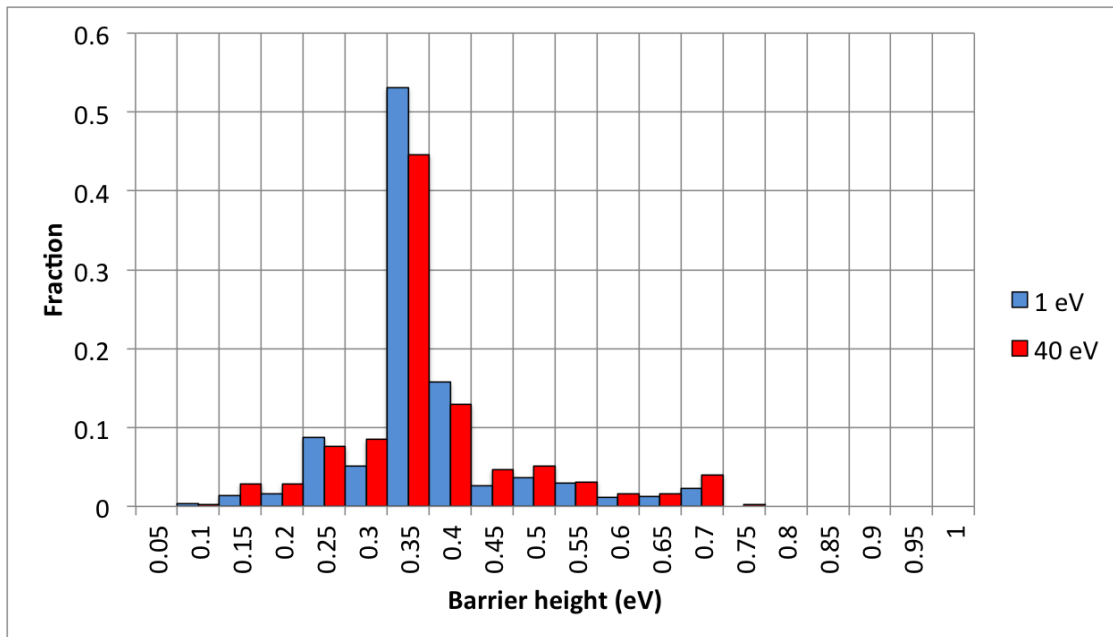


Figure 4.16: The respective energy barrier heights for all those transitions observed during the Ag (100) growth simulations. For both evaporation and sputter growth a sharp peak is observed at around 0.33 eV, which was found to be small cluster formations and rearrangements on the surface. Transitions requiring between 0.3 eV and 0.4 eV were shown to be larger cluster formation, rearrangement and addition to islands. Barriers around 0.41 - 0.42 eV represent bonding and de-bonding from the step edge of single atoms. Single ad-atom hops required 0.65 eV to take place; with such a large energy barrier this single ad-atom hop was rarely utilised (in less than 0.05 % of transitions).

the monomer hop was very rarely observed. Film growth, therefore, occurred by the formation of separate clusters on the surface, rather than layer-by-layer growth. Due to the high ES barrier, atoms rarely dropped down down to complete lower layers, therefore causing clusters to grow in height rather than merge together, forming incomplete and somewhat rough surfaces.

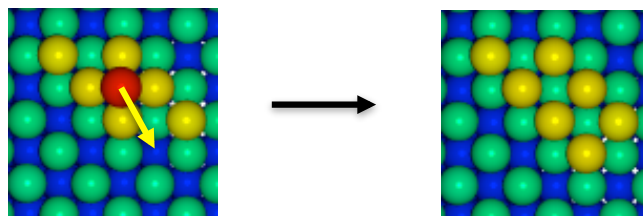


Figure 4.17: The ES barrier was found to be identical as on the (111) surface. 0.42 eV is required for an Ag atom to drop off the edge of a step. This transition rarely occurred, however, due to other transitions requiring less energy.

4.5.3 Mid Deposition Energy: 10 eV

10 eV depositions have been simulated on the (100) surface to gain a broader understanding of film growth. Growth results, illustrated in figure 4.18, indicate that 10 eV depositions do not transfer sufficient energy to the surface to allow complete layers to form. Although more complete than the low energy evaporation growth, 10 eV depositions do not allow the formation of layers as complete and dense as sputtering.

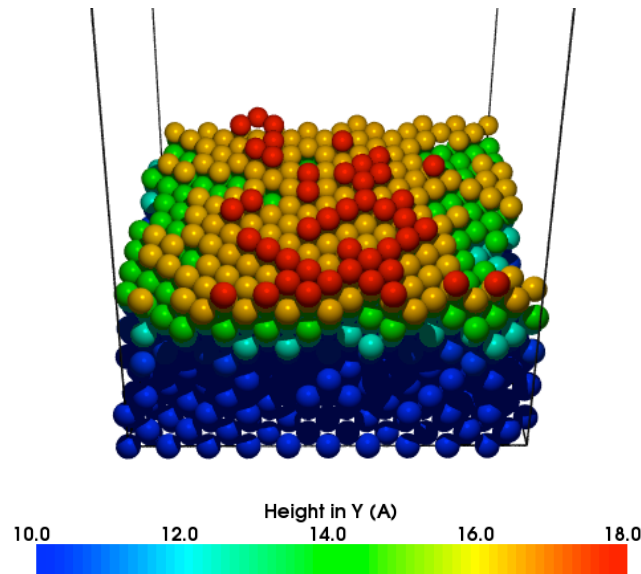


Figure 4.18: Ag (100) growth where atoms arrived at the substrate with 10 eV. The film is more complete than that grown by evaporation as the deposition energy is one order of magnitude higher, therefore transferring more energy to the surface atoms and allowing increased diffusion. However, it is clear that the higher energy sputter depositions do produce even more complete, dense, crystalline films due to the increased deposition energy.

4.6 Deposition on the Al (111) Surface

The Al (111) substrate is investigated in the same way as Ag (111). Evaporation deposition, ion-beam assist and magnetron sputtering growth are simulated, along with 10 eV depositions. Small clusters on the surface are highly mobile as on the Ag (111) surface. For Al (111), even a five atom cluster has a small energy barrier for diffusion. This is shown in figure 4.19, where the cluster switch from ABC stacking to ABAB stacking with an energy barrier of 0.3 eV. Table 4.3 presents

important transition barriers on the Al(111) surface.

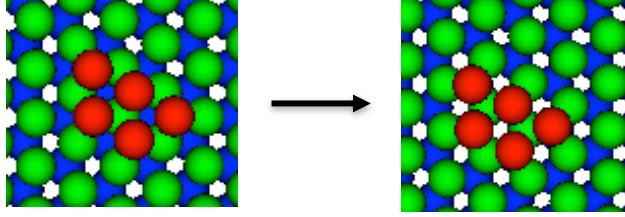


Figure 4.19: A five atom cluster on the Al (111) surface which switches from ABC to ABAB stacking sequences with a relatively low barrier of 0.3 eV. During later steps of the simulation, the cluster switches back to ABC stacking with a lower barrier and growth continues in the correct stacking formation, perhaps by chance. Atoms are coloured by height of monolayer with red being the cluster on top.

Monomer hop	5-mer hop	Bond to step edge	De-bond from step edge
< 0.1 eV	0.3 eV	0.03 eV	0.42 eV

Table 4.3: Transition barriers for single ad-atom and small cluster diffusion on the Al (111) surface.

4.6.1 Evaporation Deposition

Al (111) grown by evaporation deposition is shown in figure 4.20. After the addition of three monolayers to the system, two complete layers are produced, with a third almost complete and the fourth has just begun. Despite the low kinetic energy of arriving atoms, diffusion has occurred enabling complete layers. This is contrary to the pattern seen with the Ag (111), where evaporation growth produced incomplete growth with voids. One explanation for this difference is that the energy required for a single ad-atom hop of Ag on the (111) surface is between 0.1 and 0.15 eV, whereas for Al on the (111) surface this is reduced to <0.1 eV. This suggests that on Al (111) surface diffusion of single ad-atoms will occur more often, which enables complete film growth to occur. A single Ag ad-atom hop on Ag (111) with a barrier of 0.15 eV has a rate of $6.9 \times 10^{10} \text{ s}^{-1}$, whereas an Al ad-atom hop requiring say 0.075 eV has a rate of $8.3 \times 10^{11} \text{ s}^{-1}$, which is over one order of magnitude more likely to occur. During growth, single Al ad-atoms diffuse freely over the surface with very small energy barriers, joining onto larger islands with step edge bonding barriers of around 0.03 eV. The reverse barrier for single atoms to de-bond from edges is huge in comparison (0.42 eV). Another reason for the completeness of the evaporation growth is illustrated in figure 4.19, where clusters

form during the simulation which are mobile up to five atoms, in this case requiring 0.3 eV to diffuse. Therefore, if large clusters are able to diffuse across the surface with accessible barriers, this will aid the completion of layers as clusters have the ability to move to join one another.

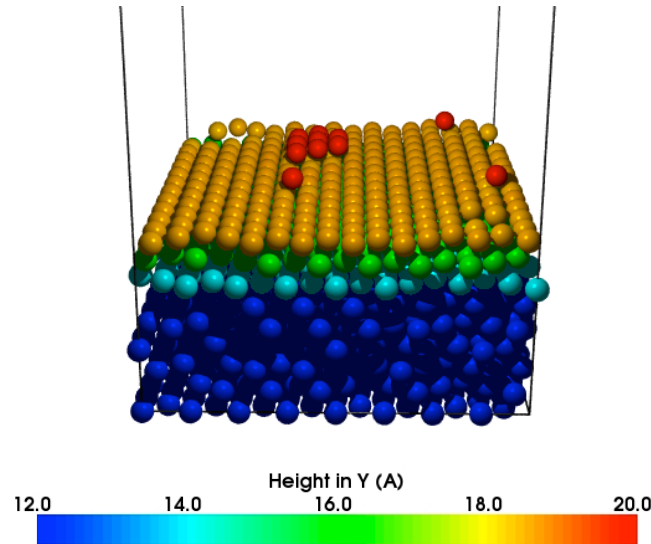


Figure 4.20: Al (111) growth via evaporation deposition after 0.29 s of real time. 672 atoms have been added to the system, equivalent to three complete monolayers. Two complete layers are formed, along with a third almost complete and a fourth just beginning. The original substrate was at 12 Å.

The most likely explanation for the completeness and crystallinity of the evaporation growth is, however, shown in figure 4.21. The ES barrier has been calculated for Al (111) to be only 0.07 eV. This ES barrier plays a key role in the better quality of growth observed in figure 4.20, as small ES barriers allow atoms to drop off islands to complete the monolayer below, thus enabling layer-by-layer growth rather than the cluster growth observed with Ag. Comparing 0.07 eV with the 0.42 eV ES barrier occurring with Ag, this provides a convincing explanation of the different growth produced by these two metals.

4.6.2 Deposition by Ion-Beam Assisted Evaporation

Figure 4.22 shows thin film growth produced when an Ar ion-beam assist is used in conjunction with the evaporation method. Ar ions bombard the surface with 100 eV of kinetic energy and strike the surface with equal probability as an Al atom. Ar bombardment has previously been found to increase the density of the material and promote surface diffusion [94, 101, 102]. Close inspection of figure 4.22

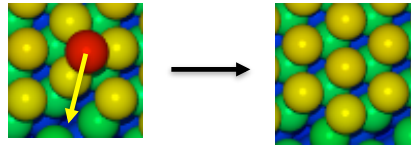


Figure 4.21: The film completes via this ES barrier, which allows layer-by-layer growth where atoms drop off step edges with a very low barrier (0.07 eV). The Al (111) grown via evaporation is clear evidence that this ES barrier plays an important role in the type of growth observed and hence the quality of the resulting film.

reveals that the Ar impacts have in fact severely damaged the new surface and the original substrate. The high energy of Ar bombardment allows penetration through three layers, displacing Al atoms from the substrate. 57 Ar ions (0.07% of Ar bombarded throughout the simulation) have remained in the system, many of which have formed into subsurface clusters as reported in the literature [97–100]. Figure 4.23 illustrates the Ar agglomeration into subsurface clusters. Ar below the surface was found to diffuse freely through the substrate with energy barriers as low as 0.05 eV, similar to previous calculations on Au [90]. During the simulation, some Ar does leave the system, usually after an Ar impact later in the simulation, which transfers sufficient kinetic energy to the subsurface Ar to allow diffusion out of the substrate. The low ES barrier did aid this simulation also by allowing layers to complete and form around the Ar subsurface clusters, however, these clusters have disrupted the growth so much that Al atoms are out of place.

4.6.3 Sputter Deposition

Figures 4.24 and 4.25 illustrate growth produced by magnetron sputtering, firstly ignoring the influence of Ar ions present in the plasma and then including their effect. When Ar is not included, new monolayers are almost complete, in a similar way to the evaporation simulation results. Due to the higher energy deposition, mixing between the original substrate and deposited atoms is more increased. This enables a damage and repair mechanism to take place, which allows increased surface diffusion and leads to more complete layers. Illustrated in figure 4.25 is the resulting growth from the inclusion of the effect of Ar ions in the simulation. It is clear that Ar bombardment at 40 eV transfers enough kinetic energy to the surface to allow almost perfect crystalline growth. Unlike the 100 eV ion-beam used during evaporation, the Ar has insufficient energy to penetrate the third layer and no Ar subsurface clusters are formed. Only 4 Al atoms are missing from the third layer,

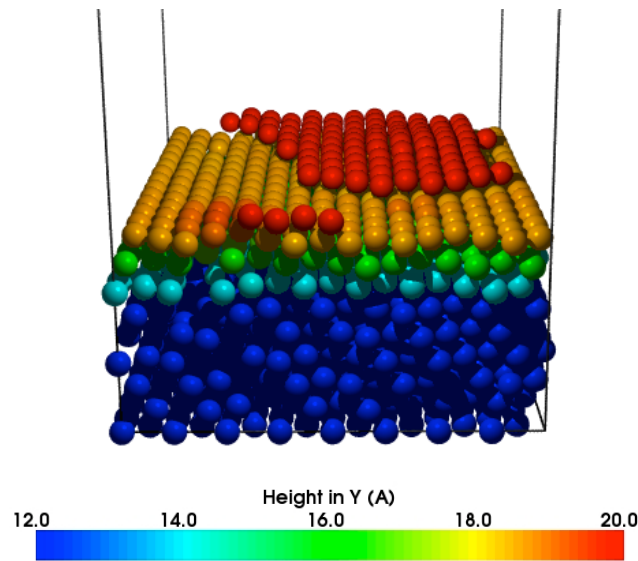


Figure 4.22: Al (111) growth via evaporation deposition with ion-assist, where Ar ions bombard the surface with 100 eV of kinetic energy. Here 0.31 s of real time is simulated. From the addition of three monolayers of atoms, no complete monolayers have been formed. In fact, the original substrate itself is damaged from the high energy Ar impacts which penetrate three layers deep in some cases. Sub-surface Ar clusters have displaced Al atoms, creating large Al voids in the substrate. Four new monolayers, all incomplete, are formed.

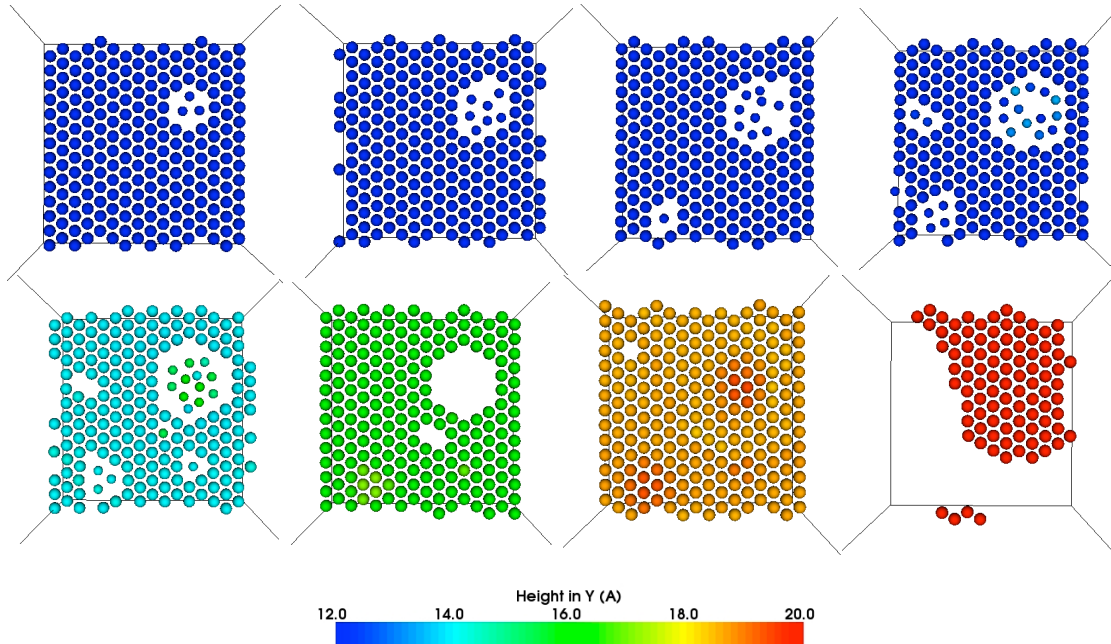


Figure 4.23: Layers of Al (111) after evaporation growth with ion-beam assist. Layers are ordered left to right, beginning with the deepest layer and ending with the very top new layer. The newly grown layers are incomplete and Ar has created voids in the Al structure by sitting in subsurface Ar clusters. Al atoms are slightly larger diameter, with the Ar represented by smaller spheres.

the rest being complete.

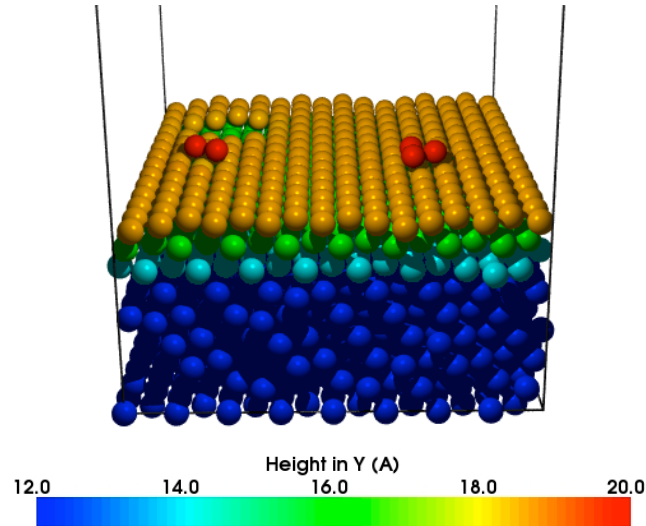


Figure 4.24: Al (111) thin film growth by magnetron sputter deposition after 0.3 s of real time. Three monolayers of Al are deposited onto the surface and four new monolayers are created, two of which are complete and the fourth has only 5 atoms. Due to the higher energy impacts than evaporation deposition, increased atomic mixing is observed.

Comparing the resulting thin films, evaporation produces a complete film, whereas the addition of the ion-beam assist damages the surface beyond repair giving an incomplete, void filled structure with subsurface Ar clusters. Sputtering produces dense, crystalline and complete films, both with and without the inclusion of the effect of the Ar atoms in the plasma.

As observed with the Ag, multiple atom concerted motions enable layers to become complete by vacancy filling and the ES barrier allows complete layers to form. Figure 4.21 illustrates the low ES barrier on Al (111), suggesting that even during low energy depositions, atoms will very often drop off a step edge enabling layers to become complete. This was confirmed in the results of the evaporation simulation, where growth was almost as complete as the sputter deposited growth. From the higher energy depositions observed during the sputtering process, we notice damage and repair mechanisms allowing the slightly more complete growth. A concerted motion observed during island formation is depicted in figure 4.26, where two Al atoms slide across in one motion to fill a vacancy with a barrier of 0.25 eV.

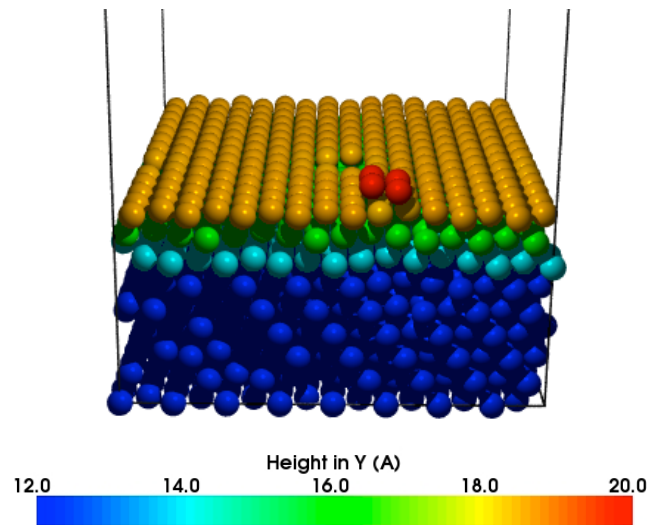


Figure 4.25: Al (111) thin film growth via magnetron sputter deposition after 0.35 s of real time, including the effect of the Ar present in the plasma. After the deposition of three monolayers onto the surface, four new monolayers are created, two of which are complete and the third is only missing 4 atoms which are sit on top creating a fourth monolayer. Atoms are coloured by height in Å.

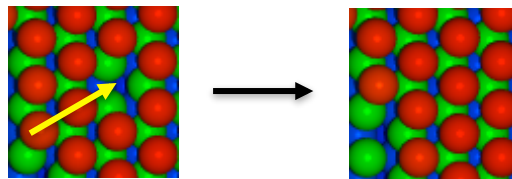


Figure 4.26: An island formed on the Al (111) surface has a vacancy within it. Here, two Al atoms slide across in a concerted motion, filling the vacancy. The energy barrier for this transition is 0.25 eV, which is highly accessible within the time frame between successive impacts. Atoms are coloured by height.

4.6.4 Mid Deposition Energy: 10 eV

We have already shown that on the Al surface, the ES barrier is very small (0.07 eV) allowing atoms to drop off islands, thus completing the layer below. This barrier plays a key role in the growth of Al films. Low energy depositions from evaporation and higher energy sputter depositions result in very similar films, which are complete and crystalline. Deposition at 10 eV results in a very similar film, shown in figure 4.27. The deposition energy does not play a huge role in the growth of Al (111) films.

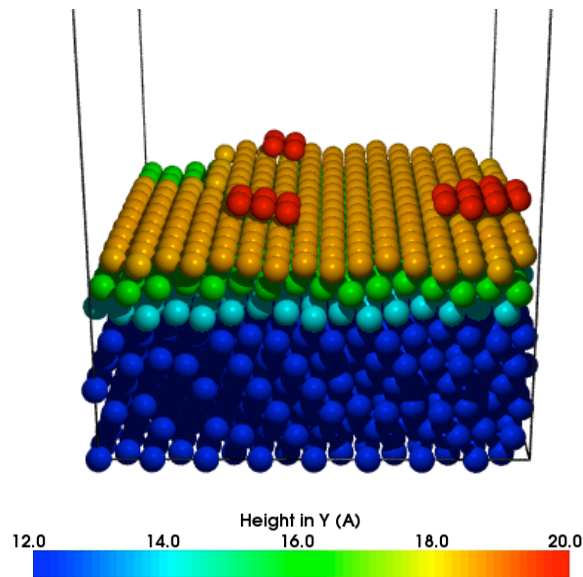


Figure 4.27: Al (111) growth where atoms arrived at the substrate with 10 eV. The low ES barrier allows complete layers to form easily and deposition energy becomes much less important. Simulations of evaporation deposition, sputter deposition and the 10 eV deposition produce very similar results.

4.7 Deposition on the Al (100) Surface

Simulations are now repeated on the Al (100) surface. Due to computational time limits, Ar is not included in any of the following simulations. For these simulations, it was noticed that energy barriers below 0.2 eV produced transitions that resulted in no net diffusion such as rotating trimers on the surface. By filtering out these low energy barriers we saved computational time, but at the possible expense of missing the occasional important transition. Table 4.4 lists some of the main transitions observed during the Al (100) simulations. Monomer diffusion and bonding and de-bonding from step edges were the most observed transitions. Figure 4.28 illustrates how an Al monomer diffuses via a replacement mechanism, requiring 0.27 eV.

Monomer diffusion via replacement mechanism	Bond to step edge	De-bond from step edge
0.27 eV	0.22 eV	0.51 eV

Table 4.4: Transition barriers observed on the Al (100) surface.

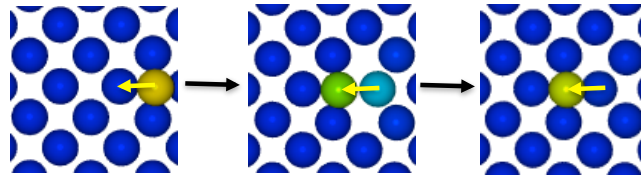


Figure 4.28: A two atom concerted replacement mechanism is shown on the Al (100) surface. Initial, saddle and final configurations are shown. This mechanism allows single Al atoms to diffuse across the surface, requiring 0.27 eV. Atoms are coloured by height, dark blue being the surface.

4.7.1 Evaporation Deposition

Figure 4.29 illustrates the growth of Al (100) from evaporation of Al onto the surface. From the addition of three monolayers of atoms to the system, two monolayers are totally complete, with the third and fourth incomplete. Some mixing between the original substrate and deposited atoms is observed, however, due to the low impact energy, Al atoms tend to stick on the surface. The ES barrier shown in figure 4.30 has been calculated to be 0.24 eV, larger than on the (111) surface but still lower than Ag and low enough for the transitions to occur between deposition events.

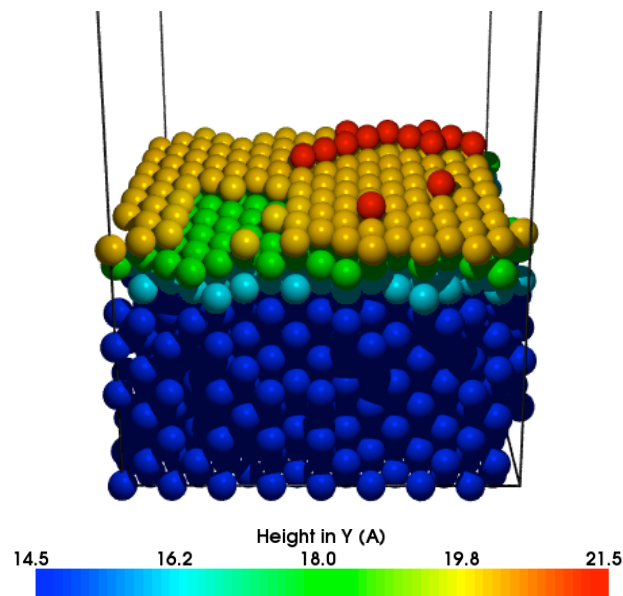


Figure 4.29: Al (100) growth from evaporation deposition simulated over 0.15 s of real time. 384 atoms are added to the system, equating to three complete monolayers. Four new monolayers are formed, two of which are complete. The original substrate was at 14.5 Å.

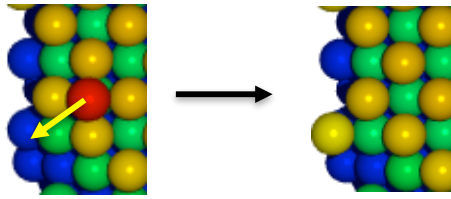


Figure 4.30: The ES barrier on Al (100) is calculated to be 0.24 eV. Relative to monomer diffusion (0.27 eV), the ES barrier will occur more often between deposition events, thus enabling layer-by-layer growth.

4.7.2 Sputter Deposition

Figure 4.31 shows the grown film from sputtering Al onto the Al (100) surface. Almost all three new monolayers are complete, missing only two atoms from the third. The higher energy transferred from the sputtering, enabling greater surface diffusion, along with the accessible ES barrier, promote the completion of monolayers.

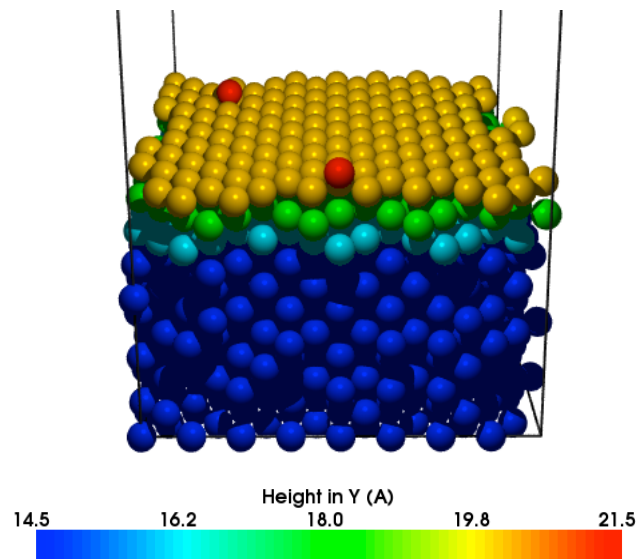


Figure 4.31: Al (100) growth produced from magnetron sputtering over 0.18 s of real time. From three monolayers added, two complete monolayer are formed, with the third missing only two atoms, which we would expect would fill in and complete if the simulation was to continue.

Comparing the resulting growth of Al (100) via evaporation deposition and sputtering, it is clear that both methods produce near-complete structures. Sputtering, however, produces a slightly more crystalline and complete film due to the increased kinetic energy transferred to the system from depositions.

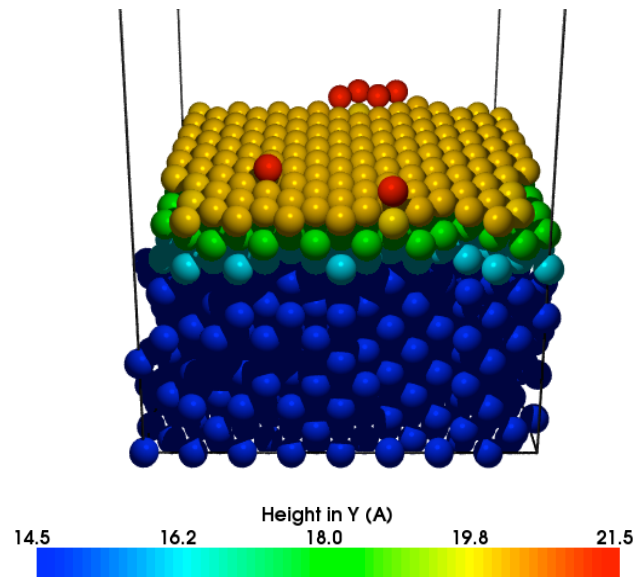


Figure 4.32: Al (100) growth where atoms arrived at the substrate with 10 eV. The film is more complete than that grown by evaporation as the deposition energy is one order of magnitude higher, therefore transferring more energy to the surface.

The most prominent growth mechanism noticed during the Al (100) simulations is the two atom replacement mechanism, illustrated in figure 4.28. An Al atom diffuses over the surface by the replacement of another surface Al by pushing the original Al out of its site and onto the surface, occurring with an energy barrier of 0.27 eV. Shown in figure 4.30 is the ES barrier, which requires 0.24 eV to occur and enables the completion of the films even from the low energy evaporation. This is similar to results observed on the Al (111) surface.

4.7.3 Mid Deposition Energy: 10 eV

The ES barrier for atoms to drop off islands on the (100) surface is 0.24 eV, giving more importance now to the deposition energy than on the (111) surface, where the ES barrier was 0.07 eV. Figure 4.32 illustrates the resulting growth from 10 eV depositions; very similar to the sputter growth. The accessible ES barrier and the deposition energy are sufficient here to produce almost an complete film. Comparing this to the low energy evaporation growth, the extra energy seems enough to almost complete the third layer, whereas evaporation leaves the third layer incomplete.

4.8 Discussion

Otf-KMC and MD have been used to model the deposition of metals onto different substrates, simulating under one second of real time. Non-intuitive, concerted transitions can be observed using the otf-KMC method, allowing a more precise understanding of metal thin film growth. Ag (111) film growth was simulated for around 0.3 s real time, allowing the deposition of three monolayers onto the surface. Deposition by evaporation produced an incomplete film full of vacancies and voids, with stacking faults occurring. The ion-beam assist promoted mixing with the original substrate during the ballistic phase of the deposition, allowing layers to become slightly more complete. Sputtering, however, produced a more dense, crystalline and complete film. The inclusion of Ar ions from the plasma did not significantly change the quality of the film, suggesting that the 40 eV Ag deposition provided sufficient energy to promote diffusion and atomic mixing. The lower energy of Ar bombardment during sputtering than the ion-beam assist, resulted in less Ar penetration into the substrate. 10 eV depositions produced a quality of growth in between the evaporation and sputter simulations. The calculation of barriers on the (111) surface showed that the monomer hop required the least energy to occur. It was this single ad-atom hop that was the most enabling mechanism when producing clusters on the surface. Stacking faults and twin boundaries, observed experimentally [89], were observed in our simulation during the lower energy depositions from evaporation and 10 eV impacts. A four atom ad-cluster on the surface was able to switch between the preferred ABC (fcc) and less stable ABAB (hcp) stacking sequences with a barrier of 0.4 eV. During the early stages of evaporation growth, switching of four atom ad-clusters between stacking sequences took place. Once a fifth atom joined the cluster, it became pinned in a stacking sequence. During evaporation and 10 eV depositions, stacking faults were observed in the deposited layers. Sputter deposition, however, transferred sufficient energy to the surface to ensure that atoms diffused to correct lattice sites, ensuring that new layers sat in the correct ABC sequence.

Thin film growth on the (100) surface followed similar patterns. The evaporation process produced highly incomplete monolayers with islands forming but no complete layers. Sputtering, however, produced a much more dense and complete film, with all layers almost complete. The mid energy 10 eV depositions produced a quality of film in between that of the PVD methods. Transitions observed during the growth simulations on the (100) surface were predominately cluster formation

and rearrangements, requiring 0.33 eV, as monomer hops required more energy to occur (0.65 eV). This caused growth to occur by clusters on the surface increasing in size and diffusing towards one another, creating larger clusters and islands.

A very important transition in enabling film growth is the ES (Ehrlich-Schwoebel) transition. On Ag surfaces the ES barrier was calculated to be 0.42 eV, which in comparison to other barriers available is high and therefore will rarely occur. Growth, therefore, occurs in a cluster-by-cluster way, where atoms rarely drop down off edges. Sputtering, however, transfers increased energy to the surface, which leads to increased atomic mixing enabling the films to be more complete.

Al (111) films grown via evaporation and sputtering appear to be very similar to one another, contrary to expectation and to that observed with the Ag. Evaporation actually grew a close to complete film, with two complete layers formed. The ES barrier was calculated to be 0.07 eV, much lower than on Ag surfaces, enabling the complete growth not usually seen from evaporation. Growth occurred in a layer-by-layer style, where atoms preferentially filled any vacancies in the layer below. Other transitions on the surface, such as the monomer hop, also required little energy (< 0.1 eV). When Ar was included via the ion-beam assist, results again were not as expected. The Ar assist, instead of aiding in densifying and completing the film as with Ag, actually damaged the film beyond repair. Al voids were produced below the surface, enabling Ar subsurface clusters to form. This subsurface Ar agglomeration observed agrees with results reported in the literature [97–100]. Sputtering also produced complete films, with vacancies only in the top layer. When the effect of the Ar in the plasma was included, results improved only very slightly due to the increase in energy transferred from the Ar bombardments allowing increased atomic mixing. The low ES barrier plays the most important role in Al (111) growth, with 10 eV depositions producing very similar results again.

The Al (100) surface showed similar results to the previous surface. Evaporation growth produced rather complete monolayers with vacancies only in the top layer. The ES energy barrier on this surface was calculated as 0.24 eV, lower than the barrier for a single ad-atom diffusing over the surface (0.27 eV). Although the ES barrier is not as low as on the (111) surface, it is still accountable for the good quality of the growth produced in comparison to the Ag evaporation growth. Higher energy sputter depositions produced a highly complete and dense film, with all

three new monolayers grown perfectly with only two vacancies in the top layer, a notable improvement on the evaporation growth. The 10 eV depositions produced nearly complete growth, similar to sputter depositions, illustrating that 10 eV is sufficient energy to promote surface diffusion and the completing of layers on Al (100).

Chapter 5

Simulation of Titanium Dioxide Thin Film Growth

5.1 Introduction

TiO₂, the natural occurring oxide of titanium and ninth most common mineral on the planet, is an important material with industrial scale uses ranging from pigmentation in paints to sunscreen to multilayer optical coatings. Due to its very high refractive index (~ 2.609) and brightness, TiO₂ is a very effective white pigment in paints, foods, medicines and plastics. TiO₂ also acts as a highly effective UV absorber [116], efficiently transforming UV light energy into heat. This allows the application in sunscreens, plastics and cosmetics. Although these practical uses of TiO₂ are very useful, we are not interested in them in this research. Here, we focus on the applications of TiO₂ in the photovoltaic industry. When applied in very thin, nanometre thick layers, TiO₂ is transparent while still able to block UV rays. This lends the material to application in photovoltaics. TiO₂ is particularly useful in dye sensitised solar cells, where a dye is injected into a thin layer of porous TiO₂. In its crystalline form, TiO₂ is used in anti-reflective coatings within optics and solar cells.

TiO₂ occurs naturally in three polymorphs; rutile, anatase and brookite. The first two forms have tetragonal crystal structures, whilst the latter has an orthorhombic structure. During this research, only the most common form, rutile, is investigated due to the applications in photovoltaics. Rutile TiO₂ forms more prevalently, particularly at higher temperatures, often forming with the (110) surface due to the minimum breakage of ionic bonds. The densely packed crystals reflect light well.

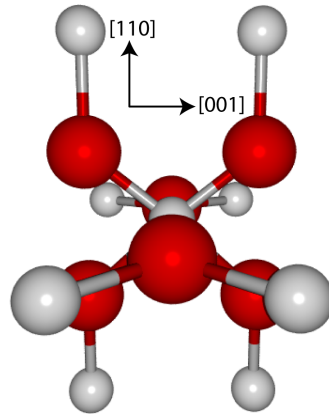


Figure 5.1: The TiO_2 rutile unit cell, where larger red spheres represent O and smaller silver spheres represent Ti (this scheme will be used throughout this chapter). The directions are indicated. [5].

Figure 5.1 shows the rutile unit cell, with the (110) and (001) surfaces highlighted.

A model for the rutile (110) surface was first proposed by Henrich [117]. During this chapter it becomes important to classify important features on the rutile (110) surface, figure 5.2 illustrates these features. Most obviously, O ad-rows run in the [110] direction, sitting proud of the surface, resulting in a trench running parallel between each ad-row. Ti atoms can sit in one of two sites, the 5-fold coordinated Ti is located in the centre of the trench, bonded to 4 neighbouring surface O atoms and a single O directly below it. The 6-fold coordinated Ti is located between successive O atoms in the O ad-row, bonded to 2 ad-row O atoms, 2 surface O atoms and 2 O atoms below it.

Rutile has two main uses in photovoltaics which will be investigated in this chapter, dye sensitised solar cells and anti-reflective coatings. In industry, these applications require the deposition of the material onto a substrate. This chapter, therefore, investigates the deposition techniques available and the effects these have on the resulting film and its properties. Some of the work included in this chapter has been published in peer-reviewed journals and conference proceedings [90, 91, 118].

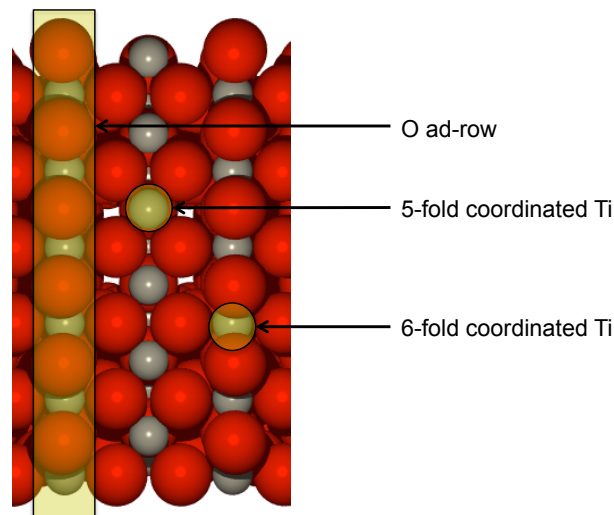


Figure 5.2: The structure of the rutile (110) surface. O ad-rows run in the [110] direction, with trenches running parallel between individual ad-rows. The Ti atoms sitting in the trenches are the 5-fold coordinated Ti and those sitting directly below the O ad-row are the 6-fold coordinated Ti.

5.2 Previous Work

TiO₂ is an important material in many industries and has been the focus of many experimental and theoretical studies, which provide insight into rutile growth.

5.2.1 Experimental

Metal-oxide thin films can be deposited using the industrial-scale processes introduced in chapter 1. These include evaporation (thermal and electron beam), ion-beam assisted evaporation [119–121] and reactive magnetron sputtering [120, 122–125]. The evaporation process involves evaporation of Ti_xO_y molecules onto the substrate with kinetic energy typically <1 eV. An ion source (usually Ar) may be used to densify the film, this ion-beam introduces energy into the growing film [120, 121] to enhance mixing. During evaporation deposition, Ar inclusion has been shown to improve the density of films due to the Ar bombardment transferring momentum to the substrate, thus enhancing surface mobility. The increased film quality also results in a higher refractive index [119, 122, 123].

Magnetron sputtering is also used to deposit thin films of titania using RF, DC or pulsed DC power. Targets can be purely metallic Ti (DC), TiO₂ (RF) or TiO_x (pulsed DC). Sputtering in the presence of a reactive gas is necessary to different

degrees, depending on the precise deposition configuration. In all cases, Ar is used as the working gas to sputter material from the target. Ar ion bombardment during deposition, occurring due to back reflection, effects the density and stoichiometry of the thin film [124, 126]. Eufinger *et al.* deposit TiO₂ films using DC magnetron sputtering, increasing the Ar pressure gradually in the chamber, concluding that film density decreases with an increased sputtering pressure [126]. Amin *et al.* compare DC sputter deposition with ion-assisted sputter deposition, where back reflection does not allow sufficient energy transfer to the substrate. It was found that ion bombardment strongly promotes the growth of rutile films, whereas little or no ion bombardment promotes the anatase phase [127]. Karmaker *et al.* also suggest that high energy ion bombardment on the substrate leads to a change of stoichiometry and the formation of vacancies [128].

In the crystalline form, TiO₂ is particularly interesting for anti-reflective coatings and in its porous form for dye sensitised solar cells. Experimentally, these applications have been widely studied. Evaporation deposition has been used to prepare porous TiO₂ films for use in dye sensitised cells [129]. Porous TiO₂ is immersed in a ruthenium-polypyridine dye where a thin film of the dye bonds to the TiO₂ [130, 131], which acts as an anode within a photovoltaic cell. High quality, dense films of TiO₂ are used extensively in multilayer optical coatings because of their high refractive index and ability to absorb UV radiation [116]. Anti-reflective coatings require these properties and sputter deposition has been used successfully to prepare dense films for these coatings [132].

Looking more closely at TiO₂ thin film composition, it has been shown that stoichiometry of films depends on deposition temperature and the O partial pressure [133]. Deposited films are usually slightly O deficient with severe consequences for the film properties [134], although this is usually more of an issue in sputtered films due to the nature of reactive and metallic modes. It is also known that Ar ion bombardment of transition metal oxides sputters O until an O deficient surface is obtained [135]. Therefore, sputtering in an Ar only ambient would also result in this O deficiency [136]. The O deficit in films was originally assumed to be the product of O vacancies in the film [137], however, Henderson later showed that the deficit was in fact due to a high proportion of Ti interstitials [138]. The influence of increasing temperature, either during deposition or during a post-annealing process, has been investigated by numerous groups, concluding that an increasing temperature restored the stoichiometry and structure of films [139]. At higher

temperatures, approaching 700 °C, annealing was found to increase the amount of rutile phase in the film [140]. Lower temperatures have been shown to propagate the formation of anatase [141]. The first atomic scale visualisation of TiO₂ was undertaken by Onishi and Iwasawa, where a scanning tunnel microscopy (STM) was used to observe the influence of an O atmosphere on an O deficient surface at 800 K [142]. Conclusions drawn suggested that the O atmosphere enabled the complete re-oxidation of the surface by the annealing of Ti interstitials, where O ad-atoms in the trenches drew interstitials to the surface.

5.2.2 Simulation

To perform any simulations, it is first necessary to define an interatomic potential that describes the terms by which particles will interact. Within the TiO₂ rutile system, many potentials have been proposed to attempt to realistically describe the behaviour during growth, usually based on a stoichiometric system. Formation energies in rutile have also been previously investigated, finding specific barriers for point defect formation [42].

Chapter 2 introduced the need for interatomic potentials in MD simulations and fixed and variable charge potentials applicable to TiO₂ were discussed. In 1996, Collins and Smith investigated 9 Ti-O fixed charge potentials, which modelled the 3 polymorphs of TiO₂. They concluding that most potentials provided poor agreement with experimental results [37], except the Matsui and Akaogi potential and one they had developed. Matsui and Akaogi's potential [34], implemented in 1991, has previously been shown to accurately reproduce bulk properties [35, 143]. The fixed charge nature of the Matsui and Akaogi potential means it deals poorly with locally non-stoichiometric configurations, a huge drawback for the simulation of growth as the configuration will not always be stoichiometric. Surface interaction is also a problem as the fixed charge applies the full bulk charge to the surface, which is clearly not realistic, therefore a variable charge potential is desirable for growth simulation.

Rappé and Goddard, in 1991, proposed a method to allow the variation of charge distribution within a system [39], allowing the introduction of the QEq scheme, a variable charge equilibrating potential. Hallil *et al.*, however, found inaccuracies with the QEq potential. The repulsive potential did not describe defect ener-

gies very well. Therefore, a modification was made whereby a second-moment-Buckingham potential implemented the QEq scheme, creating the SMB-QEq [38]. Vernon recently investigated the reliability of the Hallil *et al.* potential for application to growth simulations. The formation of an O₂ dimer, found to be important during surface growth, was not accurately described. Therefore, an attractive O-O interaction at the surface was added [5]. The Ti-O interaction was also found to require modification in the form of compensation for the covalent energy of the bond. A Ti-Ti interaction was also introduced as a short ranged ZBL interaction [31]. This modified potential (MQEq) form, proposed by Vernon [1,5], is used for the description of TiO₂ systems during this project.

Binding energies and formation energies of point defects have previously been studied by many groups. Sawatari and Iguchi, in 1982, used the shell model to investigate point defects in rutile to attempt to gap the bridge in knowledge and understanding of the nature of defects in rutile [144]. The formation energy of an O vacancy was found to be a lot higher than experimentally predicted, allowing the questioning of the reliability of experimental data. More recently, Cho *et al.* studied the Ti interstitial and O vacancy formation energies using DFT, finding values of 7.09 eV and 4.44 eV [145]. Mulheran *et al.* then used the Hallil *et al.* SMB-QEq potential to investigate the binding energies and specific barriers on the (110) surface, finding that the Ti interstitial binding energy was overestimated in comparison to DFT results [43]. Identifying the problem as excessive charge transfer on O atoms, Mulheran *et al.* fixed the charges on O atoms to match the Ti interstitial binding energy to DFT results. This, however, caused new problems and Ti surface barriers became inaccurate. Most recently, Vernon implemented the MQEq potential to rutile growth, finding that the new form of the potential matched DFT results very well for TiO, TiO₂ and O₂ binding energies [5,42]. Some artefacts were introduced to the interactions such as the instability of TiO units which stood normal to the surface, but overall this potential most accurately described the (110) surface.

Recent studies on the rutile (110) surface investigated specific mechanisms by which rutile growth occurs. Wendt *et al.* investigated the role of interstitial sites on the defect state in the band gap of TiO₂, finding that Ti interstitials near the surface are largely responsible for the defect states [146]. Ti interstitials are an integral artefact of rutile that require annealing for crystalline TiO₂ to form. Vernon *et al.* discovered the important growth mechanism allowing the annealing of Ti intersti-

tials. In the presence of an O rich surface, the energy required for the Ti interstitial to diffuse to the surface was reduced [1]. Also investigated, was the optimum energy for Ti_xO_y particle bombardment for surface growth. Particles arriving with 20 eV were found to produce the most crystalline growth [147]. Sanville *et al.* looked specifically at the surface and diffusion barriers, calculating values for Ti, O, O_2 , TiO and TiO_2 transitions on the rutile surface. DFT and MQEq results were compared, providing barriers between 1.2 eV and 3.5 eV for small cluster transitions and 0.13 eV for O_2 dimer diffusion [42]. Specific studies focused on the deposition processes of TiO_2 have been carried out by Vernon, where Ti_xO_y particles were deposited with energies between 10 eV and 40 eV to simulate the magnetron sputtering process. It was found that, irrespective of the cluster impacting the surface, almost every time a Ti interstitial was formed, usually by the displacement of a surface Ti into an interstitial site [148]. Smith and Möller looked specifically at O bombardment on the TiO_2 surface, finding that energetic O bombardment causes surface erosion [149]. Energies up to 400 eV were simulated, where O atoms saturate the surface and then begin to sputter the surface, causing erosion. Applying this to the deposition process, pure O deposition will etch the surface after the initial oxidisation has occurred.

5.2.3 Modelling the TiO_2 Interactions

During this chapter, we require the description of interactions between many pairs of atoms; Ti-O, Ti-Ti, O-O, Ar-O, Ar-Ti and Ar-Ar. These are required for the single point depositions, high temperature growth and for the otf-KMC simulations as all of these use MD. Chapter 2 introduced MD and the need for interatomic potentials to describe the interaction between atoms. For TiO_2 interactions, a modified version of Hallil *et al.*'s variable charge QEq model by Vernon [1,150] is applied, the SMB-QEq potential. This potential form has been proven to show good agreement with DFT results for transition barriers in rutile (110) [42]. The Ar-Ar interaction is described by a Lennard-Jones simple pair potential [115], whilst a ZBL purely repulsive potential described the Ar-O and Ar-Ti interactions [31].

5.3 Single Point Depositions on the Rutile (110) Surface

Before performing any growth simulations of TiO_2 it is very useful to first perform single point depositions. These provide an initial insight into the behaviour of the surface during impacts at different energies and the typical defects that occur as a result of atomic impacts. Various Ti_xO_y clusters, shown in figure 5.3, were deposited onto the (110) rutile surface at various energies between 20 eV and 100 eV.

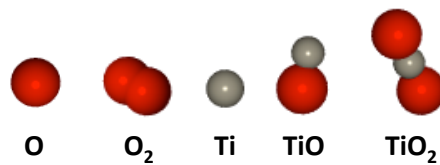


Figure 5.3: The species that are deposited normally to the (110) surface in order to provide initial statistical data on the behaviour of different deposition species.

The substrate used was 8 layers deep, consisting of 1920 atoms. A deep lattice was required for the high energy impacts, which can result in defects deep within the lattice, 8 layers proved to be large enough to contain any defects within the system. In order for results to be statistically correct, species were deposited onto an area of irreducible symmetry on the surface, the unit cell, shown in figure 5.4.

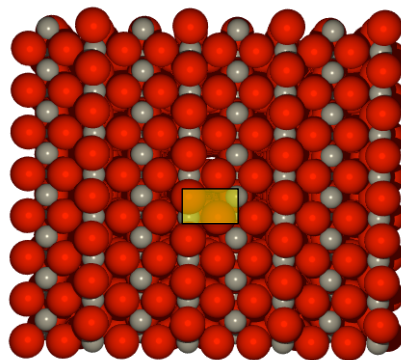


Figure 5.4: The deposition area, the unit cell, is highlighted on the rutile TiO_2 (110) surface. Deposition of all species onto a point in this irreducible area provides statistically meaningful results.

In order to simulate a single point deposition, the chosen deposition species must be initialised above the surface, in this case 7 Å above. Orientation and position are

randomised, as illustrated in figure 5.5. The bottom layer of the lattice was fixed, with a Berendsen thermostat [59] attached to the next two layers to take excess energy out of the system after a deposition, as described in chapter 2. A 60 Å vacuum was added in the y direction to simulate a real vacuum. Once initialised, the cluster is given the desired amount of kinetic energy, such that when MD evolves the time of the system, the cluster will approach the surface and impact on the specified area.

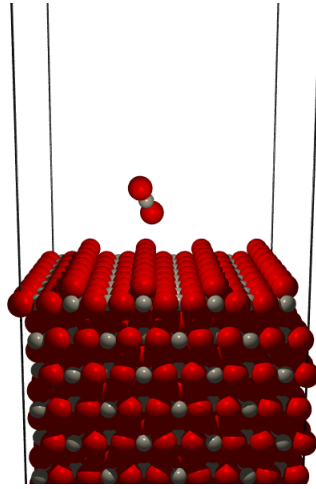


Figure 5.5: The initialisation of a deposition species above the surface before a single point deposition onto the rutile surface.

To explore the effect of varying the deposition energy, 1,000 simulations were performed per deposition species, at deposition energies of 20 eV, 40 eV and 100 eV, totalling 15,000 depositions. This data was analysed, enabling us to further understand how and when defects form and which deposition energy is the most appropriate to use.

5.3.1 Typical Defects

The single point depositions have provided large amounts of data giving information about the typical defects created during an impact. The defects observed include interstitials, vacancies, ad-atoms and reflected or sputtered atoms.

Interstitials

We define an interstitial as an atom which occupies a site in the crystal structure where there is not usually an atom. During the depositions, mainly Ti interstitials are observed, illustrated in figure 5.6. However, we also observe a small number of O interstitials, usually formed from knock on effects of the deposited cluster, illustrated in figure 5.7.

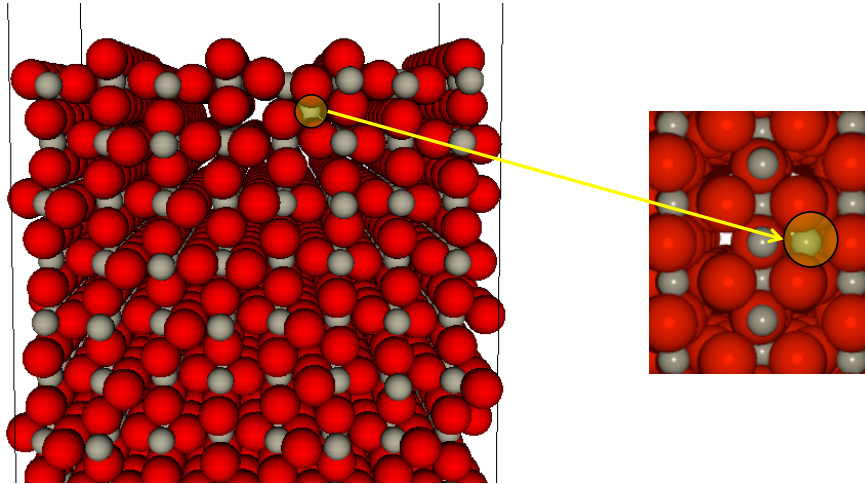


Figure 5.6: A Ti interstitial, commonly formed in the first layer of the rutile TiO₂ lattice, views from the side of the lattice and above are shown.

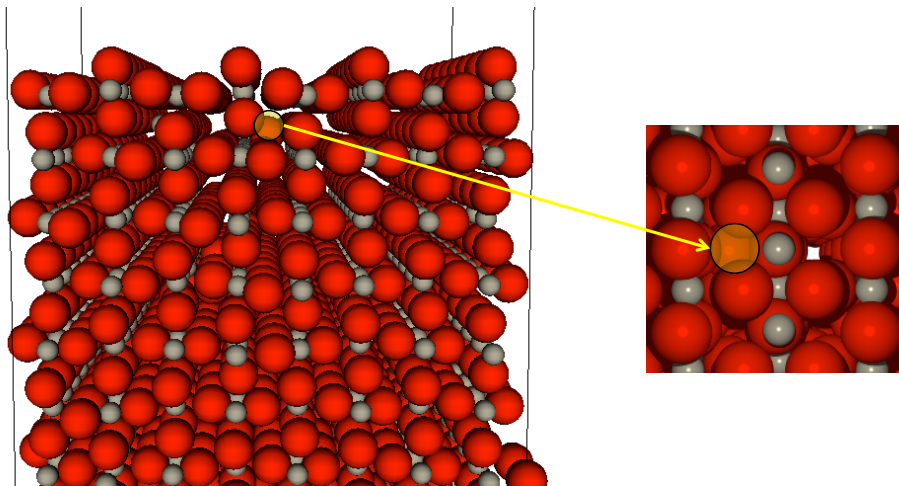


Figure 5.7: An O interstitial formed in the first layer of the rutile TiO₂ lattice.

During single point depositions, the number of interstitials formed is as high as 7 for the higher energy impacts, demonstrating the effect of deposition energy. The interstitials can form as deep as the 7th layer in some cases at 100 eV. Figures 5.8, 5.9, 5.10 and 5.11 illustrate the number of interstitials created during Ti, O, TiO

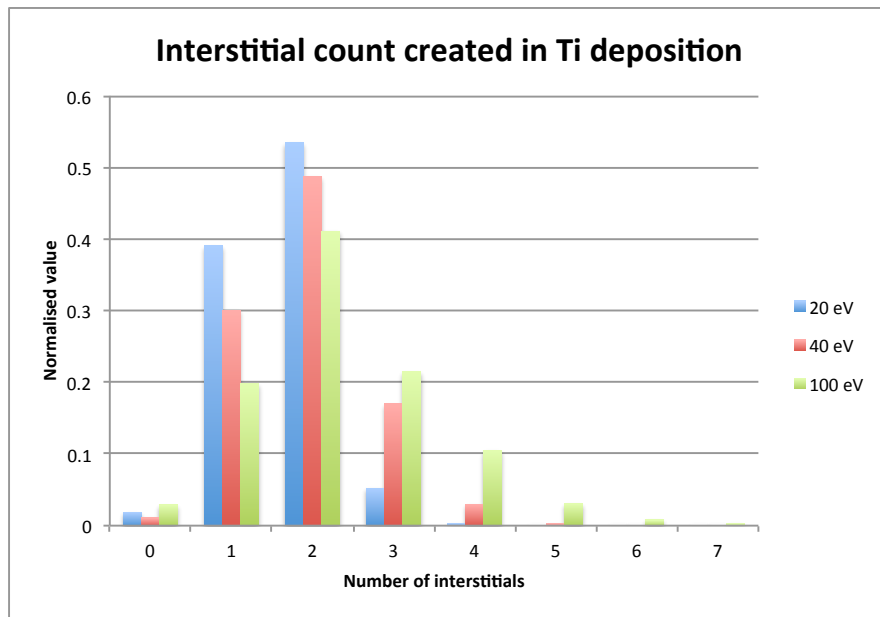


Figure 5.8: The number of interstitials created in the Ti depositions at different energies. 90% of 20 eV depositions produce either 1 or 2 interstitials, similar to 40 eV depositions, although at 100 eV we begin to see around 20% of the cases producing 3 interstitials. 100 eV depositions peak at 2 interstitials, but produce up to 7.

and TiO_2 depositions respectively.

These graphs highlight some important points. When there is either an equal or higher proportion of Ti in the depositing cluster, in most cases between 1 and 3 interstitials are created, depending on the deposition energy (higher energy produces up to 7 interstitials). However, when the proportion of O is either equal to or higher than the proportion of Ti in the cluster, less interstitials are created. Single O depositions at lower energies typically produce no interstitials and at higher energy can produce 1 or 2. A conclusion we can make at this point is that we are more likely to see interstitials being formed when a Ti atom is in the deposition cluster. Figures 5.8 and 5.10 show very similar data for the Ti and TiO depositions, concluding that the O in the deposition cluster plays a very small role.

Figures 5.12, 5.13 and 5.14 show the depth into the lattice reached by interstitials, which as can be as deep as the 7th layer. Ti, O and TiO deposition results are shown and with these we are able to estimate the pattern for the other two deposition species.

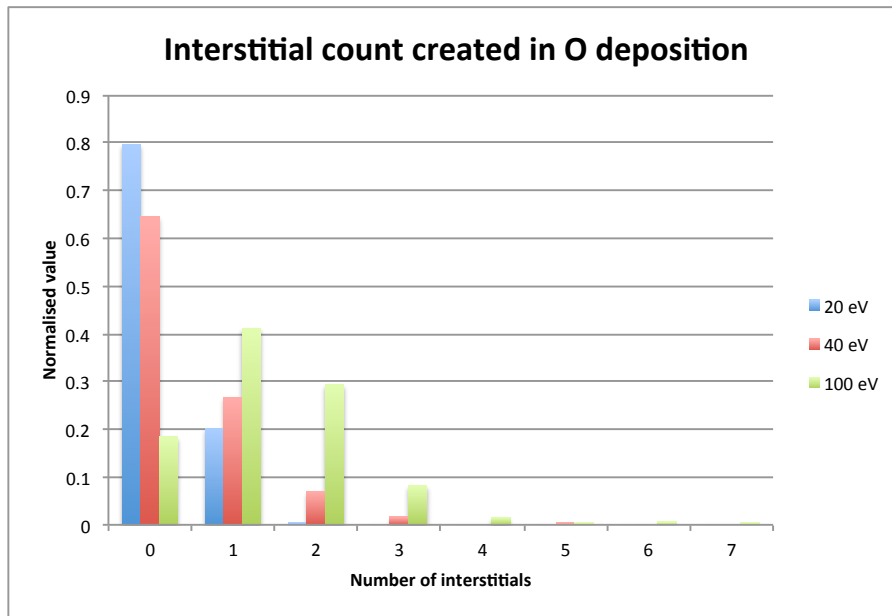


Figure 5.9: The number of interstitials created in the O depositions. At 20 eV and 40 eV, we observe predominantly no interstitials or in around 20% of cases only 1 interstitial. At 100 eV, often 2 or 3 interstitials are created, however, up to 7 are seen. O₂ depositions produce very similar data so we are omitting the graph.

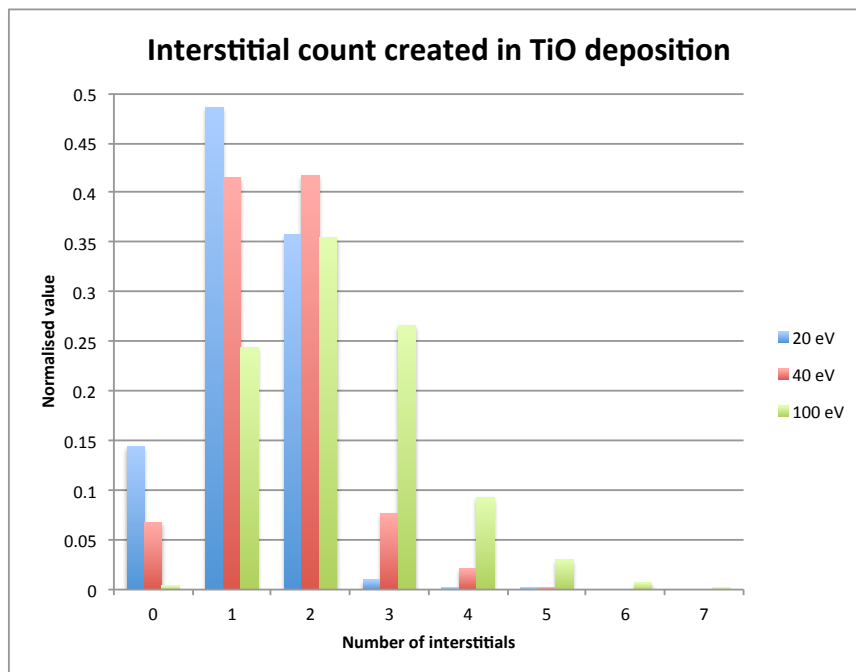


Figure 5.10: The number of interstitials created in the TiO depositions for all three energies. 20 eV depositions more often form either 1 or 2 interstitials and 100 eV depositions are more likely to produce 2 or 3 interstitials. This is due to higher energy depositions disturbing the lattice more, knocking atoms into interstitial locations.

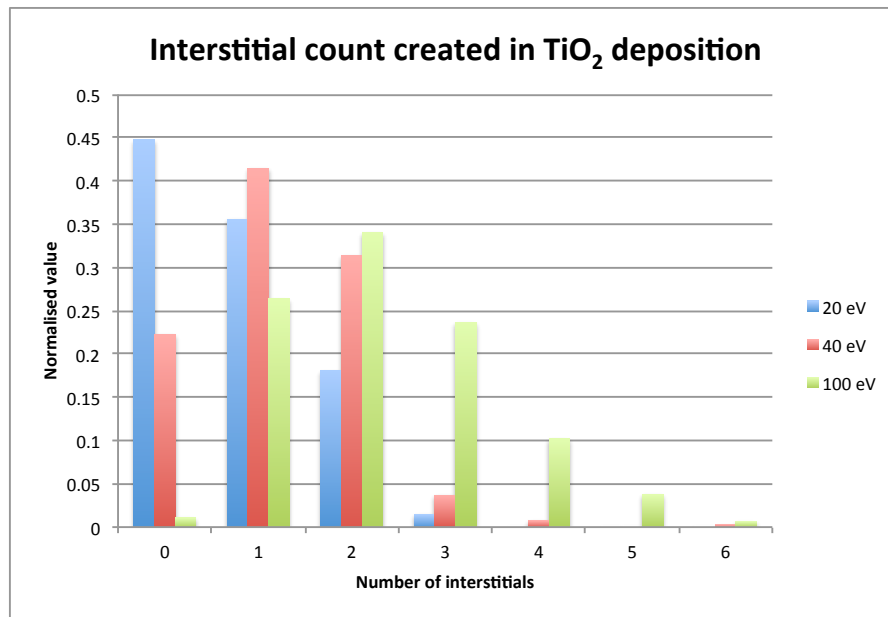


Figure 5.11: The number of interstitials created during TiO₂ depositions. At 20 eV we see predominantly either 0 or 1 interstitial, although up to 3 interstitials are observed. However, at 100 eV, we see a peak at 2 interstitials created, with a maximum of 6.

We can conclude that the impacting cluster plays no major role on the depth reached by the interstitials, rather it is the deposition energy that greatly affects the outcome. Interstitials formed from 20 eV and 40 eV depositions rarely penetrate deeper than the 1st layer, where a layer is described as the area between layers of Ti and one layer is approximately 4 Å deep. However, when using the higher 100 eV deposition energy, we see interstitials are equally as likely to reach the 2nd layer as the 1st and a very small portion reach as deep as the 7th layer.

Vacancies

Vacancies, defined as unoccupied lattice sites, have also been analysed. We observe both O and Ti vacancies and the exact ratios are examined later. Ti vacancies are often created when the 5-fold or 6-fold coordinated Ti is knocked out of its site into an interstitial location, resulting in a vacancy, as illustrated in figure 5.15. O vacancies are created either when an O atom is knocked out of the ad-row on the surface (as in figure 5.16), perhaps by the depositing cluster, or when an O is pulled out of its lattice site, perhaps due to being sputtered.

Figures 5.17, 5.18 and 5.19 illustrate the findings from the O, Ti and TiO₂ single

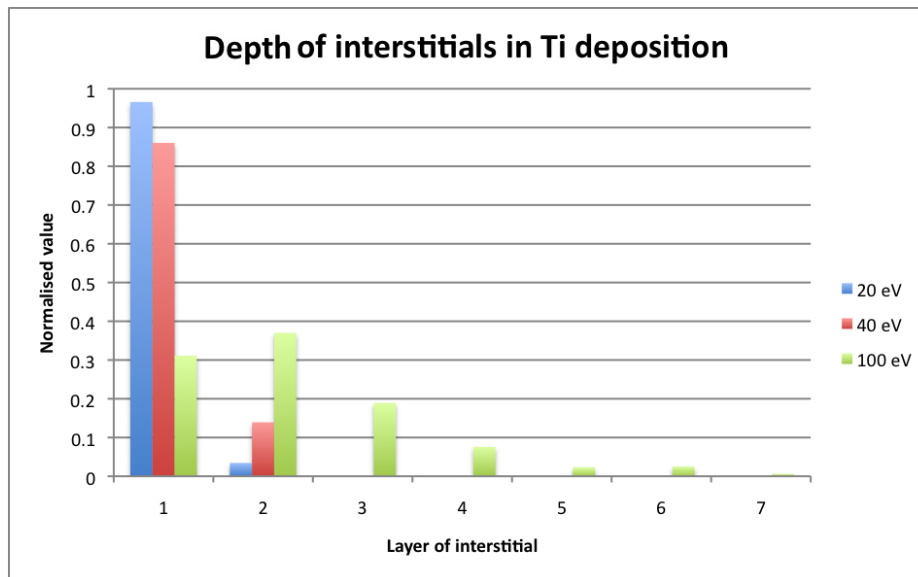


Figure 5.12: The depth of interstitials during Ti depositions. 20 eV and 40 eV are similar, with most interstitials ending up in the 1st layer of the lattice, whilst 100 eV produces interstitials in the top 7 layers of the lattice due to the higher energy deposition allowing atoms to penetrate the lattice with more energy.

depositions at all energies. Single O depositions often create either 0 or 1 vacancies in the lattice at 20 eV, but at 100 eV produce typically 1, 2 or 3 vacancies and up to 16. Ti depositions at 20 eV and 40 eV tend to create also 0 or 1 vacancies, whilst 100 eV more often creates 2 vacancies in the lattice (but up to 10). Finally, the TiO_2 depositions at 20 eV and 40 eV produce more often 0 or 1 vacancies and at 100 eV produce with similar probabilities between 0 and 4 vacancies, but up to 11.

Vacancies created through deposition of O_2 and TiO were also analysed. O_2 is similar to the O deposition case. At 20 eV, in most cases no vacancies were created, but at 100 eV up to 12 vacancies were created. TiO also produces similar results to TiO_2 , 20 eV and 40 eV creating 0 or 1 vacancies, with 100 eV creating more vacancies per deposition (up to 11). We can also analyse the ratio of Ti:O vacancies to predict which is more likely to occur during growth simulations. Figures 5.20, 5.21 and 5.22 illustrate the ratio of Ti to O vacancies during 20 eV, 40 eV and 100 eV depositions.

We can conclude from these ratios that a higher percentage of vacancies created during depositions are Ti and considering the stoichiometric ratio of TiO_2 , this is especially interesting. At 20 eV, we observe the largest ratio of Ti vacancies. Once

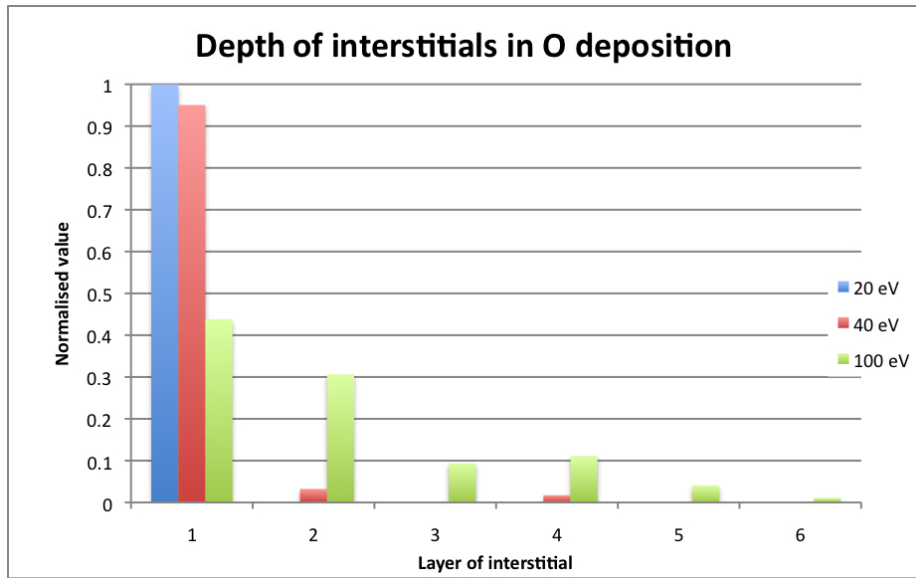


Figure 5.13: The depth of interstitials during O depositions. 20 eV and 40 eV are similar, most interstitials end up in the 1st layer of the lattice. 100 eV, however, allows interstitials to penetrate as deep as the 6th layer but in almost 50% of cases interstitials only reach the 1st layer.

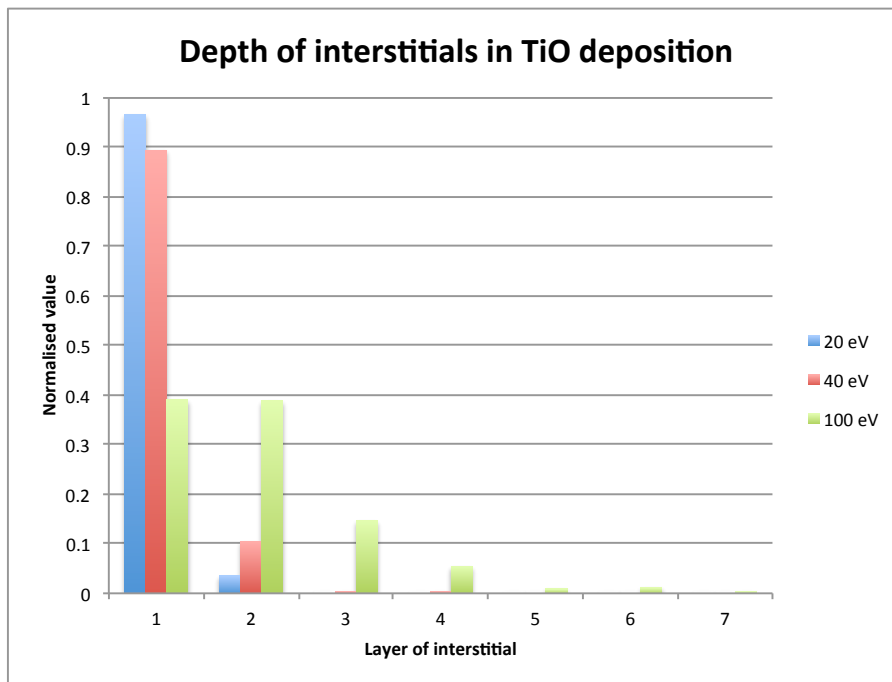
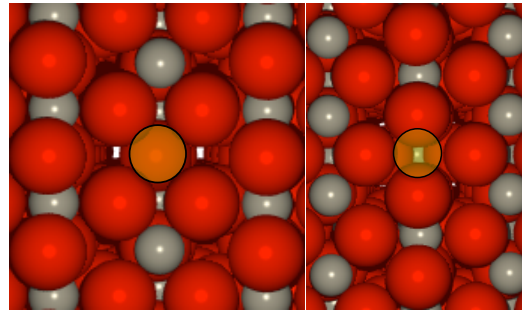


Figure 5.14: The depth of interstitials during TiO depositions. 20 eV and 40 eV allow interstitials to form in the 1st layer of the lattice, with up to 10% forming in the 2nd layer. 100 eV, however, interstitials equally in the 1st and 2nd layers, and as deep as the 7th layer.



(a) 5-fold Ti vacancy. (b) 6-fold Ti vacancy.

Figure 5.15: Two examples of Ti vacancy sites.

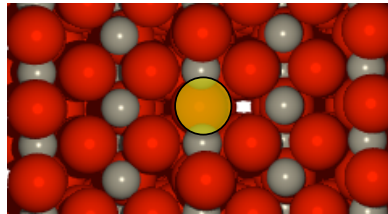


Figure 5.16: An O atom has been knocked out of its position in the surface ad-row creating an O vacancy. This often occurs when a cluster knocks the atom out of its lattice site.

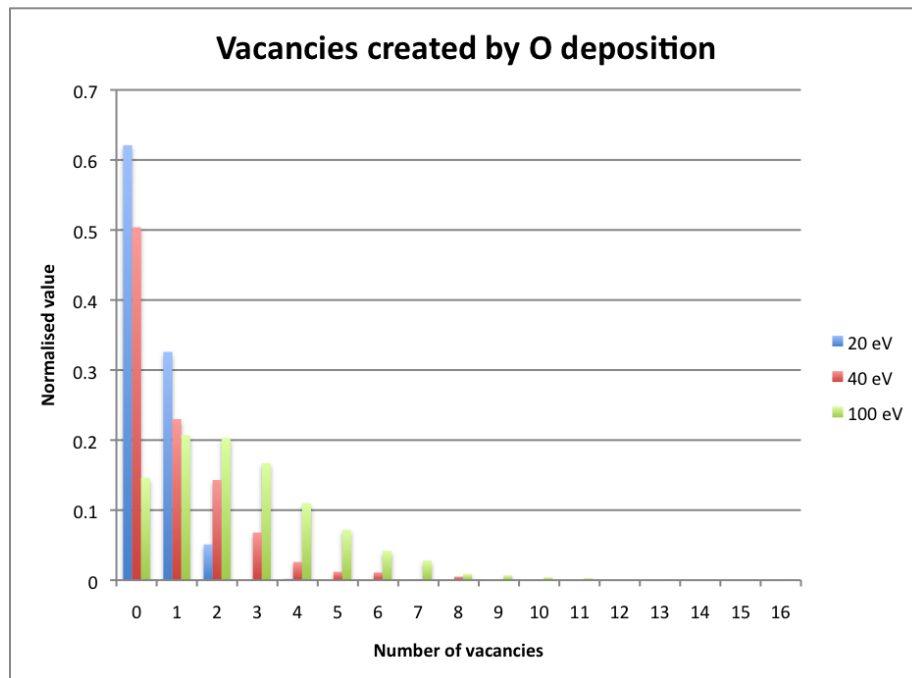


Figure 5.17: The number of vacancies created from O deposition at all energies. More often we see few or no vacancies, but at 100 eV we see up to 16.

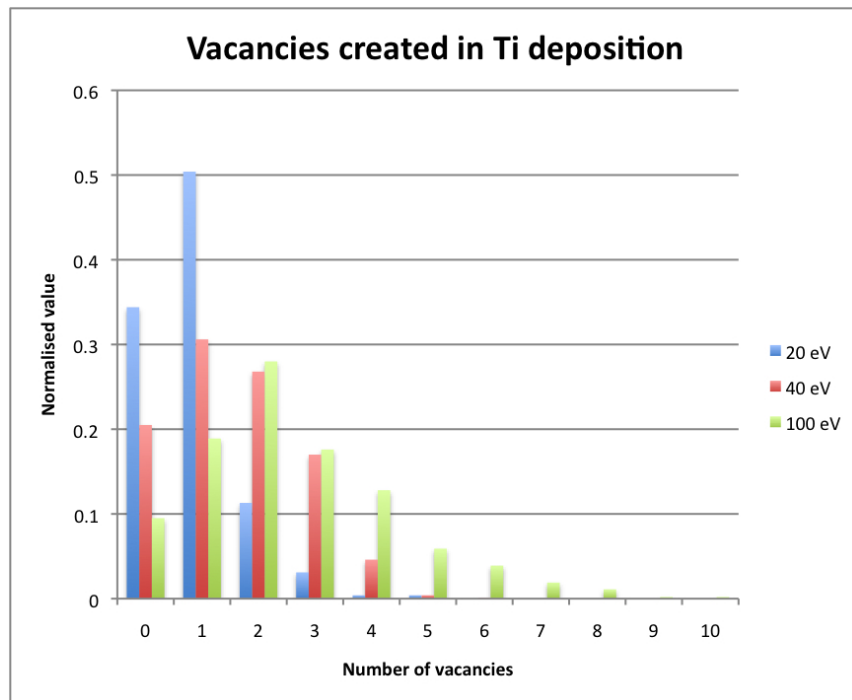


Figure 5.18: The number of vacancies created from Ti deposition. We see a shift for 20 eV depositions, from predominantly 0 vacancies with O depositions, to predominantly 1 vacancy with Ti depositions. At 100 eV, vacancies created peak at 2.

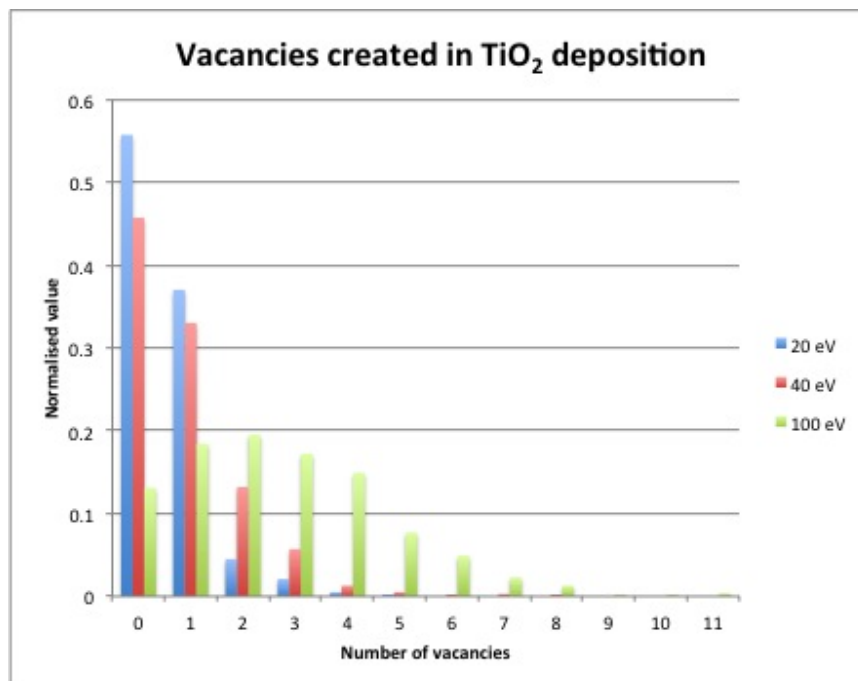


Figure 5.19: The number of vacancies created during the deposition of TiO₂ clusters. At 20 eV and 40 eV predominantly 0 or 1 vacancies are formed and at 100 eV, in 80% of cases, 0 to 4 vacancies are formed.

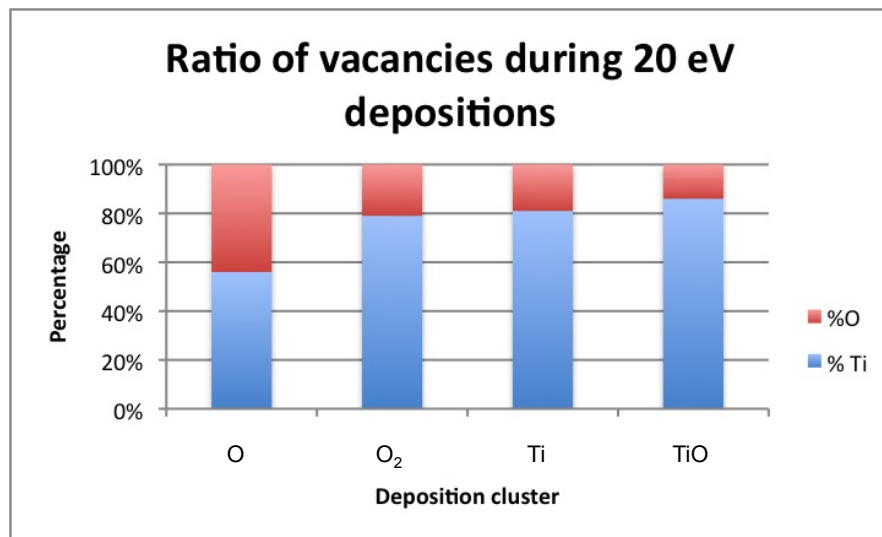


Figure 5.20: Clusters deposited at 20 eV produce a higher percentage of Ti rather than O vacancies, especially when there is a Ti atom within the cluster.

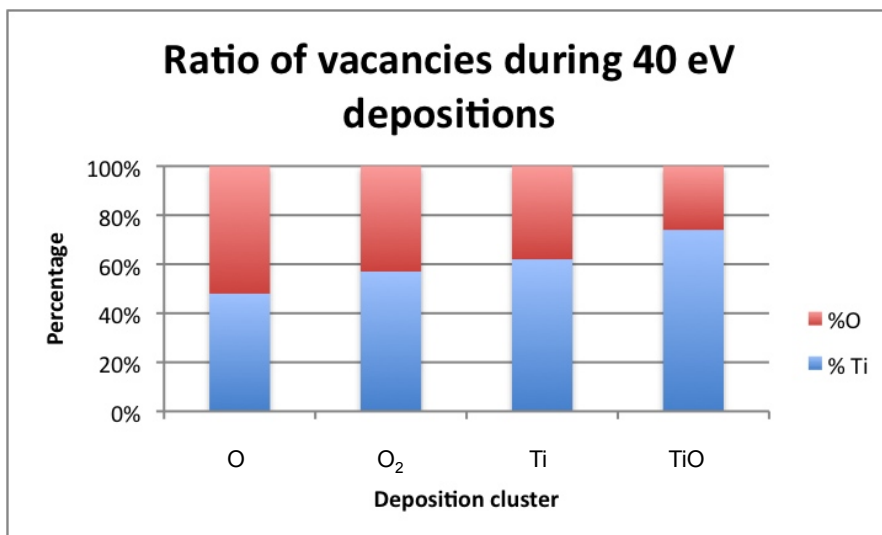


Figure 5.21: Clusters deposited at 40 eV. We observe from O deposition slightly more O vacancies produced, but for the other clusters we again see a higher proportion of Ti vacancies.

we reach 100 eV, regardless of the deposition cluster, we still observe at least a slightly higher portion of Ti vacancies. So it seems that at lower energies we observe the largest difference in Ti to O vacancies and at higher energies the cluster species plays a lesser role and we observe only a small difference between Ti and O vacancies. However, we notice that the deposition cluster can play a small role especially at the lower energies. At 20 eV and 40 eV, it is noticeable that clusters including a Ti atom produce increased Ti vacancies due to the Ti atom knocking

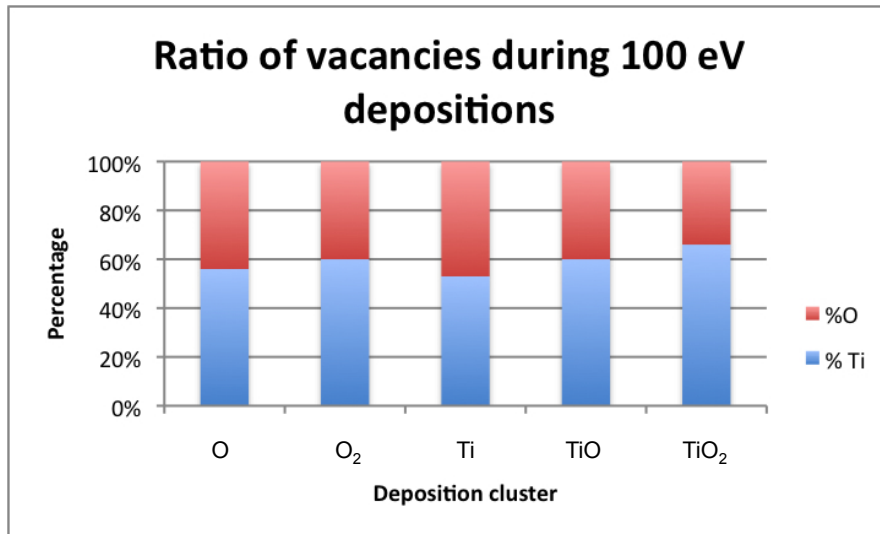


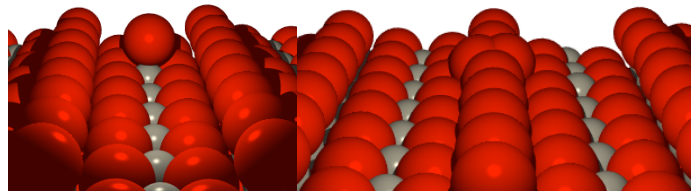
Figure 5.22: Deposition at 100 eV, where we observe for all clusters a slightly higher proportion of Ti vacancies produced. An average of around 58% are Ti.

Ti atoms within the system into interstitial locations producing Ti vacancies. Similarly, the clusters including O atom(s) produce a higher portion of O vacancies than those clusters including no O atoms due to the O atom displacing O from the surface to produce O vacancies.

Ad-atoms

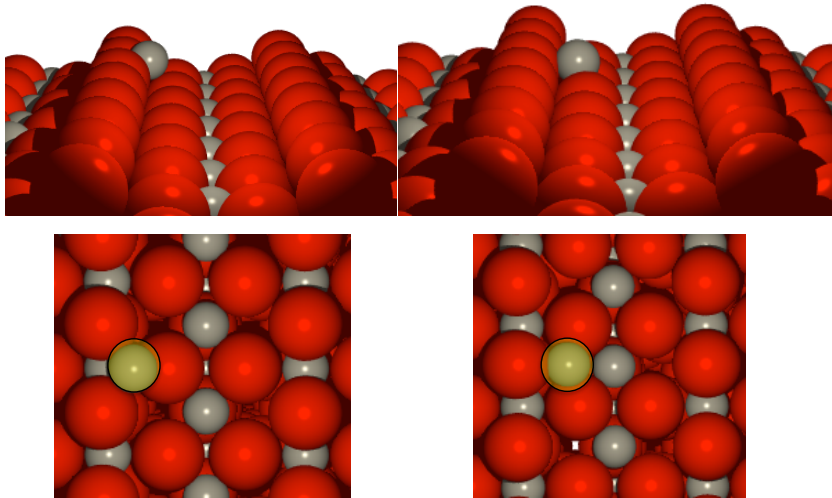
Ad-atoms can be defined as atoms that lie on a surface, in a previously unoccupied site. In our simulation we observe both O and Ti ad-atoms. An O ad-atom is often formed when an O relaxes above the 5-fold coordinated Ti. We also observe split O ad-atoms, illustrated in figure 5.23. A Ti ad-atom forms when the deposited cluster includes a Ti atom and it comes to rest on the surface in one of two positions, shown in figure 5.24.

Our results illustrate that, as expected, the higher the percentage of O in the deposition cluster, the more ad-atoms will be created. Conversely, a higher percentage of Ti in the cluster creates less ad-atoms. This is expected as usually a Ti ad-atom is only formed if it is deposited along with an O atom as O is more favourable to becoming an ad-atom on the surface. This is illustrated in figures 5.25 and 5.26.



(a) O ad-atom on the lattice surface above a 5-fold Ti. (b) O split ad-atom on the surface.

Figure 5.23: O ad-atoms on the surface of a rutile TiO_2 lattice.



(a) Ti ad-atom sitting in the upper hollow site. (b) Ti ad-atom sitting in the lower hollow site.

Figure 5.24: Two Ti ad-atom locations on the rutile surface.

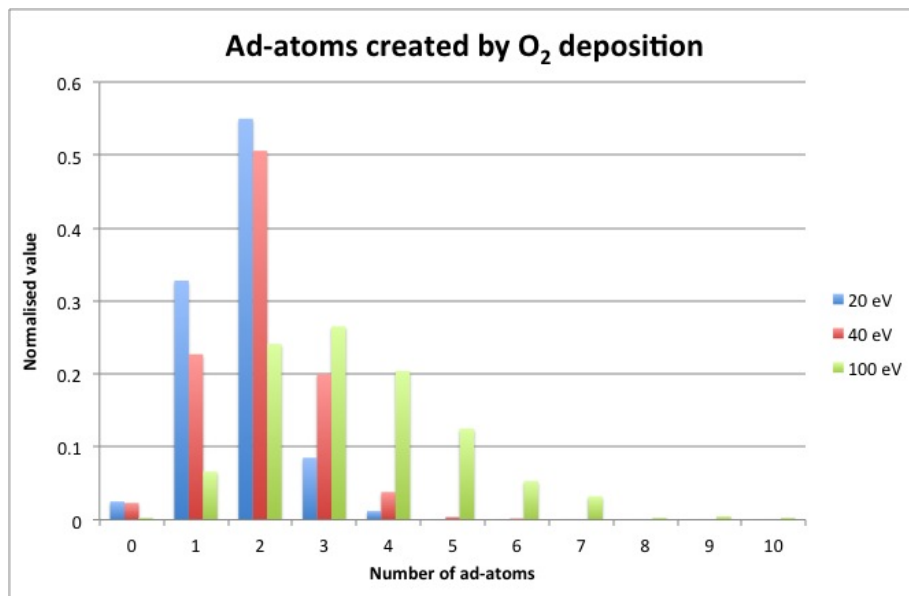


Figure 5.25: Ad-atoms created during O_2 deposition. At 20 eV and 40 eV, it is likely that 2 ad-atoms will be created. At 100 eV, we may see more ad-atoms created due to the higher deposition energy knocking some surface O atoms out of their location and into ad-atom sites.

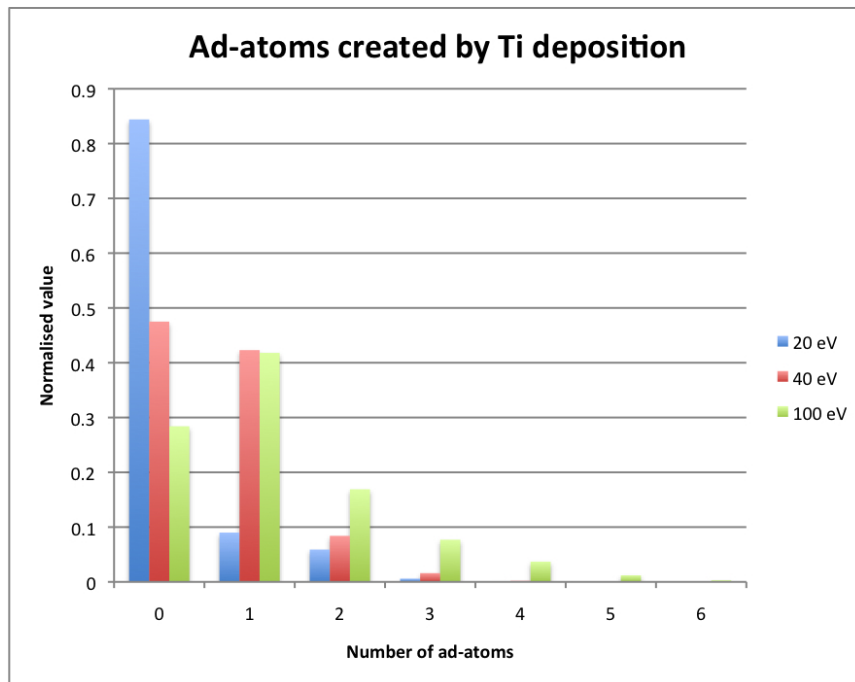


Figure 5.26: Ad-atoms created during Ti deposition. As expected, predominantly no ad-atoms are created at 20 eV. However at 40 eV and 100 eV, we see that a vacancy may be created during the deposition. This is due to the higher energy knocking atoms on the surface out of their locations into ad-atom sites.

Reflected or Sputtered Atoms

The final defects analysed are reflected and sputtered atoms. We observe reflection or sputtering of atoms when either the deposited cluster is directly reflected off the surface or when the deposited cluster displaces other atoms from their lattice sites. We have only observed O atoms leaving the surface, suggesting that O escapes the system more easily than Ti. As the deposition energy increases from 20 eV to 100 eV, we see higher rates of reflected/sputtered atoms, as expected. The figures below illustrate that deposition of clusters containing O atom(s) are more likely to cause atoms to reflect or sputter off the surface. Figure 5.27 shows that deposition of Ti atoms causes only a very small amount of sputtering and only during 100 eV depositions. Whereas figure 5.28 confirms that when O is in the deposition cluster, we observe increased reflected or sputtered atoms (in 20-30% of cases).

Single point depositions have provided interesting and useful insight into the behaviour of TiO₂.

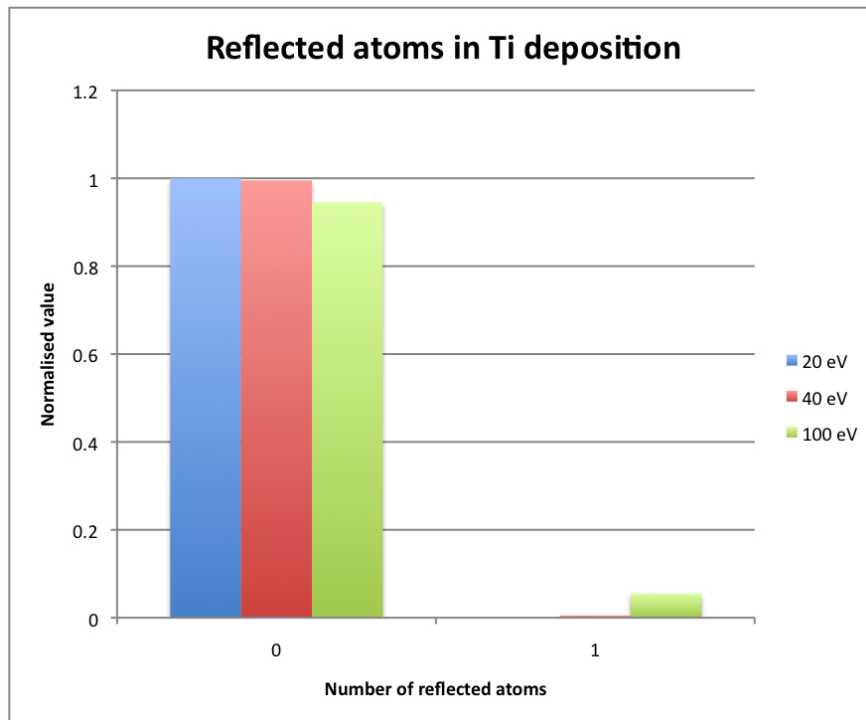


Figure 5.27: During Ti deposition we observe very little sputtering from the surface. It is only when reaching 100 eV that a very small amount of sputtering does occur.

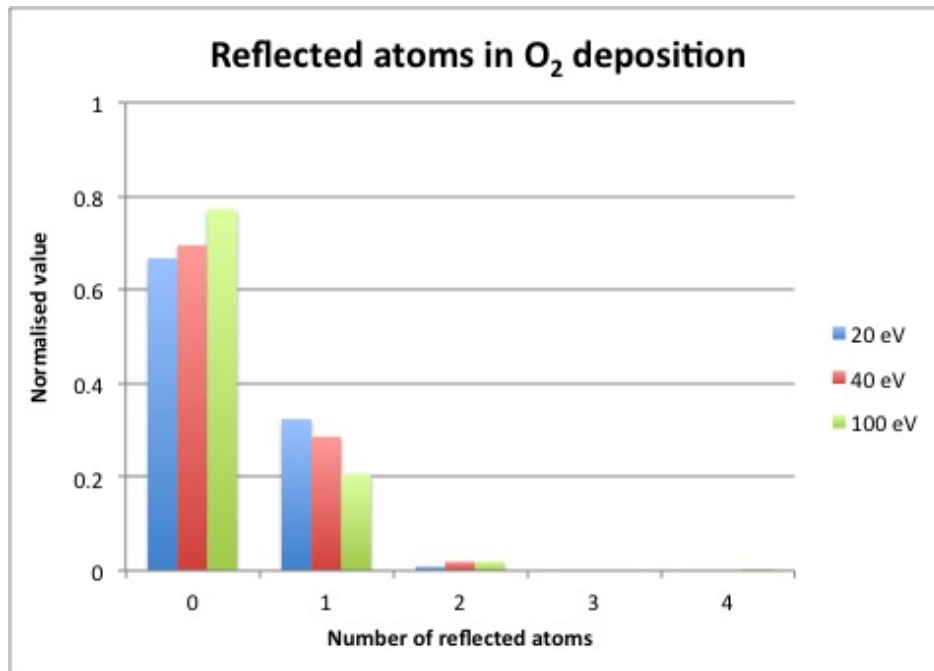


Figure 5.28: During O₂ deposition we observe a higher proportion of reflections/sputtering than during Ti depositions. Up to 30% of depositions have caused 1 atom to leave the surface either by reflection or sputtering. Very rarely, 2 atoms are ejected or reflected.

5.4 High Temperature MD: An Initial Insight into Rutile Growth

Modelling growth with classical MD over realistic time scales is not feasible with present computers. It is therefore necessary to use techniques to accelerate the simulation. In this chapter, two techniques are used, high temperature MD and otf-KMC. High temperature MD has been applied to rutile in order to gain an initial insight into the behaviour during successive depositions. In this case the simulations can be performed locally. Otf-KMC is then applied to rutile growth in such a way that the PVD experimental deposition techniques are simulated and investigated, as previously demonstrated with Ag and Al.

High temperature MD works by increasing the lattice temperature from room temperature (300 K) to 1000 K in order to speed up transitions, therefore increasing surface diffusion and decreasing computational time required. This then allows a proportional increase in the deposition flux rate. Here, we increase the attempt frequency of a target diffusion barrier such that the scaling corresponds to the increase in deposition rate. We have used high temperature MD to grow rutile TiO_2 with deposition energies of 20, 40 and 100 eV, in order to gain an insight into the role of deposition energy during growth. Experimental PVD methods base themselves on deposition energies between 1 eV and 40 eV, however, high temperature MD has been used here to investigate even higher deposition energies to provide a better understanding of the behaviour of rutile. Table 5.1 gives three different distributions of various deposition species which are used, stoichiometric, Ti rich and O rich. The clusters deposited are randomly chosen to maintain as much realism in the simulation as possible. For example, during the industrial process of sputtering, only a random proportion of the TiO_x units become oxidised on route to the substrate.

For the purpose of this research, we concentrate mainly on the stoichiometric distribution as it is closest to what happens in experiment.

5.4.1 20 eV and 40 eV Depositions at 1000 K

For the two lower energy depositions, a substrate containing 432 atoms was found to be suitable. Figure 5.29 illustrates the substrate, which is four layers deep. Pe-

Species	Stoichiometric	Ti rich	O rich
O	0.1	0.1	0.2
O ₂	0.3	0.1	0.15
Ti	0.3	0.2	0.05
TiO	0.1	0.2	0.2
TiO ₂	0.2	0.4	0.4

Table 5.1: The distribution of various deposition species arriving at the rutile surface (shown as a %).

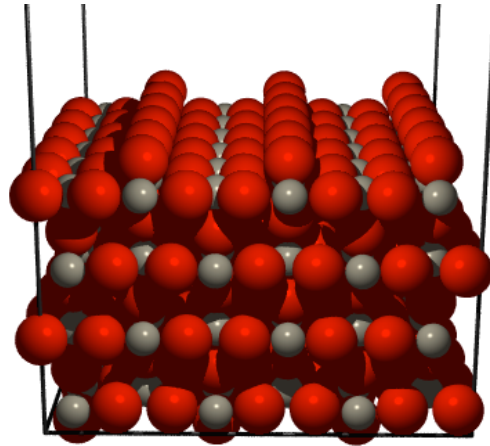


Figure 5.29: The rutile TiO₂ substrate on which 20 eV and 40 eV depositions occur during high temperature growth. The substrate contains 432 atoms in four layers, where 288 atoms are O and 144 are Ti. The lattice is 12 Å deep.

periodic boundary conditions have been applied to the x and z dimensions to allow atoms to wrap around and mimic a bulk. The bottom layer of the lattice is fixed to ensure stability, with a Berendsen thermostat [59] attached to the two layers above the bottom to control the system temperature. To simulate the deposition events, the chosen species is initialised 10 Å above the surface, impacting the surface at normal incidence. Before running MD to simulate the deposition event, the species is given the desired kinetic energy. Unlike the single point depositions, species are given energy according to a normal distribution function, with a standard deviation of one tenth of the deposition energy. For example, a 40 eV deposition will have a standard deviation of 4 eV.

Figures 5.30 and 5.31 illustrate the high temperature growth of TiO₂ at 20 eV and 40 eV respectively. With 20 eV depositions we observe a uniform growth, where two new layers have been almost perfectly formed. No defects are present below the surface. At 40 eV we still observe a uniform growth, however, we begin

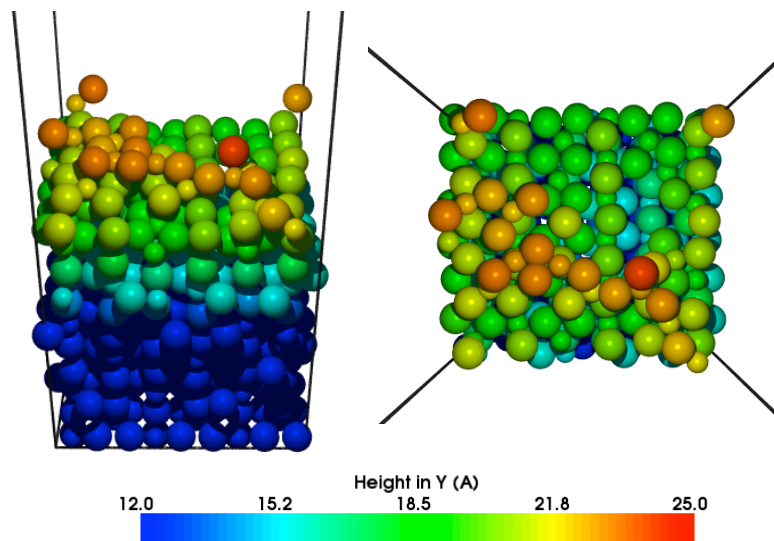


Figure 5.30: TiO_2 growth at 1000 K, where a random mix of clusters arrive at the substrate with 20 eV. Using a small lattice, we see that after 135 successive depositions (252 atoms added), we have some uniform growth. Two complete layers have been successfully formed and no interstitials or defects are present below the surface.

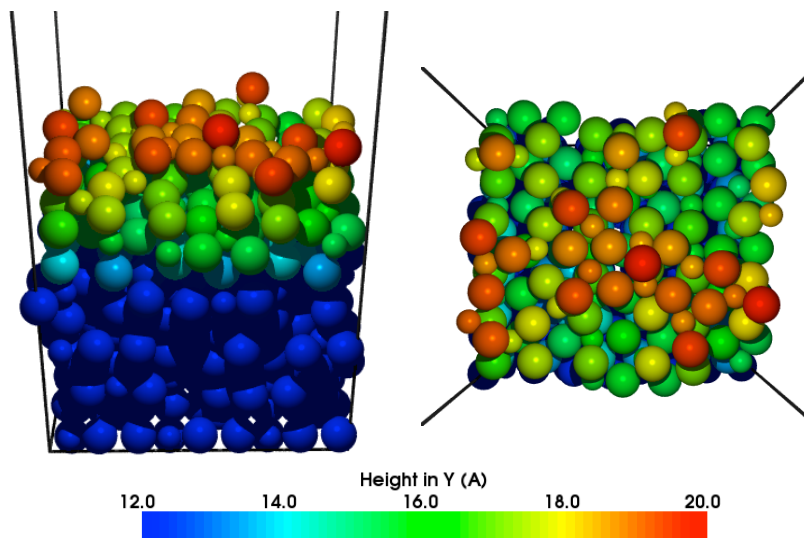


Figure 5.31: TiO_2 growth at 1000 K where a random mix of clusters arrive at the substrate with 40 eV. After 100 depositions, 177 atoms have been added. As with the 20 eV growth, we see uniform growth, however, more defects exist below the surface.

to see defects below the surface with occasional Ti interstitials in the 2nd and 3rd layers, 5 Ti interstitials in the 1st layer, plus interstitials in the newly formed layers.

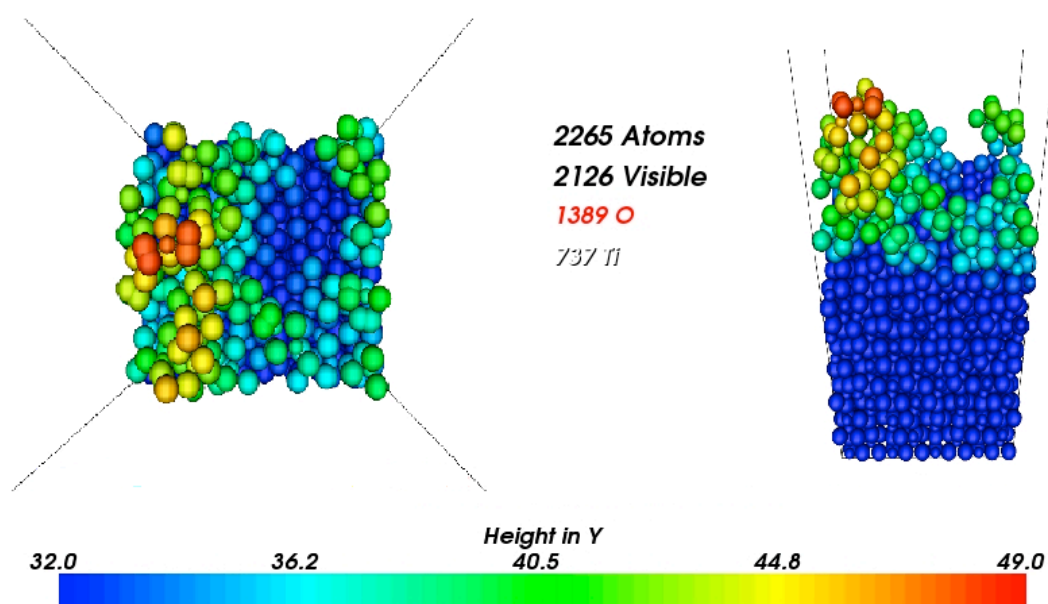


Figure 5.32: TiO_2 growth at 1000 K, with 100 eV depositions of a stoichiometric distribution of ad-units. The lattice started with 1920 atoms, illustrated here is the growth after 185 successive depositions (345 atoms have been added to the system). We observe a highly defective growth, with many voids due to sputtering of atoms and a high portion of Ti interstitials.

5.4.2 Higher Energies

High temperature MD enables simulations to complete quicker than with other methods, therefore providing excellent opportunity to investigate the effect of higher energy depositions which would, with traditional MD, be totally unfeasible. Due to the higher impact energy, a deeper substrate is used (1920 atoms) and the MD stage lasts longer in order to allow the thermostat to remove all the excess heat from the system. Identical procedures to those for the lower energies are used otherwise. Figure 5.32 illustrates how TiO_2 growth at 1000 K with high energy 100 eV depositions produces a highly defective growth. We observe a high portion of Ti interstitials both below the surface and in the newly deposited material. Voids are also observed where perhaps the high energy depositions have damaged the surface, sputtering atoms from the surface (here 149 atoms have been sputtered or reflected off the surface). An advantage of this type of growth may, however, lie in the porous growth, useful for dye sensitised solar cells.

The resulting films from a stoichiometric distribution of deposition species are illustrated in figure 5.33, where the black line shows the original surface before any

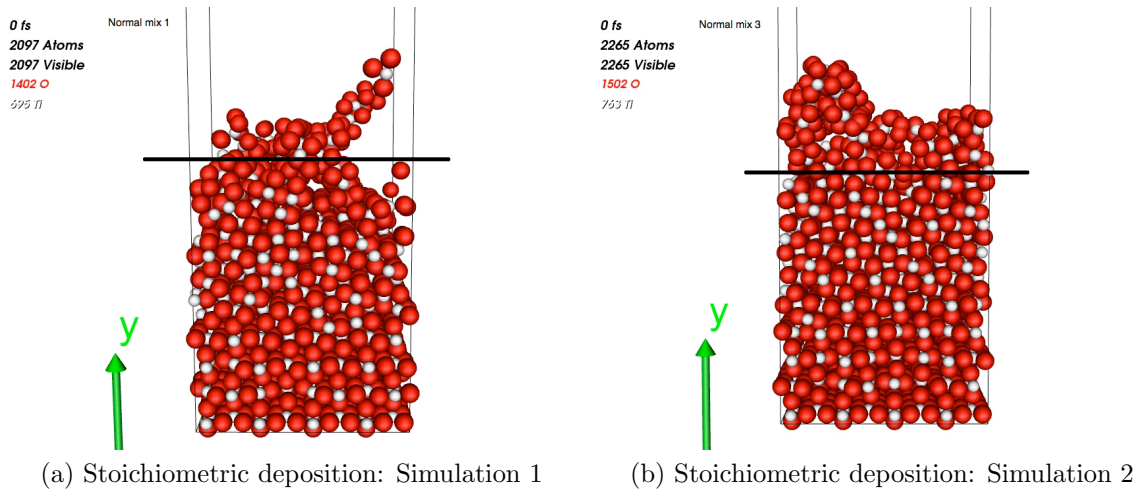


Figure 5.33: The growth resulting from the stoichiometric deposition of TiO_2 onto a rutile TiO_2 surface.

growth. It can be seen that both simulations, using the same stoichiometric deposition distribution, have grown rather differently. Simulation 1 has formed a string coming from the surface and some of the material has eroded from the surface. Voids have formed throughout the system and the whole lattice has become very rich in Ti interstitials.

Growth produced from Ti rich distributions of deposition species are compared in figure 5.34. The two identical simulations show that using identical distributions of deposition species does not necessarily mean that simulations will produce the same growth patterns. Both simulations have, however, produced a huge number of Ti interstitials throughout the lattice and formed voids.

Growth produced from O rich distributions of deposition species are compared in figure 5.35. In both simulations, we can see that the patterns of growth are varied and again many voids are observed. The lattice is also rich in Ti interstitials.

5.4.3 Drawbacks of High Temperature Growth

Some problems do, however, arise when growing oxides at an elevated temperature. Due to the rate of deposition being far too high when MD is used, the temperature is increased so as to rebalance diffusion and deposition rates. However, results are skewed due to transitions being selected with different probabilities than would be

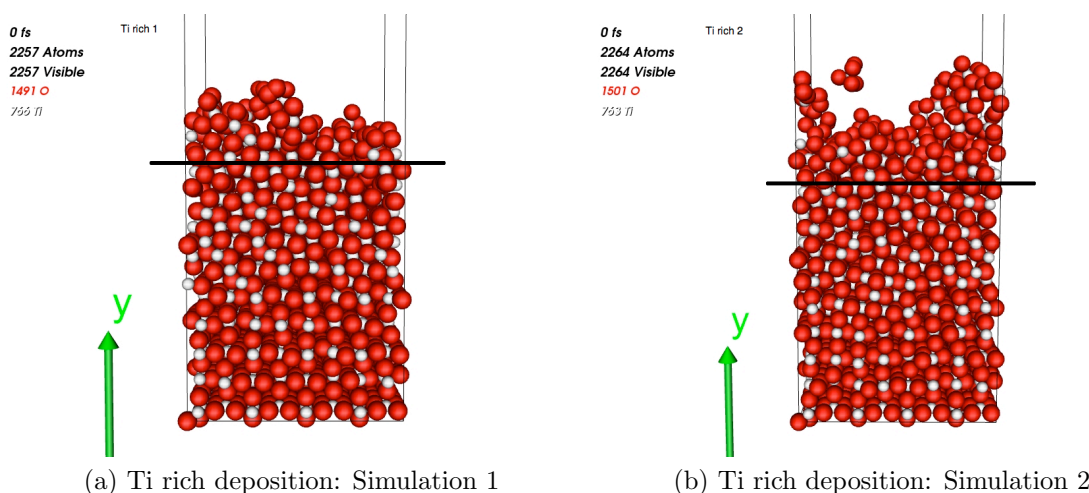


Figure 5.34: The growth resulting from Ti rich distributions of deposition species onto a rutile TiO_2 surface.

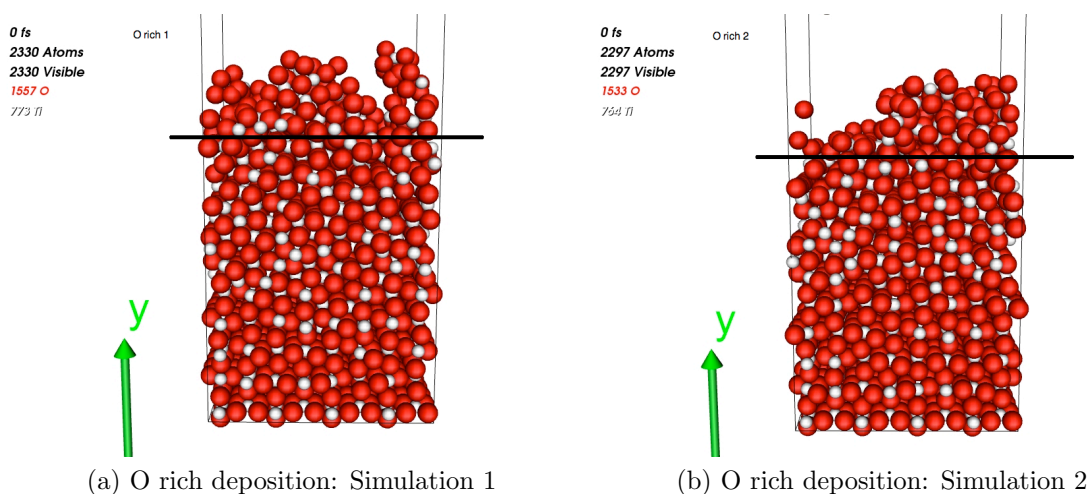


Figure 5.35: The growth resulting from O rich distributions of deposition species onto a rutile TiO_2 surface.

the case at lower temperature. Due to the system being heated to such a high temperature, we also found that the simulations took a long time to run as we had to allow enough time for the system to cool down between steps. When performing the 100 eV high energy growth, this cooling down time became even longer as the depositions heated the system up further.

5.5 Otf-KMC: Depositions on the Rutile (110) Surface

Otf-KMC is an alternative method used for accelerating atomistic simulations without the need for elevated temperature. A relatively novel long time scale dynamics (LTSD) technique, otf-KMC, requires the implementation of saddle point searches followed by the use of a barrier calculating method to calculate exact barriers. The LTSD method is further described in chapter 3, MD and otf-KMC are combined to simulate atomic depositions and the surface diffusion occurring between depositions. Here, otf-KMC has been used to simulate rutile TiO_2 growth at 350 K, a realistic deposition temperature.

In order to carry out otf-KMC simulations, interatomic potentials are required. The same are used here as for the high temperature MD simulations. The substrate, a rutile (110) TiO_2 lattice, begins with 1536 atoms, split into 6 layers of 256 atoms per layer. Periodic boundary conditions have been applied to the x and z dimensions to allow atoms to wrap around and mimic a bulk. The bottom layer of the lattice is fixed to ensure stability, with a Berendsen thermostat [59] attached to the two layers above the bottom to control the system temperature. To simulate the deposition event, the chosen species is initialised some 10 Å above the surface with random x and z coordinates, impacting the surface at normal incidence. Before running MD to simulate the deposition event, the species is given kinetic energy. For example, when evaporation deposition is simulated, atoms are assumed to arrive with < 1 eV, whereas during sputtering the energy is much higher at ~ 40 eV. As with the high temperature growth, species are given energy according to a normal distribution function, with a standard deviation of one tenth of the deposition energy. Once the deposition species has been initialised with a direction and kinetic energy, MD is used to evolve the system, allowing the deposition species to impact the surface at normal incidence. MD runs for between 4 and 10 ps, depending upon the deposition energy. The lower arrival energy of deposition species requires less MD time due to the impacts dissipating less energy into the lattice.

After a deposition, the system is relaxed using a conjugate gradient minimiser. The otf-KMC method then requires the employment of transition searches on the surface using the RAT and NEB methods described in chapter 3. The deposition

event requires a “rate”, which is entered into the KMC roulette as a deposition frequency. Experimental thin film growth of TiO_2 typically grows at rates of around half a monolayer per second and we assume a frequency of 50 Hz for the deposition of atoms as this will provide growth of close to this rate. Just as important as deposition rate is the substrate temperature, which during evaporation and magnetron sputtering, can be altered. During these simulations, higher temperatures require more KMC time. Therefore, 350 K is chosen as a suitable temperature, reasonable also from an experimental view point. The Berendsen thermostat ensures that the temperature remains constant throughout the simulations. The following simulations deposit four monolayers of atoms, simulating up to 9 seconds of real time, totally inaccessible using traditional MD. Here, MD and off-KMC combine to simulate thin film growth, working over 48 cpu cores.

In this section, eight long time scale dynamics simulations have been completed. The main aim of the simulations is to predict and understand the growth resulting from the PVD methods described in chapter 1. However, other deposition energies have been simulated in order to gain a more precise understanding of the behaviour of TiO_2 during bombardment and growth. During all the simulations, TiO_2 is deposited stoichiometrically (refer to table 5.1), to attempt to recreate the most realistic experimental environment. Due to the high computing cost of running the simulations, we have not been able to recreate the O rich or the O deficient conditions.

5.5.1 Modelling Specific PVD Methods: Evaporation Deposition

Four monolayers of atoms have been deposited, simulating the evaporation process where deposition species arrive at the substrate with low kinetic energy <1 eV. Figure 5.36 shows the growth from evaporation deposition without any ion-beam assist. New layers are incomplete, with both O and Ti atoms missing. The original substrate on which the depositions take place retains its completeness. Table 5.2 shows the variation in the number of O and Ti atoms from a complete layer, the original surface has gained Ti atoms in the form of interstitials. Four monolayers worth of atoms have been deposited, but due to the new layers not forming completely, the new growth actually covers six new layers. Analysis of the first three of these new layers has been included in table 5.2, a steady state has not yet been

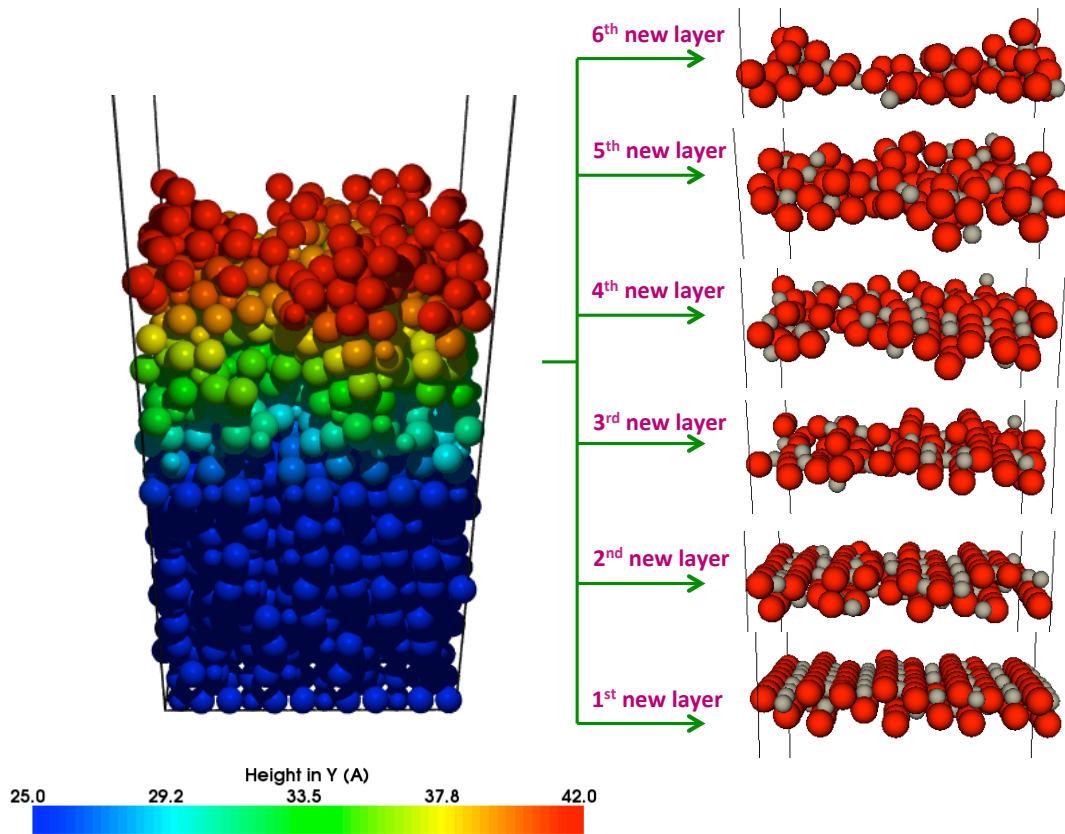


Figure 5.36: The resulting growth of rutile TiO_2 after 1 eV depositions, simulating 5.8 seconds of evaporation deposition. The entire lattice is shown, with a breakdown of the newly deposited layers. Atoms are either coloured by height using the key or using the original Ti and O colour scheme. Layers are incomplete as atoms do not have sufficient kinetic energy to mix efficiently during the ballistic phase of the deposition.

reached on the others and clearly all the new layers are highly incomplete. The low kinetic energy of the arriving atoms does not transfer sufficient energy during the ballistic phase for much diffusion to occur, therefore leaving the layers incomplete with poor crystallinity.

	4th deep	3rd deep	2nd deep	Original surface	1st new	2nd new	3rd new
O	0	0	0	0	-3	-9	-42
Ti	0	0	0	+2	-4	-9	-27

Table 5.2: The variation in O and Ti atoms in specific layers of the lattice deposition by evaporation. The 4th layer of the original substrate and up to the 3rd newly deposited layer are shown. The original substrate has a slight Ti excess, in the form of interstitials, whilst in new layers a deficit is observed for both O and Ti.

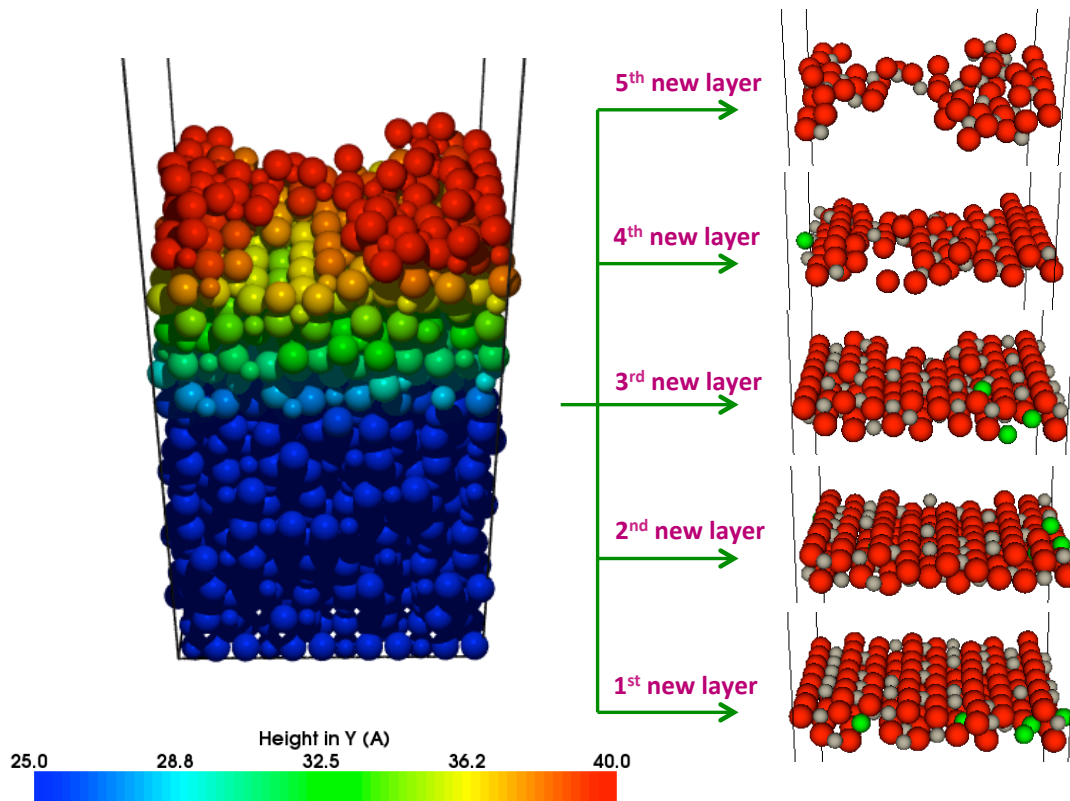


Figure 5.37: The growth of TiO_2 with an ion-beam assist, where Ar bombarded the surface with 40 eV. 6.2 seconds of real time are simulated. The Ar impacts supplied extra energy to the surface, promoting mixing and diffusion, thus enabling a slightly more crystalline surface to form. Ar atoms implanted within the lattice are coloured in green, implantation occurs down to the 2nd layer deep of the original substrate.

5.5.2 Modelling Specific PVD Methods: Ion-Beam Assisted Evaporation

As described in chapter 1, evaporation is often assisted by an ion-beam (usually Ar). Two variations of ion-beam assist are simulated, low energy and high energy assist, where Ar bombarded the surface with either 40 eV or 100 eV, respectively. There was equal probability that either a Ti_xO_y cluster or Ar atom would impact upon the surface. Figures 5.37 and 5.38 show the effects of the low and high energy ion-beam assist on the evaporation growth.

It is clear that the low energy ion-beam assist, where Ar arrives with 40 eV, improves crystallinity, however, does not have a hugely significant effect on the growth. Layers may be slightly more crystalline than without Ar as the Ar bombardment introduces more energy into the system, thus allowing slightly more mixing to oc-

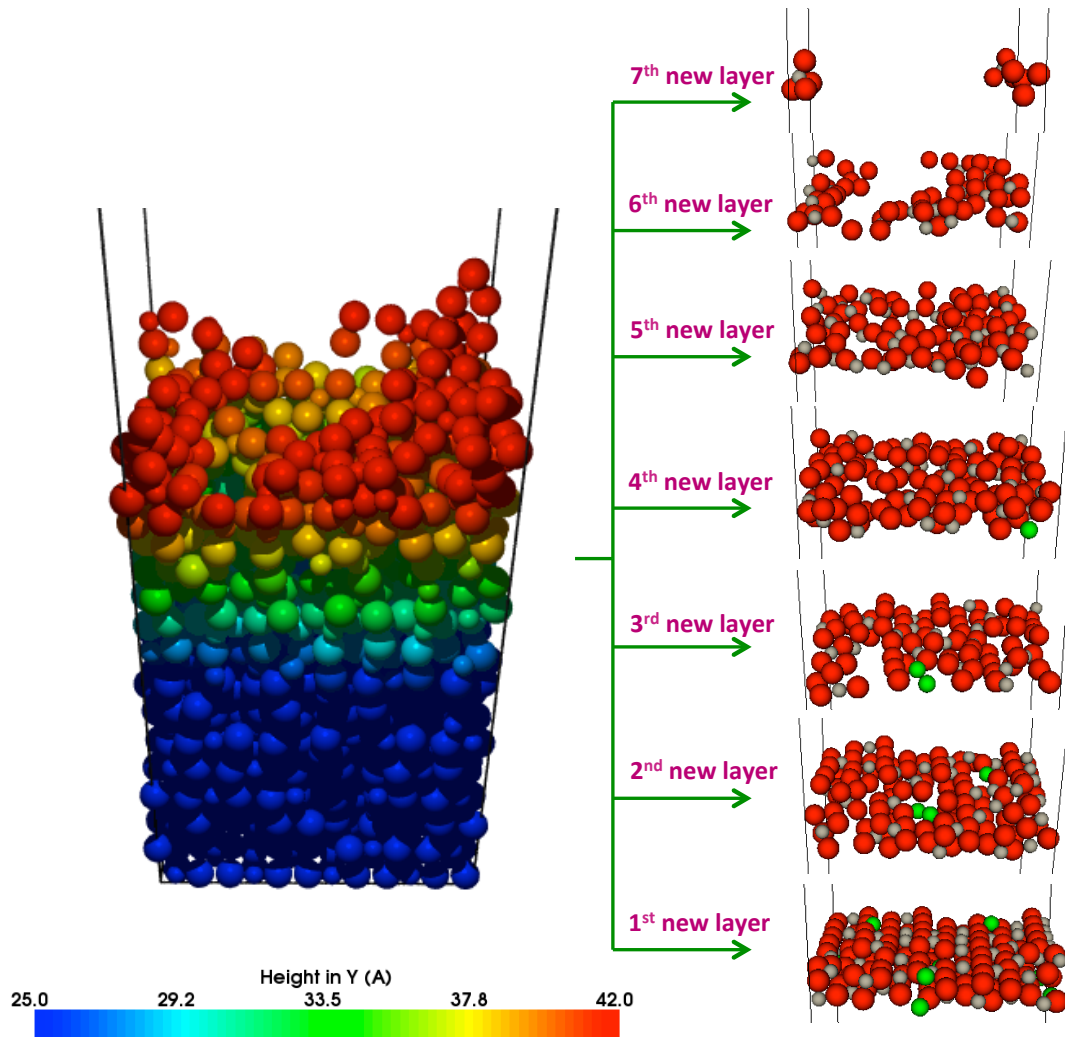


Figure 5.38: The growth of TiO_2 with an ion-beam assist, where Ar bombarded the surface with 100 eV. 5.2 seconds of real time are simulated. The higher energy of the ion-beam caused increased damage to the film, leading to a loss of crystallinity and the formation of voids. Ar now implants as deep as the 4th layer of the original substrate.

cur during the ballistic phase, allowing a more crystalline structure to form over time. Conversely, the higher energy ion-beam assist (100 eV) introduced too much energy into the system, causing damage to the surface and hence disrupting the crystallinity whilst appearing to densify the film. At 100 eV, there is implantation of Ar deep into the lattice. From the experimental results, we expected to see that ion-beam assist would improve film density, however, from our calculations an increased density cannot be definitely concluded as growth has not yet reached a steady state.

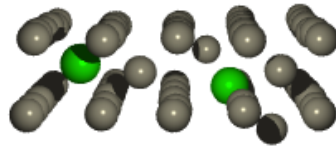


Figure 5.39: The Ti sub-lattice after Ar bombardment. Ti atoms are grey and Ar atoms are green. Ar in the lattice sits in one of two sites, either in an interstitial location between Ti layers or as a substitutional defect.

Figure 5.39 shows the positions of Ar within the lattice. We see that Ar preferentially sits in one of two locations, either in an interstitial location between Ti layers, or as a substitutional atom in a Ti lattice site after knocking the original Ti into a deeper interstitial site. Important here is the impact of Ar on the number of Ti interstitials and their penetration depth. The higher energy Ar assist creates more Ti interstitials, deeper within the lattice. It has previously been found that the presence of Ti interstitials below an O rich surface allows an important rutile growth mechanism to occur through the migration of Ti interstitials up to the surface [146,147]. This growth mechanism is observed throughout all the simulations. However, Ti interstitials deep within the lattice require more time to diffuse upwards and thus often remain stuck in the lattice.

5.5.3 Modelling Specific PVD Methods: Sputter Deposition

Four monolayers of atoms have been deposited by simulating magnetron sputtering where species arrive at the surface with ~ 40 eV. During sputtering, it is, however, possible to bias the substrate in order to increase the deposition energy. Deposition energies of up to 100 eV were simulated and are presented later. However, it was found that 100 eV produces too much lattice damage, giving a very incomplete and porous film where Ti interstitials penetrate as deep as the 4th layer of the substrate (which is too deep for the rutile growth mechanism to work). This would change the optical properties of the film. For this reason it is the 40 eV case that is investigated here as a direct simulation of sputter deposition. Figure 5.40 shows the resulting growth from the sputter deposition of TiO_2 , ignoring the effect of simultaneous Ar bombardment. Layers are much more complete and crystalline than the previous evaporation simulations. The increased deposition energy allows atoms to diffuse on the surface between depositions into correct lattice sites. Table

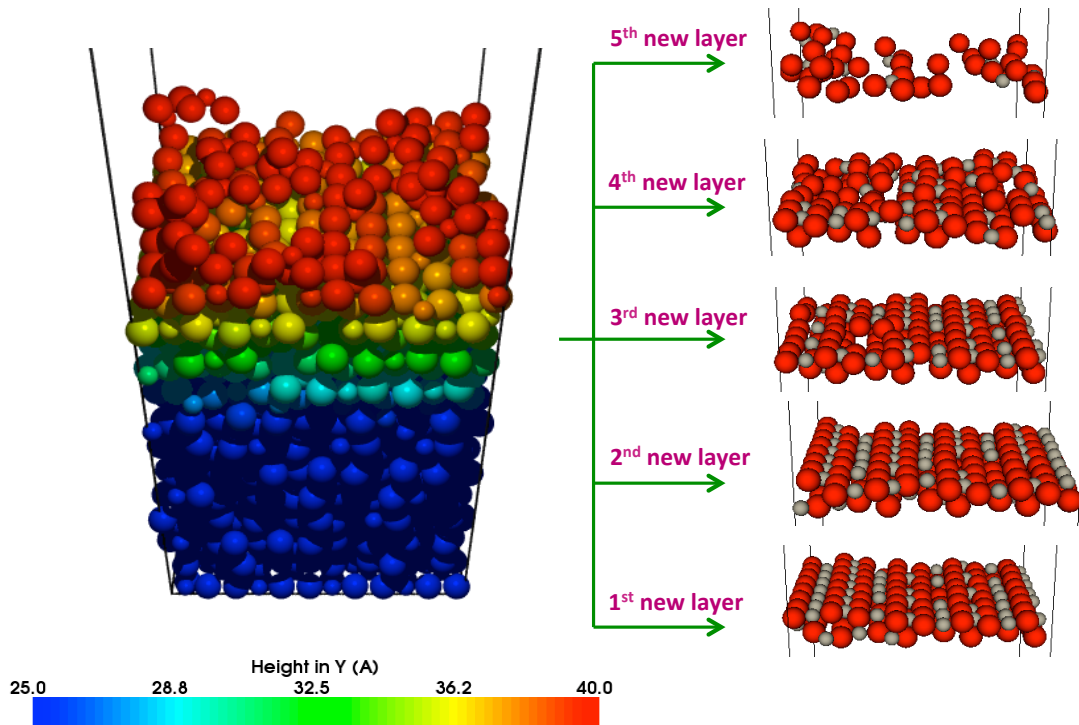


Figure 5.40: The resulting growth obtained from the simulation of magnetron sputter deposition where the effect of Ar is ignored. 5.3 seconds of real time are simulated. Layers are much more complete and crystalline than those obtained from evaporation deposition simulations. Ti interstitials are still evident throughout the layers, but the 1st and 2nd new layers especially are crystalline, missing only some Ti atoms from crystal sites.

5.3 shows the excess/deficits of O and Ti atoms in various layers of the lattice. Comparing this to the results of evaporation growth it is very clear that layers are more complete.

	4th deep	3rd deep	2nd deep	Original surface	1st new	2nd new	3rd new
O	0	0	0	0	0	0	-2
Ti	0	0	0	+12	+6	+3	-8

Table 5.3: The variation in O and Ti atoms in specific layers of the lattice after sputter growth, showing O and Ti excess and deficits. The 4th layer deep into the original substrate, up to the 3rd newly deposited layer, are shown. Further new layers are not included due to not yet having reached steady states.

As described in chapter 1, during sputter deposition, Ar in the plasma simultaneously bombards the substrate. We simulated this by giving equal probability for the deposition of a TiO_2 cluster or an Ar atom. In the case of an Ar impact,

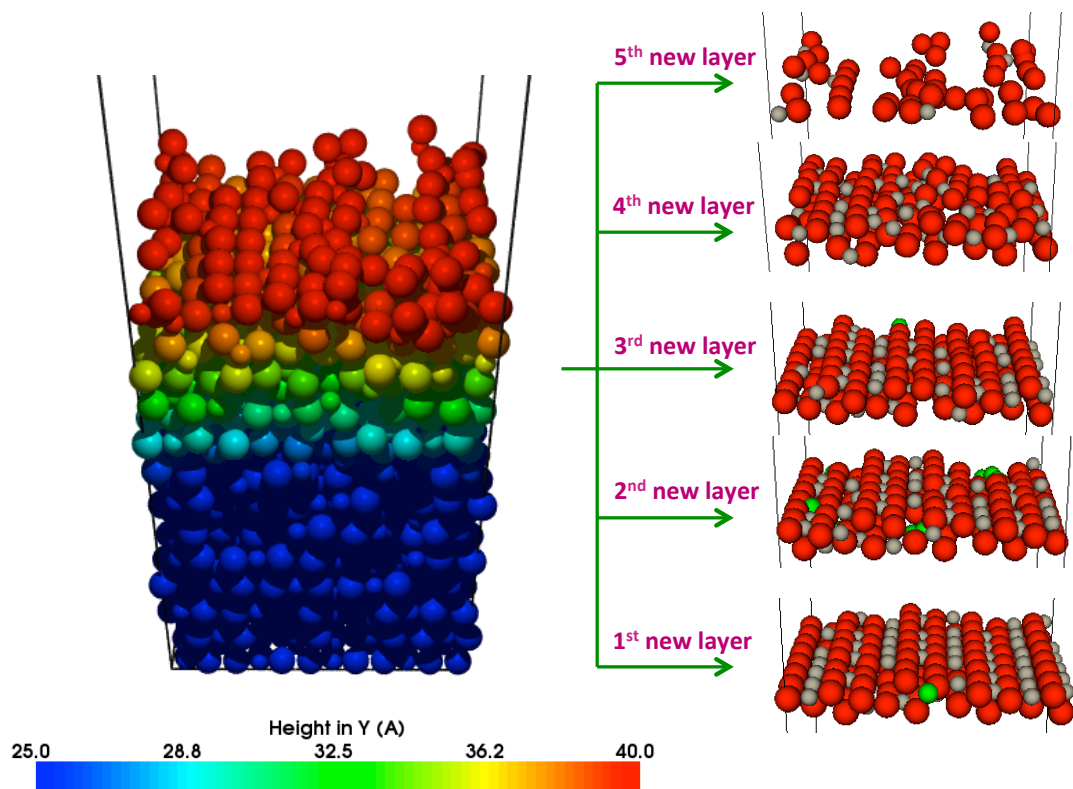


Figure 5.41: The resulting growth from the simulation of magnetron sputter deposition of TiO_2 and Ar simultaneously, where 4.3 seconds of real time are simulated. Layers are much more complete and crystalline than those obtained from the evaporation deposition simulations. It was assumed that an Ar bombardment at 40 eV occurred with equal probability as a Ti_xO_y molecule deposition. There is not a huge difference from the Ar bombardment. Layers are still more complete and crystalline than evaporation and Ti interstitials are still present. Ar penetrates the surface, relaxing in sites as deep as the 2nd layer of the original substrate.

the same deposition energy is used (40 eV). Figure 5.41 illustrates the resulting growth from the simulation. Experimental results suggest that Ar bombardment would improve film density, however, our simulations show no conclusive evidence of this as growth has not reached a steady state. It is noticeable, however, that when investigating the final position of those atoms from the original substrate (both O and Ti atoms), the simulation which included the Ar caused slightly more disruption and damage to the substrate. This resulted in more atomic mixing, illustrated in figure 5.42. The Ar bombardment created an increased number of Ti interstitials in the substrate, which would aid the rutile growth mechanism in forming more crystalline rutile, however, a significant difference in growth quality is not evident.

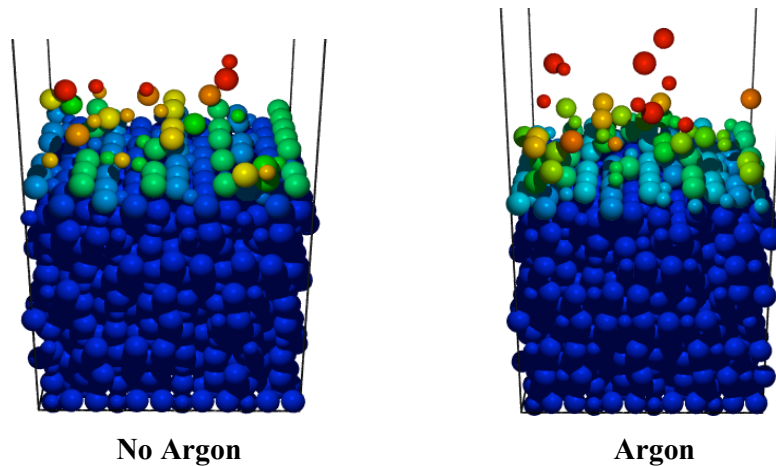


Figure 5.42: The final positions of those atoms from the original substrate (both O and Ti atoms) coloured by height, after the deposition of 4 monolayers. The simulation that included the effect of Ar suffered more disruption and damage to the original substrate. Ar bombardment disrupts the surface more than Ti_xO_y molecule depositions alone, suggesting that Ar should enable or allow more atomic mixing and diffusion to occur.

Notice a small number of Ar atoms remain implanted within the substrate, illustrated in figure 5.43. The implanted Ar sits in either interstitial locations between layers or in Ti lattice sites (shown previously in figure 5.39). It is known from Auger electron spectroscopy that in experiment, $\sim 1\%$ of the Ar stays within the film [151], consistent with the simulation model where we saw 0.06-1% of Ar remaining in the film.

5.5.4 Other Deposition Energies

Evaporation, ion-beam assisted evaporation and magnetron sputter deposition are all popular PVD techniques. TiO_2 growth via these methods has now been illustrated, however, other deposition energies have also been simulated in order to gain a broader understanding of the behaviour of rutile growth. 10 eV, 30 eV and 100 eV deposition energies have been simulated using the same MD and otf-KMC methods. 10 eV and 30 eV depositions, illustrated in figures 5.44 and 5.45 respectively, produce very similar results. Atoms have just about enough energy in order to move into crystalline sites, especially O atoms. There are, as before, many Ti interstitials within the lattice. 30 eV depositions cause more atomic mixing between original substrate atoms and newly deposited atoms.

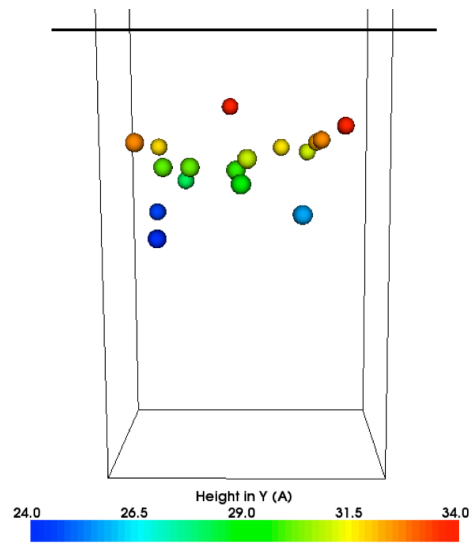


Figure 5.43: Ar atoms which have remained implanted within the film. 0.06% of Ar remains implanted, in close agreement with the $\sim 1\%$ observed experimentally. Atoms are coloured by height, with the surface height indicated by the line.

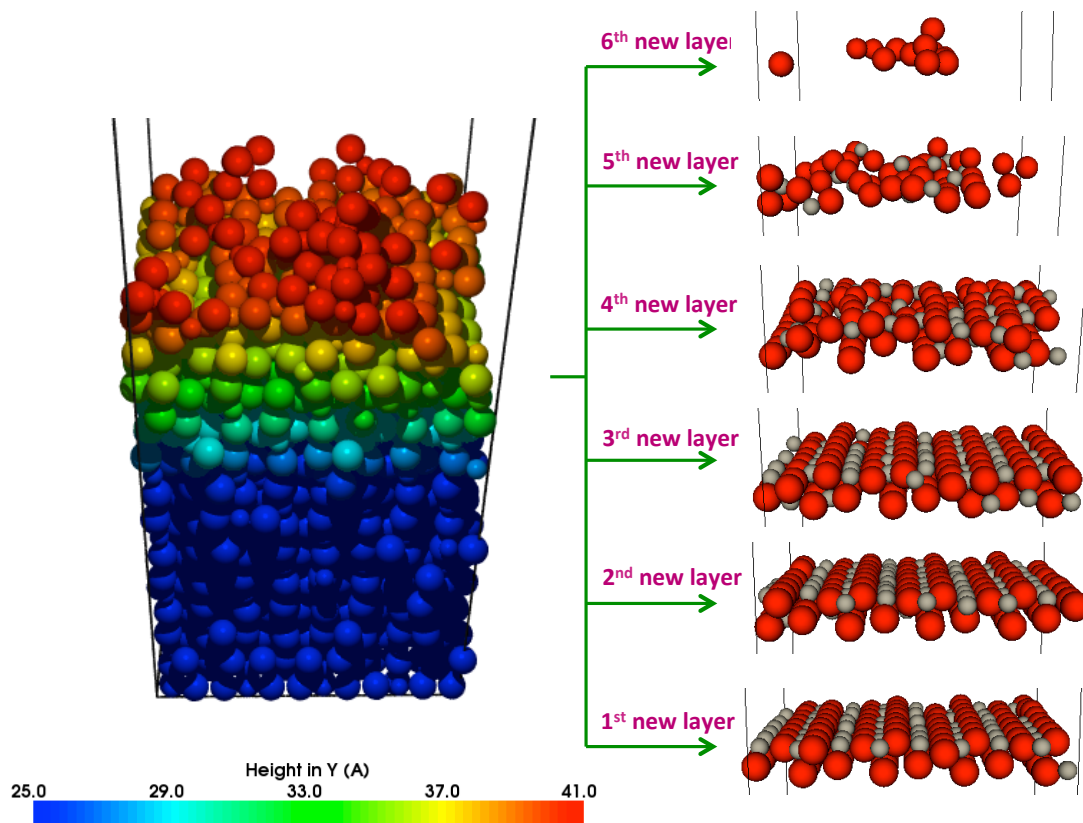


Figure 5.44: The resulting growth from 10 eV depositions onto the rutile surface, where 6.2 seconds of real time are simulated. Growth is more complete and crystalline than the evaporation growth but not as good quality as the sputter growth.

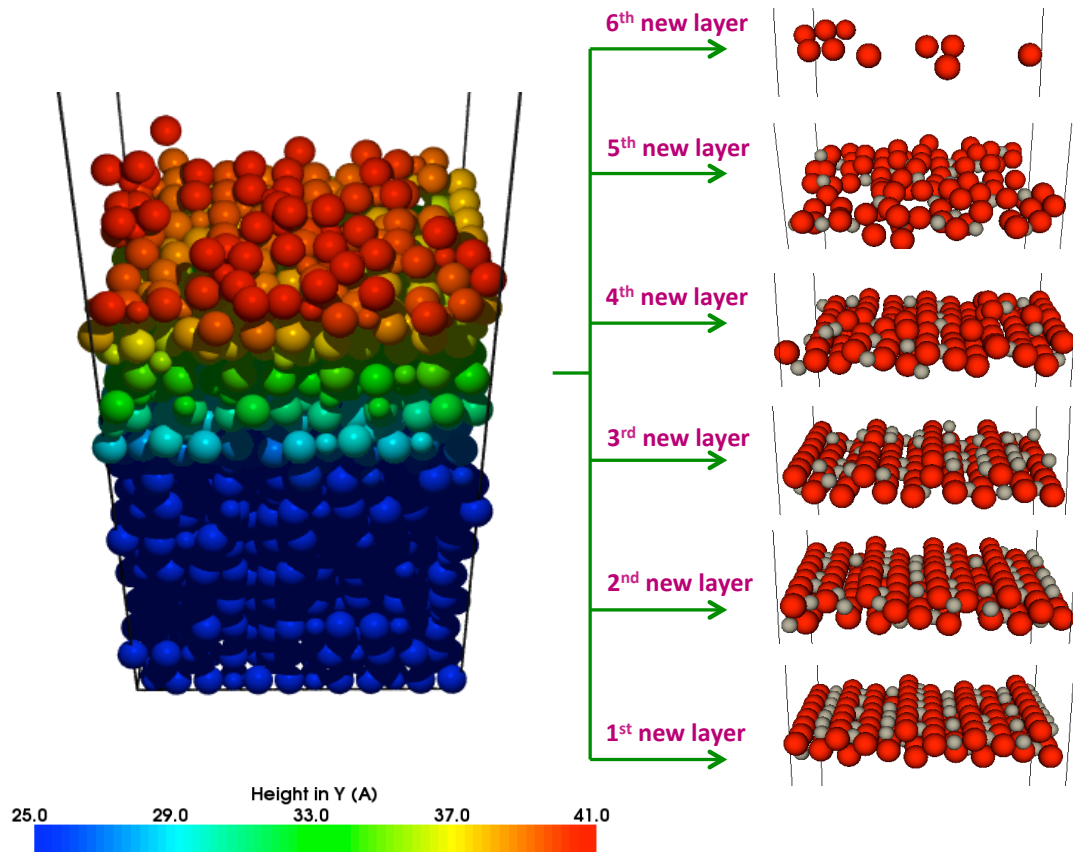


Figure 5.45: The resulting growth from 30 eV depositions, where 6.4 seconds of real time are simulated. The film appears very similar to that produced by 10 eV depositions, with increased atomic mixing occurring during the ballistic phase. Some new layers are complete and crystalline, similar to 40 eV depositions simulating sputtering.

100 eV depositions onto the rutile surface have already been investigated using the high temperature MD. Results from otf-KMC provide more accurate results due to the ability to search for transitions between successive depositions and the more realistic temperature. Figure 5.46 illustrates the resulting growth from the high energy TiO_2 impacts. Unlike the results from high temperature MD, layers appear to be rather complete with some crystallinity in the first few new layers. Atomic mixing between new atoms and the original substrate atoms has increased due to the damage created from high energy impacts. Ti interstitials are created as deep as the 4th layer of the original substrate, shown in figure 5.47. The increased depth and number of Ti interstitials within the film will greatly effect the optical properties of the film and thus 100 eV is too high a deposition energy for the production of photovoltaic films. The high energy also lends itself to densifying the film, however, mainly through the production of Ti interstitials.

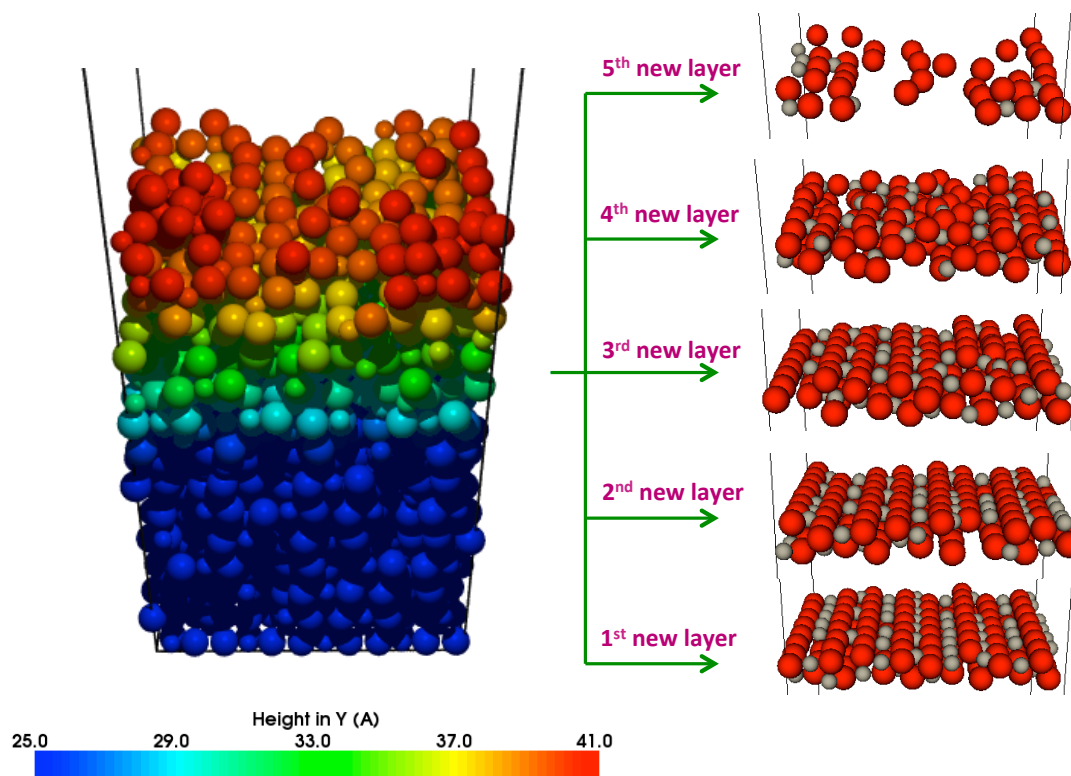


Figure 5.46: Higher energy depositions, where atoms arrive at the surface with 100 eV, simulating 8.7 seconds of real time. Growth results in a somewhat dense film. However, there is a huge presence of Ti interstitials throughout the film, as deep as the 4th layer of the original substrate.

5.5.5 Growth Mechanisms

Otf-KMC allows specific growth mechanisms and important transitions to be investigated. An important mechanism is observed throughout the simulations. A Ti interstitial below the surface has a high escape barrier, however, the presence of an O rich surface above the interstitial lowers the escape barrier allowing the annealing of Ti interstitials up to the surface. This mechanism, observed experimentally [146, 147], enables crystalline rutile to form by the migration of these Ti interstitials up towards the surface. Figure 5.48 illustrates the movement of a Ti interstitial via this mechanism. Only the Ti atoms are shown for simplicity, but it is still clear that the interstitial diffuses upwards and across to a surface lattice site. Knowledge of this key growth mechanism in rutile allows a better understanding of why some deposition energies produce a poor quality film. Higher energy depositions (100 eV) produce Ti interstitials deep into the substrate, whilst the

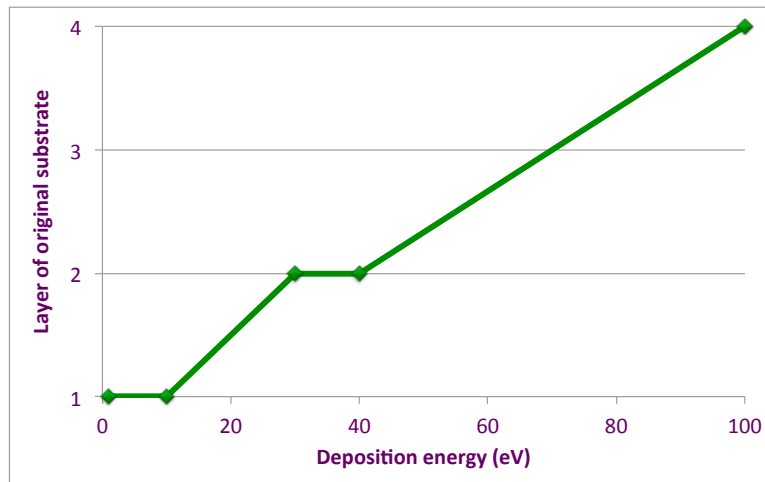


Figure 5.47: The depth of formed Ti interstitials against the deposition energy. The higher the energy of deposition, the deeper within the original substrate are Ti interstitials formed.

mechanism enables the drawing out of Ti interstitials from only the top few layers. Those interstitials formed very deep in the substrate would require too much energy to escape. These interstitials, therefore, remain stuck in the lattice.

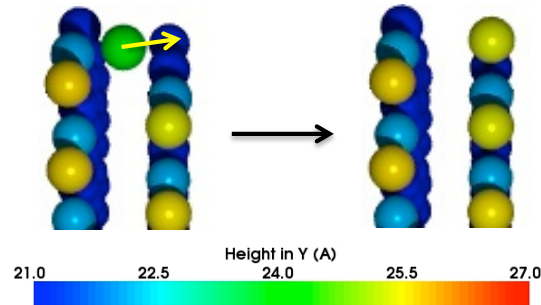


Figure 5.48: A Ti interstitial in the 1st layer is drawn out by the presence of an O rich surface (not shown here), requiring 0.61 eV to take place. The atoms are coloured by height and only Ti is shown.

Single O ad-atom diffusion also plays an important role in the surface construction during simulations. In figure 5.49 an O ad-atom diffuses along the trench above the 5-fold coordinated Ti row with energy barriers of between 0.65 eV and 0.75 eV. This allows the migration of O atoms towards Ti interstitial rich areas to aid the rutile growth mechanism by lowering the Ti interstitial escape barrier. Figure 5.50 illustrates another important role of O ad-atoms. A vacancy on the surface in the O ad-row is filled by diffusion of the O ad-atom into the vacant site, with an energy barrier of 0.81 eV.

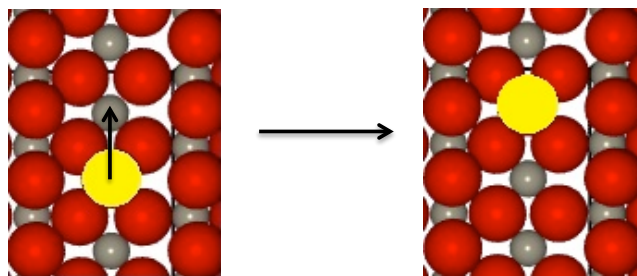


Figure 5.49: An O ad-atom diffuses along the trench, requiring between 0.65 eV and 0.75 eV. This diffusion enables the movement of surface O towards a Ti interstitial rich area, thus lowering the Ti interstitial escape barrier and encouraging the rutile growth mechanism to take place.

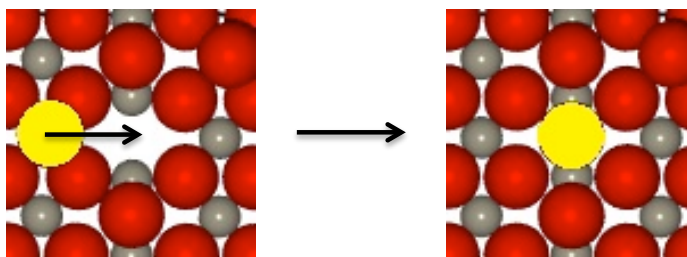


Figure 5.50: An O ad-atom sitting in the trench above the 5-fold coordinated Ti row diffuses across to fill an O ad-row vacancy, requiring 0.81 eV for the transition.

The advantage of the otf-KMC methods is also the ability to observe and understand concerted, multi-atom motions. Many diffusion mechanisms are non-intuitive and not able to be observed using traditional MD. In figure 5.51, a TiO_3 ad-unit on the surface rotates around an O ad-atom in order to diffuse along the trench. The transition may have been incorrectly understood without the ability to view saddle points and thus understand the transition pathway. The energy required for this concerted motion is 0.83 eV, only slightly higher than that required to move a single O atom.

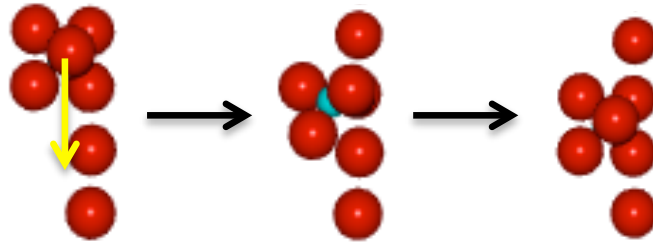


Figure 5.51: A multi-atom, concerted motion, allowing the diffusion of a TiO_3 unit across the surface. 3 atoms move in this transition, requiring 0.83 eV. Initial and final configurations are shown along with the intermediate saddle point to illustrate the transition pathway.

5.6 Discussion

15,000 single point depositions of Ti_xO_y molecules onto an irreducible area of the rutile (110) surface were simulated using traditional MD in order to gain some initial understanding of the surface and typical defects. Deposition energies ranged from 20 eV to 100 eV, providing an insight into low and high energy impacts. From these simulations, four main defects could be classified, interstitials, vacancies, ad-atoms and reflected/sputtered atoms. Interstitials are usually Ti atoms, although a small number of O interstitials are observed. During single impacts, up to 7 interstitials were formed per impact, as deep as the 7th layer of the substrate. The higher the deposition energy, the more interstitials are created per deposition. Interestingly, when there is Ti in the deposition cluster, most depositions produce between 1 and 3 interstitials. Whereas, when no Ti is in the deposition cluster, in 60-80% of lower energy depositions, no interstitials are created. The 100 eV depositions, however, create 1 or 2 interstitials in 70% of cases. Therefore, interstitials are more likely to be formed when a Ti atom is in the deposition cluster. It was found that the deposition cluster, unlike with interstitial count, played no role on the depth, rather it was the deposition energy which played a large role. The higher the deposition energy, the deeper into the lattice were interstitials created and over 80% of interstitials created during 20 and 40 eV depositions were in the 1st layer of the lattice. Vacancies, unoccupied lattice sites, were observed for both O and Ti. Ti depositions resulted in a larger proportion of vacancies in comparison with other deposition clusters, creating 1 vacancy in 50% of 20 eV cases and up to 8 vacancies in the 100 eV depositions. At 20 and 40 eV, other clusters, more often than not, created no vacancies. The ratio of Ti to O vacancies showed that it is more likely that a vacancy will occur from a missing Ti atom, however, once the deposition energy

reached 100 eV, O and Ti vacancies become almost equal. O ad-atoms form easily on the rutile surface. When there is a higher portion of O in the deposition cluster, more ad-atoms are created due to the favourability of O to form surface ad-atoms. During depositions, only O atoms have been observed leaving the surface, due to the lower O escape energy. Ti depositions very rarely sputter any atoms, only in 0.05% of cases for 100 eV depositions. O depositions, however, cause the sputtering or reflection of 1 atom in between 20-30% of all cases. These results provided an initial insight into the behaviour of rutile under the effect of surface bombardments.

The growth of rutile TiO_2 has been simulated firstly using high temperature MD, where temperature was raised from room temperature to 1000 K in order to speed up the transitions and thus growth. Simulations modelled the growth of rutile where deposition energies included 20, 40 and 100 eV. The results from 20 eV and 40 eV depositions showed similar patterns of growth. 40 eV depositions, however, resulted in increased defects below the surface, often in the form of Ti interstitials. Different distributions of deposition species were investigated for the 100 eV depositions. Stoichiometric, Ti rich and O rich distributions of deposition species were simulated at 1000 K. The stoichiometric distribution shows voids throughout the film, where vacancies have been created. The deposition of a Ti rich distribution observed a large count of Ti interstitials throughout the film, again with the presence of voids. Deposition of an O rich distribution produced similar results, with Ti interstitials and voids. The high temperature MD provided interesting results, providing some initial insight into the way in which rutile grows, however, due to the high temperature some skewing in results occur. Higher energy barriers are sampled at a higher rate, due to the increased temperature, thus causing inaccuracies in the results.

Otf-KMC combined with MD, allows the simulation of rutile growth over realistic time scales without the need to elevate temperatures. Up to 9 seconds of film growth have been simulated using otf-KMC. The main interest of the growth simulations was the realistic simulation of rutile growth via the PVD methods introduced in chapter 1, although other deposition energies were also investigated for a broader understanding. Evaporation growth, modelled by low energy (<1 eV) deposition of Ti_xO_y clusters on rutile (110), produces incomplete layers containing voids as there is not enough energy in the system for much diffusion to take place during the ballistic phase. Low energy ion-beam assist at 40 eV injected more energy into the system, thus growth is slightly more crystalline. The 40 eV Ar

bombardment created some Ti interstitials in the substrate, thus enabling an important rutile growth mechanism to take place. High energy ion-beam assist at 100 eV caused disruption and damage to the substrate, resulting in less than perfect crystalline growth, with significant mixing and formation of Ti interstitials deep into the substrate (too deep to be immediately drawn out). A slightly denser film was observed, however, we cannot be certain this is a real effect as growth has not yet reached a steady state. For a deeper insight, we would be required to deposit several more layers, which currently is too computationally expensive.

Growth via magnetron sputtering was simulated by Ti_xO_y depositions at 40 eV, the optimal deposition energy to produce dense and almost completely crystalline Titania [5]. The higher arrival energy of atoms during sputter deposition enables increased atomic mixing during the ballistic phase and increased surface diffusion, thus forming a more crystalline film than evaporation. Layers were a lot more complete than the evaporation deposition grown layers. The direct effect of the Ar during sputtering was investigated by simulating the system with simultaneous Ar bombardment. The probability of a Ti_xO_y or Ar atom impacting the surface was equal. It was found that Ar bombardment caused an increase in atomic mixing and an increase in Ti interstitials produced, however, this did not seem to have a significant influence on the quality of growth. Ar implantation of around 0.06-1% was observed, comparing to $\sim 1\%$ observed experimentally [151]. It was expected from experimental data that Ar bombardment would increase film density, however, in all of our simulations we cannot draw clear conclusions as only four monolayers have been deposited which does not yet put the system in a steady state. Several more monolayers would need to be deposited in order for a steady state to be reached and hence to obtain conclusive evidence for the effect of Ar bombardment on thin film densification.

10 eV, 30 eV and 100 eV deposition energies were also investigated using the off-KMC methods. 10 eV and 30 eV produced similar results. Films were crystalline and complete but some Ti interstitials were still present within the lattice. The 30 eV depositions did allow increased atomic mixing with the original atoms, similar to the behaviour at 40 eV. 100 eV, previously simulated using the high temperature MD, showed different results, with the newly grown layers showing crystallinity. However, Ti interstitials were implanted deeper into the substrate, which experimentally would greatly effect the film's optical properties. The number of Ti interstitials also increased from the higher energy impacts, suggesting again that

optical properties would be altered.

Important growth mechanisms and transitions observed during rutile TiO_2 growth were investigated and a key rutile growth mechanism for the annealing of Ti interstitials was observed. The presence of an O rich surface lowered the escape barrier for a Ti interstitial sitting in the layer below to 0.61 eV. In order for Ti interstitials to be drawn out, they must be close to the surface as interstitials too deep will become stuck within the lattice, effecting the film's properties. Single O ad-atoms diffusing on the surface were also found to play an important role. An O ad-atom requires between 0.65 eV and 0.75 eV to diffuse along the trench, above the 5-fold coordinated Ti row. This allows the movement of O ad-atoms towards areas rich in Ti interstitials, enabling the key rutile growth mechanism to take place by decreasing the Ti interstitial escape barriers. O ad-atoms may also reduce the number of O vacancies by diffusing into vacant sites. For example, a barrier of 0.81 eV is relevant when an O ad-atom in the trench diffuses across filling an O ad-row vacancy.

The methods used within the otf-KMC allow the observation of multi-atom, concerted transitions which, using traditional methods, would not be easily identifiable. One of these concerted transitions is the movement of a TiO_3 ad-unit along the trench via the rotation of three atoms around an O ad-atom. This transition requires 0.83 eV and without the ability to view the saddle point, this non-intuitive transition may have been mistaken for a simple sliding mechanism.

Chapter 6

Simulation of Zinc Oxide Thin Film Growth

6.1 Introduction

Zinc oxide is an inorganic compound with many uses, including an additive in plastics, ceramics, glass, paints, pigments and foods. Materials science has, within the last decade, highlighted ZnO as an excellent alternative to other, more expensive and less abundant materials. As a transparent semiconductor, with a wide band gap of 3.37 eV [152], ZnO has become the material of choice in the production of transparent electrodes for silicon thin film solar cells. ZnO is commonly doped with Al to form AZO, a transparent conductive oxide (TCO), which is a huge industry alone within the photovoltaic sector [153]. AZO typically incorporates 0.5% of Al, but for simplicity in the simulations, only intrinsic ZnO is investigated. ZnO also has applications in intrinsic n-type semiconductors. ZnO thin film growth is simulated due to the uses mentioned, however, TCO's are the main interest for the modelling carried out here.

ZnO crystallises in one of two main polymorphs, hexagonal wurtzite or cubic zinc blende, both of which are tetrahedrally coordinated. At high pressures, ZnO may also recrystallise into the rocksalt phase [154]. The only difference between the two main polymorphs is the bond angle of the second nearest neighbours which causes a different stacking sequence of close packed planes. The wurtzite structure is made of triangularly arranged alternating close packed planes, with a stacking sequence of AaBbAa... in the (0001) direction [155]. The zinc blende structure also has triangularly arranged atoms in the close packed (111) planes, but with a stack-

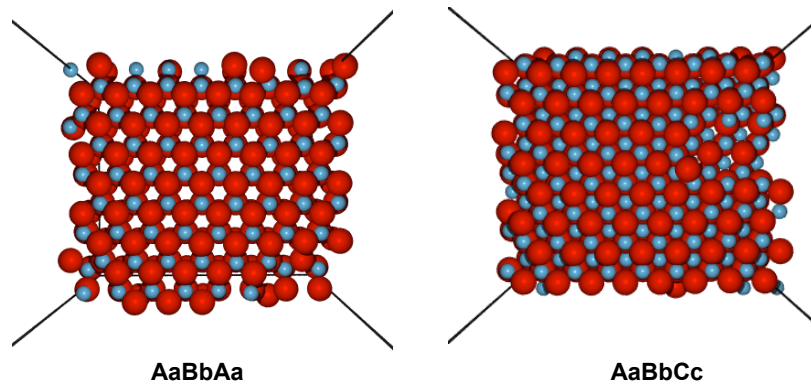


Figure 6.1: View from above, where three monolayers of ZnO have been sliced out in order to illustrate the stacking sequences. The image on the left shows the wurtzite structure with AaBbAa... stacking, and on the right is the zinc blende AaBbCc.. structure. In the wurtzite structure the fcc hollows are clearly seen throughout the film, whereas the zinc blende structure involves filling these fcc hollows. Smaller spheres represent Zn, whilst larger red spheres represent O.

ing order of AaBbCc... [155]. Upper and lower case letters stand for the different species. Figure 6.1 shows three monolayers of ZnO in the wurtzite and the zinc blende sequences.

The wurtzite structure is the most stable and therefore most common form and thus it is this structure that we investigate throughout this chapter. ZnO, in the wurtzite hexagonal crystal structure, has alternating planes of tetrahedrally coordinated O^{2-} and Zn^{2+} stacked along the c -axis [152]. Two polar surfaces exist in the ZnO wurtzite phase (Zn-terminated (0001) and O-terminated (000 $\bar{1}$)) [156,157]. After some initial tests documented in this chapter, we chose to take the O-terminated surface as our initial substrate upon which the depositions take place. Figure 6.2 illustrates the O-terminated wurtzite surface with the unit cell highlighted. High-symmetry adsorption sites are indicated. In order to follow a crystalline growth, atoms should sit either in the ‘on top’ or ‘hcp’ sites. Stacking faults, however, can form when atoms bind in the fcc hollow site. This is further investigated later in this chapter.

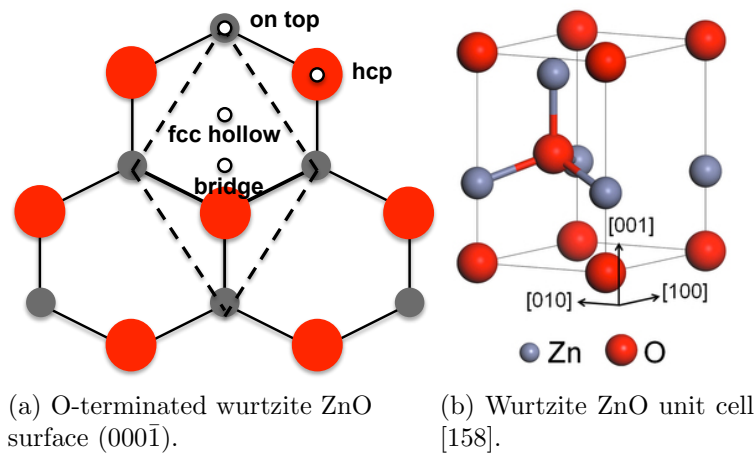


Figure 6.2: With its hexagonal structure, wurtzite requires arriving atoms to follow the hexagonal nature in order to continue the crystalline growth. The unit cell is shown, with the high-symmetry adsorption sites for arriving species.

6.2 Previous Work

ZnO, an important material in the future of photovoltaics as a TCO alternative, has been studied for many years both experimentally and theoretically. An explosion in ZnO research began towards the end of the 20th century, continuing in more recent years. Figure 6.3 illustrates this explosion with a huge increase in ZnO focused publications. This section highlights some of the most important findings from relevant studies.

6.2.1 Experimental

Metal-oxide thin films can be deposited using a variety of industrial scale processes, including evaporation (thermal and electron beam) and reactive magnetron sputtering [159–162]. The evaporation process involves evaporation of Zn_xO_y molecules onto the substrate with kinetic energy of typically <1 eV. An ion source (usually Ar) may also be used to densify the film, by introducing energy into the growing film and enhancing atomic mixing.

Magnetron sputtering deposits thin films of ZnO using RF, DC or pulsed DC power [161–163]. Targets can be metal Zn (DC), ZnO (RF) or Zn_xO_y (pulsed DC). Sputtering in the presence of a reactive gas is necessary to different degrees depending on the precise deposition configuration. For the sake of simplicity we assume

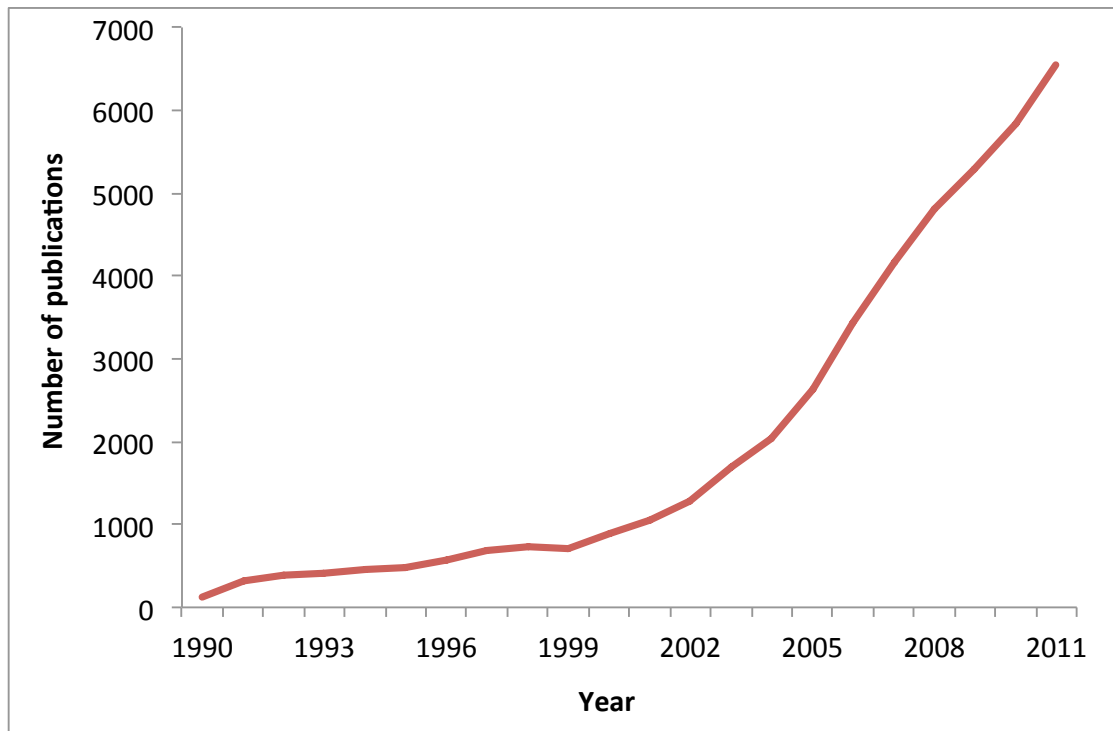


Figure 6.3: ZnO journal publications from 1990 to 2011. Information was sourced from the Web of Knowledge.

that all particles arrive at the surface with ~ 40 eV, influenced by the applied or self bias on the substrate. This is a parameter that can be varied in the model. In all cases Ar is used as the working gas to sputter material from the target. Ar ion bombardment during deposition also affects the density and stoichiometry of ZnO film [164]. However, we do not simulate the presence of Ar in this simulation as studies on other oxides, namely TiO_2 , show that the addition of a working gas does increase crystallinity but not significantly [118]. The inclusion of Ar would require more computing time.

ZnO thin film growth often involves a post-annealing treatment. AZO is often post-annealed in order to recrystallise and reduce defects within the lattice, thus improving film properties. Previous experiments have found that annealing AZO films between 770 K and 920 K ($\sim 500^\circ\text{C}$ - $\sim 650^\circ\text{C}$) enables recrystallisation to take place [165–168]. Post-annealing has become an important step, therefore, in the production of AZO films.

It is known that ZnO can grow with inherent stacking faults and twin boundaries in the film, often referred to as planar defects. In highly mismatched wurtzite

substrates, there is usually some zinc blende phase separated by crystallographic defects from the wurtzite phase [155,169]. ZnO, in thin film or nanostructure form, often results in stacking faults where both wurtzite and zinc blende phases are observed. Other materials with similar crystal structures, such as CdTe, exhibit similar stacking faults and twin boundaries where the wurtzite and zinc blende phases form side by side [170,171]. Planar defects can significantly effect the electronic properties of nanowires [172].

6.2.2 Simulation

In order to improve general understanding of the properties of ZnO, simulations are a highly valuable tool, complementing experimental work. Quantum-mechanical methods (*ab initio* or density-functional theory (DFT)) have been extensively applied to the investigation of surfaces [173,174], point defects [175–177] and grain boundaries [178]. These Q-M methods provide accurate calculations, however, time scales are very limited. Analytical potentials have also been used in the investigation of ZnO films. The definition of an appropriate interatomic potential is required before performing any sort of useful simulations. In chapter 2, two interatomic potentials were described which can model the ZnO interactions. The Albe potential, introduced by Albe *et al.* in 2006, employed a previously successful analytic bond-order potential scheme [44,45]. The potential has been successfully applied to the modelling of purely metallic, covalent, molecular and mixed ionic-covalent systems [44–47] and specifically defect production in ZnO by ion irradiation [48]. The second potential described is the reactive force field (ReaxFF) [54], a bond order potential where all energy terms depend on the bond orders. Van Duin *et al.* applied the ReaxFF potential to various materials, including ZnO [56]. MD calculations were successfully carried out using the ReaxFF potential, simulating half a monolayer of ZnO deposition onto the (0001) surface [56].

Simulations of ZnO film growth have been carried out by several groups using techniques including MD and KMC. Kubo *et al.* [179] investigated homoepitaxial growth mechanisms of ZnO (0001) using traditional MD simulations. Dee *et al.* later used traditional KMC methods to simulate the deposition of ZnO [180]. However, important features such as surface reconstruction were ignored during the study and the main focus was surface roughness. Simulations of AZO films are rather less abundant, due to the complexity of the interatomic potentials for doped

materials.

6.3 Initial Testing of Interatomic Potentials

Interatomic potentials provide the basis for a simulation, describing the atomic interactions and behaviour. The more accurate the potential is, the more realistic the simulation becomes. In Chapter 2, interatomic potentials used within this project were described in detail. In order to make an informed decision as to which potential to apply to our ZnO simulations, some initial tests were carried out using both potentials. Behaviour was examined to find which potential recreates the most realistic behaviour. Along side testing for which potential to use, the substrate surface was also investigated as two polar surfaces exist in the wurtzite phase (Zn-terminated (0001) and O-terminated ($000\bar{1}$)) [156].

Single point depositions onto each polar surface have been modelled with the Albe and ReaxFF potentials. Different arrival energies have been used, from 1 eV to 100 eV and four species have been deposited, O, O₂, Zn and ZnO. In order for results to be statistically correct, species were deposited onto an area of irreducible symmetry on the surface, the unit cell, shown in figure 6.4. In total, 64,000 single point depositions have been simulated on both ZnO polar surfaces.

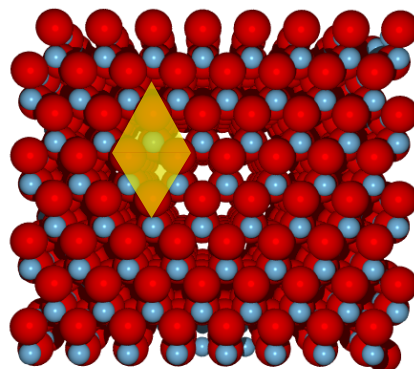


Figure 6.4: The deposition took place on the unit cell, an area of irreducible symmetry, which is highlighted here on the O-terminated ($000\bar{1}$) surface. Deposition of all species onto a point in this irreducible area provides statistically correct results by modelling depositions onto 1000 random points within this area.

6.3.1 O-terminated Surface

Four species (O, O₂, Zn and ZnO) have been deposited with arrival energies of 1 eV, 10 eV, 40 eV and 100 eV onto the O-terminated surface. In order to have statistically accurate results, 1,000 single point depositions have been carried out for each case and data was then normalised. Figure 6.5 illustrates the behaviour of deposited species in relation to each deposition energy and each potential. If the deposited species penetrates the substrate, the depth reached is shown, otherwise if the species is reflected off the surface this is also shown.

The 1 eV depositions, modelled with both potentials, show similar behaviour. It is expected that the low arrival energy of deposited species, realistically, would not penetrate the surface and hence should result in ad-atoms on the surface or immediate reflection. The Albe potential suggests that 5% of depositions result in penetration below the surface, whereas the ReaxFF suggests no penetration from 1 eV depositions. Looking at the reflection of species, O₂ clusters reflect in up to 85% of cases, which is expected as the O-terminated surface does not provide many sites for the O₂ dimer to bind to. The 10 eV depositions, again, see the Albe potential allowing deeper penetration of deposited atoms than the ReaxFF, especially from the O depositions. O₂ dimers reflect in 20% more cases with the ReaxFF potential, in agreement with realistic behaviour. The 40 eV and 100 eV depositions show similar behaviour with both potentials. Figure 6.6 illustrates these statistics.

Looking at atoms reflected or sputtered from 1 eV and 10 eV depositions, it is clear that O, Zn and ZnO clusters rarely split or cause material to sputter. O₂ dimers deposited with the Albe potential, however, split and reflect in 50-60% of cases, compared to only 2% of cases with the ReaxFF potential. This value from the Albe potential is highly unrealistic given the high binding energy of O₂ dimers (5 eV), hence we could expect the ReaxFF to be more favoured for modelling O₂ dimer behaviour. The higher energy depositions, 40 eV and 100 eV, produce similar results as the increased kinetic energy causes the split of O₂ dimers, irrespective of any effect that may come from the different potentials.

6.3.2 Zn-terminated Surface

1,000 single point depositions of the same 4 species were also deposited onto the Zn-terminated polar surface, in order to continue to aid the choice of potential for

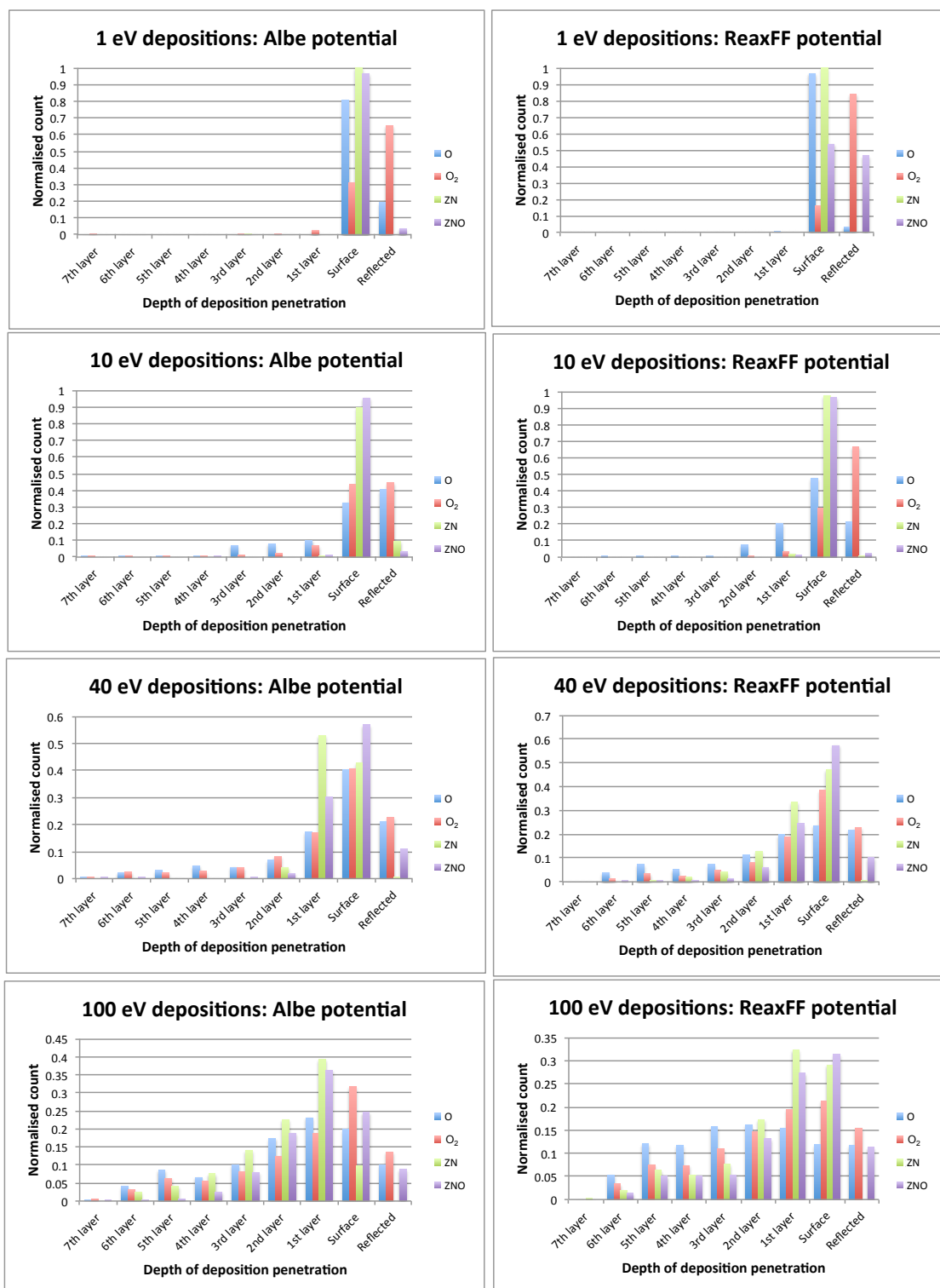


Figure 6.5: A comparison of the Albe and ReaxFF potentials used to model depositions onto the O-terminated surface. Statistics are shown for the depth of penetration of the deposited species or reflection rate. The key is shown.

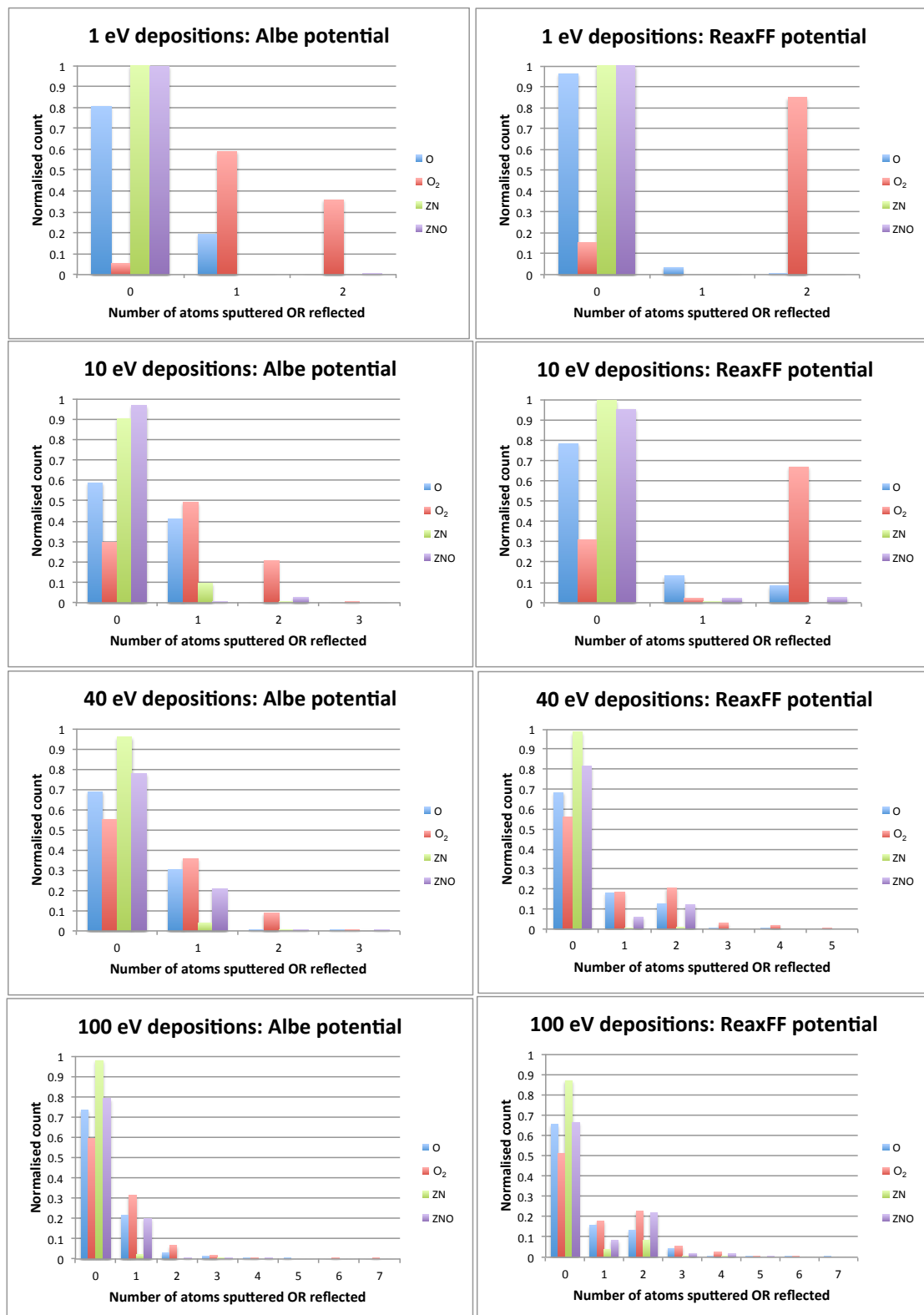


Figure 6.6: A comparison of the Albe and ReaxFF potentials used to model depositions onto the O-terminated surface. Statistics are shown for the number of atoms either sputtered or reflected off the substrate during depositions. The key is shown.

growth simulations. Figure 6.7 illustrates a comparison of the Albe and ReaxFF potentials for the different arrival energies and deposited species.

The 1 eV depositions on the Zn-terminated surface highlight a difference between Albe and ReaxFF potentials. As with the O-terminated surface, we would not expect O₂ dimers to split at such low deposition energies, however, the Albe potential predicts that 50% of dimers split. The ReaxFF potential, however, predicts that only 15% of O₂ dimers split. The Zn-termination of the surface provides a lot more binding sites for O atoms on the surface, which should result in less reflection as recreated by the ReaxFF. The higher energy depositions provide very similar behaviour, so comparison is not useful.

6.3.3 Interatomic Potential and Polar Surface for Growth

After performing 64,000 single point depositions on both polar surfaces using the Albe potential and the ReaxFF potential to describe the interactions between atoms, the ReaxFF has been chosen to simulate the growth of ZnO using an O-terminated (000 $\bar{1}$) surface as the initial substrate. The ReaxFF potential has been chosen for several reasons, including the ability of the variable charge potential to model both the Zn and ZnO pairs better. Also, the behaviour of O₂ dimers is modelled more realistically than with the Albe potential, which does not respect the high binding energy of dimers (5 eV), allowing dimers to split far too easily during low energy depositions. Some previous tests carried out by past students at Loughborough University also highlighted the superiority of the ReaxFF over the Albe potential [181].

The choice of polar surface to use as the initial substrate for the growth simulations, was based predominantly on experimental knowledge. During the deposition process of a ZnO thin film by magnetron sputtering, the plasma inside the vacuum chamber is usually O rich [182], which has been found to form an O-terminated surface [157].

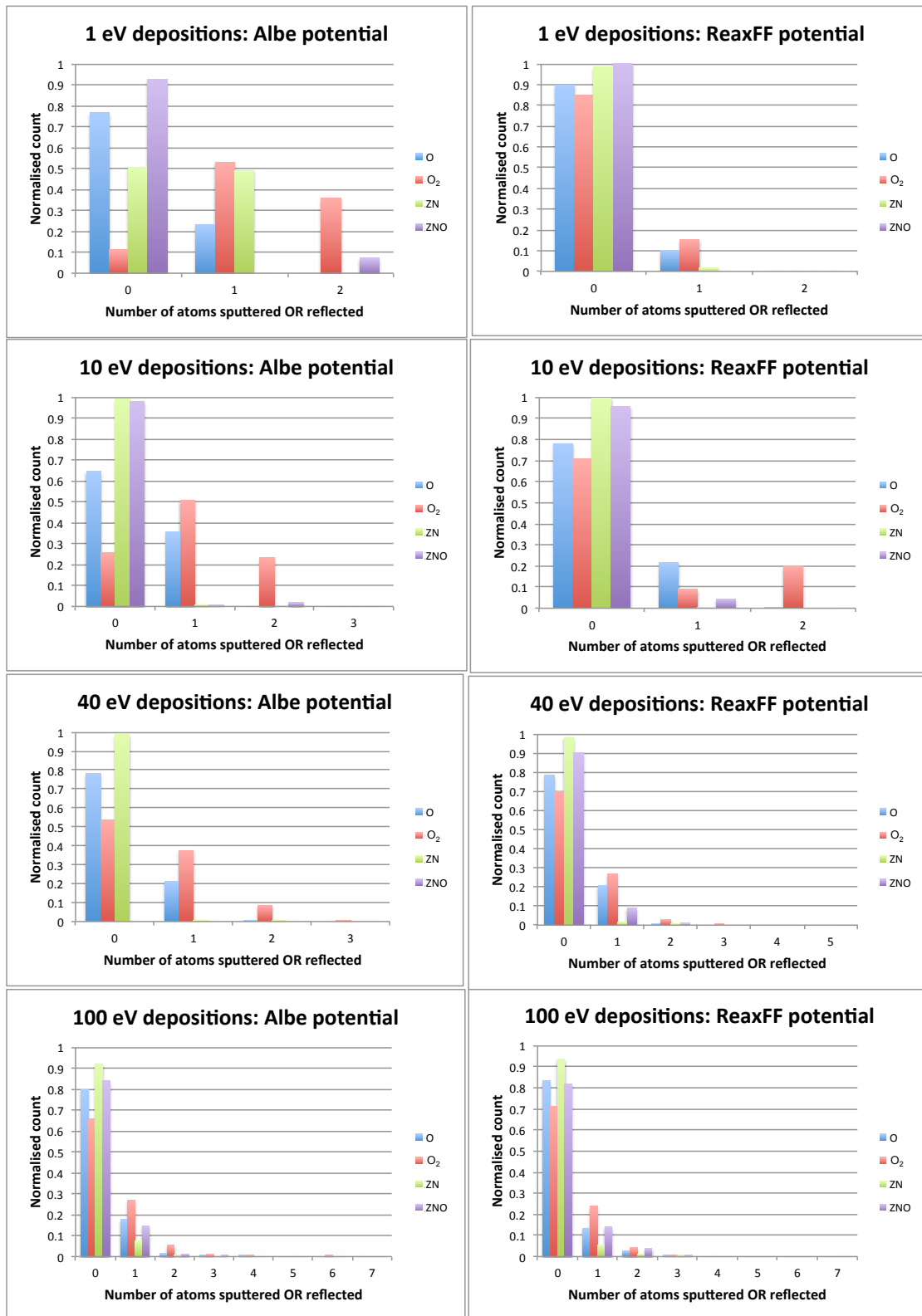


Figure 6.7: A comparison of the Albe and ReaxFF potentials used to model depositions onto the Zn-terminated surface. Statistics are shown for the number of atoms either sputtered or reflected off the substrate during a deposition. The key is shown.

6.4 Growth Simulations

ZnO depositions are simulated onto the O-terminated (000 $\bar{1}$) surface using a long time scale dynamics technique, which was introduced in chapter 3. Traditional MD was used to model the deposition, with otf-KMC allowing the simulation of surface diffusion during impacts.

The ZnO substrate was taken as an O-terminated lattice, 8 layers deep, with 128 atoms per layer. Periodic boundary conditions have been applied in each case to the x and z dimensions to allow atoms to wrap around and thus mimic a bulk. The bottom layer of the lattice is fixed to ensure stability, with a Berendsen thermostat [59] attached to the two layers above the bottom to control the system temperature. A deposition event was simulated by initialising the chosen deposition species some 10 Å above the surface, at a random angle and providing it with some amount of kinetic energy in the direction of the surface. Species are therefore initialised with either 1 eV or 40 eV directional kinetic energy, simulating evaporation and sputtering. Exact energies are altered slightly with a standard deviation of one tenth of the relative energy. The x and z coordinates were completely random, ensuring a random impact occurring normally to the surface.

After initialisation of the deposition species above the surface with the desired kinetic energy, MD runs for between 4 and 10 ps evolving the system, thus allowing the species to impact the surface at normal incidence. Running MD for longer allows excess heat to dissipate, therefore higher energy impacts require longer MD time. Once the system has been relaxed, RAT and NEB methods can find transitions between impacts, modelling the surface diffusion. Otf-KMC simulates surface growth by choosing a deposition or a transition at each KMC step. The deposition event is given a frequency, corresponding to specific deposition rate. Experimental deposition of ZnO occurs at a rate of around 3 monolayers per second, equating here to between 192 Hz and 320 Hz, depending upon which distribution of deposition species is used. Literature states that ZnO films can be deposited at temperatures ranging from room temperature (350 K) to \sim 670 K [162]. During these simulations, the lower temperature (350 K) is used. Three monolayers worth of atoms are deposited, simulating around one second of real time. MD and otf-KMC combine, running in parallel over 48 cpu cores.

Transition searches form a large part of the simulations, with each unique transition

having a unique energy barrier. In order to save computational time, transitions with energy barriers above 1.0 eV were ignored as they would rarely occur on our time scales. During the initial test simulations of ZnO growth, it was found that a very low energy barrier was taking up a large amount of the simulation time, therefore slowing the simulations down unacceptably. Upon investigation, these low energy barriers were found to belong to O₂ dimer rotation on the surface. An O₂ dimer rotation adds no net diffusion, hence we were able to modify the methods in order to ignore these irrelevant transitions, thus saving computational time. This specific barrier was discussed in chapter 3, figure 3.8, where a filter was added to the perl codes which identified O₂ dimer rotation allowing for only those transitions to be ignored.

6.4.1 Post-Annealing

Post-annealing of the substrate was achieved by taking the lattice after a completed growth simulation and running MD at an elevated temperature for 10 ns and then minimising the system. Literature states that ZnO films have been annealed at temperatures between 770 K and 920 K [165–168], resulting in films with far better crystallinity. We are able to directly compare pre and post-annealed films, allowing for a more precise understanding of the effect of post-annealing.

6.5 Deposition on the ZnO (000 $\bar{1}$) Surface

In this section, simulation results are presented for film growth by two industrial deposition processes described in chapter 1, evaporation and reactive magnetron sputtering. Various distributions of deposition species have been studied, including O rich, O deficient and stoichiometric. Table 6.1 describes the exact distribution of deposition species used during the simulations. Within the stoichiometric distributions, for evaporation, it is assumed that all species arriving at the substrate would be ZnO units. Whereas for sputtering, two variations of distribution are considered. Sputtering A assumes that most Zn atoms oxidise in the plasma en route to the substrate, whilst sputtering B assumes no reactive gas is used and therefore a large part of arriving species are single Zn and O and O₂ atoms rather than ZnO clusters.

Species	Stoichiometric (evaporation)	Stoichiometric (sputtering A)	Stoichiometric (sputtering B)	O rich	O deficient
O	0.0	0.0	0.1	0.02	0.0
O ₂	0.0	0.04	0.2	0.15	0.0
Zn	0.0	0.1	0.5	0.08	0.1
ZnO	1.0	0.86	0.2	0.75	0.9

Table 6.1: The distribution of various deposition species arriving at the surface at normal incidence (shown as a %).

6.5.1 Evaporation Deposition

Deposition by evaporation is an industrial process used to grow ZnO films [159,160], modelled here by simulating 1 eV depositions. After simulating each flux distribution, we found that the best quality evaporated film resulted from the stoichiometric distribution where all arriving species were ZnO clusters. Figure 6.8 shows the resulting film and it is clear that the original substrate is undamaged and still perfectly crystalline, whilst the first new layer is stoichiometric and almost complete. Atoms in the second new layer are not all in the expected stacking sequences or crystalline sites, resulting in a stacking fault. The layer is slightly O rich. The low arrival energy of the ZnO molecules means that atoms will not all have enough energy to pass activation barriers and diffuse into correct lattice sites. The equivalent of three monolayers of atoms are deposited during the simulation but there are actually four new layers, illustrating that the deposited structure is not dense or complete.

Post-annealing of ZnO films at 920 K has the ability to recrystallise the structure and decrease the number of defects [165–168]. Using MD we have simulated the annealing process. Figures 6.9 and 6.10 show the effects of annealing the system shown in figure 6.8 at 770 K and at 920 K respectively. At 770 K there is some recrystallisation, however, due to an inherent stacking fault already present, a phase boundary forms in the film, where wurtzite and zinc blende are both present and this is discussed later. At 920 K, there is almost complete recrystallisation and all stacking faults are eradicated.

O deficient and O rich distributions were also simulated, producing less complete films than the stoichiometric distribution. Figure 6.11 illustrates the resulting growth obtained from an O deficient distribution, where layers are incomplete and show low density with stacking faults throughout the new layers which now sit in

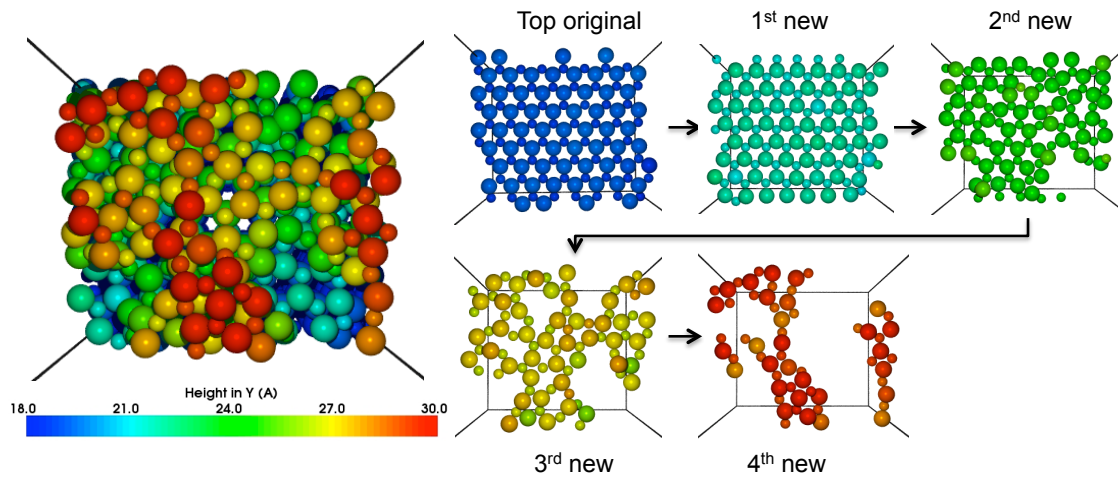


Figure 6.8: The evaporation deposition grown ZnO film, where a stoichiometric distribution of species was deposited. Larger spheres represent O and smaller spheres represent Zn. Atoms are coloured by height as shown on the colour bar. Layers have been broken down for clarity purposes, with the original surface at top left, followed by first new layer and so on, ending with the last new layer. The second new layer shows a stacking fault where atoms are not in correct sites.

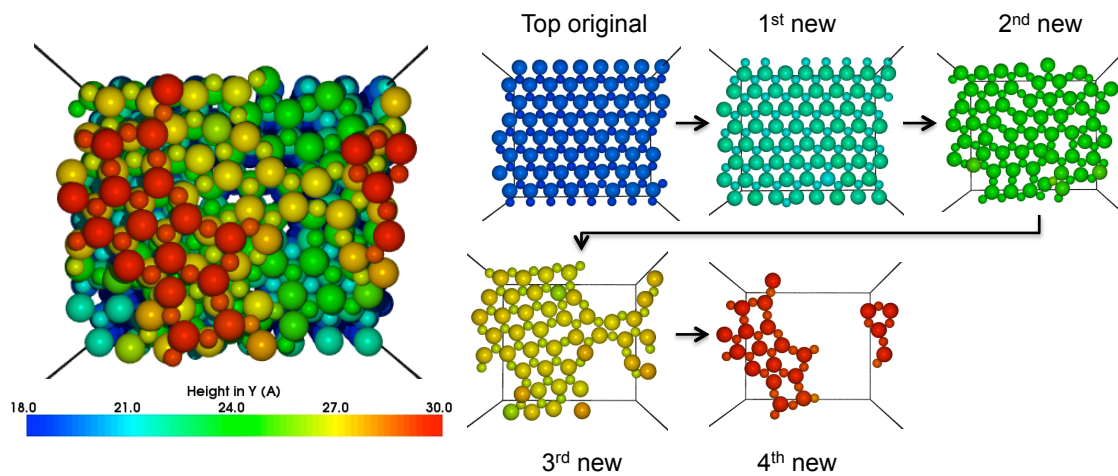


Figure 6.9: The post-annealed evaporation grown film where a stoichiometric distribution of species was deposited. The system was heated to 770 K for 10 ns to simulate the post-annealing treatment. Results indicate that the temperature is not high enough for complete recrystallisation to take place. The first new layer is complete, the post-annealing process has removed a point defect which was previously present. The second new layer, however, has failed to recrystallise into the correct sites and a stacking fault previously apparent has formed a phase boundary due to the annealing process allowing the layer to become O deficient (this is discussed later).

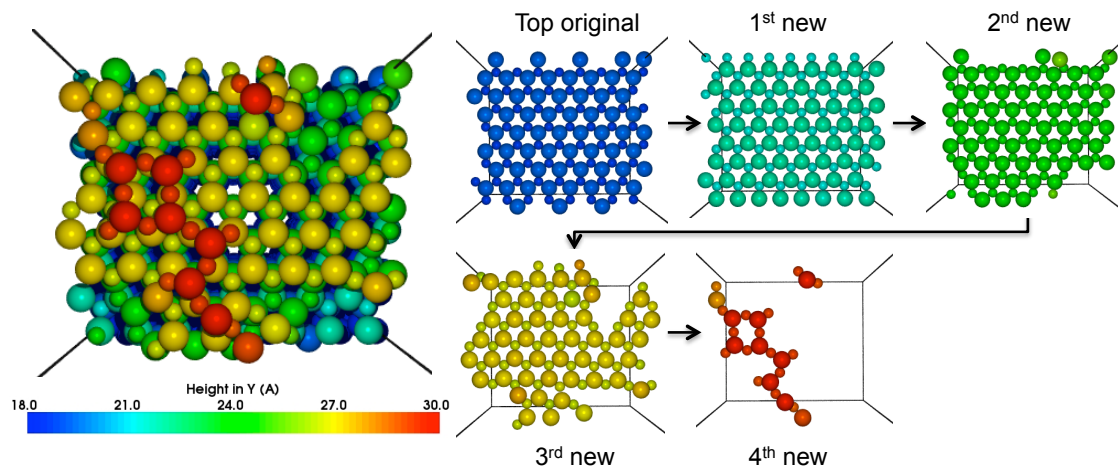


Figure 6.10: The post-annealed evaporation grown film where a stoichiometric distribution of species was deposited. The system was heated this time to 920 K to simulate a more aggressive post-annealing treatment. In this case perfect, crystalline ZnO has formed. The first, second and third new layers are all in the wurtzite phase with no stacking faults or phase boundaries present.

the zinc blende phase. Post-annealing at 920 K transfers sufficient energy to the lattice for atoms to drop down, completing layers below and thus densifying the film, shown in figure 6.12. However, all new layers have become stuck in the zinc blende phase, suggesting that an inherent O deficiency promotes the presence of stacking faults. This is investigated further later in this chapter.

Figure 6.13 illustrates the resulting film, where an O rich distribution of deposition species is used. Point defects are present and layers are incomplete. However, all new layers sit in the correct wurtzite sites, recreating the correct AaBbAa... sequence. This would suggest that the presence of O atoms decreases the probability of a stacking fault forming, this is discussed later on.

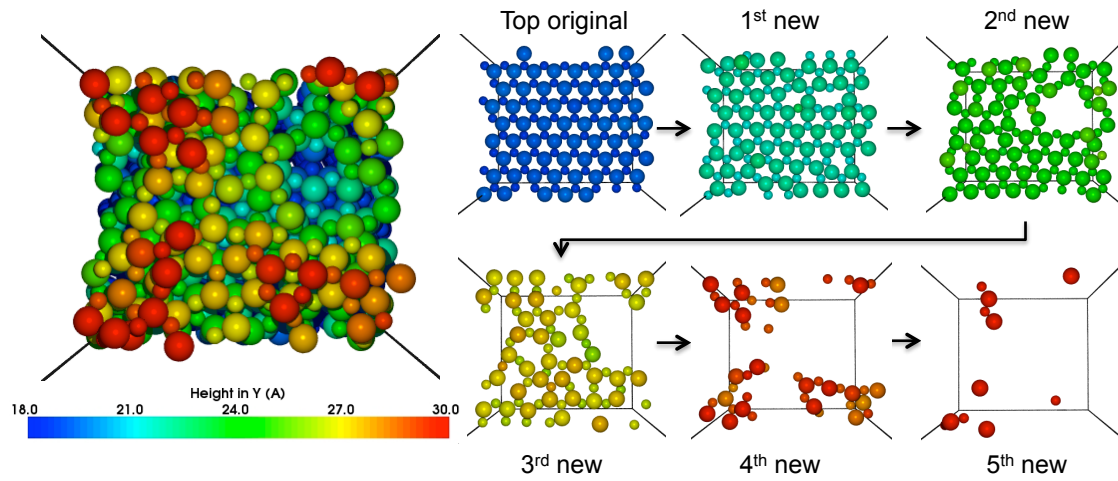


Figure 6.11: ZnO film growth obtained from the evaporation of an O deficient distribution of deposition species. The film is incomplete with voids where many O vacancies are present. Five new layers are partially formed, demonstrating a low density throughout the new layers. The deposited layers have switched to the zinc blende structure, indicating that the O deficiency throughout the film promotes stacking faults.

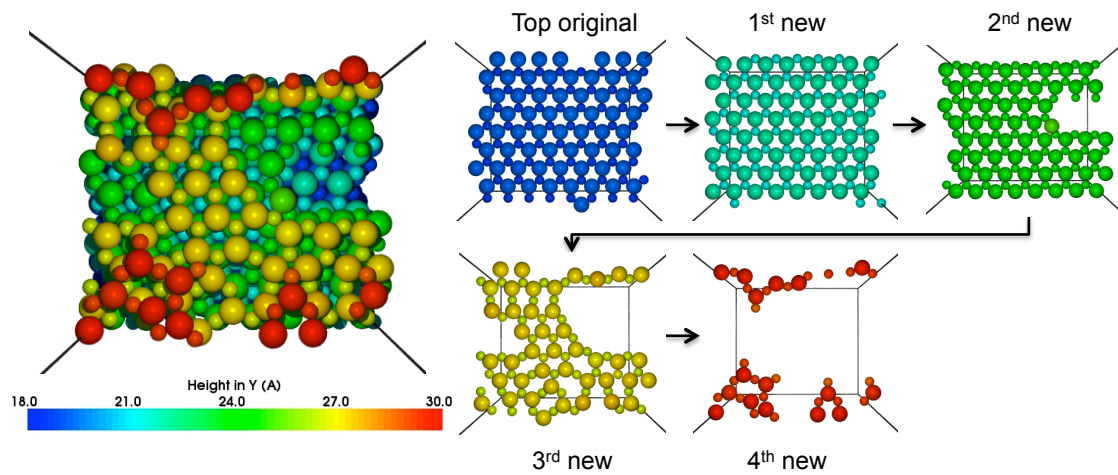


Figure 6.12: The post-annealed O deficient film, where the system was heated to 920 K during post-annealing. The energy transferred through the lattice from the annealing treatment has enabled atoms to move to lattice sites and to densify. However, all of the new layers still exhibit the zinc blende structure, sitting in the AaBbCc... sequence.

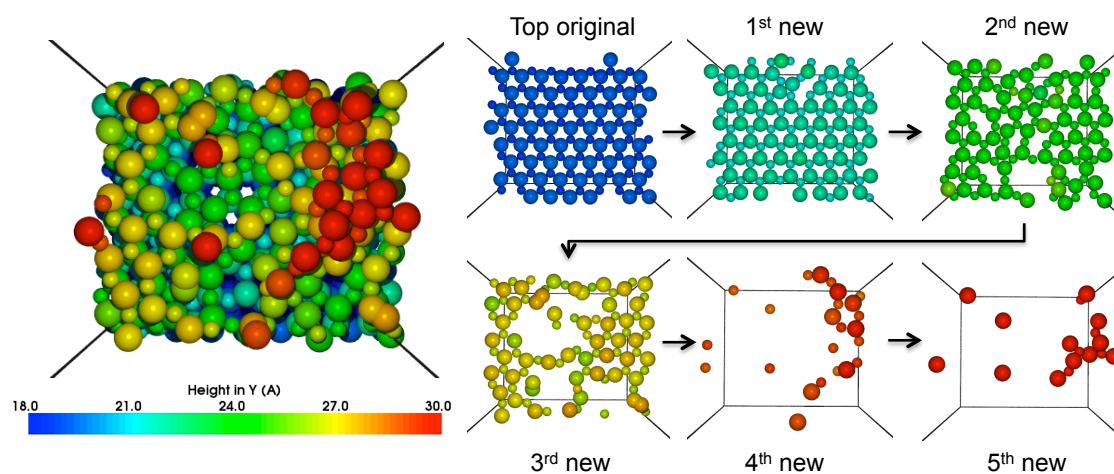


Figure 6.13: ZnO film growth obtained from the evaporation of an O rich distribution of deposition species. Although layers still exhibit point defects and vacancies, most of the new atoms sit in correct wurtzite sites.

6.5.2 Sputter Deposition

The best quality growth, shown in figure 6.14, resulted from sputtering an O rich distribution of species, as defined in table 6.1. We observe a higher density of film, as the fourth layer here has very few atoms. The original substrate surface and first new layer are undamaged and complete. The second new layer does have some defects, however, and is slightly O deficient.

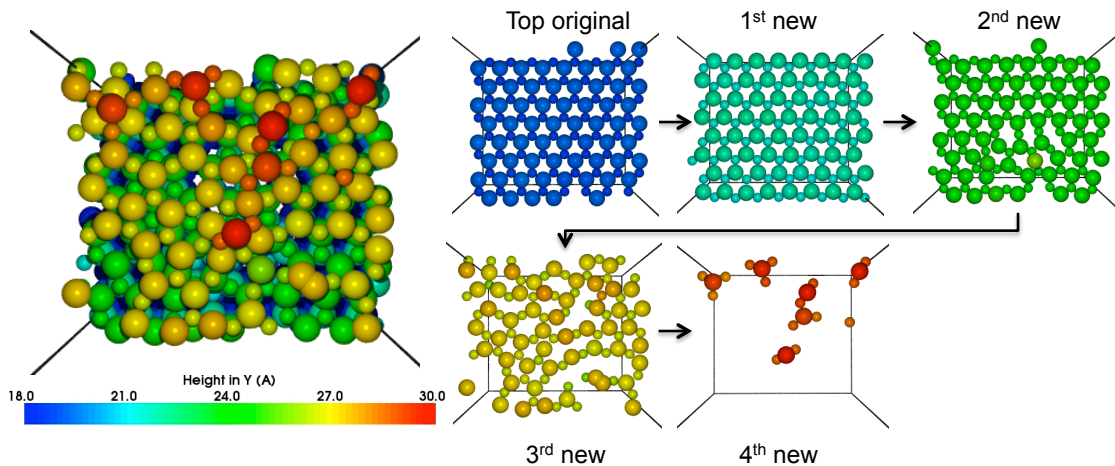


Figure 6.14: The resulting film from the sputter deposition of an O rich distribution of species, after the deposition of the equivalent to three new layers. Due to new layers not being totally complete we have four new layers. However, with only 21 atoms in the fourth layer, we would expect these to complete the layer below if growth continued and reached a steady state. The first new layer is stoichiometric and complete, whilst the second and third new layers are very slightly O deficient and not all atoms are sitting in correct lattice sites.

Sputtering alone does not allow the complete and crystalline growth which is often sought, for example in photovoltaic uses. The increased deposition energy does allow increased diffusion of atoms into correct sites, however, layers are still incomplete and contain phase boundaries. Figure 6.15 shows, in comparison, the film after a post-annealing treatment, heating the system to 920 K for 10 ns. Comparing pre-annealed and post-annealed structures it is clear that the extra temperature has caused the movement of atoms into correct sites. The film still has an inherent O deficiency but the completed layers are perfectly crystalline.

The O deficient distribution of deposition species was also investigated. Figure 6.16 illustrates the pre-annealed film where the wurtzite structure is present in the first

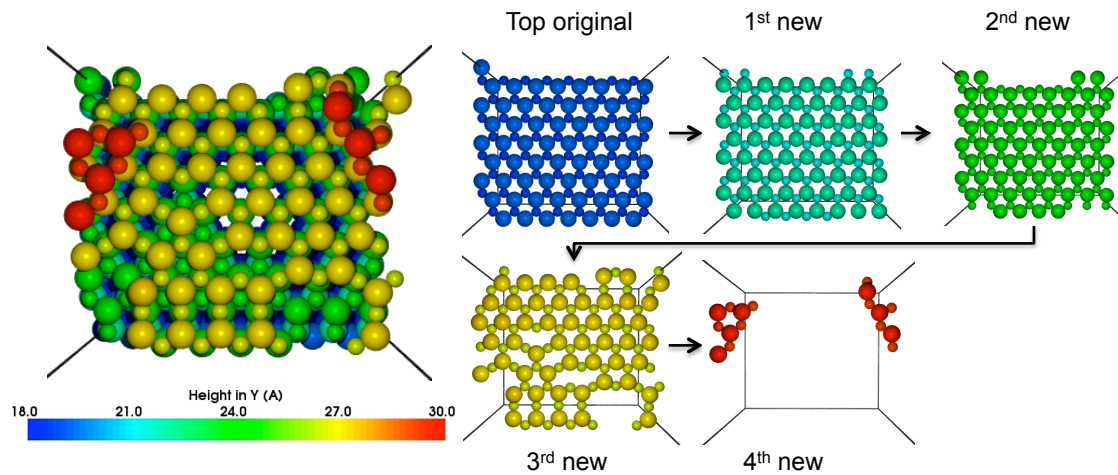


Figure 6.15: The post-annealed, sputter deposited film, where an O rich distribution of deposition species was used. The post-annealing treatment involved heating the system to 920 K for 10 ns. The first two new layers are now perfectly crystalline and in the wurtzite phase. The third new layer is O deficient and a stacking fault with a phase boundary has formed between the wurtzite and zinc blende phases.

new layer, whilst the second new layer has an O deficiency causing many defects in the layer. Post-annealing at 920 K does not provide sufficient energy for O atoms to join the layer from above. As a result, the O deficiency becomes stuck in the layer allowing a phase boundary to form around an area of zinc blende, shown in figure 6.17.

Stoichiometric distributions of deposition species did also provide good results of film growth. As described in table 6.1, two distributions were considered for the sputtering of stoichiometric ZnO, sputtering A and sputtering B. The effect on the growth of this change in distribution of species is of great importance and interest to experimentalists. The first stoichiometric distribution, sputtering A, assumes that the majority of species arrive at the substrate as ZnO units. The growth resulting from this distribution is shown in figure 6.18. It is clear that there is an O deficiency throughout the newly deposited film of 10%, although the original surface and the first new layer are almost perfect with only one point defect from a missing O atom. The second new layer does have higher O deficiency compared to the first new layer, with stacking faults and O vacancies. The second stoichiometric distribution considered, sputtering B, assumes that Zn and O atoms rarely combine in the plasma, arriving often as single Zn or O species onto the substrate. We were able to investigate the effect of this variation in the species distribution by com-

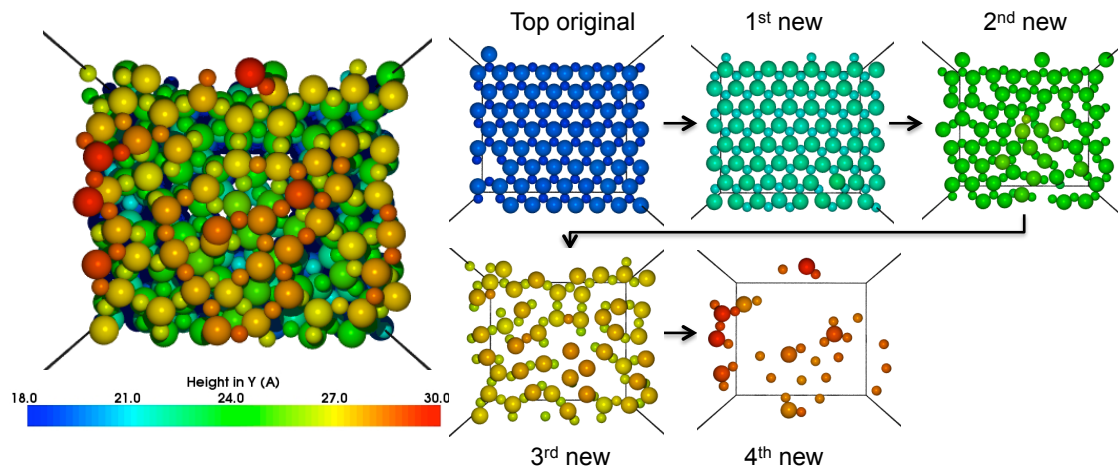


Figure 6.16: The resulting film from the sputter deposition of an O deficient distribution of deposition species. The first new layer sits in the correct wurtzite phase suggesting that the 40 eV deposition energy can be sufficient to produce some crystallinity, however, the second new layer has an area of O deficiency where some atoms are sitting in the zinc blende phase.

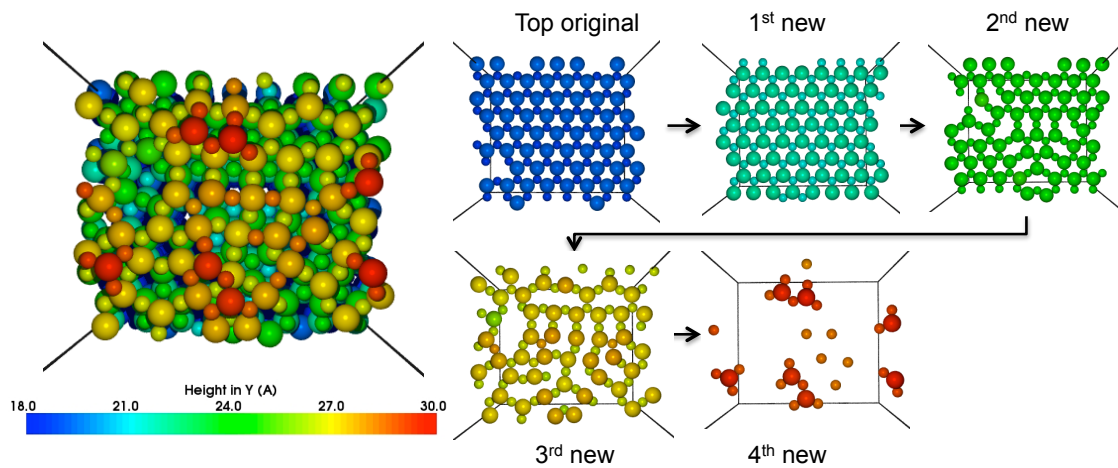


Figure 6.17: Post-annealing the film grown by O deficient evaporation at 920 K allows atoms to diffuse to neighbouring lattice sites. In this case, however, due to an inherent O deficiency in the second new layer before annealing, a phase boundary forms around an area of zinc blende.

paring the subsequent growth from the sputtering B distribution, shown in figure 6.19. The original substrate has an O vacancy, which causes some point defects. The first new layer exhibits a large O deficiency, along with a highly mismatched phase structure. The high defect density, coupled with the O deficiency has allowed the formation of a phase boundary between the wurtzite and zinc blende phases,

described more fully later. The second new layer, is again O deficient and highly mismatched, with many defects. The O deficiency throughout the newly deposited film for this distribution is almost double that of the sputtering A configuration at 18%.

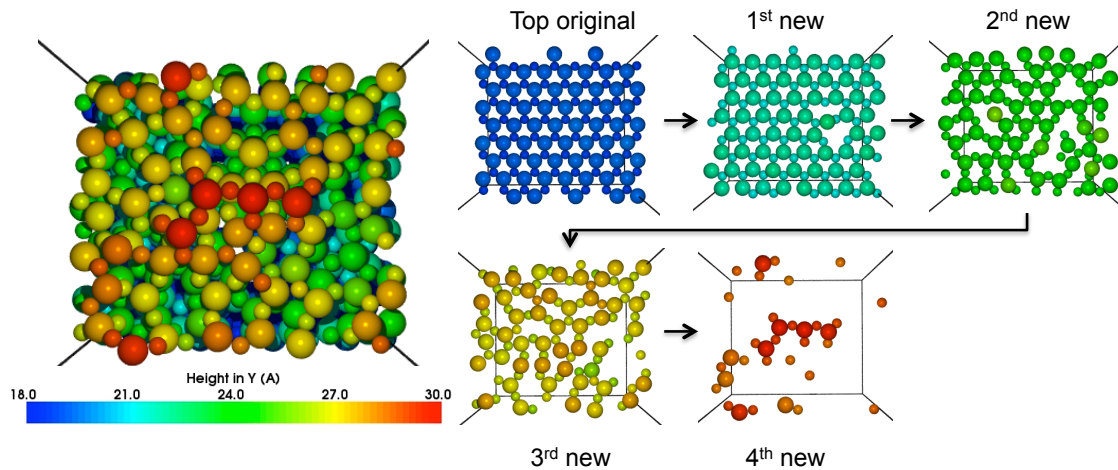


Figure 6.18: A sputter deposited film where the distribution of deposition species was a stoichiometric mix where most species arrived at the surface as ZnO units (sputtering A distribution described in table 6.1). O deficiency is evident throughout the deposited film (10% O deficient), although the original surface and the first new layer are almost perfect with only one point defect from a missing O atom. The second new layer does have higher O deficiency, with stacking faults and O vacancies.

It is now clear that the distribution of deposition species plays a huge role on the resulting growth. The distribution described by sputtering A, where largely ZnO units and a very small amount of single Zn and O₂ dimers were deposited, has produced a slightly O deficient film with a first new layer which is almost perfectly ordered in the correct wurtzite phase. Conversely, sputtering B, where over half of arriving species were single atoms, has produced a much more O deficient film with unordered and mismatched layers where stacking faults exist and phase boundaries are already evident. Even post-annealing at 920 K, as shown in figure 6.20, does not allow atoms to move into correct lattice sites. The phase boundary in the first new layer has become frozen in due to the O deficiency. O atoms have been drawn down from the surface in an attempt to restore the stoichiometry of layers below, however, this addition of O atoms is not enough to eradicate any faults or phase boundaries.

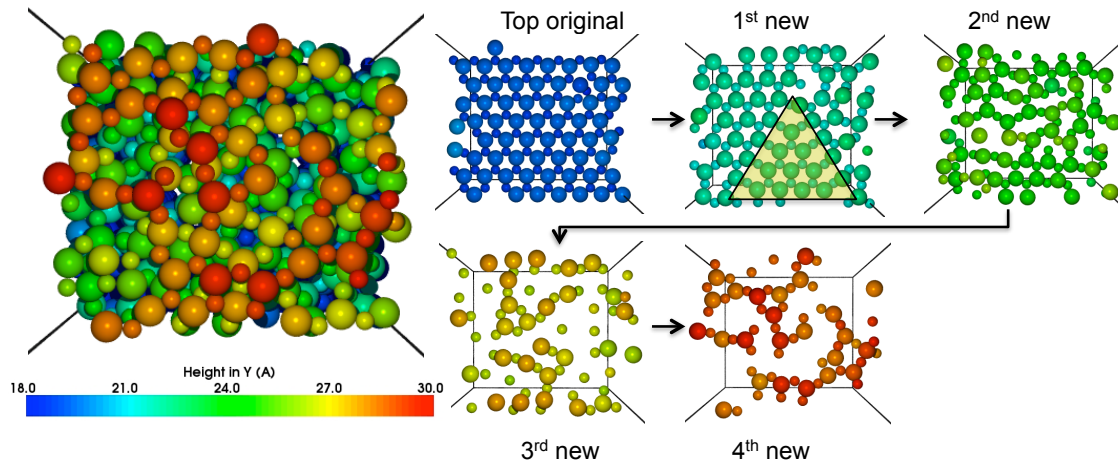


Figure 6.19: A sputter deposited film where the distribution of deposition species was a stoichiometric mix where most species arrived at the surface as single Zn or O species (sputtering B distribution described in table 6.1), resulting in high O deficiency (18% O deficient). The original substrate exhibits an O vacancy and the first new layer exhibits a large O deficiency along with a highly mismatched phase structure. The O deficiency and high defect density has allowed a phase boundary (highlighted) to form between the wurtzite and zinc blende phases. The second new layer is also O deficient and highly mismatched with stacking faults and point defects throughout.

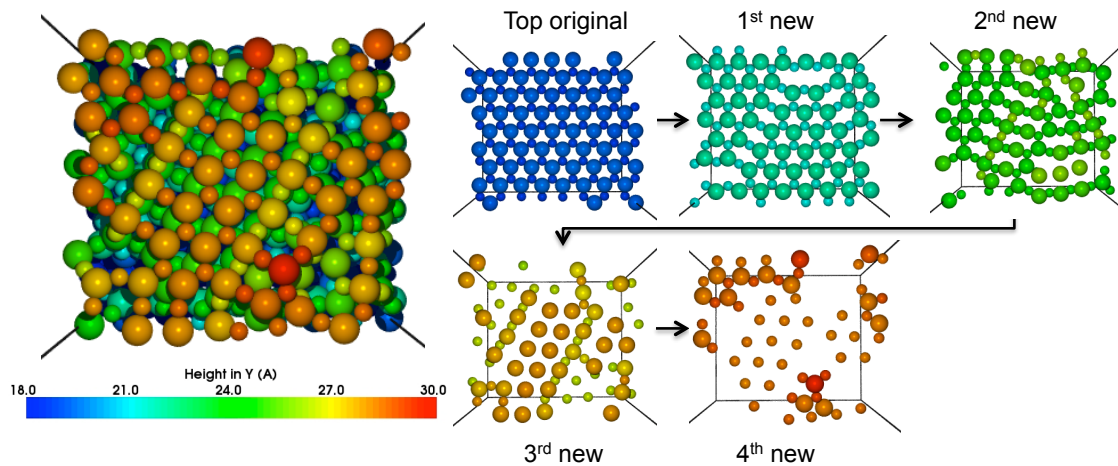


Figure 6.20: The post-annealed, sputter deposited film, where the stoichiometric sputtering B distribution of deposition species was used. The post-annealing treatment, heating the system to 920 K for 10 ns, has not been capable here of recrystallising the atoms. Instead, stacking faults already present have become fixed in, with phase boundaries forming around areas of zinc blende.

An interesting comparison between the simulations of the two sputtering deposition distributions (A and B) is the behaviour of deposition species at the surface. The first simulation, sputtering A, observes a large proportion of surface O sputtered by the arrival of ZnO clusters. The sputtering B simulation, however, observes a large proportion of arriving O and O₂ either reflecting or sputtering other O atoms from the surface, along with a small proportion of arriving Zn also sputtering O atoms. Some ZnO depositions do still cause the sputtering of O atoms. The difference in behaviour of the species deposited plays a huge role in the subsequent growth quality.

6.5.3 Growth Mechanisms

During all simulations O and O₂ reflect off the surface, are sputtered from the surface or evaporate during MD stages (around 0.1-0.2 % of depositions involve an O or O₂ cluster reflecting off the surface). As described above, O ejection from the surface is caused by the deposition of any of the deposition species. This leaves an inherent O deficiency in the film, which reflects results seen in the literature [183]. No Zn atoms have been observed leaving the surface, agreeing with experimental evidence that films are Zn rich [184]. We do indeed observe an O deficiency in all of our simulations. The closest film to stoichiometric is the evaporated film grown using a stoichiometric distribution of deposition species where only ZnO is deposited (0.006% O deficiency). The highest O deficiency (18%), however, is observed from sputtered growth using a stoichiometric distribution (sputtering B), where mainly single species arrive at the surface, increasing the number of O atoms ejected from the substrate.

During early stages of growth, Zn atoms bind to the O-terminated surface. Free O ad-atoms or O₂ dimers aid the Zn diffusion by binding to the Zn, as illustrated in figure 6.21. This ad-atom cluster can then diffuse across the surface. The Zn atom then splits from the cluster when it reaches an appropriate site. Energies required for these transitions are typically below 0.35 eV, with ZnO₂ diffusion requiring as little as 0.1 eV. Although Zn diffusion takes place preferentially when bonded to an O or O₂ dimer, single Zn atoms can also diffuse. Figure 6.22 illustrates an important single atom Zn transition whereby a Zn below the surface sitting in an interstitial site diffuses towards a surface lattice site, requiring only 0.09 eV. This mechanism aids the crystallisation of the structure during growth. Other single Zn

atom diffusion pathways over the surface, typically involving a hop of the atom to an adjacent lattice site, require ~ 0.2 eV. Thus, the least energy expensive method for Zn diffusion on the surface is by bonding to O_2 dimers to form ZnO_2 .

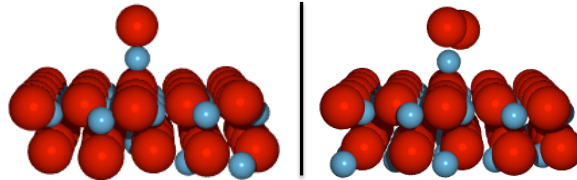


Figure 6.21: A Zn atom on the surface is often bound by a O or O_2 dimer to form a $ZnO_{(2)}$ cluster, both of which are illustrated here. The energy required for a ZnO ad-unit to diffuse on the surface is between 0.15 eV and 0.35 eV, whereas a ZnO_2 unit requires much less (usually < 0.1 eV). Smaller, grey spheres represent Zn, whilst larger, red spheres represent O.

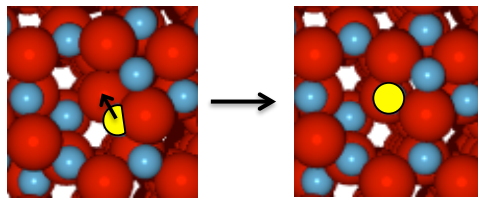


Figure 6.22: During a simulation, interstitials form below the surface due to bombardment and disruption of the surface. The energy required for this Zn interstitial, marked in yellow, to diffuse to its correct lattice site, is 0.09 eV. This small barrier indicates that this is a key mechanism by which Zn atoms reach their correct sites and thus crystalline ZnO is formed.

An important mechanism for the nucleation of ZnO growth is the formation and movement of Zn_xO_y strings on the surface. These strings form on the surface via complicated, concerted motions as illustrated in figure 6.23, where 0.44 eV is required for the formation of the string. Figure 6.24 illustrates the behaviour of these string like structures, where the vibration of a string on the surface occurs with energy barriers of between 0.2 and 0.3 eV. Later in the simulation, after tens of milliseconds, neighbouring strings and atoms become attached, forming a larger structure of strings, with a formation energy of 0.42 eV. Finally, in order for crystalline ZnO to form, some hundreds of milliseconds later, the strings interconnect even more and diffuse and flip to form a hexagonal structure on the surface.

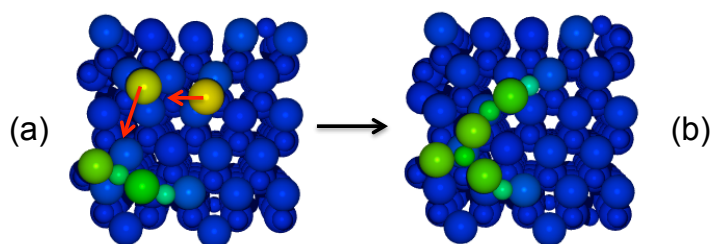


Figure 6.23: Two ZnO units marked by the arrows move as indicated towards a Zn_2O_2 string to form a longer string. The Zn atom lies under the O atom in the unit and is not visible in (a). This transition involves a concerted motion of 5 atoms, requiring 0.44 eV to occur. Smaller spheres represent Zn, larger spheres represent O and the atoms are coloured by height, where the atoms higher up are lighter in colour.

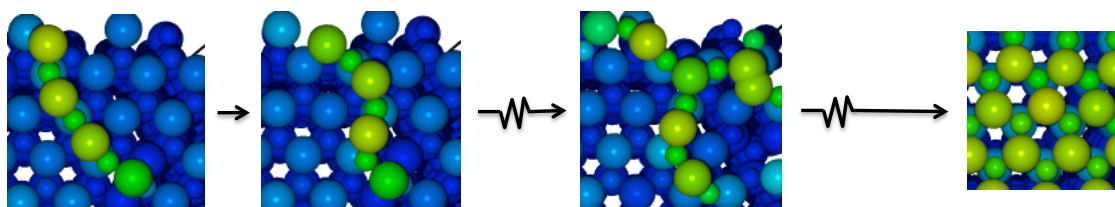


Figure 6.24: Zn_xO_y strings on the ZnO surface act as a nucleation site for growth. These strings move with small energy barriers (0.2-0.3 eV), as shown in the first two configurations. The third configuration shows strings forming together with new atoms joining on to make larger structures, overcoming a barrier of 0.42 eV. Finally, after hundreds of milliseconds, a hexagonal structure forms, as required for the crystalline ZnO growth.

6.5.4 Stacking Faults

Stacking faults and twin boundaries have been observed experimentally [155], however, what is not yet understood is how stacking faults occur. The correct wurtzite structure would be the AaBbAaBb stacking sequence, however, we observe some zinc blende (AaBbCc) structures during some of the simulations. Figure 6.1 shows the difference between the two phases of ZnO. The most obvious difference is the filling of fcc hollow sites in the zinc blende phase (see figure 6.2 for high symmetry adsorption sites). The hcp site used in the wurtzite phase is the most stable site for an O atom. However, the energy difference between an O atom sitting in the hcp site or in the fcc hollow (zinc blende phase), as shown in figure 6.25, is <0.05 eV, in agreement with DFT studies [185]. This explains how, using very little energy, some films have formed the zinc blende structure during growth.

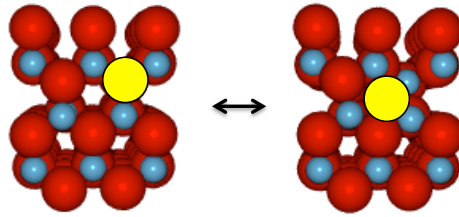


Figure 6.25: Growth switching between the preferred, more stable wurtzite structure and the zinc blende structure often occurs during a simulation. The energy difference for the O atom, marked in yellow, to switch to the zinc blende phase is <0.05 eV. This small difference in energy enables atoms and layers to switch to the zinc blende phase.

During our simulations, we observed stacking faults and phase boundaries. Figure 6.26 illustrates a zinc blende phase within a wurtzite structure, which forms a phase boundary on the surface. 6 O atoms sit in fcc hollows, in the Cc stack. Correct wurtzite sites are indicated and it is clear that a shift of the whole zinc blende phase to wurtzite would result in 4 O vacancies, hence confirming an O deficiency in the film, which is common in ZnO deposited films [186,187]. The presence of O vacancies in the film leads to a phase change, where zinc blende forms within the wurtzite phase. This forms a phase boundary, which requires less O atoms than if the layer sat in one phase. The presence of a phase boundary in a film will change optical and electrical properties of the film. For systems that are observed to be O deficient, we see a mixture of wurtzite and zinc blende phases in a single layer. The phase boundary between these two phases is O deficient. It is not clear whether it is the presence of the phase boundary that drives the O deficiency, or the presence of the O deficiency that drives the formation of a phase boundary.

Pre-annealed, evaporated ZnO films almost all exhibit stacking faults or a phase boundary. Sputtered films, however, do not all exhibit faults. The evaporation growth, shown in figure 6.8, illustrates a phase boundary even when annealed at the lower temperature (figure 6.9). When evaporation deposition was simulated using an O deficient distribution of deposition species, the pre-annealed film had a mixture of wurtzite and zinc blende phases. Annealing this film at 920 K actually changed the phase of the new layers to zinc blende. Once a film has inherent defects and stacking faults, annealing at temperature is not always sufficient to recrystallise and reorder the atoms into the wurtzite phase. As previously discussed, it costs <0.05 eV for O ad-atoms to shift from a wurtzite to zinc blende site, suggesting that during annealing, the heated atoms could cross this barrier to change phase.

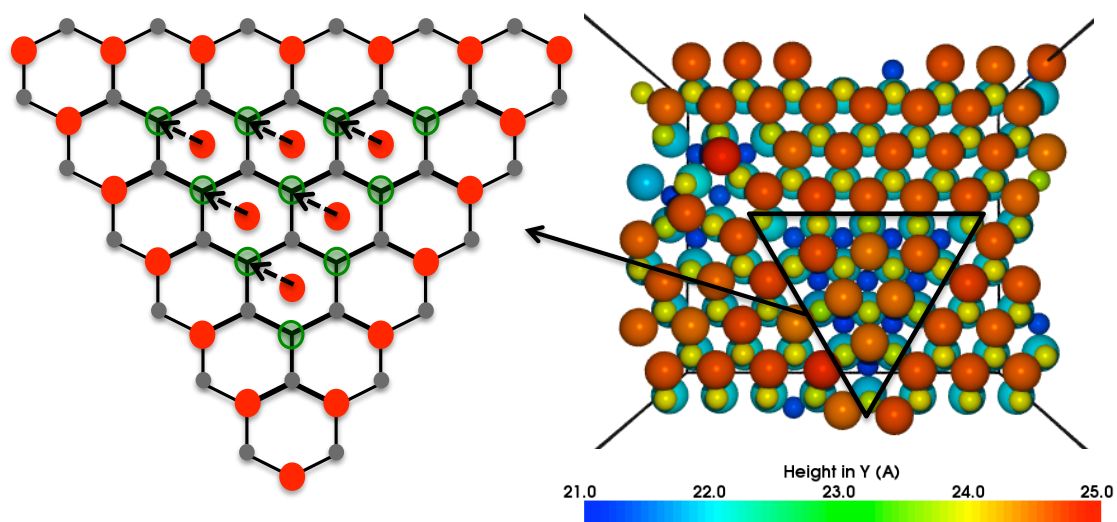


Figure 6.26: Sputtered growth using the O deficient distribution of deposition species. Annealing at 920 K attempts to recrystallise the film, however, due to an already inherent defect in the layer and an O deficit, annealing actually forms a phase boundary in the layer. On the right is an image taken from above a stacking fault. The highlighted area shows a zinc blende phase within a wurtzite structure, forming a phase boundary. On the left is a simple, atomistic diagram of the stacking fault where the light, transparent green circles represent an O vacancy. Arrows show clearly where atoms would need to diffuse for reordering to the wurtzite phase.

All simulations of sputter deposition initially followed the correct AaBbAa wurtzite structure, at least in the first few new layers (only the first and second new layers are considered due to a steady state not yet being reached). The O deficient simulation, shown in figure 6.26, shows that annealing does not always have the ability to recrystallise ZnO into the wurtzite structure. If a defect or O deficiency is already present in the film then there is not always enough kinetic energy for the defects to stabilise and diffuse to correct sites.

6.6 Discussion

Initial testing of the interatomic potentials and different polar surfaces of ZnO by the simulation of 64,000 single point depositions allowed an insight into the behaviour of ZnO under bombardment. The ReaxFF potential [56] was found to reproduce the most realistic behaviour of ZnO, with the variable charge and more

realistic O₂ dimer behaviour on the surface. The Albe potential allowed O₂ dimers to split too easily, whereas the ReaxFF respected the high binding energy of dimers. With regards to which polar surface to use as the substrate during growth simulations, O-terminated was thought to be more realistic due to the presence of O₂ in a typical deposition chamber [182]. This O₂ within the plasma would bind to a Zn-terminated surface very quickly, producing an O-terminated surface.

ZnO film growth was simulated for ~ 1 second of real deposition time using long time scale dynamics, allowing for the deposition of three monolayers of atoms onto the O-terminated wurtzite substrate. Different distributions of deposition species were used in order to simulate stoichiometric, O rich and O deficient environments. Stacking faults and phase boundaries have been observed during many of our simulations. During some simulations, part or all of a layer switches to the zinc blende phase requiring very little energy (a single O atom moves from wurtzite to zinc blende with < 0.05 eV). Growth can switch to the zinc blende phase creating a stacking fault, or if only part of a layer has switched to the zinc blende phase, then this is a phase boundary. These phase boundaries have been found to occur more often in O deficient layers, however, it is unclear whether the phase boundary is caused by an O deficiency or vice versa.

Deposition by evaporation of stoichiometric, O rich and O deficient distributions of deposition species produced incomplete films with various vacancies, defects and inherent stacking faults. The best quality film, however, resulted from purely ZnO units impacting upon the surface, where the film was almost stoichiometric (only 0.001% O deficient). The film has an almost perfectly complete and crystalline first layer. However, the second layer exhibits a phase boundary whereby some of the layer is in the correct wurtzite phase and some of the layer has switched to the zinc blende phase.

To simulate the annealing treatment, the deposited film is heated up using MD. The films deposited by evaporation are annealed at 770 K and 920 K. The lower temperature annealing produces a lattice which no longer has point defects in the first layer, but the second layer still exhibits a phase boundary. The higher temperature, however, promoted recrystallisation by eradicating phase boundaries and stacking faults. The high temperature of the annealing introduces enough energy to atoms to enable them to overcome barriers to move to correct wurtzite sites.

Sputter deposition transfers more kinetic energy to the substrate from the higher energy impacts, hence growth is generally more complete, dense and crystalline than evaporation growth, also exhibiting less stacking faults. The best distribution of deposition species was found to be the O rich distribution. The film is, however, slightly O deficient, confirmed by a statistical analysis showing that 0.1-0.2 % of O or O₂ reflects off the surface during deposition, resulting in a 0.03% O deficiency. No Zn is observed to leave the surface, suggesting that Zn binds to the surface with a high energy. The O deficit means that the wurtzite structure cannot form correctly due to O vacancies in the layer, thus enabling the zinc blende phase to occur, resulting in these phase boundaries. Annealing of this film at 920 K enables the completion and recrystallisation of layers. A layer in the pre-annealed film which had a phase boundary is rectified by the post-annealing treatment. The film becomes denser and more crystalline, with a phase boundary now only in the third new layer, although this layer is not so important as a steady state for that layer will not be reached during our simulations.

During the sputtering simulations, two variations of a stoichiometric distribution of deposition species were compared. The first distribution, sputtering A, deposited largely ZnO units which resulted in a film with 10% O deficiency. The second distribution, sputtering B, deposited largely single species, causing increased sputtering and reflection and thus a higher O deficiency (18%). The higher O deficiency led to a higher defect density, thus enabling the formation of stacking faults and phase boundaries. An O deficiency within a layer was found to exist due to the presence of O vacancies and the formation of a phase boundary, where O atoms sit in both zinc blende and wurtzite sites.

Methods used enabled the in-depth analysis of growth mechanisms seen during growth, including complicated concerted, multi-atom motions which are not intuitive. An initial mechanism observed during early stages of growth was the Zn ad-atom transportation to correct lattice sites via bonding to O ad-atoms or O₂ dimers. These 2 or 3 atom clusters require as little as 0.1 eV to diffuse across the surface, transporting Zn atoms to correct lattice sites. Single Zn atoms on the surface also have the ability to diffuse alone, with energy barriers of ~ 0.2 eV. An important mechanism to deal with Zn interstitials below the surface involves a Zn interstitial diffusing to a correct lattice site in the surface with only 0.09 eV.

Found to be of great importance in the growth of ZnO acting as a nucleation site

for growth are the Zn_xO_y strings on the surface. These are formed by complicated, concerted motions where 0.44 eV is required for the transition. Once formed, these strings move with energy barriers of between 0.2-0.3 eV until neighbouring atoms and strings then join to form a larger structure of strings. This process occurs after some tens of milliseconds, with hexagonal structures appearing hundreds of milliseconds later once enough atoms have been deposited, allowing the strings to join together and diffuse correctly into the wurtzite structure.

These simulations have allowed a more detailed understanding of the process of ZnO film growth and the important mechanisms involved, a lot of which are non-intuitive. It is clear from this work that the deposition process used does play a significant role on the resulting surface morphology and film quality and that annealing treatments can be very useful for recrystallisation, although not all defects and phase boundaries can be eradicated even from this high temperature annealing.

Chapter 7

Conclusions

The goal of the thesis was to model the thin film growth of various materials over experimentally realistic time scales. Industrial PVD techniques were modelled in order to understand the role of deposition energy on the resulting thin film morphology, quality and properties. In the experiments, there are many parameters which are altered during the deposition processes. Experiments require time and money to allow these parameters to be altered and optimised. Simulation enables the optimising of parameters without the need for real life experiment, allowing a more precise understanding of the effect of different parameters on the resulting thin film growth. This research aimed to provide an understanding of the specific mechanisms observed during growth, allowing either crystalline or porous films to grow.

Thin film growth occurs over longer time scales than can be modelled using traditional MD methods. Long time scale dynamics techniques allow simulation over this longer time scale and in this project up to 9 seconds have been simulated. Otf-KMC has been successfully applied to surface growth, without requiring unrealistically high temperatures.

Metal thin film growth was simulated for around 0.3 seconds, allowing for the deposition of three monolayers by evaporation, ion-beam assisted evaporation and magnetron sputtering. Ag (111) and (100) produced similar results. Evaporation deposition did not provide sufficient kinetic energy for atoms to diffuse or for layers to become complete. Whereas sputtering on both Ag surfaces allowed more complete structures to form due to the increased deposition energy. Ion-beam assist on the (111) surface illustrated the effect of the increased energy transfer from Ar

ion bombardment, allowing layers to become slightly more complete than evaporation alone. Stacking faults were observed on the (111) surface from the low energy evaporation, where a four atom cluster was found to switch between fcc and hcp stacking sequences until pinned by the addition of a fifth atom. Higher energy depositions during sputtering, however, did not produce any stacking faults, suggesting that the increased energy eradicates stacking faults. Al (111) and (100), although being structurally very similar to Ag, showed differences in the resulting thin film growth. Evaporation and sputtering produced very similar results, suggesting that the deposition energy for Al does not play a significant role on the resulting surface morphology. Inclusion of an ion-beam assist on the (111) surface illustrated that perhaps an ion-beam is not always helpful, it may in fact hinder the growth. Instead of aiding growth by transferring extra kinetic energy to the film, the ion-beam damaged the film by producing Al subsurface voids where subsurface Ar clusters formed. Ag and Al, both fcc simple metals, showed opposing results for evaporation deposition. The simulation methods allowed us to examine specific diffusion pathways on the surface, of which a very important one was found to be the Ehrlich-Schwoebel transition. This ES transition, allowing layer-by-layer growth by the dropping of atoms off edges to complete layers, was found to be very different for Ag and Al. On Ag surfaces the ES barrier was found to be 0.42 eV, whereas on Al it was between 0.07 eV (111) and 0.24 eV (100). This difference in barrier height accounts for the observed differences between Ag and Al thin film growth.

In order to gain understanding of the behaviour of the rutile (110) TiO_2 surface, first 15,000 single point depositions were simulated using MD. Deposition energies between 20 eV and 100 eV were simulated, enabling the classification of four main defects. Interstitials were found to be Ti atoms in most cases, with up to 7 interstitials forming per impact. Linear correlations between deposition energy and the number of interstitials and the depth of interstitials was observed. However, for low energy impacts with no Ti in the deposition cluster, often no interstitials were formed. Both O and Ti vacancies were observed, with Ti depositions creating the most vacancies. O ad-atoms were found to form easily on the surface, however, due to the low escape energy for O, atoms were observed to reflect or sputter from the surface. With an initial insight to rutile surface behaviour, growth was first simulated using MD at 1000 K to speed up transitions. Stoichiometric, Ti rich and O rich distributions of deposition species were simulated, with deposition energies ranging from 20 eV to 100 eV. Stoichiometric deposition resulted in films with voids

throughout, whilst both Ti rich and O rich depositions created large Ti interstitial counts throughout the film, with O rich depositions also producing voids. The use of the high temperature provided an initial insight into film growth. Otf-KMC allowed the simulation of rutile growth for up to 9 seconds without elevated temperatures skewing the results, investigating the stoichiometric deposition of four monolayers of atoms. Evaporation deposition did not transfer sufficient energy to the surface for complete, crystalline layers to form. A low energy ion-beam assist (40 eV) promoted more atomic mixing, with high energy assist (100 eV) damaging the substrate. Sputter deposition, however, produced a much more complete and crystalline film due to the higher arrival energy of atoms. The simultaneous Ar bombardment did not have a significant effect on the film. 100 eV depositions were also simulated, producing a seemingly crystalline film, however, increased Ti interstitials were created, which would effect the film's optical properties. During rutile growth, otf-KMC methods allowed an understanding of the mechanisms enabling growth to be gained. A key mechanism was found to be the annealing of Ti interstitials upwards in the presence of an O rich surface. However, if interstitials are more than a few layers deep within the lattice, they will diffuse to the surface at a much slower rate.

In order to simulate ZnO film growth, 64,000 single point depositions were first modelled to test different interatomic potentials and polar surfaces. The ReaxFF potential was chosen based on O₂ dimer behaviour and variable charge inclusion, with the O-terminated surface chosen for the growth simulations based on experimental knowledge. Otf-KMC methods allowed simulation for around 1 second, enabling the deposition of three monolayers onto a wurtzite substrate. Stoichiometric, O rich and O deficient distributions of deposition species were investigated, simulating evaporation and magnetron sputter deposition. Evaporation produced incomplete films with stacking faults and defects, with the stoichiometric distributions providing the best quality film, however, a phase boundary is present where a zinc blende phase is surrounded by wurtzite. Annealing the film at 770 K and 920 K allowed some recrystallisation to occur, with 920 K enabling the eradication of the phase boundary by the addition of kinetic energy. Sputter deposition, due to the increased kinetic energy transferred from depositions, produced a more complete, crystalline film with less defects. The O rich distribution of deposition species produced the best quality film, however, an O deficiency was still observed throughout the new layers due to O reflection during deposition. Zn has a higher binding energy to the surface than O, resulting in no Zn reflection. The O deficit

in the film allowed the formation of a phase boundary, suggesting that an inherent O deficit promotes the formation of a zinc blende phase within a wurtzite structure. Annealing the film at 920 K allows the removal of the phase boundary by promoting the diffusion of O atoms from zinc blende sites to more stable wurtzite sites. During sputtering, simulation allows us to understand the effect of Zn oxidising either in the plasma, en route to the surface or on the surface itself. When Zn oxidises in the plasma, thus arriving mainly as ZnO units, a 10% O deficiency was observed in the new film. Whereas, when Zn oxidises on the surface, the O deficiency is almost double, suggesting that we would prefer Zn to oxidise in the plasma as an O deficiency in the film has been shown to promote the formation of stacking faults and phase boundaries. The simulation methods have encouraged a deeper understanding of how twin boundaries form. O atoms switch phase from wurtzite to zinc blende over very short time scales, suggesting that zinc blende can form easily and with no extra energy transferred to the system. Once we have an O deficiency within a film, some O atoms easily shift to the zinc blende phase, forming a phase boundary which requires less O atoms. Therefore, phase boundaries are almost promoted and encouraged by an O deficit. The post-annealing does not always provide sufficient energy to eradicate phase boundaries. An important mechanism observed for the nucleation of ZnO growth is the formation and diffusion of Zn_xO_y strings on the surface until many strings come together and form the desired hexagonal wurtzite structure.

The otf-KMC methods used throughout this thesis have provided a more precise understanding of the processes during thin film growth. Specific transitions have been studied on each surface to understand how the films grow and which mechanisms are key. Often, multiple atom, concerted motions were found to be of significant importance during growth.

The methods applied throughout this thesis have been shown to provide realistic, accurate results which agree with experimental work. Allowing simulation to aid experimental decisions is a great advantage and now that results of numerous materials have shown excellent agreement with experiment, it becomes an ideal time to form a partnership with experiment.

7.1 Future Work

The methods used throughout this thesis were implemented in the last few years. During this work, modifications were made to the method codes in order to try to optimise the methods for each material. Continued code development is required for the methods to be fully optimised for the application to a wider variety of materials. Currently, a group at Loughborough University is carrying out this continued code development, rewriting the codes in Python. Modifications to the codes aim to include a method to reuse transitions by recognising the geometry, in order to save computational time if symmetrical transitions are found. Faster saddle point finding methods are also being investigated such as combining the dimer and Lanczos methods.

Otf-KMC methods have allowed the investigation of intrinsic metallic and oxide thin film growth over realistic time scales, however, in many applications of thin films doping is an important aspect. During this research intrinsic ZnO has been investigated due to its important role in newly developed TCO's, however, for TCO use the ZnO is doped with a small amount of Al (0.5%). In order to simulate AZO, interatomic potentials require fitting to the AZO interactions, allowing the effect of the Al within the film to be investigated. During the scope of this research this was not possible. Future work could involve finding an appropriate potential to model AZO and thus applying the otf-KMC methods to surface growth, providing an excellent insight into TCO development. CdTe is another material of great importance in the coming years in thin film photovoltaics. Experimental evidence suggests that stacking faults and twin boundaries are highly prevalent in CdTe thin films and these have huge effects on the properties of the film. Therefore, simulation would provide insight into why and how these stacking faults and twins occur, allowing experimentalists to understand how to eradicate them from their films or learn how to deal with them. Many other materials could also benefit from the partnership of simulation with experiment in order to understand how to take advantage of new materials.

During this work, evaporation, ion-beam assisted evaporation and magnetron sputtering have been investigated. However, many other PVD techniques exist such as pulsed laser deposition. The methods have the ability to simulate other deposition techniques by altering the parameters of the deposition phase. Pulsed laser deposition could be simulated by applying short pulses of depositions, with diffusion

steps in between. In the future, more deposition techniques should be added to the models, allowing for an even greater understanding of thin film growth. Simulation has the ability to provide experimentalists and industrialists with guidelines by which thin films grow. It is therefore important that this power is harvested and used to really understand the processes occurring during deposition. The ability to change so many parameters during simulations, without the need for experiment, must be utilised to drive the industry forwards in the understanding of deposition and growth processes.

References

- [1] L. J. Vernon, S. D. Kenny, R. Smith, and E. J. Sanville. Growth mechanisms for TiO_2 at its rutile (110) surface. *Physical Review B*, 83:075412, 2011.
- [2] W. J. Hehre. Ab-initio molecular orbital theory. *Accounts of Chemical Research*, 9(11):399–406, 1975.
- [3] P. Hohenberg and W. Kohn. Inhomogeneous electron gas. *Physical Review*, 136(3B):B864–B871, 1964.
- [4] R. Smith, editor. *Atomic and ion collisions in solids and at surfaces: theory, simulation and applications*. Cambridge University Press, 1997.
- [5] L. J. Vernon. *Modelling Growth of Rutile TiO_2* . Ph.D. thesis, Loughborough University, 2010.
- [6] G. Henkelman and H. Jónsson. Improved tangent estimate in the nudged elastic band method for finding minimum energy paths and saddle points. *Journal of Chemical Physics*, 113(22):9978, 2000.
- [7] G. Henkelman, B. Uberuaga, and H. Jónsson. A climbing image nudged elastic band method for finding saddle points and minimum energy paths. *Journal of Chemical Physics*, 113(22):9901, 2000.
- [8] M. Robinson. Atomic visualisation and analysis (AVA). <http://avas.sourceforge.net/>, 2010.
- [9] Persistence of Vision Pty. Ltd. Persistence of vision raytracer (version 3.6). <http://www.povray.org/download/>, 2004.
- [10] P.B. Barna. *Diagnostics and Applications of Thin Films*, chapter Crystal growth and recrystallization during structure evolution of thin films, pages 295–310. Institute of Physics Publishing, Bristol, 1992.

-
- [11] I. Petrov, P. B. Barna, L. Hultman, and J. E. Green. Microstructural evolution during film growth. *Journal of Vacuum Science and Technology A*, 21(5):S117–S128, 2003.
- [12] J. A. Thornton. Influence of apparatus geometry and deposition conditions on the structure and topography of thick sputtered coatings. *Journal of Vacuum Science and Technology*, 11(4):666, 1974.
- [13] L. I. Maissel and R. Glang. *Handbook of Thin Film Technology*, chapter 4: Application of Sputtering to the Deposition of Films, pages 4.1–44. McGraw-Hill, New York, 1970.
- [14] B. J. Alder and T. E. Wainwright. Studies in molecular dynamics: 1. general method. *Journal of Chemical Physics*, 31(2):459–466, 1959.
- [15] A. Rahman. Correlations in the motion of atoms in liquid argon. *Physical Review*, 136(2A):A405–A411, 1964.
- [16] J. E. Lennard-Jones. On the determination of molecular fields. ii. from the equation of state of a gas. In *Proceedings of the Royal Society of London. Series A, Containing Papers of a Mathematical and Physical Character (1905-1934)*, volume 106, pages 463–477, 1924.
- [17] G. Moore. Cramming more components onto integrated circuits. *Electronics Magazine*, 38(8), 1965.
- [18] W. C. Swope, H. C. Andersen, P. H. Berens, and K. R. Wilson. A computer simulation method for the calculation of equilibrium constants for the formation of physical clusters of molecules: Application to small water clusters. *Journal of Chemical Physics*, 76(1):637–650, 1982.
- [19] W. T. Rankin. *Efficient Parallel Implementations of Multipole Based N-body Algorithms*. PhD thesis, Duke University, 1999.
- [20] P. Ewald. Die berechnung optischer und elektrostatischer gitterpotentiale. *Annalen der Physik*, 369(3):253–287, 1921.
- [21] W. W. Wood and F. R. Parker. Monte carlo equation of state of molecules interacting with the lennardjones potential. i. a supercritical isotherm at about twice the critical temperature. *Journal of Chemical Physics*, 27(3):720–734, 1957.

- [22] R. A. Buckingham. The classical equation of state of gaseous helium, neon and argon. In *Proceedings of the Royal Society of London. Series A, Mathematical and Physical Sciences (1934-1990)*, volume 168, pages 264–283, 1938.
- [23] M. S. Daw and M. I. Baskes. Semiempirical, quantum mechanical calculation of hydrogen embrittlement in metals. *Physical Review Letters*, 50(17):1285–1288, 1983.
- [24] M. S. Daw and M. I. Baskes. Embedded-atom method: Derivation and application to impurities, surfaces, and other defects in metals. *Physical Review B*, 29(12):6443, 1984.
- [25] S. M. Foiles, M. I. Baskes, and M. S. Daw. Embedded-atom-method functions for the fcc metals Cu, Ag, Au, Ni, Pd, Pt and their alloys. *Physical Review B*, 33(12):7983, 1986.
- [26] M. I. Baskes. Modified embedded-atom potentials for cubic materials and impurities. *Physical Review B*, 46(5):2727–2742, 1992.
- [27] M. S. Daw, S. M. Foiles, and M. I. Baskes. The embedded-atom method: a review of theory and applications. *Materials Science Reports*, 9:251–310, 1993.
- [28] G. J. Ackland, G. Tichy, V. Vitek, and M. W. Finnis. Simple n -body potentials for the noble metals and nickel. *Philosophical Magazine A*, 56:735, 1987.
- [29] G. J. Ackland and V. Vitek. Many-body potentials anti atomic-scale relaxations in noble-metal alloys. *Physical Review B*, 41(15):10324–10333, 1990.
- [30] A. F. Voter and S. P. Chen. Accurate interatomic potentials for Ni, Al, and Ni₃Al. In *Materials Research Society Symposia Proceedings*, volume 82, pages 175–180. Pittsburgh, Materials Research Society, 1987.
- [31] J. F. Ziegler, J. P. Beirsack, and U. Littmark. *The stopping and range of ions in solids*, volume 1. Pergamon, New York, 1985.
- [32] L. Greengard. *The Rapid Evaluation of Potential Fields in Particle Systems*. ACM distinguished dissertations. The MIT Press, 1988.
- [33] J. Barnes and P. Hut. A hierarchical $o(n \log n)$ force-calculation algorithm a hierarchical $O(N \log N)$ force-calculation algorithm. *Nature*, 324:446–449, 1986.

- [34] M. Matsui and M. Akaogi. Molecular dynamics simulation of the structural and physical properties of the four polymorphs of TiO_2 . *Molecular Simulation*, 6:239–244, 1991.
- [35] V. Swamy, J. D. Gale, and L. S. Dubrovinsky. Atomistic simulation of the crystal structures and bulk moduli of TiO_2 polymorphs. *Journal of Physics and Chemistry of Solids*, 62:887–895, 2001.
- [36] B. P. Uberuaga and X. Bai. Defects in rutile and anatase polymorphs of TiO_2 : kinetics and thermodynamics near grain boundaries. *Journal of Physics: Condensed Matter*, 23:435004, 2011.
- [37] D. R. Collins and W. Smith. Evaluation of TiO_2 force fields. Technical Report DL-TP-96-001, Daresbury Laboratory, 1996.
- [38] A. Hallil, R. Tetot, F. Berthier, I. Braems, and J. Creuze. Use of a variable-charge interatomic potential for atomistic simulations of bulk, oxygen vacancies, and surfaces of rutile TiO_2 . *Physical Review B*, 73:165406, 2006.
- [39] A. K. Rappé and W. A. Goddard. Charge equilibration for molecular dynamics simulations. *Journal of Physical Chemistry*, 95:3358, 1991.
- [40] J. Creuze, F. Berthier, R. Tetot, and B. Legrand. Intergranular segregation and ordering effect: A mixed monte carlo mean-field approach. *Physical Review B*, 62(4):2813–2824, 2000.
- [41] M. Born and J. E. Mayer. Zur gittertheorie der ionenkristalle. *Z. Physik*, 75:1–18, 1932.
- [42] E. J. Sanville, L. J. Vernon S. D. Kenny, R. Smith, Y. Moghaddam, C. Browne, and P. Mulheran. Surface and interstitial transition barriers in rutile (110) surface growth. *Physical Review B*, 80:235308, 2009.
- [43] P. A. Mulheran, C. S. Browne, and Y. Moghaddam. Adatoms and interstitials in the rutile TiO_2 (110) surface: structure and dynamics. *Molecular Simulation*, 35(7):532–537, 2009.
- [44] K. Albe, K. Nordlund, and R. S. Averback. Modeling the metal-semiconductor interaction: Analytical bond-order potential for platinum-carbon. *Physical Review B*, 65:195124, 2002.

- [45] K. Albe, K. Nordlund, J. Nord, and A. Kuronen. Modeling of compound semiconductors: Analytical bond-order potential for Ga, As, and GaAs. *Physical Review B*, 66:035205, 2002.
- [46] J. Nord, K. Albe, P. Erhart, and K. Nordlund. Modelling of compound semiconductors: analytical bond-order potential for gallium, nitrogen and gallium nitride. *Journal of Physics: Condensed Matter*, 15:5649–5662, 2003.
- [47] N. Juslin, P. Erhart, P. Traskelin, J. Nord, K. O. E. Henriksson, K. Nordlund, E. Salonen, and K. Albe. Analytical interatomic potential for modeling nonequilibrium processes in the W–C–H system. *Journal of Applied Physics*, 98:123520, 2005.
- [48] P. Erhart, N. Juslin, O. Goy, K. Nordlund, R. Müller, and K. Albe. Analytic bond-order potential for atomistic simulations of zinc oxide. *Journal of Physics: Condensed Matter*, 18:6585–6605, 2006.
- [49] P. Erhart and K. Albe. Pontifix/penguin: A program package for fitting interatomic potentials of the bond-order type. <http://www.mm.mw.tu-darmstadt.de/pontifix>.
- [50] G. C. Abell. Empirical chemical pseudopotential theory of molecular and metallic bonding. *Physical Review B*, 31(10):6184–6196, 1985.
- [51] J. Tersoff. Empirical interatomic potential for carbon, with applications to amorphous carbon. *Physical Review Letters*, 61(25):2879–2882, 1988.
- [52] D. W. Brenner. Empirical potential for hydrocarbons for use in simulating the chemical vapor deposition of diamond films. *Physical Review B*, 42(15):9458–9471, 1990.
- [53] S. J. Stuart, A. B. Tutein, and J. A. Harrison. A reactive potential for hydrocarbons with intermolecular interactions. *Journal of Chemical Physics*, 112:6472–6487, 2000.
- [54] A. C. T. van Duin, S. Dasgupta, F. Lorant, and W. A. Goddard III. ReaxFF: A reactive force field for hydrocarbons. *Journal of Physical Chemistry A*, 105:9396–9409, 2001.
- [55] A. C. T. van Duin, A. Strachan, S. Stewman, Q. Zhang, X. Xu, and W. A. Goddard III. *ReaxFF_{SiO}* reactive force field for silicon and silicon oxide systems. *Journal of Physical Chemistry A*, 107:3803–3811, 2003.

- [56] D. Raymand, A. C. T. van Duin, M. Baudin, and K. Hermansson. A reactive force field (ReaxFF) for zinc oxide. *Surface Science*, 602(5):1020–1031, 2008.
- [57] E. Polak and G. Ribière. Note sur la convergence de méthodes de directions conjuguées. *Revue Francaise d’Informatique et de Recherche*, 1969.
- [58] R. Fletcher. Function minimization by conjugate gradients. *The Computer Journal*, 7(2):149–154, 1964.
- [59] H. J. C. Berendsen, J. P. M. Postma, W. F. van Gunsteren, A. DiNola, and J. R. Haak. Molecular dynamics with coupling to an external bath. *Journal of Chemical Physics*, 81(8):3684–3690, 1984.
- [60] S. Nosé. A molecular dynamics method for simulations in the canonical ensemble. *Molecular Physics*, 52(2):255–268, 1984.
- [61] S. Nosé. A unified formulation of the constant temperature molecular dynamics methods. *Journal of Chemical Physics*, 81(1):511–519, 1984.
- [62] W. G. Hoover. Canonical dynamics: Equilibrium phase-space distributions. *Physical Review A*, 31(3):1695–1697, 1985.
- [63] G. Henkelman and H. Jónsson. Long time scale kinetic monte carlo simulations without lattice approximation and predefined event table. *Journal of Chemical Physics*, 115(21):9657–9666, 2001.
- [64] H. Jónsson, G. Mills, and K. W. Jacobsen. *Classical and Quantum Dynamics in Condensed Phase Simulations*, chapter Nudged Elastic Band Method for Finding Minimum Energy Paths of Transitions, pages 385–404. World Scientific, 1998.
- [65] B. Peters, A. Heyden, A. T. Bell, and A. Chakraborty. A growing string method for determining transition states: comparison to the nudged elastic bank and string methods. *Journal of Chemical Physics*, 120(17):7877–7886, 2004.
- [66] W. E, W. Ren, and E. Vanden-Eijnden. Simplified and improved string method for computing the minimum energy paths in barrier-crossing events. *Journal of Chemical Physics*, 126(16):164103–164108, 2007.
- [67] G. Henkelman and H. Jónsson. A dimer method for finding saddle points on high dimensional potential surfaces using only first derivatives. *Journal of Chemical Physics*, 111(15):7010–7022, 1999.

- [68] G. T. Barkema and N. Mousseau. Travelling through potential energy landscapes of disordered materials: The activation-relaxation technique. *Physical Review E*, 57(2):2419–2424, 1998.
- [69] G. T. Barkema and N. Mousseau. Event-based relaxation of continuous disordered systems. *Physical review letters*, 77(21):4358–4361, 1996.
- [70] G. Henkelman and H. Jónsson. Multiple time scale simulations of metal crystal growth reveal the importance of multiatom surface processes. *Physical Review Letters*, 90(11):116101–1–4, 2003.
- [71] D. Mei, L. Xu, and G. Henkelman. Potential energy surface of methanol decomposition on Cu(110). *Journal of Chemical Physics*, 113:4522–4537, 2009.
- [72] L. Xu, D. Mei, and G. Henkelman. Adaptive kinetic monte carlo simulation of methanol decomposition on Cu(100). *Journal of Chemical Physics*, 131:244520, 2009.
- [73] A. Pedersen, G. Henkelman, J. Schiotz, and H. Jónsson. Long time scale simulation of a grain boundary in copper. *New Journal of Physics*, 11:073034, 2009.
- [74] K. A. Fitchthorn and M. Scheffler. Island nucleation in thin-film epitaxy: a first-principles investigation. *Physical Review Letters*, 84(23):5371–5374, 2000.
- [75] A. F. Voter. Parallel replica method for dynamics of infrequent events. *Physical Review B*, 57(22):R13985–R13988, 1998.
- [76] A. F. Voter, F. Montalenti, and T. C. Germann. Extending the time scale in atomistic simulation of materials. *Annual Review of Materials Research*, 32:321–346, 2002.
- [77] A. F. Voter. A method for accelerating the molecular dynamics simulation of infrequent events. *Journal of Chemical Physics*, 106:4665–77, 1997.
- [78] A. F. Voter. Hyperdynamics: Accelerated molecular dynamics of infrequent events. *Physical Review Letters*, 78:3908, 1997.
- [79] M. R. Sorensen and A. F. Voter. Temperature-accelerated dynamics for simulation of infrequent events. *Journal of Chemical Physics*, 112(21):9599–9606, 2000.

- [80] F. Montalenti, M. R. Sorensen, and A. F. Voter. Closing the gap between experiment and theory: crystal growth by temperature accelerated dynamics. *Physical Review Letters*, 87:126101:1–4, 2001.
- [81] J. A. Sprague, F. Montalenti, B. P. Uberuaga, J. D. Kress, and A. F. Voter. Simulation of growth of Cu on Ag(001) at experimental deposition rates. *Physical Review B*, 66(20):205415:1–10, 2002.
- [82] G. Henkelman, D. Sheppard, and R. Terrell. Optimization methods for finding minimum energy paths. *Journal of Chemical Physics*, 128(134106):1–10, 2008.
- [83] S. Gordon. *Atomistic Modelling of Diffusion*. PhD thesis, Loughborough University, 2006.
- [84] G. H. Vineyard. Frequency factors and isotope effects in solid state rate processes. *Journal of Physics and Chemistry of Solids*, 3(1-2):121–127, 1957.
- [85] G. Henkelman and H. Jónsson. Long time scale simulations of Al (100) crystal growth. *Atomistic Aspects of Epitaxial Growth*, pages 63–74, 2002.
- [86] M. Brogren, P. Nostell, and B. Karlsson. Optical efficiency of a PV-thermal hybrid CPC module for high latitudes. *Solar Energy*, 69(6):173–185, 2001.
- [87] J. S. Coventry. Performance of a concentrating photovoltaic/thermal solar collector. *Solar Energy*, 78(2):211–222, 2005.
- [88] D. A. Jaworske. Reflectivity of silver and silver-coated substrates from 25 °C to 800 °C [for solar collectors]. In *Energy Conversion Engineering Conference, 1997. IECEC-97., Proceedings of the 32nd Intersociety*, volume 1, pages 407–411, 1997.
- [89] C. J. Howe, M. D. Cropper, R. M. Wardle, P. Bailey, and T. C. Q. Noakes. Stacking faults in ultra-thin films of silver on Al(111) investigated by medium energy ion scattering. *Surface Science*, 604:1658–1665, 2010.
- [90] C. Scott, S. Blackwell, L. J. Vernon, S. D. Kenny, J. M. Walls, and R. Smith. Atomistic surface erosion and thin film growth modelled over realistic time scales. *Journal of Chemical Physics*, 135:174706, 2011.

- [91] S. Blackwell, R. Smith, S. D. Kenny, and J. M. Walls. Modeling the sputter deposition of thin film photovoltaics using long time scale dynamics techniques. In *MRS Proceedings: Symposium G- Complex Oxide Materials for Emerging Energy Technologies*, volume 1327, 2011.
- [92] S. Blackwell, R. Smith, and S. D. Kenny. Modeling evaporation, ion-beam assist, and magnetron sputtering of thin metal films over realistic time scales. *Physical Review B*, 86:035416–1–12, 2012.
- [93] J. T. Cheung and H. Sankur. Growth of thin films by laser-induced evaporation. *Critical Reviews in Solid State and Materials Sciences*, 15(1):63–109, 1988.
- [94] F. A. Smidt. Use of ion beam assisted deposition to modify the microstructure and properties of thin films. *International Materials Reviews*, 35:61–128, 1990.
- [95] I. Safi. Recent aspects concerning DC reactive magnetron sputtering of thin films: a review. *Surface and Coatings Technology*, 127:203–219, 2000.
- [96] K. Reichelt and X. Jiang. The preparation of thin films by physical vapour deposition methods. *Thin Solid Films*, 191:91–126, 1990.
- [97] R. S. Dhaka, K. Gururaj, S. Abhaya, G. Amarendra, S. Amirthapandian, B. K. Panigrahi, K. G. M. Nair, N. P. Lalla, and S. R. Barman. Depth-resolved positron annihilation studies of argon nanobubbles in aluminum. *Journal of Applied Physics*, 105:054304–1–054304–5, 2009.
- [98] C. J. Rossouw and S. E. Donnelly. Superheating of small solid-argon bubbles in aluminum. *Physical Review Letters*, 55(27):2960–2963, 1985.
- [99] C. Biswas, A. K. Shukla, S. Banik, S. R. Barman, and A. Chakrabarti. Argon nanobubbles in Al(111): A photoemission study: A photoemission study. *Physical Review Letters*, 92(11):115506–1–115506–4, 2004.
- [100] M. Schmid, W. Hebenstreit, P. Varga, and S. Crampin. Quantum wells and electron interference phenomena in Al due to subsurface noble gas bubbles. *Physical Review Letters*, 76(13):2298–2301, 1996.
- [101] R. D. Bland, G. J. Kominiak, and D. M. Mattox. Effect of ion bombardment during deposition on thick metal and ceramic deposits. *Journal of Vacuum Science and Technology*, 11:671–674, 1974.

- [102] D. M. Mattox and G. J. Kominiak. Structure modification by ion bombardment during deposition. *Journal of Vacuum Science and Technology*, 9:528–532, 1972.
- [103] V. Fournée, J. Ledieu, T. Cai, and P. A. Thiel. Influence of strain in Ag on Al(111) and Al on Ag(100) thin film growth. *Physical Review B*, 67:155401, 2003.
- [104] M. I. Baskes. Meam for covalent Si. *Physical Review Letters*, 59:2666–2669, 1987.
- [105] M. I. Baskes, J. S. Nelson, and A. F. Wright. Meam for covalent Si and Ge. *Physical Review B*, 40:6085–6100, 1989.
- [106] R. L. Schwoebel and E. J. Shipsey. Step motion on crystal surfaces. *Journal of Applied Physics*, 37:3682, 1966.
- [107] G. Ehrlich and F. G. Hudda. Atomic view of surface self diffusion: Tungsten on tungsten. *Journal of Chemical Physics*, 44:1039, 1966.
- [108] M. Li, Y. Han, P. A. Thiel, and J. W. Evans. Formation of complex wedding-cake morphologies during homoepitaxial film growth of Ag on Ag(111): atomistic, step-dynamics, and continuum modeling. *Journal of Physics: Condensed Matter*, 21:084216, 2009.
- [109] C. L. Liu, J. M. Cohen, and J. B. Adams A. F. Voter. EAM study of surface self-diffusion of single adatoms of Fee metals Ni, Cu, Al, Ag, Au, Pd, and Pt. *Surface Science*, 253:334–344, 1991.
- [110] S. Xiao and W. Hu. Molecular dynamics simulations of grain growth in nanocrystalline Ag. *Journal of Crystal Growth*, 286(2):512–517, 2006.
- [111] V. Georgieva, A. F. Voter, and A. Bogaerts. Understanding the surface diffusion processes during magnetron sputter-deposition of complex oxide Mg-Al-O thin films. *Crystal Growth and Design*, 11:2553–2558, 2011.
- [112] D. P. Woodruff and J. Robinson. Sb-induced surface stacking faults at Ag(111) and Cu(111) surfaces: density-functional theory results. *Journal of Physics: Condensed Matter*, 12(35):7699, 2000.
- [113] R. Meyer and L. J. Lewis. Stacking-fault energies for Ag, Cu, and Ni from empirical tight-binding potentials. *Physical Review B*, 66(5):052106, 2002.

- [114] J. Xu, W. Lin, and A. J. Freeman. Twin-boundary and stacking-fault energies in Al and Pd. *Physical Review B*, 43(3):2018–2024, 1991.
- [115] N. W. Ashcroft and D. N. Mermin. *Solid State Physics*, chapter 20: Cohesive Energy, pages 395–414. N. W. Ashcroft and D. N. Mermin, 1976.
- [116] Z. Zhang, W. A. Anderson, and M. Moo-Young. Rigorous modeling of uv absorption by TiO₂ films in a photocatalytic reactor. *American Institute of Chemical Engineers Journal*, 46:1461–1470, 2000.
- [117] V. E. Henrich. The nature of transition-metal-oxide surfaces. *Progress in Surface Science*, 14(2):175–199, 1983.
- [118] S. Blackwell, R. Smith, S. D. Kenny, L. J. Vernon, and J. M. Walls. Modeling evaporation, ion-beam assist, and magnetron sputtering of TiO₂ thin films over realistic timescales. *Journal of Materials Research*, 27(5):799–805, 2012.
- [119] D. E. Wolfe and J. Singh. Microstructural evolution of titanium nitride TiN coatings produced by reactive ion beam-assisted, electron beam physical vapor deposition RIBA, EB-PVD. *Journal of Materials Science*, 34:2997–3006, 1999.
- [120] K. Bange, C. R. Ottermann, O. Anderson, U. Jeschkowski, M. Laube, and R. Feile. Investigations of TiO₂ films deposited by different techniques. *Thin Solid Films*, 197:279–285, 1991.
- [121] F. Zhang, S. Jin, Y. Mao, Z. Zheng, Y. Chen, and X. Liu. Surface characterization of titanium oxide films synthesized by ion beam enhanced deposition. *Thin Solid Films*, 310:29–33, 1997.
- [122] S. H. Kim, J. H. Lee, C. K. Hwangbo, and S. M. Lee. DC reactive magnetron sputtering with Ar ion-beam assistance for titanium oxide films. *Surface and Coatings Technology*, 158-159:457–464, 2002.
- [123] S. H. Kim and C. K. Hwangbo. Influence of Ar ion-beam assistance and annealing temperatures on properties of TiO₂ thin films deposited by reactive DC magnetron sputtering. *Thin Solid Films*, 475:155–159, 2005.
- [124] P. Zeman and S. Takabayashi. Nano-scaled photocatalytic TiO₂ thin films prepared by magnetron sputtering. *Thin Solid Films*, 433:57–62, 2003.

- [125] J. Sicha, J. Musil, M. Meissner, and R. Cerstvy. Nanostructure of photocatalytic TiO₂ films sputtered at temperatures below 200C. *Applied Surface Science*, 254:3793–3800, 2008.
- [126] K. Eufinger, E. N. Janssen, H. Poelman, D. Poelman, R. de Gryse, and G. B. Marin. The effect of argon pressure on the structural and photocatalytic characteristics of TiO₂ thin films deposited by d.c. magnetron sputtering. *Thin Solid Films*, 515:425–429, 2006.
- [127] A. Amin, D. Kohl, and M. Wuttig. The role of energetic ion bombardment during growth of TiO₂ thin films by reactive sputtering. *Journal of Physics D: Applied Physics*, 43:405303, 2010.
- [128] P. Karmakar, G. F. Lui, and J. A. Yarmoff. Sputtering-induced vacancy cluster formation on TiO₂(110). *Physical Review B*, 76:193410, 2007.
- [129] Y. S. Jin and H. W. Choi. Properties of dye-sensitized solar cells with TiO₂ passivating layers prepared by electron-beam evaporation. *Journal of Nanoscience and Nanotechnology*, 12(1):662–7, 2012.
- [130] O. Schwarz, D. Loyen, S. Jockusch, N. J. Turro, and H. Durr. Preparation and application of new ruthenium(ii) polypyridyl complexes as sensitizers for nanocrystalline TiO₂. *Journal of Photochemistry and Photobiology A: Chemistry*, 132:91–98, 2000.
- [131] H. Wang, C. Su, H. Chen, Y. Liu, Y. Hsu, N. Hsu, and W. Li. Preparation of nanoporous TiO₂ electrodes for dye-sensitized solar cells. *Journal of Nanomaterials*, 2011:7, 2011.
- [132] J. Szczyrbowski, G. Brauer, G. Teschner, and A. Zmelty. Antireflective coatings on large scale substrates produced by reactive twin-magnetron sputtering. *Journal of Non-Crystalline Solids*, 218:25–29, 1997.
- [133] W. T. Pawlewicz, P. M. Martin, D. D. Hays, and I. B. Mann. Recent development in reactively sputtered optical thin films. In *Proceedings of SPIE-The International Society for Optical Engineering*, volume 325, pages 105–116, 1982.
- [134] M. J. J. Jak, A. van Kreuningen, J. Verhoeven, and J. W. M. Frenken. The effect of stoichiometry on the stability of steps on TiO₂(110). *Applied Surface Science*, 201:161–170, 2002.

- [135] J. T. Mayer, U. Diebold, T. E. Madey, and E. Garfunkel. Titanium and reduced titania overlayers on titanium dioxide (110). *Journal of Electron Spectroscopy and Related Phenomena*, 73:1–11, 1995.
- [136] Jeong S-H, Kim B-S, Lee B-T, H. R. Park, and J-K. Kim. Structural and optical properties of TiO₂ films prepared using reactive RF magnetron sputtering. *Journal of the Korean Physical Society*, 41(1):67–72, 2002.
- [137] P. Kofstad. Thermogravimetric studies of the defect structure of rutile TiO₂. *Journal of Physics and Chemistry of Solids*, 23(11):1579–1586, 1962.
- [138] M. Henderson. A surface perspective on self-diffusion in rutile TiO₂. *Surface Science*, 419(2-3):174–187, 1999.
- [139] R. H. Tait and R. V. Kasowski. Ultraviolet photoemission and low-energy-electron diffraction studies of TiO₂ (rutile) (001) and (110) surfaces. *Physical Review B*, 20(12):5178–5191, 1979.
- [140] G. J. Exarhos. Raman determination of molecular structure and physical properties of dielectric coatings. *Journal of Vacuum Science and Technology A*, 4(6):2962, 1986.
- [141] P. Lobl, M. Huppertz, and D. Mergel. Nucleation and growth in TiO₂ films prepared by sputtering and evaporation. *Thin Solid Films*, 251:72–79, 1994.
- [142] H. Onishi and Y. Iwasawa. Dynamic visualization of a metal-oxide-surface/gas-phase reaction: time-resolved observation by scanning tunneling microscopy at 800 K. *Physical Review Letters*, 76(5):791–794, 1996.
- [143] B. Thomas, N. Marks, L. Corrales, and R. Devanathan. Threshold displacement energies in rutile TiO₂: A molecular dynamics simulation study. *Nuclear Instruments and Methods in Physics Research Section B: Beam Interactions with Materials and Atoms*, 239(3):191–201, 2005.
- [144] H. Sawatari and E. Iguchi. Formation energies of point defects in rutile TiO₂. *Journal of Physics and Chemistry of Solids*, 43(12):1147–1155, 1982.
- [145] E. Cho, S. Han, H. Ahn, K. Lee, S. Kim, and C. Hwang. First-principles study of point defects in rutile TiO_{2-x}. *Physical Review B*, 73:19, 2006.
- [146] S. Wendt, P. T. Sprunger, E. Lira, G. K. H. Madsen, Z. Li, J. Hansen, J. Matthiesen, A. Blekinge-Rasmussen, E. Lægsgaard, B. Hammer, and

- F. Besenbacher. The role of interstitial sites in the Ti3d defect state in the band gap of titania. *Science*, 320:1755, 2008.
- [147] L. J. Vernon, S. D. Kenny, and R. Smith. Growth of TiO₂ surfaces following low energy (≤ 40 eV) atom and small cluster bombardment. *Nuclear Instruments and Methods in Physics Research B*, 268:2942–2946, 2010.
- [148] L. J. Vernon, R. Smith, and S. D. Kenny. Modelling of deposition processes on the TiO₂ rutile (110) surface. *Nuclear Instruments and Methods in Physics Research B*, 267:3022–3024, 2009.
- [149] R. Smith and W. Möller. Surface erosion of TiO₂ subjected to energetic oxygen bombardment. In *Materials Research Society Symposium Proceedings*, volume 1298, pages 191–196. Cambridge University Press, 2011.
- [150] L. J. Vernon. *Modelling the Growth of TiO₂*. Ph.D. thesis, Loughborough University, 2010.
- [151] J. M. Walls, D. D. Hall, D. G. Teer, and B. L. Delcea. A comparison of vacuum-evaporated and ion-plated thin films using auger electron spectroscopy. *Thin Solid Films*, 54:303–308, 1978.
- [152] Z. L. Wang. Zinc oxide nanostructures: growth, properties and applications. *Journal of Physics: Condensed Matter*, 16:R829–R858, 2004.
- [153] T. Minami. Transparent conducting oxide semiconductors for transparent electrodes. *Semiconductor Science and Technology*, 20(4):S35–S44, 2005.
- [154] C. H. Bates, W. B. White, and R. Roy. New high-pressure polymorph of ZnO. *Science*, 137:993, 1962.
- [155] H. Morkoç and U. Özgür. *Zinc Oxide: Fundamentals, Materials and Device Technology*, chapter 1. General Properties of ZnO, pages 1–76. Wiley-VCH, 2009.
- [156] K. Ellmer, A. Klein, and B. Rech. *Transparent Conductive Zinc Oxide: Basics and Applications in Thin Film Solar Cells*. Springer Series in Materials Science. Springer, 2008.
- [157] Z. Lin and P. D. Bristowe. Microscopic characteristics of the Ag(111)/ZnO(0001) interface present in optical coatings. *Physical Review B*, 75:205423–1–13, 2007.

- [158] T. S. Heng, A. Kumar, C. S. Ong, Y. P. Feng, Y. H. Lu, K. Y. Zeng, and J. Ding. Investigation of the non-volatile resistance change in noncentrosymmetric compounds. *Scientific reports*, 2(587), 2012.
- [159] O. A. Fouad, A. A. Ismail, Z. I. Zanki, and R. M. Mohamed. Zinc oxide thinfilms prepared by thermalevaporation deposition and its photocatalytic activity. *Applied Catalysis B: Environmental*, 62(1-2):144–149, 2006.
- [160] F. Chowdhury. Influence of thickness variation on the optical properties of ZnO thin films prepared by thermal evaporation method. *Journal of Electron Devices*, 10:448–455, 2011.
- [161] F. C. M. van de Pol, F. R. Blom, and Th. J. A. Popma. R.F. planar magnetron sputtered ZnO films i: Structural properties. *Thin Solid Films*, 204:349–364, 1991.
- [162] U. Özgür, Y. I. Alivov, C. Liu, A. Teke, M. A. Reshchikov, S. Dogan, V. Avrutin, S. J. Cho, and H. Morkoç. A comprehensive review of ZnO materials and devices. *Journal of Applied Physics*, 98:041301, 2005.
- [163] E. Chitanu and G. Ionita. Obtaining thin layers of ZnO with magnetron sputtering method. *International Journal of Computers*, 4(4):243–250, 2010.
- [164] D. Kohl, M. Luysberg, and M. Wuttig. Structural improvement of zinc oxide films produced by ion beam assisted reactive sputtering. *Journal of Physics D: Applied Physics*, 43:205301, 2012.
- [165] K. Y. Lee, C. Becker, M. Muske, F. Ruske, S. Gall, B. Rech, M. Berginski, and J. Hupkes. Temperature stability of ZnO:Al film properties for poly-Si thin-film devices. *Applied Physics Letters*, 91:241911, 2007.
- [166] F. Ruske, M. Roczen, K. Lee, M. Wimmer, S. Gall, J. Hupkes, D. Hrunski, and B. Rech. Improved electrical transport in Al-doped zinc oxide by thermal treatment. *Journal of Applied Physics*, 107:013708, 2012.
- [167] M. Warzecha, J. I. Owen, M. Wimmer, F. Ruske, J. Hotovy, and J. Hupkes. High mobility annealing of transparent conductive oxides. In *E-MRS 2011 Fall Symposium I*, volume 34 of *IOP Conf. Series: Materials Science and Engineering*, page 012004. IOP Publishing Ltd, 2012.

- [168] M. Wimmer, F. Ruske, S. Scherf, and B. Rech. Improving the electrical and optical properties of DC-sputtered ZnO:Al by thermal post deposition treatments. *Thin Solid Films*, 520(12):4203–4207, 2012.
- [169] Y. Ding, Z. L. Wang, T. Sun, and J. Qui. Zinc-blende ZnO and its role in nucleating wurtzite tetrapods and twinned nanowires. *Applied Physics Letters*, 90:153510, 2007.
- [170] Y. Yan, M. M. Al-Jassim, K. M. Jones, S-H. Wei, and S. B. Zhang. Observation and first-principles calculation of buried wurtzite phases in zinc-blende CdTe thin films. *Applied Physics Letters*, 77(10):1461–1463, 2000.
- [171] Y. Yan, M. M. Al-Jassim, and K. M. Jones. Characterization of extended defects in polycrystalline CdTe thin films grown by close-space sublimation. *Thin Solid Films*, 389:75–77, 2001.
- [172] Z. Ikonic, G. P. Srivastava, and J. C. Inkson. Optical properties of twinning superlattices in diamond-type and zinc-blende-type semiconductors. *Physical Review B: Condensed Matter*, 52(19):14078–14085, 1995.
- [173] J. E. Jaffe, N. M. Harrison, and A. C. Hess. Ab-initio study of ZnO (10 $\bar{0}$) surface relaxation. *Physical Review B*, 49:11153, 1994.
- [174] G. Kresse, O. Dulub, and U. Diebold. Competing stabilization mechanism for the polar ZnO(0001)-Zn surface. *Physical Review B*, 68:245409, 2003.
- [175] A. F. Kohan, G. Ceder, D. Morgan, and C. G. Van de Walle. First-principles study of native point defects in ZnO. *Physical Review B*, 61:15019, 2000.
- [176] S. B. Zhang, S. H. Wei, and A. Zunger. Intrinsic n-type versus p-type doping asymmetry and the defect physics of ZnO. *Physical Review B*, 63:075205, 2001.
- [177] F. Oba, S. R. Nishitani, S. Isotani, H. Adachi, and I. Tanaka. Energetics of native defects in ZnO. *Journal of Applied Physics*, 90:824, 2001.
- [178] W. Korner, P. D. Bristowe, and C. Elsasser. Density functional theory study of stoichiometric and nonstoichiometric ZnO grain boundaries. *Physical Review B*, 84:045305, 2011.
- [179] M. Kubo, Y. Oumi, H. Takaba, A. Chatterjee, A. Miyamoto, M. Kawasaki, M. Yoshimoto, and H. Koinuma. Homoepitaxial growth mechanism

- of ZnO(0001): Molecular-dynamics simulations. *Physical Review B*, 61(23):16187–16192, 2000.
- [180] C. F. Dee, J. D. Lee, C. H. Sow, B. Y. Majlis, A. Hamzah, H. Abdullah, and S-K. Lee. Simulation for deposition of ZnO thin film layer by kinetic monte carlo method. *Materials Research Innovations*, 13(3):135–138(4), 2009.
- [181] I. Gheewala. *Multiscale modelling of nanoindentation of multilayered systems*. PhD thesis, Loughborough University, 2010.
- [182] J. B. Lee, H. J. Kim, S. G. Kim, C. S. Hwang, S-H. Hong, Y. H. Shin, and N. H. Lee. Deposition of ZnO thin films by magnetron sputtering for a film bulk acoustic resonator. *Thin Solid Films*, 435:179–185, 2003.
- [183] T. David, S. Goldsmith, and R. L. Boxman. Dependence of zinc oxide thin film properties on filtered vacuum arc deposition parameters. *Journal of Physics D: Applied Physics*, 38(14):2407, 2005.
- [184] S. W. Whangbo, H. K. Jang, S. G. Kim, M. H. Cho, K. Keong, and C. N. Whang. Properties of ZnO thin films grown at room temperature by using ionized cluster beam deposition. *Journal of the Korean Physical Society*, 37(4):456–460, 2000.
- [185] B. Meyer. First-principles study of the polar O-terminated ZnO surface in thermodynamic equilibrium with oxygen and hydrogen. *Publication: Physical Review B*, 69(4):045416, 2004.
- [186] E. S. Jung, J. Y. Lee, H. S. Kim, and N. W. Jang. Structural and optical characteristics of ZnO films with oxygen content. *Journal of the Korean Physical Society*, 47:S480–S484, 2005.
- [187] C. Li, X. C. Li, P. X. Yan, E. M. Chong, Y. Liu, G. H. Yue, and X. Y. Fan. Research on the properties of ZnO thin films deposited by using filtered cathodic arc plasma technique on glass substrate under different flow rate of O₂. *Applied Surface Science*, 253:4000–4005, 2007.